

IMPERIAL COLLEGE LONDON

**CREEP MONITORING
USING PERMANENTLY INSTALLED
POTENTIAL DROP SENSORS**

by

Joseph Corcoran

A thesis submitted to Imperial College London for the degree of
Doctor of Philosophy

Non-Destructive Evaluation Group
Department of Mechanical Engineering
Imperial College London
London SW7 2AZ

August 2015

Declaration of Originality

The work contained in this thesis is entirely my own, conducted under the supervision of Professor Peter Cawley and Professor Peter B. Nagy. Reference to published or unpublished material and any other contribution from others has been given full and clear acknowledgement.



Joseph Corcoran

29th August 2015

Copyright Declaration

The copyright of this thesis rests with the author and is made available under a Creative Commons Attribution Non-Commercial No Derivatives licence. Researchers are free to copy, distribute or transmit the thesis on the condition that they attribute it, that they do not use it for commercial purposes and that they do not alter, transform or build upon it. For any reuse or redistribution, researchers must make clear to others the licence terms of this work.

Abstract

Creep is the primary life limiting mechanism of static high temperature, high pressure power station components. Creep state evaluation is currently achieved by surface inspection of microstructure during infrequent outages; a methodology which is laborious, time consuming and considered inadequate. The objective of this work is to develop a monitoring technique that is capable of on-load creep damage monitoring. A continuous update of component integrity will enable better informed, targeted inspections and outage maintenance providing increased power generation availability.

A low-frequency, permanently installed potential drop system has been previously developed and will be the focus of this thesis. The use of a quasi-DC inspection frequency suppresses the influence of the electromagnetic skin effect that would otherwise undermine the stability of the measurement in the ferromagnetic materials of interest; the use of even low frequency measurements allows phase sensitive detection and greatly enhanced noise performance.

By permanently installing the electrodes to the surface of the component the resistance measurement is sensitive to strain. A resistance - strain inversion is derived and validated experimentally; the use of the potential drop sensor as a robust, high temperature strain gauge is therefore demonstrated.

The strain rate of a component is known to be an expression of the creep state of the component. This concept was adopted to develop an interpretive framework for inferring the creep state of a component. It is possible to monitor the accumulation of creep damage through the symptomatic *relative increase in strain rate*. By taking the ratio of two orthogonal strain measurements, instability and drift common to both measurements can be effectively eliminated; an important attribute considering the necessity to monitor very low strain rates over decades in time in a harsh environment.

A preliminary study of using the potential drop technique for monitoring creep damage at a weld has been conducted. Welds provide a site for preferential creep damage accumulation and therefore will frequently be the life limiting feature of power station components. The potential drop technique will be sensitive to both the localised strain that is understood to act as precursor to creep damage at a weld and also the initiation and growth of a crack.

Through the course of this project, two site trials have been conducted in power stations. A measurement system and high temperature hardware that is suitable for the power station environment has been developed. The focus of this thesis is the effective transfer of the technique to industry; the realisation of this is detailed in the final chapter.

Acknowledgements

Although it is my name on the cover of this thesis, the work has benefitted directly or indirectly from the contributions of so many.

First and foremost I am indebted to Peter Cawley and Peter Nagy; it has been an invaluable opportunity to work so closely with such distinguished engineers and academics. I have been fortunate to learn so much from their technical insight and mentorship. I am grateful in particular to their encouragement, however blunt, to meet their expectations and their patience when I did not.

Additionally, I'd like to thank Catrin Davies, Richard Challis and Paul Hooper for their expertise in their respective fields, the many undergraduate and postgraduate students who have contributed to this project and the technical staff, particularly Phil Wilson, who has enabled much of the experimental work. The work devoted to installing sensors in power stations will be grossly underrepresented in this thesis. Numerous people have contributed their time and effort into realising this goal but I'd like to particularly thank Colin Brett, Scott Lockyer, Andy Morris and Steve Lormor for their additional effort.

It has been a pleasure to work in the NDE group which has not only been a fantastic academic environment but more importantly has forged many friendships and provided many happy memories.

The most significant contributors to this thesis are my parents who have always encouraged me to fulfil my potential and, looking back, I am sure I would not be writing this now without the foundations that they provided. Likewise, I am thankful to the rest of the Corcoran's *et al.* for providing the support that they may not realise they have frequently been and particularly to Grandad who has shown such a keen interest in this work.

Above all I am thankful for the extraordinary patience and support of Agnieszka. You have directly contributed more to this thesis than probably anyone will appreciate and indirectly contributed more to this thesis than you appreciate.

Contents

1. Introduction	10
1.1 Introduction and Industrial Background	10
1.1.1 Industrial Motivation.....	10
1.1.2 Creep in Static Power Station Components	11
1.2 NDE for Creep in Pressurised Power Station Components	17
1.2.1 Replica Metallography.....	18
1.2.2 Ultrasonic Measurements.....	20
1.2.3 Magnetic methods.....	20
1.2.4 Hardness.....	21
1.2.5 Positron annihilation, x-ray diffraction and small angle neutron scattering	21
1.2.6 Strain.....	21
1.2.7 Potential Drop Measurements.....	24
1.3 Project Aims.....	25
1.4 Outline of Thesis.....	26
2. Low-Frequency Potential Drop Measurements	28
2.1 Introduction.....	28
2.2 Conventional Potential Drop Measurements	28
2.2.1 Direct Current Potential Drop	29
2.2.2 Alternating Current Potential Drop (ACPD).....	32
2.3 Low-Frequency Potential Drop Potential Drop Background.....	33
2.3.1 Systematic DC Interference	33
2.3.2 Flicker Noise.....	33
2.3.3 Suppression of the Skin Effect.....	35
2.4 Electrode Configuration: A Directional Resistance Measurement	36
2.5 Sensitivity Overview.....	37
2.6 Temperature Compensation	41

2.6.1	Thermocouple Compensation	41
2.6.2	The Normalised Resistance Ratio	41
2.7	Measurement Instrumentation.....	42
2.7.1	Lock-in Amplifiers.....	43
2.7.2	Measurement System	44
2.8	Example Measurement.....	46
2.8.1	Potential Drop Array.....	47
2.8.2	Elastic Loading	48
2.8.3	Plastic Loading.....	49
2.9	High Temperature Testing	52
2.10	Conclusions.....	53
3.	Electrical Conductivity Changes in Creep Exposed Power Station Steels	55
3.1	Introduction.....	55
3.2	Overview of the Microstructural Evolution of Creep Exposed Components	56
3.2.1	Dislocation Density.....	56
3.2.2	Carbide Evolution: Solute depletion and Carbide Coarsening.....	57
3.2.3	Grain Boundary Separation.....	57
3.3	Overview of conductivity in creep resistant steels.....	57
3.4	Dislocations.....	60
3.5	Carbide Evolution	60
3.5.1	Experiment Results on the Influence of Carbide Evolution from Literature	62
3.5.2	Continuous Measurement of the Influence of Carbide Evolution.....	63
3.6	Grain Boundary Separation.....	67
3.7	Discussion.....	73
3.7.1	Monitoring Strategies.....	73
3.8	Conclusions.....	75
4.	Strain Inversion of Potential Drop Measurements	76
4.1	Introduction.....	76

4.2	Creep Strain in Power Station Components.....	76
4.3	Inversion	79
4.3.1	Electrode Configurations	79
4.3.2	Strain Inversion of a Square Electrode Potential Drop Sensor on a Thick Walled Component.....	84
4.4	Small Component Considerations.....	87
4.4.1	Edge Effects	87
4.4.2	Imperfect Electrode Placement	90
4.5	Experimental Demonstration	92
4.5.1	Room Temperature Tensile Test.....	92
4.5.2	High Temperature Creep Tests	98
4.6	Discussion.....	105
4.6.1	The Normalised Resistance Inversion.....	106
4.6.2	The Normalised Resistance Ratio Inversion.....	106
4.7	Conclusion	107
5.	Interpretation of Potential Drop Data for the Creep State Assessment of Power Station Components	108
5.1	Introduction.....	108
5.1.1	Use of Strain Rate to Infer Creep Damage.....	109
5.2	Creep Rate Measurement Uncertainty	112
5.2.1	Rate Uncertainty Associated with Random Errors	112
5.2.2	Rate Uncertainty Associated with Systematic Errors	113
5.2.3	Creep Rate Measurement Uncertainty Conclusions	115
5.3	Normalised Resistance Ratio as a Metric for Strain Rate	116
5.3.1	The Normalised Resistance Ratio is a Function of Aspect Ratio	117
5.3.2	Aspect ratio is a Linear Function of Strain	117
5.3.3	Incorporation of the Normalised Resistance Ratio into Remnant Life Calculations ..	120
5.3.4	Experimental Demonstration	121
5.3.5	Application to Power Station Conditions.....	128

5.4	Conclusion	129
6.	Potential Drop Monitoring of Weldments	131
6.1	Introduction.....	131
6.1.1	Industrial Background.....	131
6.1.2	PD Measurements at a Weld.....	135
6.2	Potential Drop Monitoring at the Interface of Material Domains.....	135
6.2.1	Typical Weld/Parent Combinations	139
6.2.2	Reversible Temperature Dependency	140
6.2.3	Irreversible Thermally Activated Resistivity Change.....	142
6.2.4	Summary of Potential Drop Monitoring at the Interface of Material Domains	143
6.3	Influence of Cracking on Potential Drop Measurements	143
6.3.1	Simulation 1	145
6.3.2	Simulation 2	146
6.3.3	Summary	148
6.4	Cross-weld Uniaxial Creep Test	148
6.5	Conclusions.....	152
7.	Implementation of Potential Drop Creep Sensors in a Power Station Environment	154
7.1	Introduction.....	154
7.2	Sensor Hardware	154
7.3	Measurement System	156
7.4	E.ON Ratcliffe-On-Soar.....	157
7.5	EDF West Burton.....	158
7.5.1	Normalised Resistance.....	158
7.5.2	Normalised Resistance Ratio	162
7.6	Conclusions.....	164
8.	Conclusions	165
8.1	Thesis Review	165
8.2	Summary of Main Contributions	169

8.3	Future Work.....	170
A.	An Analytical Solution for Square Electrode Configuration Potential Drop Measurements	172
B.	Remnant Life Predictions from Strain Rate Measurements	175
B.1	Introduction.....	175
B.2	Kachanov & Rabotnov, Creep Damage Parameters	176
B.3	Voight, A Relation to Describe Rate-Dependent Material Behaviour.....	177
B.4	Materials Testing Council –The Omega Method.....	178
B.5	Discussion.....	179
B.6	Conclusion	181
C.	Uncertainty of Linear Rate Estimates Calculated from a Series of Measurements	182
	References	185

Chapter 1

Introduction

1.1 Introduction and Industrial Background

1.1.1 Industrial Motivation

Creep is the time dependent deformation of components which, in crystalline metallic materials, occurs under stress and at elevated temperature. In conventional power stations steam is heated to in excess of 550 °C and 150 bar pressure (Morris, 2015b) and as a result the life limiting damage mechanism for pressurised components is often creep (Furtado & May, 2004; Viswanathan & Stringer, 2000; Viswanathan, 1989; Webster & Ainsworth, 1994).

The cost associated with creep damage comes from many sources. Catastrophic component failure is uncommon but may result in loss of life, reputational damage, and will accumulate direct economic costs in repair, litigation, and lost generation. The total cost of the hot reheat pipe failure at the Mohave Power Station in 1986 is reported to be in excess of 400 million US dollars (in 1986 value) and 6 lives (EPRI, 2003; Viswanathan & Stringer, 2000). More commonly the currency of creep damage is lost unit availability and generation revenue; each day of outage can cost 500,000 US dollars in lost revenue (depending on market prices) (Viswanathan & Stringer, 2000). The emphasis therefore has to be the avoidance of unplanned outages due to component failure and the reduction of time in statutory outage. To achieve both of these goals information on component integrity is key.

Due to the demanding operating conditions it is accepted that power station components will degrade over time and therefore will be designed with a target fitness for service criterion of usually 100,000 hours service (EPRI, 2007; Viswanathan, 1989). A safety factor is then applied resulting in a 30-40 year expected component design life. In reality many power station components can operate safely beyond their original design life and life extension may be justified, but equally, due to unexpected adverse factors failure may be premature and early replacement necessary (Viswanathan, 1989). It is required that the component integrity is assessed to ensure that the components firstly reach their design life, and if so, provide confidence for life extension.

Conventionally, components are inspected during infrequent planned outages, which may be separated by years. This strategy has two inherent drawbacks; a) the component must be on outage for inspection to be carried out, costing generation availability and the ability to plan outage works in advance b) the data gathered will be so infrequent that rates and trends may be very difficult to infer. The adoption of an on-load creep monitoring technique will provide real time information on component integrity, providing confidence in the safe operation of plant and enabling shorter well planned outages.

1.1.2 Creep in Static Power Station Components

1.1.2.1 Creep

Introductions to creep are usually based on the simplified ‘primary’, ‘secondary’ and ‘tertiary’ description of the strain – time curve as shown in Figure 1.1 (Evans & Wilshire, 1993; Viswanathan, 1989; Webster & Ainsworth, 1994). Typically, such graphs are produced in a laboratory from small samples heated in a constant temperature furnaces while a constant uniaxial stress or load is applied by a tensile test machine. In the first instance the description of creep will assume this case of uniaxial loading and stress will be considered a scalar.

The three stages of creep are segmented according to the rate of strain accumulation caused by the underlying microstructural mechanisms that result in this characteristic form. The microstructural mechanisms are interdependent and result due to the presence of stress and elevated temperature. The dominance of different processes depends on the material properties and the subjected stress and temperature; the domains of different dominant mechanisms are conveniently displayed on ‘deformation mechanism maps’ (Viswanathan, 1989; Webster & Ainsworth, 1994). At temperatures above 40% of the melting point and at intermediate and high stresses the dislocation creep mechanism is operative, it is the only mechanism of significance for most engineering applications (Viswanathan, 1989) and the one that will be the focus of this thesis.

During primary creep the strain rate decreases to a constant steady state. The decrease in strain rate is attributed to strain hardening, the multiplication and production of dislocations. As a result of the elevated temperature, increased diffusion reduces the number and energy state of dislocations in a process of ‘recovery’ (Callister, 2006). The steady state ‘secondary’ creep results from a balance of strain hardening and softening processes resulting in an equilibrium (Callister, 2006; Evans & Wilshire, 1993; Viswanathan, 1989; Webster & Ainsworth, 1994).

The strain rate during secondary creep, $\dot{\epsilon}_s$, in the dislocation creep domain is generally understood to be a function of stress, σ , and temperature, T ,

$$\dot{\epsilon}_s = u(T) v(\sigma) . \tag{1.1}$$

As creep is a thermally activated process, the temperature sensitivity obeys an Arrhenius rate expression,

$$u(T) = A \exp\left(-\frac{Q}{RT}\right) \quad (1.2)$$

where A is a material constant, Q is the activation energy and R is the universal gas constant. The stress dependency follows the ‘Norton power law’,

$$v(\sigma) = B\sigma^n \quad (1.3)$$

where B and n are often considered material constants, n is frequently referred to as the Norton stress exponent which typically has a value of 5-15 for the materials of interest (Wasmer, 2003).

Numerous damage mechanisms may play a role in reducing the creep tolerance of a component. The accumulation of damage disturbs the balance of secondary creep and the strain rate accelerates into tertiary creep.

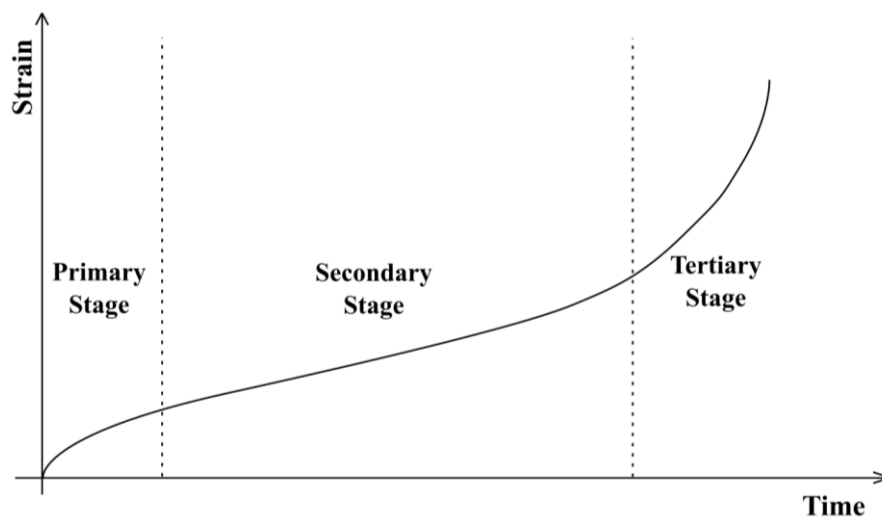


Figure 1.1: Illustration of the strain - time creep curve. The conventional description of primary, secondary and tertiary regimes separated by strain rates are shown.

The creep damage mechanisms may be considered as internal or external as shown in Figure 1.2, following the terminology of Dyson (Ashby & Dyson, 1984; Dyson, 2000). External damage mechanisms act by increasing the net stress by reducing the remaining cross section of the component. Creep strain and particularly necking will reduce the available cross section by conservation of volume. Interaction with the environment in the way of oxidation, corrosion, spalling etc. may also reduce cross section. Equation 1.3 suggests that even small changes in cross section will result in very substantial increases in strain rate. Internal damage reduces the materials capacity to sustain load by either loss of internal cross section (by grain boundary separation) or weakening of the remaining cross section, most

notably by thermally activated solute depletion and coarsening of carbides. Ultimately, it is usually grain boundary separation, the nucleation of cavities and the subsequent coalescence of micro, and eventually macro cracks, that leads to eventual component failure (Evans & Wilshire, 1993). It is worth noting that it is often grain boundary separation that is referred to as creep ‘creep damage’ as it is the mechanism that results exclusively from creep. In this thesis all mechanisms which compromise the creep sustaining integrity of a component will be considered damage.

Figure 1.2: Illustrations of Internal and External Damage Mechanisms. Adapted from (Ashby & Dyson, 1984).

In reality, damage accumulates through the entire life of the component. The weakening of the material must therefore cause a symptomatic continuously increasing strain rate following primary creep. It is therefore more appropriate to consider the secondary creep rate a minimum creep rate, which accelerates through the remaining life of the component, as illustrated in Figure 1.3 (Abe, 2008; Naumenko &

Altenbach, 2007; Wilshire & Burt, 2005, 2008). The *increase in strain rate* may then provide information on the damage state of the component.

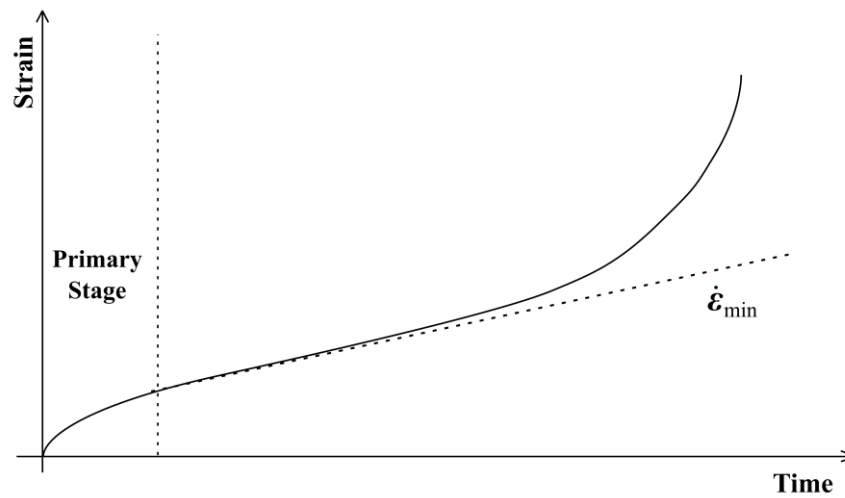


Figure 1.3: Illustration of the strain - time creep curve. The revised model based on increasing strain rate from a minimum due to the accumulation of creep damage is shown.

Due to the 100,000+ hour design life of power station components, testing components under realistic conditions becomes infeasible and tests must be carried out using increased stresses and/or temperatures to accelerate creep. Different ductility materials subjected to different stresses and temperatures alter the balance of the different creep mechanisms with a resulting impact on the dominance of the ‘primary’, ‘secondary’ and ‘tertiary’ appearance of the curves; a range of characteristic curve shapes result. Typically, the higher stresses and temperatures in accelerated component tests reduces the extent of the primary stage and practically eliminates the secondary stage with tertiary dominating throughout. Decreasing temperatures and stresses makes the first two stages more pronounced, usually at the expense of the tertiary stage and the total elongation (Viswanathan, 1989).

1.1.2.2 Power Station Components

Creep has the potential to be problematic in components subjected to the elevated temperature and pressures of the boiler outlet. Of particular concern are headers, steam pipes and superheater reheat pipes (Viswanathan & Stringer, 2000) shown in Figure 1.4. Current specification for main steam pipes are that they are to be forged with a controlled inner diameter of 224 mm and nominal wall thickness of 63 mm making them suitable for operation at 165 bar and 569°C (Morris, 2015a). The maximum principal stress, in general, arises from internal pressure and will be greatest in the circumferential direction, as will be discussed in Section 4.2. It is also necessary to identify life-limiting sites, or features that are particularly susceptible to excessive damage accumulation. Due to the high stress dependence of creep, the reduced cross section of the pipe bend extrados makes it vulnerable and a site

of concern. Additionally, the altered microstructure at welded joints makes them susceptible to creep damage; both seam and circumferential welds are problematic (EPRI, 2003; Morris et al., 2006; Viswanathan, 1989).



Figure 1.4: *Photograph of CMV hot reheat pipes. Two pipes are shown during an outage. Hangers to suspend the pipes are shown in addition to thermal insulation which covers the pipes during normal operation.*

It is useful to provide a brief description of the nature of creep strain that is expected in power station components in this introduction, though further consideration will be given in Chapter 4. Components are designed to limit operational stresses to a ‘maximum permissible stress’; for example one that would result in 1% creep strain per 100,000 hours of service (EPRI, 2007). In a well-designed, problem free component, the strain rate is therefore expected to be less than this value. Power station components will invariably be multiaxially stressed; the exact stress state depending on internal pressure, bending stresses, geometry, position on the component *etc.*. The strain tensor at a given location is a function of the multiaxial stress state and it may therefore be necessary to measure the biaxial strain of the component surface.

1.1.2.3 Metallurgy of Power Station Components

In order to understand the specific nature of creep in power station components and inform appropriate monitoring strategies an appreciation of the metallurgy of the components is required. Advancement in the improved creep resistance of steels is driven by the motivation to achieve higher plant efficiency by increasing operational temperatures, and also to reduce component wall thickness whilst maintaining the same strength (Abson & Rothwell, 2013; I. A. Shibli & Coleman, 2006; Viswanathan, 1989).

The design of creep-resistant steels is achieved by increasing the resistance of grains and grain boundaries to flow, while retarding recovery and other softening processes. As already stated, in the

temperature and stress conditions of interest, creep flow is dominated by dislocation movement. Solid solution strengthening and precipitation hardening are used to impede dislocations movement (Abe, 2008; Viswanathan, 1989; Webster & Ainsworth, 1994).

Ferritic 'Cr-Mo-V' and 'Cr-Mo' steels have been used extensively in the fabrication of steam headers and the associated pipe work of interest since the 1940's (Maharaj et al., 2009; Mayer & Masuyama, 2008; Robertson, 2014). The chromium, molybdenum and vanadium alloying elements are added to solute strengthen the material and form a fine dispersion of precipitates that impede dislocation movement (Maharaj et al., 2009; Viswanathan, 1989; Webster & Ainsworth, 1994). The most frequently used materials are listed with composition in Table 1.1.

Austenitic stainless steels are used on various other components, however, their low thermal conductivity and high coefficient of linear thermal expansion make them susceptible to thermal fatigue in the thick walled components of interest (Viswanathan, 1989). Instead, metallurgical development has come in the form of '9-12%Cr' steels. These higher chrome steels have enhanced creep and oxidation resistance whilst maintaining satisfactory thermal fatigue characteristics (Ennis & Czyska-Filemonowicz, 2003; Viswanathan, 1989). This promise led to the wide spread adoption of 'P91' material (see Table 1.1 for composition) in new plant and in retrofitting ageing plant (I. A. Shibli & Coleman, 2006; TWI Ltd., 2008).

Ferritic steels however have the disadvantage of susceptibility to weld failure. Due to the thermal exposure during welding a 'creep soft' zone forms in the heat affected zone (HAZ) which acts as a life-limiting site of damage accumulation (Cerjak & Mayr, 2008; Perrin & Hayhurst, 1996; I. A. Shibli & Coleman, 2006). The high-chromium steels have proven to be particularly prone to weld failure and as a result many failures have occurred in times significantly less than their 100,000 hour design life (Abson & Rothwell, 2013; TWI Ltd., 2008). As a result it has been suggested that ASME will reduce the maximum allowable stresses for P91 welded pipe, rendering existing pipework to be designated as unsafe (TWI Ltd., 2008). The majority of this thesis will be dedicated to volumetric creep damage in plain volumetric components and the problem of creep damage at welds will be considered separately in Chapter 6.

Table 1.1: Composition of Steel Alloys Frequently Used in Power Stations (Abe, 2014; Robertson, 2014).

Common name	ASTM designation	EN designation	Composition (% -wt.)				
			C	Cr	Mo	V	Other
CMV (0.5Cr-0.5Mo-0.25V)	-	14MoV6-3	0.10-0.15	0.30-0.60	0.50-0.70	0.22-0.28	Si 0.15-0.35, Mn 0.40-0.70, Ni 0.30, Al 0.040
2.25Cr-1Mo	P22	10CrMo9-10	0.05-0.15	1.90-2.60	0.85-1.13	-	Si 0.5, Mn 0.30-0.60
-	P91	-	0.08-0.12	8.00-9.50	0.85-1.05	0.18-0.25	Si 0.20-0.50, Mn 0.30-0.60, Ni <0.40, Al <0.02

1.2 NDE for Creep in Pressurised Power Station Components

Sposito *et al.* (Sposito, Ward, et al., 2010) conducted an in depth review of non-destructive techniques for the detection of creep damage in power stations. It covered replication, ultrasonic methods, electrical and magnetic methods, positron annihilation, x-ray diffraction, small angle neutron scattering as well as hardness and strain measurements. The conclusions of the review are given in this section with additional information.

Usually, failure results from the development of grain boundary separation; many NDE inspection techniques therefore attempt to quantify the state of grain boundary separation. However, the reliability of monitoring grain boundary separation has been questioned. ‘Cr-Mo’ steels may show little, if any, void formation at failure (Furtado & May, 2004). Additionally, it is often reported that significant grain boundary separation is rarely evident until very late in life, undermining its utility as a robust indicator of creep state (Le May & Furtado, 1999; Prager, 2000). Predominantly thermally activated mechanisms such as carbide evolution may have an equally detrimental effect on the component integrity. ‘External’ damage mechanisms, acting to reduce the load bearing cross section of the component, will be more or less significant depending on the initial geometry; small cross section components (such as those used in accelerated uniaxial creep tests) may be overwhelmed by a large fractional loss of cross section by the formation of even a thin oxide layer (Cane & Williams, 1987; Singh Raman & Al-Mazrouee, 2007).

Evaluation of an NDE technique must be based on the sensitivity and selectivity of the sensing principle to different damage mechanisms and must be sufficiently encompassing to provide an overall representation of component state.

1.2.1 Replica Metallography

Replica metallography is at present the standard means of creep assessment. When the component is off-line, a small area on the surface is ground, polished and etched. Following this a thin film is applied to the surface and treated causing the film to take up the morphological features of the surface, particularly the grain boundaries, carbides and cavities. The replica, now imprinted with metallurgical features, may be examined under a microscope in a laboratory. E.ON undertook approximately 20,000 such replicas across the company in 2011 (C. Brett, 2015). The process is clearly labour intensive and, when coupled with the large number of replicas taken, it represents a major investment on behalf of the power industry.

Aside from being extremely laborious, the use of replica metallography is questionable. Firstly, it is believed that creep damage may often initiate below the surface, particularly in the case of weldments (Parker, 2014b). Clearly, only surface breaking defects are evident in replica metallography and so subsurface damage will go undetected. Interpretation is reported to be very subjective (Parker, 2014b; van Wortel, 2007); Neubauer (Neubauer & Wedel, 1983) developed guidelines for the assessment of creep damaged microstructure which have since been developed further by a number of organisations (S. Brett et al., 2005), an example from VGB is shown in Table 1.2. Despite such assessment frameworks a good deal of variation is seen in the assessment of replica images. A recent ‘round-robin’ test conducted by EPRI asked six service providers to assess the creep state of a P91 component based on the same replicas; the results are shown in Figure 1.5 (Parker, 2014b). The range of interpretation is dramatic with assessments of the same replica ranging from level 1 (creep exposed, without cavities) to level 4 (advanced creep damage, microcracks). The scatter in assessment or classification was attributed to incorrect interpretation between cavities and artefacts, misinterpretation of specific damage mechanisms, too high magnification (so cracks were missed), the quality of replicas and time pressure and operator fatigue. Clearly, replica metallography is not a satisfactory evaluation technique and there is scope for an improved method.

Table 1.2: VGB assessment criteria based on the state of grain boundary separation (VGB-Kraftwerkstechnik GmbH, 1992).

Assessment Class	Structural and Damage Conditions
0	As received, without thermal service load.
1	Creep exposed, without cavities.
2A	Advanced creep exposure, numerous cavities without preferred orientation.
2B	More advanced creep exposure, numerous cavities without preferred orientation.
3A	Creep damage, numerous orientated cavities.
3B	Advanced creep damage, chains of cavities and/or grain boundary separations.
4	Advances creep damage, microcracks.
5	Large creep damage, macrocracks.

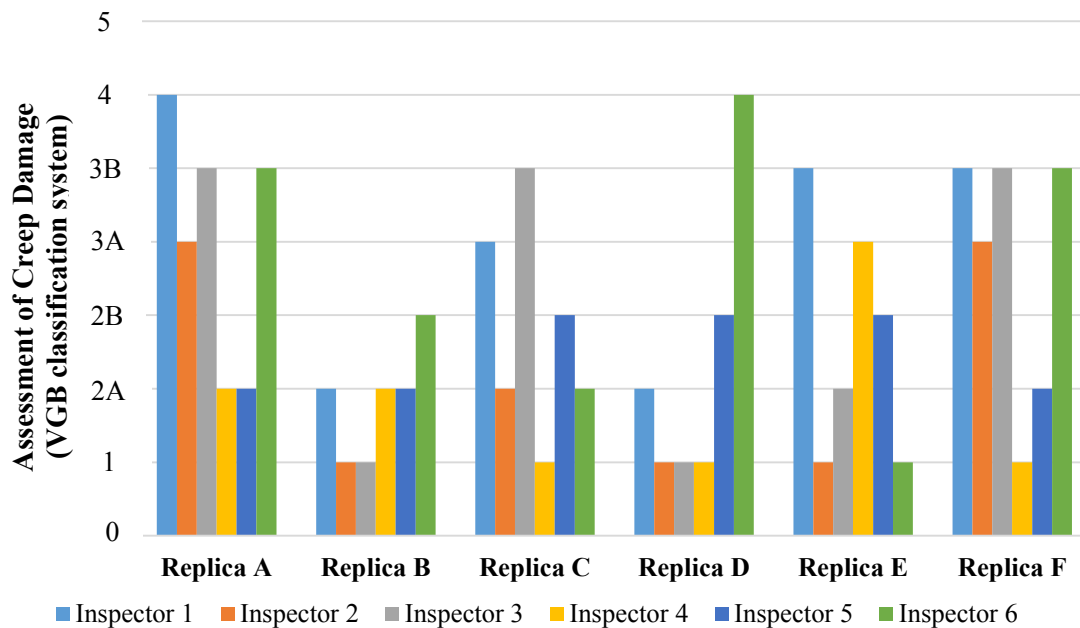


Figure 1.5: Results from a round-robin test arranged by EPRI (Parker, 2014b). Six replicas were assessed by six different service providers and asked to class the damage using the VGB classification system (Table 1.2). The wide range of results suggests that condition assessment by replica metallography may be unreliable.

1.2.2 Ultrasonic Measurements

Ultrasonic measurements are reported to give satisfactory results once microcracks start developing (Sposito, Ward, et al., 2010). Methods based on the velocity of shear or longitudinal waves or on acoustic birefringence have shown good results for volumetric damage whereas ultrasonic backscatter is considered a promising technique for detection of localised damage. Unfortunately, wave velocity is also reported to be largely affected by other mechanisms such as carbide coarsening and so selectivity between the two mechanisms may not be straightforward. (Sposito, Ward, et al., 2010)

While ultrasonic measurements are used extensively for inspections in a very wide range of applications, their use is limited in in-situ applications operating at power station temperatures. The high temperatures require a resilient or isolated transduction mechanism and dry coupling, such as those developed by Imperial College and commercialised by Permasense Ltd. (Cegla et al., 2011; Permasense Ltd., 2015).

The combination of challenging implementation at operational temperatures, sensitivity to only very late life damage and uncertain ultimate effectiveness led Sposito *et al.* to conclude that ultrasonic methods hold less promise than other methods for creep monitoring – particularly for volumetric creep damage of bulk components.

1.2.3 Magnetic methods

The magnetic properties of ferromagnetic materials are highly sensitive to numerous parameters including chemical composition, presence of phases, elastic and plastic deformation and dislocation density (Jiles, 1998). It is therefore not surprising that magnetic methods in various forms have been reported to show sensitivity to various aspects of creep exposure (Chen et al., 1994; Devine & Jiles, 1992; Govindaraju et al., 1997; Karimian et al., 2013, 2014; Liu et al., 2012, 2015, 2013; Mitra et al., 2007; Raj et al., 2003; Willems & Dobmann, 1991; Wilson et al., 2014). The broad range of sensitivity to intrinsic material parameters is considered to be the challenge in exploiting magnetic measurements for creep monitoring as isolation of a particular mechanism is an inherent issue. Magnetic state is also known to be sensitive to spatial variation in alloy composition, cold work and residual stresses (Chen et al., 1994; Govindaraju et al., 1997) which may contribute to the measurement scatter which has been seen to be prohibitive (Devine & Jiles, 1992; Govindaraju et al., 1997; Mitra et al., 2007).

Recent publications work towards in-situ measurement of magnetic properties; which, if installed permanently, may address the issue of spatial variation (Karimian et al., 2013, 2014). The results indicate ability to distinguish between different heat treatments using measurements of magnetic permeability. From a practical perspective, measurements of magnetic properties may be limited by the

effects of variations in stress and temperature (Jiles, 1998) and possibly the development of oxide scale on the outside of the component.

1.2.4 Hardness

Vickers hardness measurements have been used in a number of studies to infer the creep state of components (Gooch, 2007; Masuyama, 2006); a review is provided by Gooch (Gooch, 2007). Hardness changes are expected to occur due to recovery, solute depletion and coarsening of carbide particles. Although Masuyama additionally reports a very dramatic decrease in hardness just prior to failure (Masuyama, 2006) it is claimed that there is no theoretical backing to suggest any relationship between hardness and void formation (Thomson, 1992).

Again, the barrier to utilising hardness measurements for inspection purposes is practical. Much like replica metallography, the procedure requires extensive surface preparation to accurately size the indentation (Sposito, Ward, et al., 2010). Clearly, indentation hardness techniques cannot be made accurately under operational conditions.

1.2.5 Positron annihilation, x-ray diffraction and small angle neutron scattering

A number of techniques are frequently used in the laboratory for in depth studies of metallurgy and creep damage. Again, the review by Sposito *et al.* provides a background to these techniques (Sposito, Ward, et al., 2010). The use of such techniques in a power station environment on power station components clearly is not feasible and certainly cannot be practically deployed in a permanently installed, monitoring capacity.

1.2.6 Strain

Strain monitoring differs from the other techniques as instead of monitoring an intrinsic damage mechanism it relies on the quantification of the symptomatic result of damage. Ductility exhaustion is suggested as a starting point for residual life assessment (British Energy Generation, 1999) but, with reference to the model described in Section 1.1.2.1 the *increase in strain rate* is seen as a direct result of creep damage and a particularly valuable metric for remnant life calculations (Le May & Furtado, 1999; Penny, 1996; Prager, 1995, 2000; Voight, 1989). This inspection methodology is particularly powerful as it encompasses all mechanisms, internal and external, that reduce the capacity for the component to sustain strain; it is therefore a ‘holistic’ damage indicator. In a laboratory environment strain monitoring is the standard means of evaluating the creep state of the component under test. It has long been realised that strain monitoring of power station components can yield valuable information

(Allwood & Wilson, 1997; Cane & Williams, 1987; Cane, 1982; Ghia et al., 1995) though the ability to do so has been limited by technology.

1.2.6.1 Off-load measurements

Off-load monitoring techniques have been used for a number of years. Techniques are typically point to point measurements but the execution of the measurement may range from simple manual measurement to more sophisticated contemporary approaches. In power station components surface oxidation presents itself as the primary obstacle for accurate measurements. ‘Creep pips’, oxide resistant Stellite or austenitic projections, can be welded to the component to provide well defined reference positions for micrometer or bow gauge measurements (Cane & Williams, 1987). A conceptually similar approach is the Auto-Reference Creep Management and Control (ARCMAC) system produced by E.ON, shown in Figure 1.6. Inconel plates which carry oxidation resistant SiNi spherical markers are stud welded to the surface of the component. A specially designed portable lighting and camera unit is used to image the gauge. The two markers on one of the plates are used to provide a reference zero strain measurement. The image is processed by software to provide the strain measurement from the separation of the markers on adjacent carrying plates (Maharaj et al., 2009; Morris et al., 2006).



Figure 1.6: A photograph of a biaxial ARCMAC gauge. The two spherical SiNi targets on one carrier plate provide a strain independent reference measurement. The distance between targets on opposing carrier plates provides the strain measurement.

Digital Image Correlation (DIC) is a strain monitoring technique that has been used in various applications in the laboratory and has been suggested for future use on power station components. A random speckled pattern is sprayed onto the surface of a component. Images are taken periodically which can then be processed using correlation software to produce a strain field image. It has been suggested that this information may be particularly useful in examining weldments as local strain variation is expected in the different domains of the weld, heat affected zone and parent material (Maharaj et al., 2009). Accurate strain measurements have been reported in short term laboratory tests

(Morris et al., 2007) but it is not yet evident how the inevitable oxidation of the component surface will not corrupt the painted pattern between successive images (Sposito, Ward, et al., 2010).

1.2.6.2 On-load measurements

On-load strain monitoring techniques have the obvious advantage that the data acquisition rate can be greatly improved above the single measurement every 2-4 years facilitated by power station outages. This enables the continuous update of component state between outages, informing outage planning before the outages occur. The increased data acquisition rate also provides vastly improved strain rate estimates.

Monitoring strain in the laboratory environment is relatively straightforward as extensometry can be adopted to transfer the component displacement to ambient temperatures where it can be easily monitored. In the harsh power station environment, however, the delicate mechanical extensometry is vulnerable to damage. The challenge is therefore to move the displacement sensor to the high temperature component surface. A list of desirable capabilities of a strain monitoring technique is provided by Cane & Williams (Cane & Williams, 1987) and revised here based on the current state of the art.

1. Strain must be measured in the confined and unfavourable conditions of a power station environment.
2. Measurements should be taken under operation conditions of 550-600 °C.
3. Measurement of circumferential and axial strain should be accommodated.
4. Must be capable of measuring up to 5-10% strain.
5. Must be capable of accurately measuring strain rate of the order of 1% per 100,000 hours over 30 years of operation.
6. The system should be relatively cheap and easy to install and operate.
7. Ideally, require sufficiently low power to avoid a mains connection.

1.2.6.3 High temperature strain gauges

Conventional bondable foil strain gauges, which are very widely used in a variety of laboratory and industrial measurements, require substantial modification for use at power station operational temperatures. Vishay Precision Group, Inc. produce a strain gauge rated for up to 980 °C. It consists of wire bonded to metallic shim material, the shim can then be welded to the test component replicating a conventional strain gauge. It is however intended only for dynamic strain measurement and not static,

creep like measurements (Vishay Precision Group, Inc., 2010). As with conventional room temperature gauges, use is limited to the elastic limit of the gauge and therefore falls short of requirement 4 from the previous list.

1.2.6.4 Capacitance Gauges

Capacitance gauges have been available since the 1970's (Baumann & Schulz, 1991; Fidler, 1986; Fortmann, 1983; Noltingk, 1974) and come in a range of designs (Hoffmann, 1987). The gauges measure the change in capacitance between two plates which vary as a function of the displacement between them. Stability of 0.1×10^{-7} /hour is reported to be possible in the laboratory (SJB Engineering Ltd., 2015). Despite this, the sensors do not seem to have seen widespread adoption.

Eskom, who have adopted the technology, report the use of a design by SJB Engineering UK (van Zyl et al., 2005). SJB Engineering UK (SJB Engineering Ltd., 2015) report a number of issues with the gauges which will be inherent in any sensor which is to be mounted to the surface of a component and uses a transduction device above the surface. Notably oxide growth under the sensor or weld relaxation can cause rocking and mechanical instability and measuring strain on a curved surface (for example the creep-prone circumferential pipe strain direction and pipe bend) will require special calibration.

Sensors are known to be temperature sensitive. The temperature – capacitance relationship depends on the component and sensor materials and condition. Sensor materials must be chosen for the particular application, but still further, batch variation and sensor ageing will alter the temperature – capacitance dependency and therefore each sensor requires extensive calibration before installation. In addition, long term drift requires that dummy sensors are installed which are thermally but not mechanically coupled to the component to provide a baseline for compensation.

Finally, it is worth noting that the required power supply voltage is reported to be 50 V (ASTM, 2012), suggesting that the technology is not suited to long term, semi-continuous operation from a battery pack.

The combination of these problems makes the capacitance gauge difficult to use in practice and it is understood that this is the reason for slow adoption. Despite this, ASTM suggest it as the sensor of choice for long term, high temperature, static strain measurements (ASTM, 2012) It is acknowledged that the system proposed in this thesis must surpass the performance of capacitance gauges.

1.2.7 Potential Drop Measurements

Alternating Current Potential Drop (ACPD), Direct Current Potential Drop (DCPD), Alternating Current Field Measurement (ACFM) and Eddy Current measurements are all established electrical techniques for material or defect characterisation in electrically conductive components (Nagy, 2012; Sposito, 2009). Potential drop (PD) methods may be most appropriate for monitoring applications as

the ability to weld electrodes to the component provides a robust galvanic connection. A background to conventional potential drop methods is given in Chapter 2, in addition to a novel, low-frequency technique which draws advantages from both AC and DC measurements which will be used throughout this thesis.

Creep related changes in electrical resistivity are reported by a number of sources; most notably solute depletion and grain boundary separation are believed to be significant. Solute depletion is reported by Byeon & Kwun (Byeon & Kwun, 2003) to produce a notable initial decrease in resistivity as solute atoms leave the matrix and improve the lattice purity. Similar changes are reported empirically elsewhere (Seok et al., 2004; Yu et al., 1999).

Potential drop techniques are commonly used to inspect or monitor crack growth in the laboratory and commercial systems are available for use in industrial settings (McMaster, 1959; Nagy, 2012; Sposito, 2009). The effective conductivity of damaged materials may decrease as a result of microscopic or macroscopic impediments to current flow and therefore it may also be possible to detect lower level grain boundary separation by potential drop measurements following the suggestion of Sposito *et al.* (Sposito, Ward, et al., 2010).

Additionally, by permanently attaching electrodes to the surface of the component potential drop measurements also become sensitive to strain; as the component deforms the electrodes move relative to each other. The most convincing previously reported realisation of this as a useful tool comes from the work of Vasatis & Pelloux in a series of works in the 1980's (Pelloux et al., 1989; Vasatis & Pelloux, 1988; Vasatis, 1986). DCPD measurements were taken on narrow cylindrical uniaxial specimens and strain measurements were successfully inverted from the resistance measurements.

It was concluded by Sposito *et al.* that electrical resistance measurements are particularly promising for the purpose of creep monitoring. The technique may be adapted for continuous use at high temperature and the dual-sensitivity to material degradation and strain ensures that the creep state is monitored throughout the entire life of the component. Following this outcome, techniques and instrumentation were developed at Imperial College London and the University of Cincinnati (Madhi & Nagy, 2011a; Madhi, 2010; Prajapati et al., 2012). This thesis follows from this work with the particular focus of establishing the required understanding for using potential drop measurements for monitoring creep in power station components as well as addressing the technical barriers required to do so.

1.3 Project Aims

The objective of this work is to develop a monitoring technique that is capable and suitable for the on-load monitoring of creep damage in pressurised power station components. The information provided

by the monitoring system is a continuous update of component integrity enabling better informed, targeted inspections and outage maintenance. The system is intended to act as a supplement to established inspection techniques such as replica metallography.

Following previously reported promising results a low-frequency potential drop technique will be the focus of research efforts. The use of this method to monitor internal damage through electrical resistivity will be examined in addition to the symptomatic influence of creep damage on strain accumulation. Additionally, a suitable data processing and interpretation framework is necessary to translate resistance data into usable information for power station managers.

In parallel to the theoretical and empirical work in the laboratory, site trials at power stations will be undertaken. The effective transfer of this technology from the laboratory to the harsh power station environment presents an additional technical challenge that will be addressed.

1.4 Outline of Thesis

Chapter 2 presents the background of conventional ACPD and DCPD measurements in addition to a review of recent work on a novel low-frequency potential drop measurement. A sensitivity analysis is presented which forms the background to Chapters 3 and 4. The potential drop measurement system used in the laboratory is described and example illustrative measurements are presented.

Chapter 3 will investigate creep related electrical resistivity changes. This is of dual interest; on one hand it is possible that electrical resistivity changes can provide information on the creep state of the component. Alternatively, as strain provides valuable information on the creep state of components, resistivity changes may act to mask the influence of strain, limiting the sensitivity of a resistance-strain inversion. Of particular note, grain boundary separation and carbide evolution are investigated.

In Chapter 4 the inversion between resistance and strain is provided analytically and demonstrated on both room temperature and elevated temperature laboratory experiments. A discussion into the suitability of the potential drop technique in both the laboratory and power station components is presented.

Chapter 5 provides a methodology outline of how it is proposed that resistance measurements obtained using the low-frequency potential drop technique are to be used for on-site applications. It relates the increase in creep damage to increase in rate of change of strain; the relative increase in strain rate and remnant life have been reported to be inversely proportional and therefore a general framework for life calculations is demonstrated. Additionally, a statistical analysis on creep strain rate uncertainty is provided as a means to assess monitoring strategy.

Chapter 6 applies the low-frequency potential drop technique to weldments, a known site for creep damage accumulation. Welds require special attention as taking measurements in the vicinity of the various distinct and evolving material domains at a weld presents challenges that need to be addressed. The cracking at a weld interface provides a further contribution to the measured resistances which are investigated and further means of data interpretation are suggested.

Chapter 7 summarises the progress made in two site trials during the time of the project. Practical considerations and design of both robust hardware and measurement equipment have had to be made. Results and interpretation are presented and evaluated.

Chapter 8 provides the conclusion and summary of the thesis together with suggestions for future work.

Chapter 2

Low-Frequency Potential Drop Measurements

2.1 Introduction

Due to the promise of potential drop methods for creep monitoring, a research program was initiated at Imperial College London and the University of Cincinnati. A novel measurement technique was developed that is well suited to monitoring creep damage. The low-frequency technique draws on advantageous characteristics of both the well-established DCPD and ACPD methods. Additionally, an unusual square electrode configuration was adopted to provide directional sensitivity to anisotropic resistivity changes and enhanced strain sensitivity.

The core features of the measurement technique have remained fundamentally unchanged. Due to the novelty and its importance throughout this thesis it will be reviewed in depth in this Chapter. The context in relation to conventional potential drop methods will be established and the key features of the proposed measurement technique highlighted. An analytical description of the measurement will be given illustrating the sensitivity to different parameters. This will provide the foundation for the work in the remaining chapters. An overview of the measurement equipment will be provided in addition to an example experiment which will help elucidate many of the key themes as well as provide some detail to the practicalities of taking measurements in the laboratory.

2.2 Conventional Potential Drop Measurements

Potential drop methods have been used since the 1930's and are well established in a number of industry applications (Nagy, 2012). Despite this, it is a relatively niche technique with scant mention in a number of core electromagnetic NDE texts; notable exceptions being that authored by Nagy (Nagy, 2012) and the developmental work of Sposito (Sposito, 2009) which provide a good background. Conventional potential drop theory will be reviewed here with the specific aim of tailoring a novel technique optimised for creep monitoring.

Measurements require galvanic connection to the component under test. Electrodes are usually spring loaded pins (in a deployable, inspection capacity) or may be permanently welded to the surface of the component (facilitating long term, monitoring type measurements). Typically, measurements are taken in a four point arrangement; two electrodes inject and sink current producing a potential field, two voltage sensing electrodes then measure the potential difference between them at remote points on the surface as shown in Figure 2.1. The relationship between injected current, I , and measured potential difference, ΔV , gives an impedance measurement, $Z = \Delta V / I = R + iX$, where R is the resistance and X is the reactance (which of course equals 0 in the DC case). The term ‘transfer impedance’ is usually given to this measurement due to the fact that the current and potential are measured at different points.

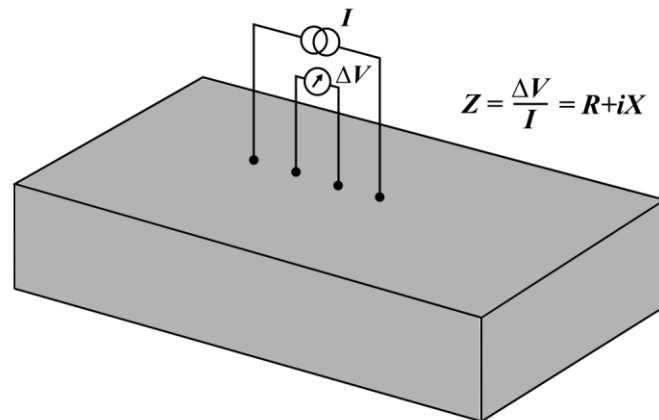


Figure 2.1: Schematic of a generic ‘in-line’ potential drop measurement. Two outer electrodes inject current through the specimen and the resulting potential is measured across two separate points. The impedance is calculated as $Z = \Delta V / I$.

Fundamentally, potential drop measurements are classified as either Direct Current Potential Drop (DCPD) or Alternating Current Potential Drop (ACPD). Clearly the distinction relates to the frequency of the injected current, but the behaviour of the two measurements is quite distinct. For this reason the two will be discussed separately in this introduction, followed by the novel low-frequency measurement.

2.2.1 Direct Current Potential Drop

Figure 2.2, adapted from the finite element solutions of (Sposito, 2009) illustrates many of the key characteristics of PD measurements. In each case the resistance is increased from the initial state (a) by a different mechanism, either by changing the material resistivity (b) or reducing the available cross section for current flow (c-e). In this way the resistance from a DCPD reading may be expressed simply as,

$$R = \rho L \quad (2.1)$$

where R is the transfer resistance to be measured, ρ is the resistivity and Λ is a geometric coefficient with units of inverse length. In Figure 2.2 (c-e) Λ is a function of the crack length, l , component thickness, t , and electrode separation, a , respectively. It is worth noting at this point that resistivity is the inverse of conductivity, σ , and the two terms will be used throughout the thesis interchangeably.

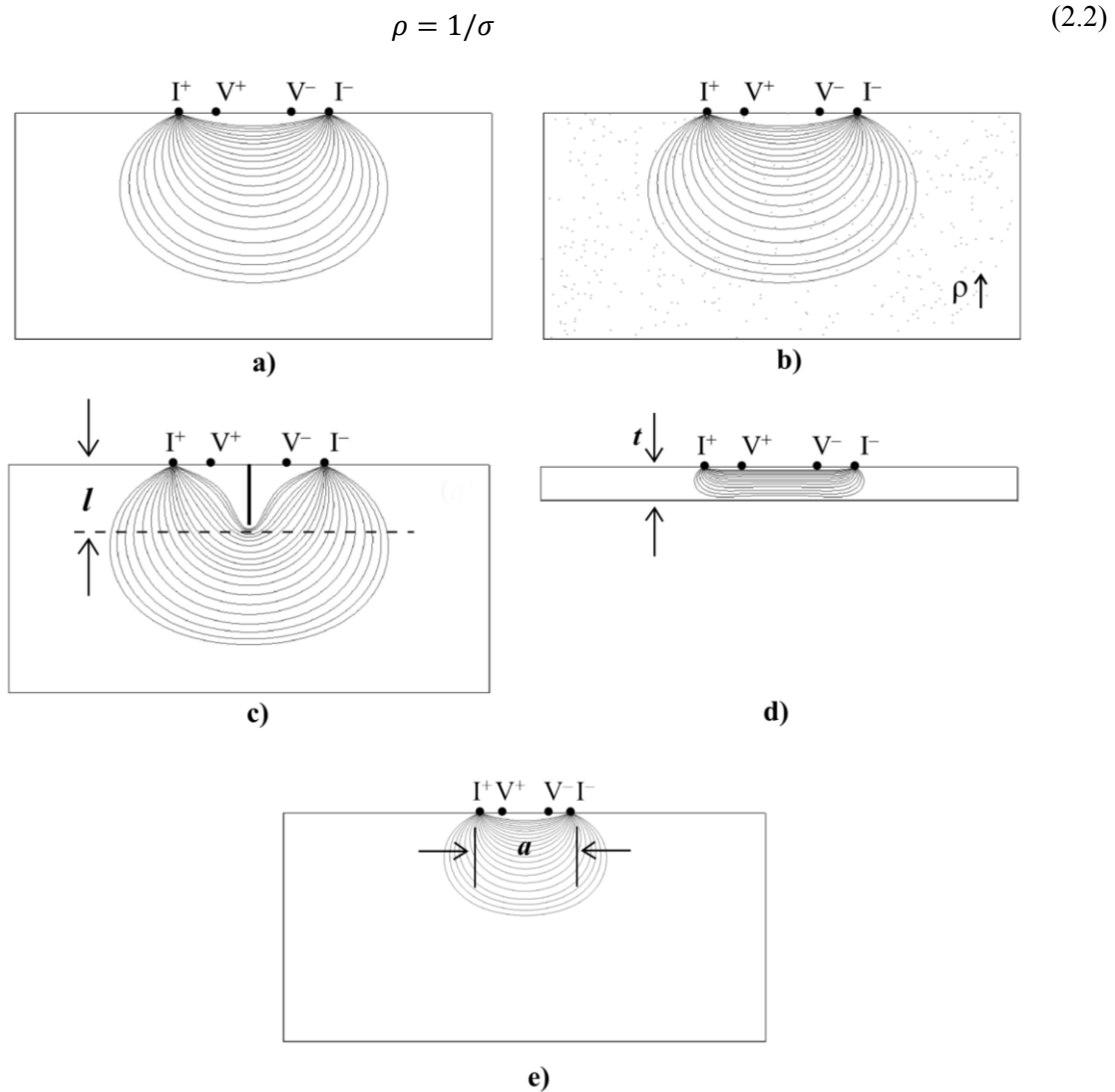


Figure 2.2: Illustration of the primary factors DCPD readings are sensitive to; adapted from the FE solutions of (Sposito, 2009). *a) Initial state. Current is injected by two outer electrodes, I^+ and I^- , and the resulting potential difference is measured across two separate electrodes, V^+ and V^- . In a ‘thick’ component the current penetration depth is limited by the separation of the injecting electrodes. b) Changes in resistivity will impede the current flow and therefore will increase the resistance but not change the spatial distribution of the current density. c) The presence of a crack will reduce the available cross section available for current flow, increasing resistance. d) Thinning of the component will also reduce the available cross section and therefore increase resistance. e) If electrodes are permanently attached to the component surface then their positions will move with strain. Increasing electrode separation will increase the distance current has to flow but, conversely, as the current penetration is limited by electrode separation the available cross section increases which has the dominating effect on resistance.*

In potential drop measurements the measured resistance will firstly be a function of resistivity as shown in Figure 2.2 (b). Clearly, the resistivity of the component will dictate the ease of current flow and therefore the measured potential. The resistivity is overwhelmingly dependent on temperature (in Section 6.2.2 it will be shown to triple between room temperature and 550 °C) but will also depend on the micro and macrostructure of the material. In the context of creep monitoring thermal ageing of the component is anticipated to alter the microstructure of the component with solute depletion having a particularly notable influence on resistivity (McMaster et al., 1986; Pollock, 1993). Additionally, grain boundary separation will form a macroscopic impediment to flow. While this is really a geometric constraint it can be treated as an effective resistivity contribution (Shafiro & Kachanov, 2000).

Figure 2.2 (c) illustrates how a macroscopic defect, usually a crack, will form a physical barrier to current flow. In DCPD measurements resistance is increased due to the diminishing cross section. In crack sizing applications a ‘dummy sensor’ is placed in a defect free region and is used to normalise out non-crack related resistances. Crack lengths may then be inverted by a number of different means (McMaster, 1959). Macroscopic defects are not expected in volumetric creep until failure is imminent. In the case of welds however, it will be shown that crack detection and monitoring may provide useful functionality.

The component thickness will limit current penetration and influence the measured resistance, as shown in Figure 2.2 (d). The sensitivity to thickness is utilised in corrosion and erosion monitoring applications (Sposito, Cawley, et al., 2010). Additionally, the component thickness will be dependent on strain. Though in pressurised component the radial stress is usually negligible, strain in the through wall direction arises from conservation of volume and tensile strain being expected in the hoop direction. As creep is known to be so highly stress dependent the remaining component cross section may be a useful metric for creep monitoring. Selectivity may become an issue however; sensitivity to too many variables can cause it to become difficult to invert useful information from the limited number of measured parameters. For this reason it is desirable to avoid sensitivity to component thickness by ensuring that the electrode separation is smaller than component thickness which means that negligible current reaches the back wall and so is insensitive to it.

Finally, in cases where electrodes are permanently attached to the component surface, as the component deforms the electrodes must move with the surface strain changing the electrode separation. The function relating strain and resistance depends on the exact configuration. As an example in Figure 2.2 (e) as the injection electrodes move closer together the distance between the electrodes reduces which will act to reduce the resistance, however, as the penetration depth is limited by the electrode separation, the available cross section reduces proportionally to the square of the separation. Therefore, counterintuitively, a smaller electrode separation increases the resistance. The measured potential will

also depend on the position of the sensing electrodes as will be explained in Section 4.3.1. Potential drop measurements can therefore be sensitive to strain, a key indicator of creep state.

2.2.2 Alternating Current Potential Drop (ACPD)

It was mentioned previously that ACPD measurements have a distinct behaviour when compared to DCPD. Alternating currents are subject to the ‘skin effect’; current passing through a conducting component will tend to ‘cling’ to the surface of the component with an exponentially decreasing current density from the surface. The skin depth, δ , is the depth from the surface at which the current density reduces to $1/e$ ($\approx 37\%$) of the surface density and can be calculated as,

$$\delta = \frac{1}{\sqrt{\pi f \sigma \mu}} \quad (2.3)$$

where f is the current frequency, σ is the electrical conductivity and μ is the magnetic permeability. Figure 2.3 (a) and (b) differentiates between DCPD and ACPD measurements respectively. The current injected in a DC measurement will not be subjected to the skin effect and therefore the current distribution will be limited by a geometrical consideration; in Figure 2.3 (a) the current is limited by the electrode separation. In Figure 2.3 (b), however, the current is electromagnetically ‘squeezed’ into the skin depth, reducing the cross section available for current flow. The ability to control the skin depth provides many important advantages in a range of applications but Equation 2.3 reveals an important limitation for power station components. The materials described in section 1.1.2.3 are all ferromagnetic and the magnetic permeability of ferritic materials is known to vary substantially as a complex function of temperature, local alloy composition, stress, cold work and weld history (Jiles, 1998). The result is that in the power station steels of interest the magnetic permeability and therefore skin depth is likely to vary significantly, causing spurious undesired resistance changes. Potential drop measurements in ferromagnetic materials must therefore be made at a DC or quasi-DC frequency where the current penetration depth is not dependent on the skin effect.

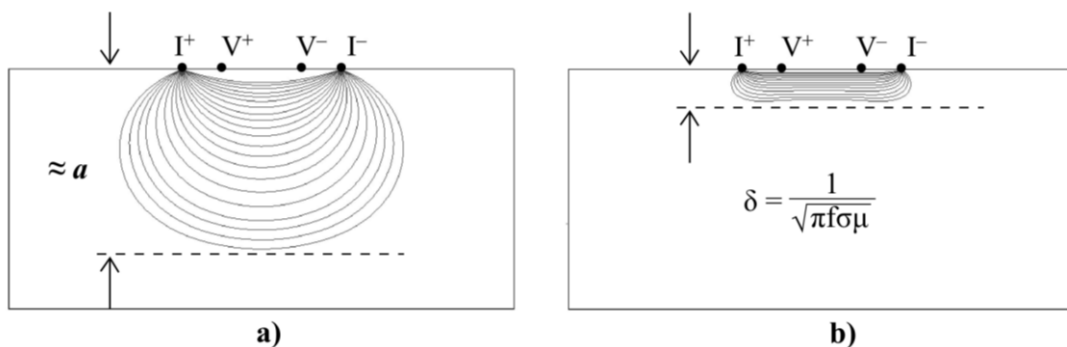


Figure 2.3: Illustration showing the current penetration depths of a) DCPD and b) ACPD measurements.

2.3 Low-Frequency Potential Drop Potential Drop Background

It has been established that in the ferromagnetic materials of interest the influence of the skin effect must be suppressed in order to negate sensitivity to magnetic permeability. Conventionally this is achieved by using DC measurements, but equally DC measurements also have characteristic features that make them poorly suited to monitoring applications.

In addition to the desirable DC signal that is to be measured, numerous other undesirable sources of DC voltage will also be present to compromise the measurements signal to noise ratio (SNR). In order to improve the signal to noise ratio it is usual to increase the inspection current to tens or even hundreds of Amps (Matelect Ltd., 2015; Nagy, 2012; Sposito, 2009). The use of such large currents is unsuitable for unsupervised monitoring applications as it could be potentially dangerous and will also require mains power which may be logistically or practically difficult. The sources of spurious DC potential will come from a number of sources and may be systematic or random in nature.

2.3.1 Systematic DC Interference

A commonly reported source of error in DCPD measurements is thermoelectric potential. If the junctions between the two sensing leads and the sample are at slightly different temperatures then a net, erroneous DC-like thermoelectric potential will result (Matelect Ltd., 2015; Nagy, 2012). In order to account for this effect the polarity of the injected current is reversed and the measurements subtracted; this process must be implemented as a rate faster than temperature fluctuations (Nagy, 2012). Aside from this, it may be possible that stray currents or instrument drift or instability may provide erroneous, systematic DC-like signals.

2.3.2 Flicker Noise

An AC measurement on the other hand may be conducted in such a way that a very narrow effective bandwidth is achieved, filtering out undesired interference outside the inspection frequency band. Clearly the mains frequency (50 Hz in the UK and Europe) may cause interference and is to be avoided but, additionally, the spectral noise density should be considered when selecting an inspection frequency.

‘Thermal’ (or ‘Johnson’) noise originates from the random motion of free electrons inside a conductive material. The thermal noise density is a function of temperature and the resistance of the component but it is approximately white with equal power spectral density across all frequencies. (Vasilescu, 2006)

‘Flicker’ noise on the other hand has a power spectral density proportional to the inverse of frequency, hence the other common name ‘ $1/f$ ’ noise. Flicker noise was first observed by Johnson in 1925 (Johnson, 1925), incidentally this is the same Johnson that lends his name to the previously mentioned

‘Thermal/Johnson’ noise. The physical origins and mechanisms of flicker noise remain a controversial subject despite almost a century of research (Balandin, 2013; Voss, 1979). Flicker noise is pertinent to many mechanical and electrical systems; a recommended review comes from Voss (Voss, 1979) which details widespread examples from the ancient flood patterns of the river Nile to the loudness and pitch variations of Sgt. Peppers Lonely Hearts Club Band.

Figure 2.4 shows the measured input noise density of the preamplifier that will be used throughout this thesis exhibiting the ‘ $1/f$ ’ behaviour and tending to the thermal noise floor (instrumentation will be discussed in Section 2.7.2).

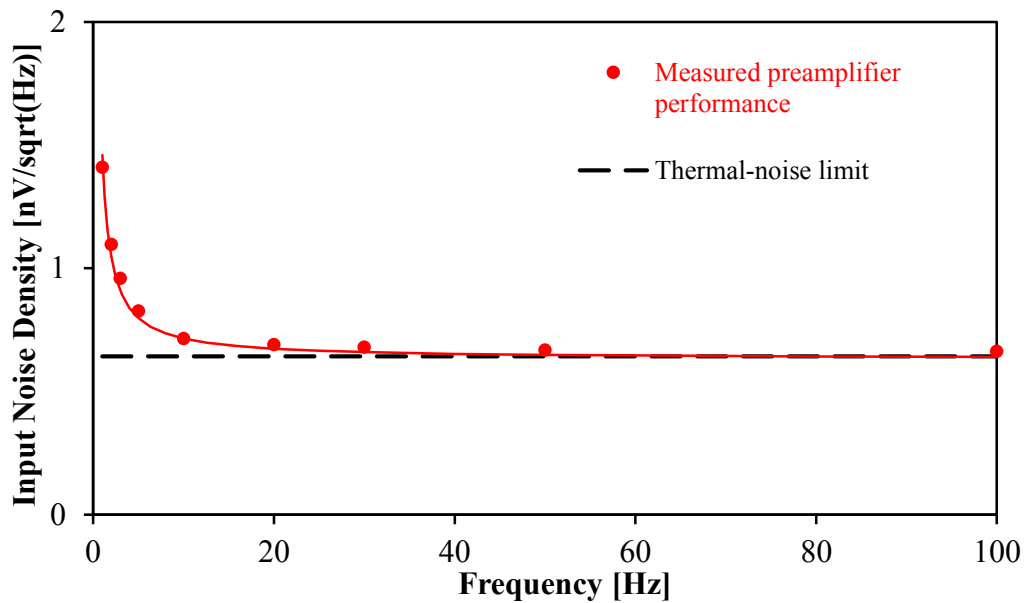


Figure 2.4: Noise performance of the 800x preamplifier. Measurements taken using a 20 Ohm serial resistor and a Stanford Research SR830 Lock-in amplifier. The continuous red line is the best fitting line with equation $N=0.63\text{nV}/\sqrt{\text{Hz}} + k/f$ where N is the noise density, k is a constant of proportionality and $0.63 \text{ nV}/\sqrt{\text{Hz}}$ is the analytically derived thermal noise floor for the measurement configuration.

In this case reducing the inspection frequency from 10 Hz to 1 Hz increases the noise density from 0.72 nV/ $\sqrt{\text{Hz}}$ to 1.41 nV/ $\sqrt{\text{Hz}}$. As the noise is random then the increased noise density can be addressed by either greater signal amplitude or longer averaging time. Unfortunately, a 2-fold increase in measurement noise requires a 4-fold increase in measurement power or time. Clearly, everything must be done in the design of measurement equipment to improve noise performance. It is evident that utilising higher inspection frequencies may improve the SNR substantially, not by increasing the signal amplitude but by reducing the noise.

2.3.3 Suppression of the Skin Effect

It was described in Section 2.2.2 that it is necessary to suppress the skin effect in order to negate sensitivity to fluctuations in magnetic permeability – this is normally done by utilising DC. Equally, in DC measurements there are systematic and random ‘noise’ sources which improve with increasing frequency. The suggested solution is the compromise of a quasi-DC measurement; an AC measurement at sufficiently low frequency that the skin effect is suppressed.

With reference to Figure 2.3, if the skin depth exceeds the electrode separation then the current penetration depth is no longer limited by the skin depth but rather the electrode separation. Similarly, if the skin depth exceeds the component thickness then the current penetration depth is no longer limited by the skin depth but rather the physically available cross section. As long as one of these conditions is satisfied the magnetic permeability will not affect the resistance and the current distribution will behave as if it was DC. From this understanding it is useful to define a ‘transition frequency’, f_T , which results in a skin depth that is equal to the smaller of the component thickness, t , or electrode separation, a . This frequency is analogous to a corner frequency separating the DC-like and AC-like behaviour. The definition of the transition frequency follows from Equation 2.3 and is given by,

$$f_T = \frac{1}{\pi\sigma\mu t^2} \quad \text{if } t < a$$

or

$$f_T = \frac{1}{\pi\sigma\mu a^2} \quad \text{if } a < t$$

(2.4)

This behaviour is reported by Sposito (Sposito, Cawley, et al., 2010; Sposito, 2009) and (Bowler, 2006). Bowler provides an empirically verified analytical solution for the complex voltage resulting from an injected alternating current. Appendix A shows the solution for a square electrode configuration on a conducting half-space (*i.e.* a thick, $a < t$, component) and is shown in Figure 2.5. The normalised resistance and reactance are normalised by the DC magnitude $|R|$, and the frequency is normalised by the transition frequency. It can be seen in Figure 2.5 that the resistance is segmented into two distinct DC-like and AC-like regimes with a transition between the two. Crucially, it can be seen that at low frequencies the resistance tends to an asymptotic DC value where it is nominally frequency and therefore skin depth independent.

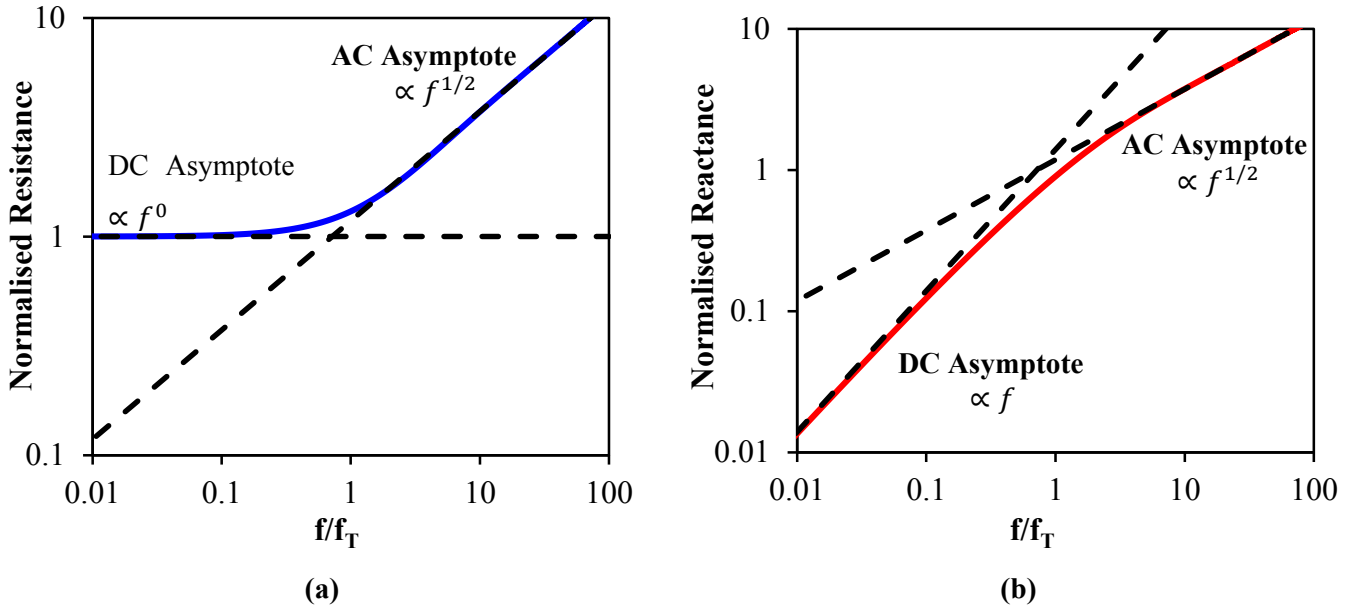


Figure 2.5: Analytical results for the impedance resulting from a square electrode configuration. Of importance is the DC asymptote of the resistance; as the resistance is frequency independent in this regime it must be independent of the skin effect.

The conclusion is that there must be an optimum measurement frequency. By utilising alternating current, systematic DC artefacts such as spurious thermoelectric potentials can be suppressed. Further, the highest frequency possible should be used to reduce the flicker noise present; the upper limit to frequency is dictated by the skin depth. The inspection frequency must be sufficiently below the transition frequency so that the current injection depth is limited by electrode separation and the remnant influence of changing permeability is suppressed.

2.4 Electrode Configuration: A Directional Resistance Measurement

The conclusion of Chapter 1 was that changes in resistivity may provide valuable information on creep state. It was suggested that the alignment of grain boundary separation normal to the maximum direction of stress may produce anisotropic effective conductivity which may help isolate this effect from other spurious resistivity changes. Additionally, the migration of the initial electrode separation will influence the measured resistance. The implementation of the potential drop measurement will need to be considered in order to maximise sensitivity to anisotropic resistivity and strain. The electrode configuration has been studied in depth previously by Madhi and Nagy (Madhi & Nagy, 2011a, 2011b; Madhi, 2010).

Most frequently potential drop measurements are conducted using the in-line configuration, shown previously in Figure 2.1. In order to measure anisotropic changes in resistivity a ‘biaxial’ measurement will need to be taken in the two orthogonal directions; the intuitive implementation is shown in Figure 2.6 (a). However, a square electrode arrangement, shown in Figure 2.6 (b) has been shown to be much more sensitive to changes in electrical anisotropy and requires fewer electrodes. For the ‘thick’ components of interest the sensitivity to anisotropy using the square arrangement is approximately 3.4 times that of the in-line arrangement (Madhi & Nagy, 2011a) and, interestingly, in thin components the in-line arrangement has no sensitivity to anisotropy at all (Tatarnikov, 1970). Further, it will be shown in Chapter 4 that the sensitivity to strain is also improved using the square configuration. The square electrode configuration is therefore adopted as the most suitable implementation of potential drop readings due to its enhanced directionality and strain sensitivity.

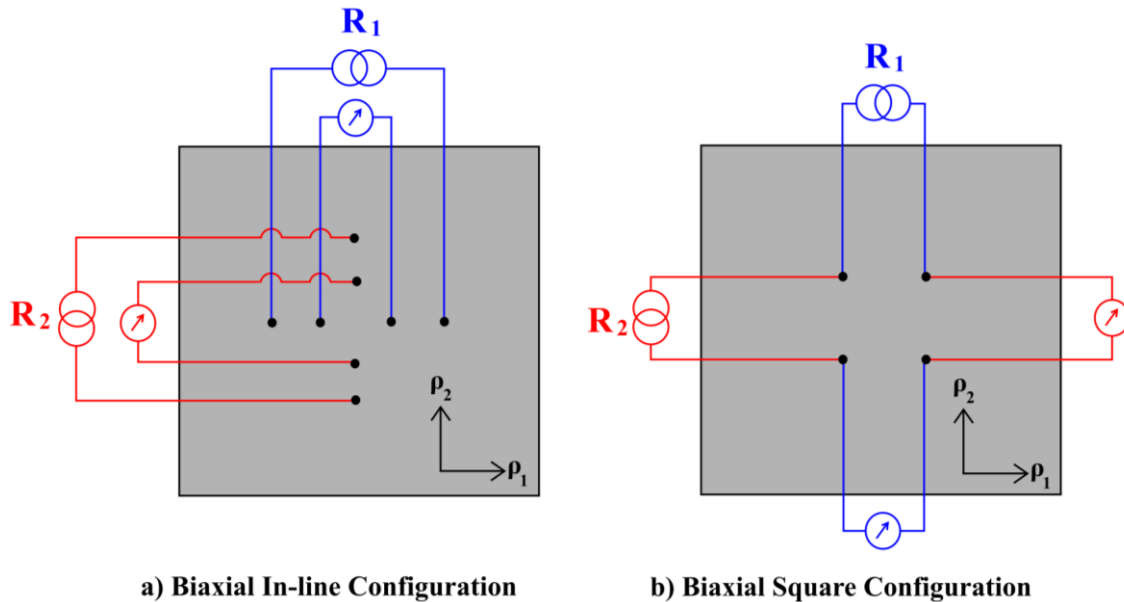


Figure 2.6: Illustration of two possible biaxial potential drop configurations. The square arrangement is more sensitive to strain and changes in anisotropy than the in-line arrangement.

2.5 Sensitivity Overview

The analysis illustrates that potential drop measurements are sensitive to numerous parameters which, unless carefully controlled, may interfere with the desired measured quantity. The following expression provides a summary of the sensitivity of a poorly controlled square electrode, four-point impedance measurement.

$$Z = \frac{\Delta V}{I} = Z(\rho_1, \rho_2, \rho_3, \Lambda(t, l, a_1, a_2), \delta(f, \mu, \rho)) \quad (2.5)$$

Again, ρ_1, ρ_2, ρ_3 are the resistivity in the three orthogonal directions; geometric constraints, Λ , come in the form of component thickness, t , inclusion length, l , electrode separation of the two square sides a_1 and a_2 and the skin depth, δ , is a function of frequency, f , magnetic permeability, μ and again resistivity. With sensitivity to so many variables, inverting useful information becomes unfeasible. Suppression of the skin depth by adopting a suitably low inspection frequency eliminates sensitivity to frequency and magnetic permeability and therefore the impedance measurement becomes, in effect, a purely resistive measurement. Reducing the electrode separation relative to the component thickness removes sensitivity to component thickness. Equation 2.4 therefore reduces to,

$$R = \frac{\Delta V}{I} = R(\rho_1, \rho_2, \rho_3, a_1, a_2) \quad (2.6)$$

Sensitivity to these parameters is desired as resistivity and orthogonal surface strain measurements are anticipated to provide useful information on creep state. In order to interpret the changes in resistance and infer from them creep information it is necessary to gain an understanding of this function. Again, this is investigated in the work of Madhi and Nagy (Madhi & Nagy, 2011b) but will be revisited and extended here. Figure 2.7 (a) shows the initial, as-installed, component state with electrode separation a_{10} and a_{20} and resistivity ρ_{10} and ρ_{20} . After some time the component is in the state shown in Figure 2.7 (b) with electrodes separated by a_1 and a_2 and with resistivity ρ_1 and ρ_2 .

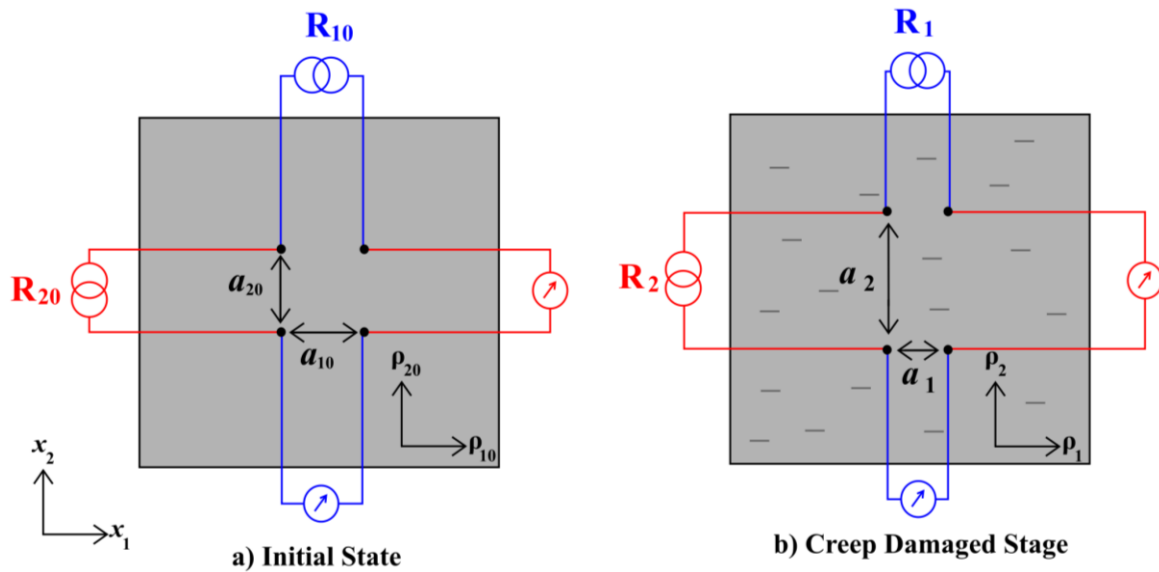


Figure 2.7: Illustration showing the terminology used in the analysis of the potential drop measurements. The distance between the electrodes changes with surface strain and electrical resistivity changes may be either isotropic or anisotropic.

Madhi and Nagy provide an analytical description of the potential distribution produced by a DC current source in an anisotropic half space (Madhi & Nagy, 2011b).

$$\varphi = \frac{I\sqrt{\rho_1\rho_2\rho_3}}{2\pi} \left(\frac{1}{\sqrt{\rho_1(x_1 - s_1)^2 + \rho_2(x_2 - s_2)^2 + \rho_3(x_3 - s_3)^2}} \right) + \varphi_0 \quad (2.7)$$

where φ is the electric potential at a given field point of spatial coordinates (x_1, x_2, x_3) from a point current source injecting current I with coordinates (s_1, s_2, s_3) . φ_0 is an integration constant that corresponds to the electric potential at some remote point which we assume to be negligible ($\varphi_0 = 0$).

Assuming the source and field point both lie on the free surface of the principal plane ($x_3 = 0$) and the electrodes are aligned in the x_1 and x_2 directions then the transfer resistances in these two orthogonal directions can be found using superposition (Madhi & Nagy, 2011b).

$$R_1 = \frac{\sqrt{\rho_1\rho_2\rho_3}}{\pi} \left(\frac{1}{\sqrt{\rho_2 a_2^2}} - \frac{1}{\sqrt{\rho_1 a_1^2 + \rho_2 a_2^2}} \right) \quad (2.8)$$

$$R_2 = \frac{\sqrt{\rho_1\rho_2\rho_3}}{\pi} \left(\frac{1}{\sqrt{\rho_1 a_1^2}} - \frac{1}{\sqrt{\rho_1 a_1^2 + \rho_2 a_2^2}} \right)$$

From these two readings, in the absence of strain, changes in resistivity anisotropy can be inferred (Madhi & Nagy, 2011a). On the assumption that the resistivity anisotropy is small, *i.e.* $\rho \approx \rho_1 \approx \rho_2 \approx \rho_3$ then significant simplifications can be made:

$$R_1 = \frac{\rho}{\pi} \left(\frac{1}{a_2} - \frac{1}{\sqrt{a_1^2 + a_2^2}} \right) \quad (2.9)$$

$$R_2 = \frac{\rho}{\pi} \left(\frac{1}{a_1} - \frac{1}{\sqrt{a_1^2 + a_2^2}} \right).$$

a_1 and a_2 can be written in terms of their initial length a_{10} and a_{20} and the orthogonal engineering strains ε_1 and ε_2 in the x_1 and x_2 directions respectively: $a_1 = a_{10}(1 + \varepsilon_1)$ and $a_2 = a_{20}(1 + \varepsilon_2)$. Assuming further that the initial electrode geometry was square, $a_o \approx a_{10} \approx a_{20}$ then,

$$R_1 = \frac{\rho}{\pi a_o} \left(\frac{1}{(1 + \varepsilon_2)} - \frac{1}{\sqrt{(1 + \varepsilon_1)^2 + (1 + \varepsilon_2)^2}} \right) \quad (2.10)$$

$$R_2 = \frac{\rho}{\pi a_o} \left(\frac{1}{(1 + \varepsilon_1)} - \frac{1}{\sqrt{(1 + \varepsilon_1)^2 + (1 + \varepsilon_2)^2}} \right)$$

It is also convenient to normalise the resistances to their initial values, the initial resistivity or geometry is usually of little interest as it is the change of state that provides the information. The initial resistances are:

$$R_{10} = R_{20} = \frac{\rho_0}{\pi a_0} \left(1 - \frac{1}{\sqrt{2}} \right) \quad (2.11)$$

The inverse of $1 - 1/\sqrt{2}$ is a value that will be frequently used throughout this thesis and so will be assigned the symbol, $s \approx 3.41$.

$$\begin{aligned} \frac{R_1}{R_{10}} &= s \frac{\rho}{\rho_0} \left(\frac{1}{(1 + \varepsilon_2)} - \frac{1}{\sqrt{(1 + \varepsilon_1)^2 + (1 + \varepsilon_2)^2}} \right) \\ \frac{R_2}{R_{20}} &= s \frac{\rho}{\rho_0} \left(\frac{1}{(1 + \varepsilon_1)} - \frac{1}{\sqrt{(1 + \varepsilon_1)^2 + (1 + \varepsilon_2)^2}} \right) \end{aligned} \quad (2.12)$$

Equation 2.12 is of significance as it will be the starting point for many studies in this thesis. Throughout the remainder of this thesis resistances will be normalised to an initial value in this fashion and be referred to using the capitalised terminology ‘*Normalised Resistance*’ or *NR*.

Equation 2.12 shows the biaxial strain dependence of the directional potential drop measurement. It is worth emphasising the nature of the strain dependency; unlike in the in-line potential drop measurement which can only be sensitive to strain in the direction of alignment, here, both resistances are coupled to both strains. Now the analysis for the square electrode arrangement reveals that separation of the injection electrodes ($\varepsilon_1 > 0$ for R_1 or $\varepsilon_2 > 0$ for R_2) now results in an increase in resistance – this is due to the increased lateral extent of the current path and the voltage sensing electrodes being out of line with the current electrodes. Further, the orthogonal strain directions are also coupled through conservation of volume. The warning is that the resistance – strain behaviour of potential drop measurements should always be calculated and intuition should not be relied on! Despite each resistance reading now being truly biaxial, the convention will remain that the current injection direction will be considered the resistance ‘direction’ as will be shown in Figure 2.13. Equation 2.12 also shows sensitivity to the (assumed) isotropic resistivity. A simplified expression can be given as,

$$\begin{aligned} \frac{R_1}{R_{10}} &= f \left(\frac{\rho}{\rho_0}, \varepsilon_1, \varepsilon_2 \right) \\ \frac{R_2}{R_{20}} &= f \left(\frac{\rho}{\rho_0}, \varepsilon_2, \varepsilon_1 \right) \end{aligned} \quad (2.13)$$

2.6 Temperature Compensation

The electrical resistivity can be separated into a reversible, intrinsically temperature dependent contribution, $\rho_{reversible}$, from thermal excitation of the crystalline lattice, and irreversible changes in resistivity, $\rho_{irreversible}$, attributed to creep exposure.

$$\rho = \rho_0 + \rho_{reversible}(T) + \rho_{irreversible} \quad (2.14)$$

The reversible temperature dependency is expected to be many times larger than the irreversible change caused by damage. It will be demonstrated in Chapter 6.2.2 that the electrical resistivity increases by approximately a factor of 3 between room temperature and 550 °C while the irreversible change in resistivity is expected to be <10%. If the temperature of the component is not constant then temperature fluctuations will cause significant spurious changes in resistance which will need to be considered.

2.6.1 Thermocouple Compensation

Fortunately the temperature – resistivity relationship, is reversible and very repeatable. Further, in the materials of interest it is monotonic and over a limited temperature range, approximately linear (Pollock, 1993). It has been demonstrated (Sposito, 2009) that local temperature monitoring using a thermocouple can be used to compensate for temperature changes using the simple quadratic approximation,

$$\rho_{reversible}(T) = \rho_0(\alpha(T - T_0) + \beta(T - T_0)^2) \quad (2.15)$$

ρ_0 is the resistivity at a chosen reference temperature, T_0 . α and β are temperature coefficients of resistivity which can be easily established by regression. In this way the influence of temperature on resistivity can be effectively suppressed.

2.6.2 The Normalised Resistance Ratio

An alternative approach to account for spurious changes in isotropic resistivity has been suggested in previous work (Madhi & Nagy, 2011a, 2011b; Madhi, 2010). If the two orthogonal Normalised Resistances are divided by each other then the isotropic resistivity, common to both measurements, will cancel and only changes in anisotropy or geometry will remain. This not only has the effect of suppressing the influence of temperature but also undesired thermally activated resistivity drift and long term instrument drift and instability. The rejection of isotropic resistivity changes has been demonstrated by Madhi (Madhi, 2010). Due to this very useful characteristic, the ratio will be used where possible in preference to the Normalised Resistance; it forms another important metric which will be referred to throughout the thesis as the ‘*Normalised Resistance Ratio*’ or ‘*NRR*’. Again, assuming isotropic resistivity then the Normalised Resistance Ratio is given by:

$$NRR = \frac{R_1}{R_{10}} / \frac{R_2}{R_{20}} = \frac{\frac{1}{(1 + \varepsilon_1)} - \frac{1}{\sqrt{(1 + \varepsilon_1)^2 + (1 + \varepsilon_2)^2}}}{\frac{1}{(1 + \varepsilon_2)} - \frac{1}{\sqrt{(1 + \varepsilon_1)^2 + (1 + \varepsilon_2)^2}}} \quad (2.16)$$

where the resistivity terms are need to cancel out. Madhi and Nagy (Madhi & Nagy, 2011b) showed that Equation 2.16 can be approximated using a power approximation,

$$NRR = \left(\frac{\frac{a_1}{a_{10}}}{\frac{a_2}{a_{20}}} \right)^{1/s} = \left(\frac{1 + \varepsilon_1}{1 + \varepsilon_2} \right)^{1/s} \quad (2.17)$$

This simple but effective approximation shows that the Normalised Resistance Ratio is in fact a function of only the aspect ratio of the sides of the rectangular electrode geometry. Clearly, by reducing to only one variable it is impossible to invert the two biaxial strain components and so the available information has been compromised. Nevertheless, in known stress situations the orthogonal strain components are not independent (for example in uniaxial stress cases they are linked by Poisson's ratio or conservation of volume) and equally, *rate of change of aspect ratio* may be sufficient for inferring information on creep damage.

2.7 Measurement Instrumentation

It is clearly advantageous for a monitoring technique to consume as little power as possible; measurements will be unattended and automated and so low power will minimise the risk of potential hazard, in many applications there are intrinsic safety requirements limiting the maximum allowable voltage, but above all it is desirable to be able to power remote sensors from a battery pack, removing the need for mains power. To maximise the number of measurements from a finite energy source, every effort should be made to minimise the power and duty cycle of the sensor whilst achieving maximum measurement accuracy and repeatability.

The steels of interest have conductivities of approximately 2-10 %IACS at room temperature (CSNDT/Eddy Current Technology, 2015). Using Equation 2.11, a square electrode configuration with electrode separation of 5-10 mm provides a possible range of transfer resistances of 1.6 – 16 $\mu\Omega$. Using a target inspection current of 100 mA then the potential difference signals will be in the range of 0.16 - 1.60 μV . Measuring signals of this amplitude to the fraction of a percent accuracy that is required is a very demanding challenge and one that requires special attention to measurement technique and hardware.

2.7.1 Lock-in Amplifiers

A lock-in amplifier is capable of accurately recovering very small AC signals, even in the presence of noise many orders of magnitude larger. Lock-in amplifiers use phase-sensitive detection to isolate the component of a signal at a specific frequency and phase, and reject noise. For detailed technical information on lock-in amplifiers application notes from instrument manufacturers are a good source of information. The following summary information is taken from application notes by Stanford Research (Stanford Research Systems, Inc., 2015) and PerkinElmer (PerkinElmer, Inc., 2015).

Lock-in measurements require a fixed reference frequency. This reference signal is typically generated by the lock-in amplifier but may be supplied by a dedicated function generator or oscillator (in which case the lock-in reference signal is synchronised with the external signal). The reference signal can be written,

$$V_{ref} = A_{ref} \sin(\omega_{ref}t + \varphi_{ref}) \quad (2.18)$$

where A_{ref} is the reference signal amplitude at frequency, ω_{ref} , with phase φ_{ref} . The experiment is excited at this fixed frequency and a return signal with amplitude, A_{sig} , frequency, ω_{sig} , and a fixed phase relationship with the reference, φ_{sig} , is input back to the lock-in amplifier.

$$V_{sig} = A_{sig} \sin(\omega_{sig}t + \varphi_{sig}) \quad (2.19)$$

The two signals are then multiplied using a ‘phase-sensitive detector’ to give,

$$\begin{aligned} V_{psd} &= A_{ref}A_{sig} \sin(\omega_{ref}t + \varphi_{ref}) \sin(\omega_{sig}t + \varphi_{sig}) \\ &= \frac{1}{2}A_{ref}A_{sig} \cos[(\omega_{ref} - \omega_{sig})t + \varphi_{ref} - \varphi_{sig}] - \\ &\quad \frac{1}{2}A_{ref}A_{sig} \cos[(\omega_{ref} + \omega_{sig})t + \varphi_{ref} + \varphi_{sig}] \end{aligned} \quad (2.20)$$

The PSD output therefore is the difference of two AC signals, one at the difference frequency and one at the sum frequency. The PSD output is then passed through a low-pass filter, removing the AC components for all frequencies where $\omega_{ref} \neq \omega_{sig}$. What remains is a DC signal corresponding to the frequency of interest, *i.e.* where $\omega_{ref} = \omega_{sig}$.

$$V_{lock-in} = \frac{1}{2}A_{ref}A_{sig} \cos(\varphi_{ref} - \varphi_{sig}) \quad (2.21)$$

While this signal is proportional to the input signal it is also sensitive to the phase, φ_{sig} . Most lock-in amplifiers are ‘dual-phase’ allowing the separation of the magnitude and phase. The PSD also multiplies the return signal with a second reference signal shifted 90° from the original,

$$V_{ref\ 2} = A_{ref} \sin(\omega_{ref}t + \varphi_{ref} + 90^\circ) \quad (2.22)$$

The second demodulated lock-in output is then,

$$V_{lock-in\ 2} = \frac{1}{2} A_{ref} A_{sig} \sin(\varphi_{ref} - \varphi_{sig}) \quad (2.23)$$

The two lock-in outputs are then the components of a vector with magnitude,

$$\sqrt{V_{lock-in}^2 + V_{lock-in\ 2}^2} = \frac{A_{ref} A_{sig}}{2} \quad (2.24)$$

and phase,

$$\varphi_{ref} - \varphi_{sig} \quad (2.25)$$

Any undesired spurious signals where $\omega_{ref} \neq \omega_{sig}$ are filtered out. It can be shown that the effective bandwidth of the lock-in amplifier is inversely proportional to the time over which the signal is integrated; in the present work the measurement time is typically several seconds reducing the bandwidth to a fraction of a Hz: in this way very small signals can be measured accurately despite the presence of much larger amplitude noise.

2.7.2 Measurement System

Throughout the experimental work contributing to this project the measurement instrumentation has been incrementally developed to improve a number of key parameters. For an in depth analysis of the technical demands of a potential difference measurement systems the reader is referred to the review by Sposito (Sposito, 2009). A brief overview of the measurement system is provided here. All of the lab experiment results reported in this thesis have been collected with the same measurement equipment as illustrated schematically in Figure 2.8.

The SIM921 AC Resistance Bridge performs the function of the Lock-in Amplifier, providing a constant amplitude differential current signal of 2-60 Hz which is applied to the test specimen by a pair of electrodes. On some occasions the SIM921 AC Resistance Bridge is replaced by a Stanford Research SR830 Lock-in Amplifier as it has a lower frequency limit capable of measurement down to 1 mHz. The potential is measured by a separate pair of electrodes and the returning signal is processed to provide the phase sensitive transfer resistance measurement. The SIM921 AC Resistance Bridge is however limited by a maximum current output of 10 mA. In order to increase the amplitude of the interrogation signal a current booster was devised with a selectable current gain of 10 – 40x. The return signal is also passed through a specially designed preamplifier to improve the SNR. The multiplexers allow measurements of the two orthogonal transfer resistances at a given location as well as in multiple measurement locations.

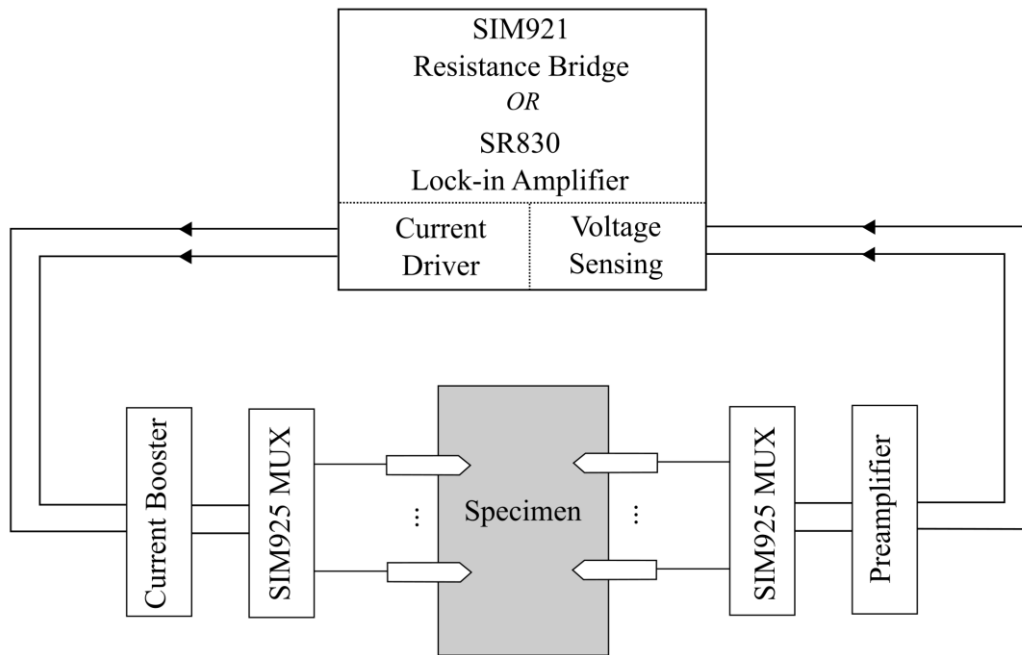


Figure 2.8: Schematic showing the Stanford Research Small Interface Module (SIM) based, low-frequency potential drop measurement system used throughout the laboratory work of this thesis.

As already mentioned, an inherent performance limiting feature of very low frequency measurements is flicker noise. In order to take measurements at the low frequencies required to suppress the influence of permeability, without extensive time averaging, a preamplifier with excellent noise performance is required. An 800x preamplifier was designed by Prof. Peter B. Nagy specifically for the purpose of suppressing the incoherent random noise. The noise performance has already been shown in Figure 2.4, the input noise density is reduced to a level essentially as low as theoretically possible as is evident by the asymptotic behaviour approaching the thermal noise floor.

A demonstration of typical performance is shown in Figure 2.9. A measurement system with current boosted to 100 mA and inspection frequency of 2 Hz was used to take measurements from a fixed resistor network designed to replicate the potential drop from a $10 \mu\Omega$ transfer resistance. Each resistance measurement is averaged over approximately 65 seconds. Values are normalised to the average of all readings. In this case the standard deviation at 2 Hz was measured to be 90 ppm.

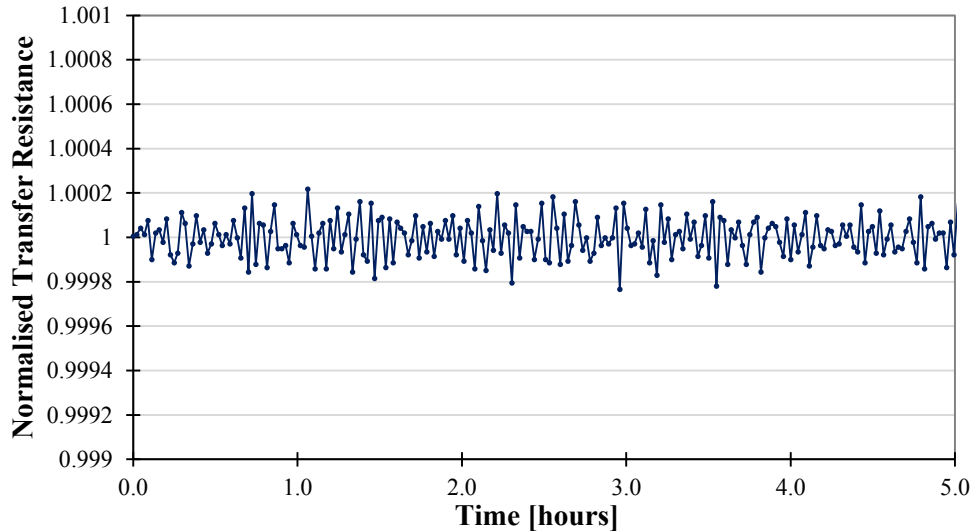


Figure 2.9: Example data. Measurements taken of a $10\ \mu\Omega$ transfer resistance fixed resistor network. Measurements were current boosted to 100 mA and 2 Hz inspection frequency was used. Each reading is an average over approximately 66 seconds.

A battery powered automated system that replicates the function of the system in Figure 2.8 was produced for the purpose of site trials and will be discussed in Chapter 7.

2.8 Example Measurement

An example measurement will be shown here to elucidate some of the previous points with the use of experimental data. This section will also serve to provide a background to some of the practical aspects of taking potential drop measurements that will be common to all the experimental work in this thesis. A room temperature tensile test was conducted for the purpose of verifying the strain - resistance inversion originating from Equations 2.12 and 2.17; the processed data is shown in Chapter 4. Data will also be used to illustrate the transition of the measurement from quasi-DC to AC and additionally, the influence of stress on magnetic permeability will be used as a convenient and easily controlled means to manipulate the skin effect in order to illustrate the undesirable consequence of operating at a frequency where the skin depth is not sufficiently suppressed. The influence of strain on resistance will then be shown throughout plastic loading.

A S275 mild steel tensile specimen with a gauge cross section of 75 mm x 24 mm and gauge length 150 mm was produced, as shown in Figure 2.10. To one side of the specimen a random speckle pattern was painted for the purpose of taking an independent strain measurement using digital image correlation. Conventional biaxial strain gauges and thermocouples were also installed to monitor the component and ambient temperature. On the reverse side of the specimen an array of potential drop sensors were installed, as is to be described. The sample was tested using a 2.5 MN Instron tensile test

machine capable of load or displacement control. A Stanford Research SR830 Lock-in amplifier was used to reach the lower limit of 0.3 Hz used in this experiment.

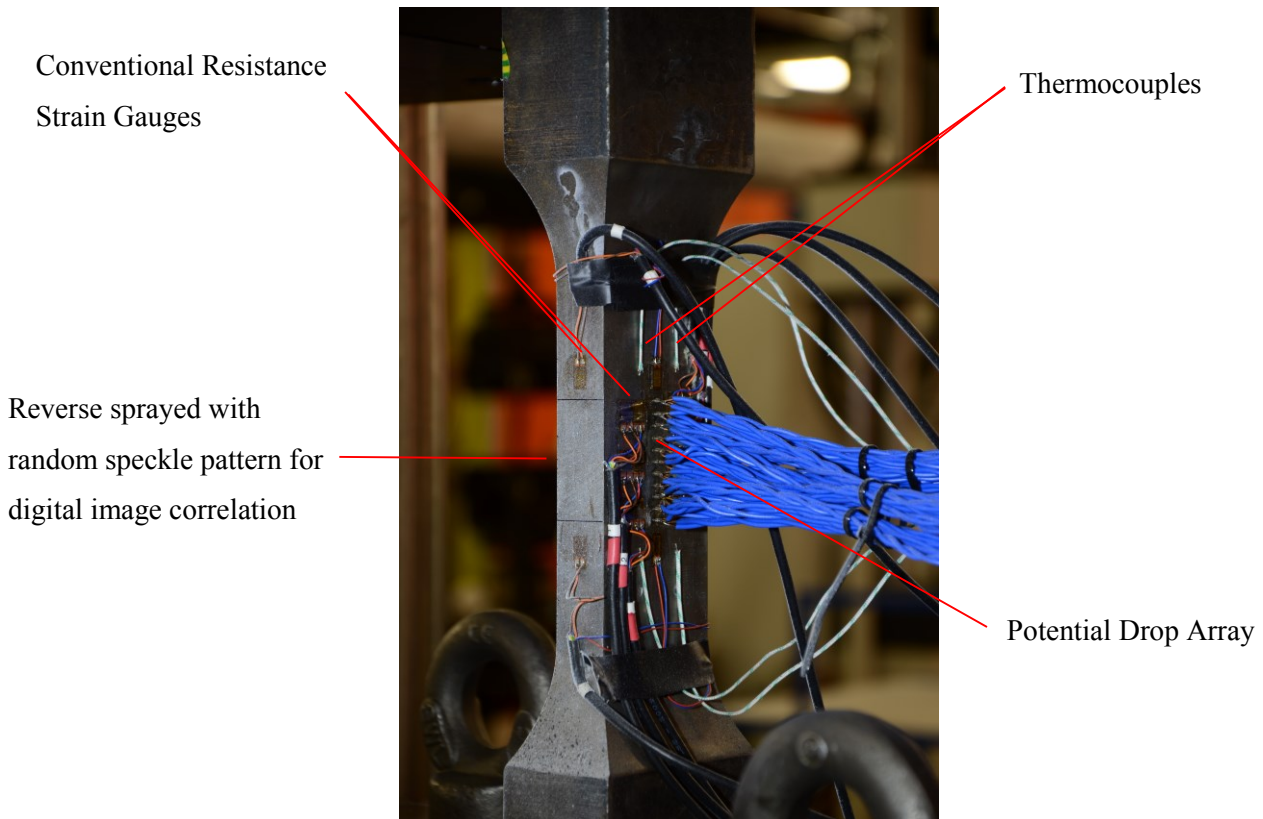


Figure 2.10: Photograph showing the arrangement of sensors on the room temperature tensile test specimen. For scale the component width was 75 mm.

2.8.1 Potential Drop Array

Often, it is beneficial to measure local changes in creep damage. In the case of welds, strain and damage accumulation is expected to be local to the distinct weld domains. In uniaxial testing of bulk material strain localisation or ‘necking’ is observed approaching failure. Due to the temperature sensitivity of creep, an uneven temperature distribution can cause non-uniform creep strain.

For these reasons a potential drop array measurement, composed of a chain of adjacent square electrode configuration sensors, has been devised. An example photograph of a 10-element array is shown in Figure 2.11. Each square of the array will be instrumented according to the previous schematic of Figure 2.11 (b), thus enabling two orthogonal Normalised Resistances to be measured on each element.

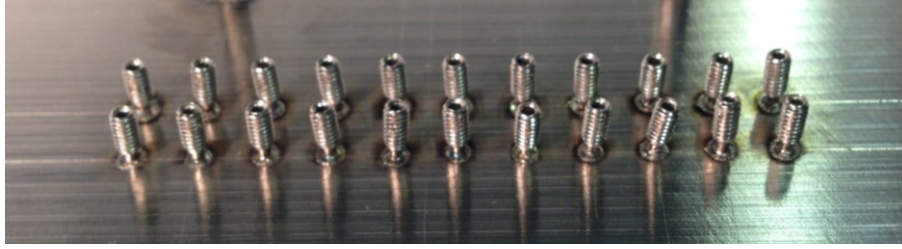


Figure 2.11: A 10 element array of potential drop sensors. Electrodes take the form of grub screws or small diameter dowel pins. For scale the electrode separation is 5 mm in this case.

In the laboratory it is necessary to scale down the potential drop measurement to fit with the scale of the test specimens, which must be suitably small to be able to impart sufficient stress. Typically in the laboratory 4-5 mm electrode separation was used. In the case of the experiment being described, ‘dog point’ grub screws were used as electrodes which were welded to the specimen using a thermocouple welder. This produced a sufficiently robust galvanic connection to the specimen and facilitated the welding of wires onto the top of them. In this room temperature experiment copper wires were used, visible in blue in Figure 2.10, whereas in high temperature applications Chromel or Constantan thermocouple wires were used.

2.8.2 Elastic Loading

Loads of -100 kN, 0 kN, 100 kN, 200 kN, 300 kN and 400 kN were applied equating to stresses of approximately -16.5%, 0%, 16.5%, 33%, 49.5% and 66% of the yield stress. At each stress potential drop measurements were taken on only one of the array elements with inspection frequencies of 0.3, 0.5, 0.7, 1, 2, 3, 4, 5, 7, 10, 20, 30 and 60 Hz.

Figure 2.12 shows the measured resistances, normalised here to the DC value, taken to be the 0.3 Hz measurement. The DC-asymptote is clearly evident and follows the anticipated behaviour shown in Figure 2.5. As the inspection frequency is increased, the skin depth is reduced. Above the transition frequency the current penetration depth is no longer limited by the electrode separation but rather the frequency dependent skin depth, constricting the current and increasing resistance.

It is also very apparent that the high frequency behaviour is stress dependent. As mentioned previously the skin depth is a function of magnetic permeability which, in ferromagnetic materials, is dependent on many different variables, including stress (Jiles, 1998). As the stress increases in the loading direction, the magnetic permeability decreases which in turn increases the skin depth and alleviates the constriction of the current. Changing the skin depth must change the transition frequency resulting in the stress shifting the frequency behaviour as shown. It is worth noting that only measurements parallel to the loading direction, shown in Figure 2.12 (a), are effected by the applied stress while the influence on the measurements orthogonal to it appears negligible, shown in Figure 2.12 (b).

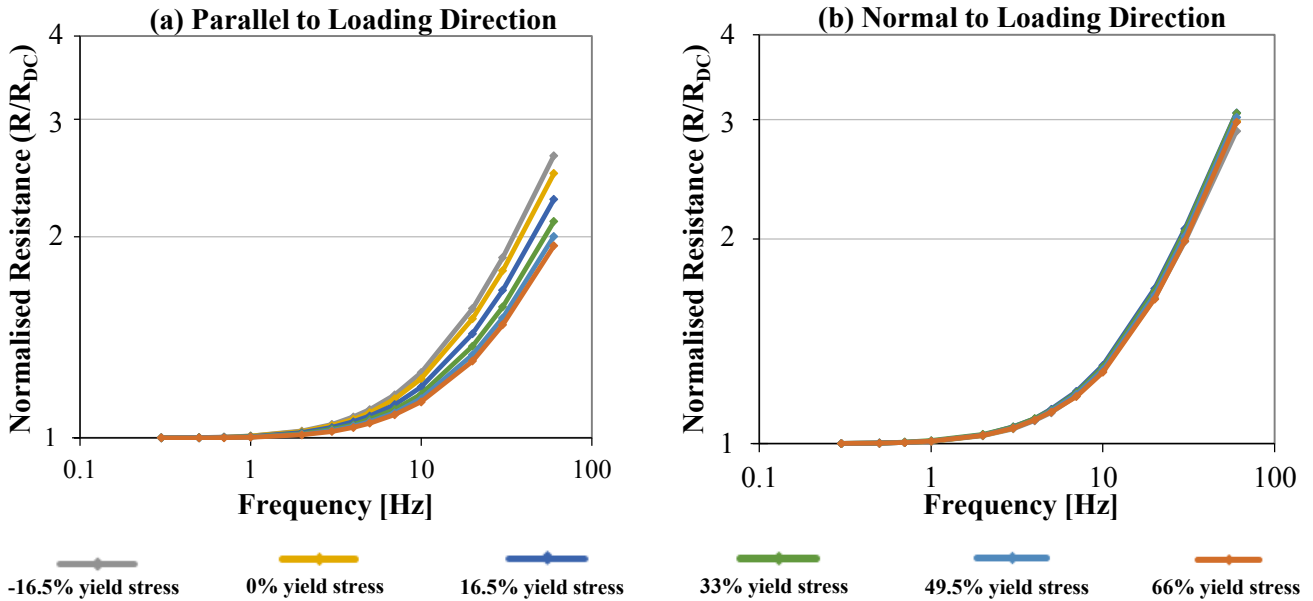


Figure 2.12: Resistance against inspection frequency for a single array element parallel and perpendicular to stress. The stress is seen to alter the resistance at high frequencies acting by changing the magnetic permeability and therefore skin depth.

Figure 2.12 is included in this thesis to highlight the peril of not using sufficiently low inspection frequency. If, for example, 10 Hz was used in this experiment then the resistance measurements would be susceptible to large swings with stress, causing substantial error. The low frequency measurements are seen to be insensitive to the enforced changes in skin depth and are therefore sufficiently below the transition frequency. In the absence of significant strain or resistivity changes, the readings are seen to be nominally constant.

2.8.3 Plastic Loading

Following elastic loading the sample was plastically deformed until failure by being subjected to a constant displacement rate. The aim of this part of the experiment was to verify the resistance-strain inversion as will be demonstrated in Section 4.5.1 but for the time being it will be used to demonstrate qualitatively the strain dependence of the resistance measurements. In this experiment the temperature was observed to be constant to within ± 1 °C and in the absence of elevated temperature resistivity was assumed to be constant and isotropic. All the changes in resistance can therefore be attributed to strain.

Figure 2.13 shows the numbering and direction convention for the array elements and each of the two orthogonal Normalised Resistances. Normalised Resistances for the 10-elements, in the two orthogonal directions (20 readings in total) are shown in Figure 2.14. As this was a uniaxial stress test the component is expected to deform with constant volume; contracting with a strain of half that of the extension in the loading direction ($\epsilon_{normal} = -0.5 \epsilon_{loading}$). In this case resistance is expected to increase in the direction of loading and decrease in the normal direction.

Superimposed onto the graph is the engineering stress as monitored by the load cell of the tensile test machine; as the experiment was conducted at a constant displacement rate this stress is expected to reflect a conventional stress-strain curve. The maxima of the engineering stress curve coincides with the point of strain localisation. This is evident in the Normalised Resistance values; the strain increases linearly and uniformly up until this point, following this strain preferentially accumulates in the central elements of the array where necking occurs.

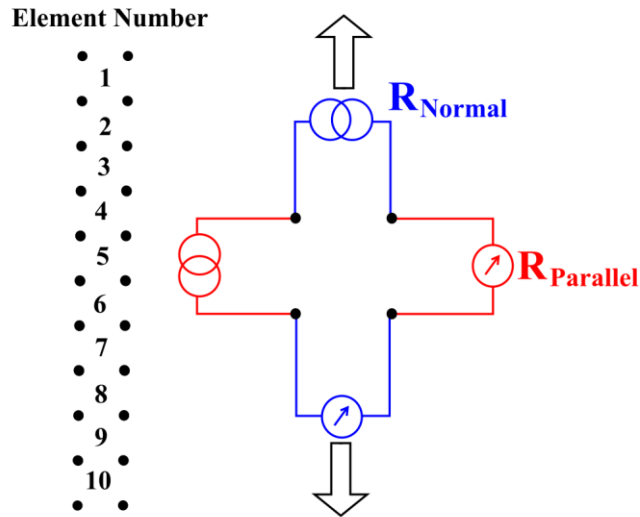


Figure 2.13: Array element numbering and direction convention.

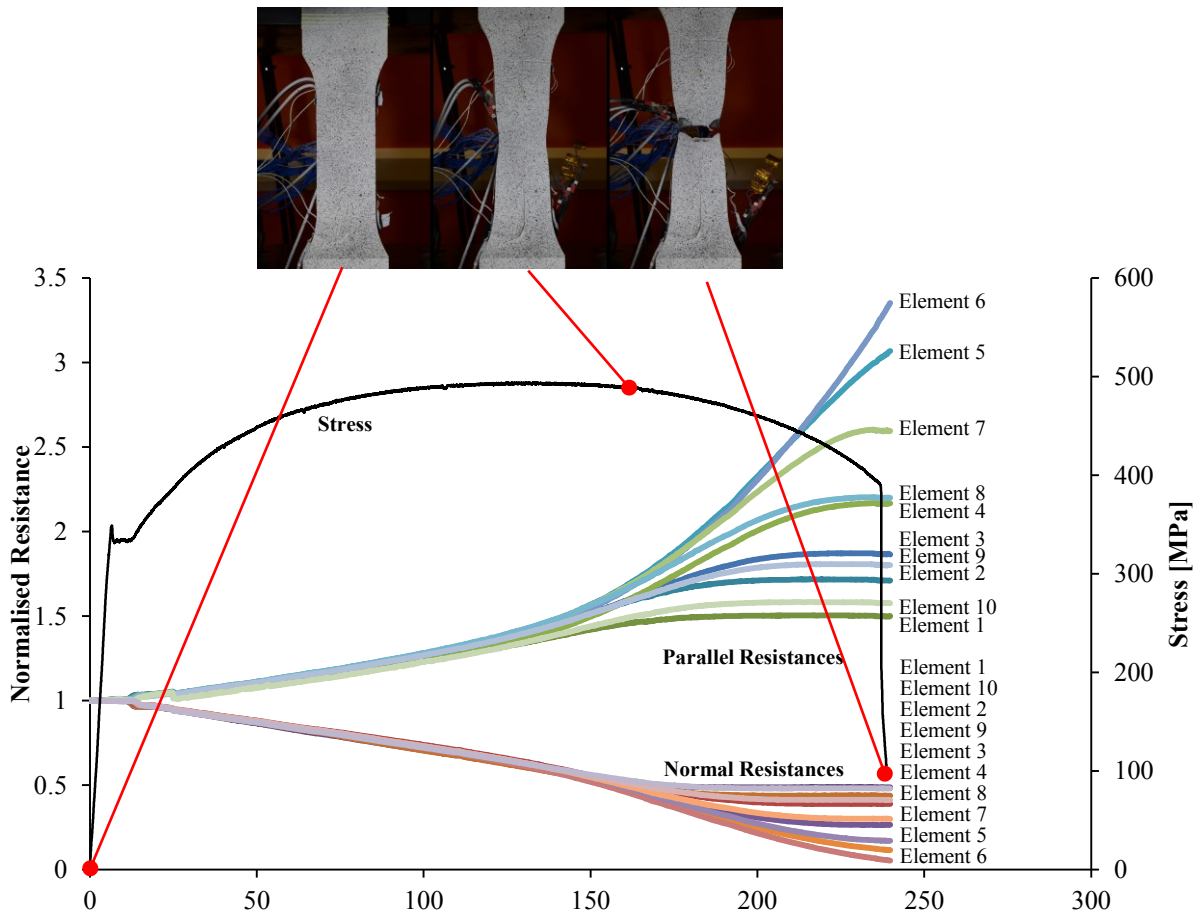


Figure 2.14: Normalised Resistance against time. 10 array elements are shown, resistances parallel to the direction of loading increase, while those normal decrease. Following the onset of necking (at the maximum engineering stress) strain begins to accumulate preferentially in the central elements at the expense of those at either end.

The Normalised Resistance is however susceptible to resistivity changes. Therefore, if there were a temperature increase during the experiment, the resistances would all increase, undermining the ability to infer any useful strain information. The Normalised Resistance Ratio on the other hand suppresses isotropic resistivity changes and therefore the results plotted in Figure 2.15 would be nominally temperature independent. Further, the division of a resistance increase by a decrease in the orthogonal direction results in very large changes. Clearly, the use of this metric may provide a great deal of value in monitoring the integrity of a component.

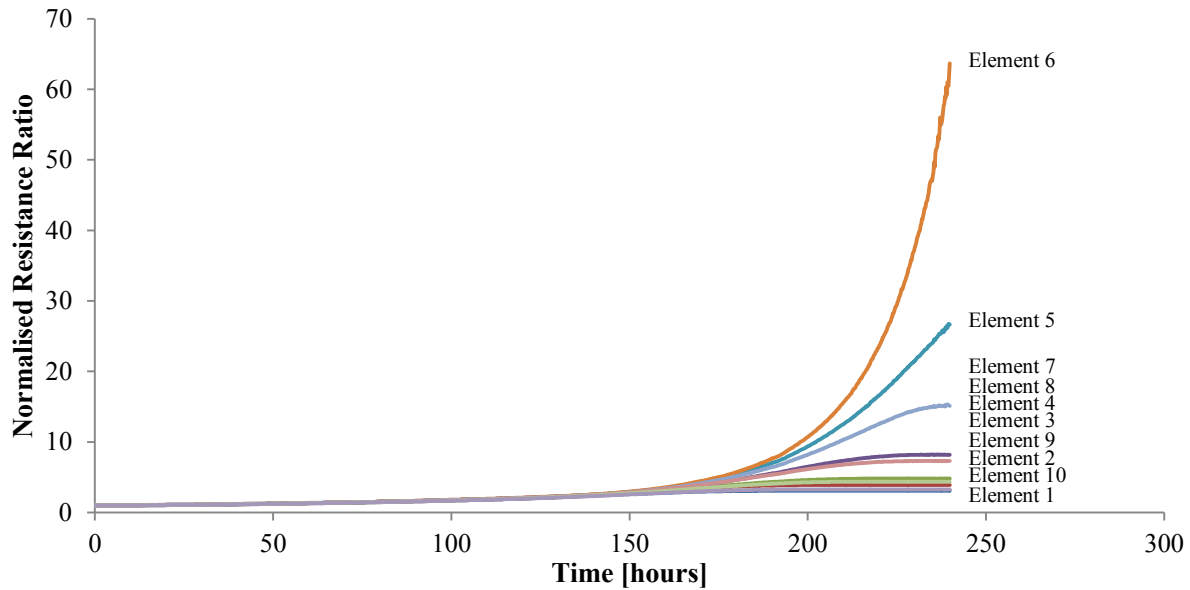


Figure 2.15: Normalised Resistance Ratio against time. This metric is nominally temperature and isotropic resistivity independent. Additionally, note the very large changes that are observed towards failure.

2.9 High Temperature Testing

The experiment discussed in this section was selected as a good example to illustrate many of the fundamental characteristics of the quasi-DC potential drop measurement. This test was conducted at room temperature for the purpose of improved control and availability of other low-temperature strain monitoring methods. In reality, monitoring creep requires tests at elevated temperatures.

A number of creep tests were performed on a range of materials over a range of conditions. Of those, three on P91 material will be reported in detail – representing the current capabilities of measurement equipment and procedure which have improved considerably over the course of the project.

For this purpose creep rupture testing machines are used; a basic overview to the fundamentals of creep testing is provided by Evans (Evans & Wilshire, 1993). Usually, creep tests are used to investigate material creep properties and for this purpose small, 5-12 mm diameter cylindrical specimens are used

(Evans & Wilshire, 1993). The tensile stress may be applied by a range of mechanisms, conventionally a lever arm arrangement is used. Due to the elevated temperature and small cross section of samples machines are typically rated <5 kN, although of course standard tensile test machines may be adapted for use which will result in a much higher capacity. Creep tests machines will have a furnace integrated into the design. The furnace will close around the specimen and will usually be capable of in excess of 700 °C.

The creep tests in this thesis were conducted using the same equipment. Special, rectangular cross section specimens were produced, providing a more suitable geometry for installing potential drop sensors. An example is shown in Figure 2.16; load is applied using rods inserted through increased cross section/low stress regions at either end.



Figure 2.16: Photograph of a high temperature creep specimen with an array of 5 mm electrode separation potential drop sensors along one face.

An independent strain measurement provides useful information for the validation of the influence of strain. Total machine displacement is easily available yet may be unreliable due to the contribution of strain outside of the gauge region; for example creep of the mounting holes. As already described in Section 1.2.6.2 in-situ creep strain monitoring is difficult to achieve in practise. A number of techniques were attempted but were inadequate; eventually an extensometry technique was devised as will be described in Section 4.5.2.

2.10 Conclusions

A directional, quasi-DC potential drop measurement technique has been presented which is primarily sensitive to strain and resistivity changes; both of which are believed to hold promise for use in creep monitoring.

The use of a DC, or quasi-DC measurement is necessary to suppress the influence of the skin effect. The skin depth is a known function of inspection frequency, conductivity and magnetic permeability. In ferromagnetic materials the magnetic permeability is known to vary significantly as a function of many different variables; in the example measurement shown here the magnetic permeability was

manipulated by the application of stress. The changing skin depth electromagnetically constricts the current penetration and therefore the measured resistance. The effect is suppressed by geometrically limiting current penetration to a depth that is smaller than the skin depth. Simultaneously, it is advantageous to adopt as high a frequency as possible to reduce the flicker noise.

An unconventional square electrode arrangement provides improved directionality and strain sensitivity. The arrangement permits two orthogonal measurements from which biaxial strain and anisotropic resistivity may be inferred. A useful interpretive strategy has been previously suggested which has the effect of negating isotropic resistivity changes. The isotropic resistivity will be common to both orthogonal measurements; therefore by dividing one by the other resistivity changes will cancel out. This presents a powerful metric as it provides a nominally temperature independent measurement which is also insensitive to resistivity drift. Unfortunately, in doing so, some strain information is lost as the Normalised Resistance Ratio is only sensitive to changes in aspect ratio as opposed to individual strain components.

A compact and self-contained measurement system has been developed using off the shelf components and the addition of a specially designed current booster and preamplifier. The noise performance has been shown to be excellent and capable of suitable SNR's at 100 mA, lending the general measurement principle to low-power monitoring. The instrumentation was demonstrated on an example measurement in this section.

Following the industrial background and problem definition of Chapter 1 and the detailed description of the measurement technique provided here, the remaining chapters will investigate the creep monitoring capabilities of the sensor in power station components.

Chapter 3

Electrical Conductivity Changes in Creep Exposed Power Station Steels

3.1 Introduction

Direct Current Potential Drop measurements were introduced in Chapter 2 using the simple expression,

$$R = \rho\Lambda \quad (3.1)$$

where R is the transfer resistance to be measured, ρ is the resistivity and Λ is a geometric coefficient with units of inverse length. Both resistivity and geometric changes have shown promise for inferring information on creep state with numerous sources reporting carbide evolution and associated solute depletion (Byeon & Kwun, 2003; Seok et al., 2004; Yu et al., 1999), grain boundary separation (Madhi & Nagy, 2011b) and dislocation density (Dyos & Farrell, 1992) all having an influence on electrical conductivity. Likewise, it is well known that strain and strain rate are good metrics of creep state (Le May & Furtado, 1999; Penny, 1996; Prager, 2000; Voight, 1989).

The challenge is whether the effects of different mechanisms can be sufficiently separated and whether the changes and measurement sensitivity are sufficient to infer useful information. If the effects of geometry can be sufficiently suppressed and the changes in conductivity from different microstructural sources isolated then information of material state may be obtained from conductivity. Conversely, if conductivity changes can be suppressed, compensated, or are negligible then it will be possible to assume that all of the measured resistance changes are associated with strain and a strain inversion will be possible. In order to suggest an appropriate strategy for the utilisation of potential drop data then it is necessary to gain an understanding of the expected changes in conductivity from creep exposure and thermal ageing.

Further, a significant question to address is concerning the isotropy of conductivity changes. The Normalised Resistance Ratio measurement detailed in Chapter 2.6.2 suppresses homogenous isotropic conductivity changes by dividing the two orthogonal resistance measurements. This may be exploited

either as a resistivity independent strain metric on the assumption of isotropy or to detect changes in electrical anisotropy. Grain boundary separation is usually observed on boundaries perpendicular to the maximum principal tensile stress axis (Viswanathan, 1989; Webster & Ainsworth, 1994). The directionality of the defects suggests that the influence on resistivity may be anisotropic and therefore influence the resistance ratio.

This chapter will first provide a brief overview of the dominant microstructural changes that are known to occur in creep exposed and thermally aged components. The theory of electrical conductivity in power station steels follows, allowing for an analysis of the anticipated influence of each of the main microstructural features in the subsequent sections. The discussion is devoted to an appropriate strategy for the utilisation of potential drop measurements for monitoring the creep state of power station components.

3.2 Overview of the Microstructural Evolution of Creep Exposed Components

For convenience the key microstructural features of creep exposed components will be repeated here. Of particular interest are:

- Dislocation density
- Carbide evolution
- Grain boundary separation

The microstructural changes that are commonly associated with creep exposure are often discussed in the framework of their symptomatic influence on strain rate and conveniently primary, secondary and tertiary creep.

3.2.1 Dislocation Density

During primary creep the material strain hardens, increasing the creep resistance and reducing the strain rate through dislocation multiplication and production (Callister, 2006; Evans & Wilshire, 1993; Viswanathan, 1989; Webster & Ainsworth, 1994). In parallel to this, as a result of the elevated temperature, the material is undergoing recovery; increased diffusion reduces the number and energy state of dislocations. When strain hardening is balanced by recovery the resulting strain rate is nominally constant and secondary creep results. The first microstructural change to be considered therefore is dislocation development.

3.2.2 Carbide Evolution: Solute depletion and Carbide Coarsening

Creep damage then accumulates throughout the remainder of the creep life, increasing the strain rate through tertiary creep until failure. The concept of ‘creep damage’ was discussed in Section 1.1.2.1 and will be developed further in Chapter 5, but it is considered to constitute a number of mechanisms which undermine the creep tolerance of the component. These may act through reducing the creep sustaining geometry (area loss through creep strain, oxidation, corrosion etc.) or by reducing the creep strength of the remaining area. The ‘Cr-Mo-V’ steels and high chrome steels common to power station applications derive their creep resistance from the addition of chromium, molybdenum and vanadium, serving to both provide solid-solution strengthening and form carbides that precipitation-harden the material (Abe, 2008; Viswanathan, 1989; Webster & Ainsworth, 1994). Both solute atoms and finely dispersed carbide precipitates impede dislocation motion. Solute depletion and carbide evolution are related mechanisms. Alloying elements initially dissolved in the matrix for solid solution strengthening will precipitate to form metastable carbides which evolve to an increasingly stable state. These carbides, and those originally designed into the material for the purpose of precipitation hardening, will gradually coarsen, reducing the number density of particles and the ability to pin dislocations and prevent grain boundary sliding (Viswanathan, 1989; Webster & Ainsworth, 1994). The second microstructural feature to examine is therefore solute depletion and the associated carbide coarsening.

3.2.3 Grain Boundary Separation

Finally, it is usually the development of microcracks which ultimately leads to creep fracture (Evans & Wilshire, 1993). Sliding grain boundaries set up stress concentrations at grain corners and at irregularities such as intergranular carbides which may result in decohesion and cavity nucleation. The growth and linking of cavities may result in grain boundary separation and eventually microcracking (Evans & Wilshire, 1993; Kassner & Hayes, 2003; Viswanathan, 1989; Webster & Ainsworth, 1994). The influence of grain boundary separation on conductivity is the final microstructural feature to be examined.

3.3 Overview of conductivity in creep resistant steels

Above about 20% of the Debye temperature, almost all metals show extended periods of linear resistivity-temperature relationships as thermal excitation of the lattice increases scattering (Pollock, 1993) (20% of the Debye temperature of Iron is 94 °K (Kittel, 2004)). Below about 20% of the Debye temperature resistivity varies with a T^5 dependency and resistivity tends to the 0°K asymptote where phonon scattering from thermal excitation is eliminated and scattering must be attributed to remnant imperfections such as dislocations (Dyos & Farrell, 1992) and alloying elements (Dyos & Farrell, 1992; Pollock, 1993; Rossiter, 1991). As the purity and crystalline perfection improves, the residual resistivity

reduces. The residual resistivity contributed by dilute alloy concentrations will increase linearly with proportion to number of alloy atoms. Further, it is assumed that the residual resistivity is nominally temperature independent as the foreign atoms vibrate as though they were host atoms. This observation constitutes Matthiessen's rule and forms a frequently used simplification (Pollock, 1993; Rossiter, 1991) and is a suitable framework for the analysis of this chapter. It separates residual 'temperature independent' resistivity from impurities and the disorder arising from thermal excitation of the lattice. Matthiessen's rule can be described as,

$$\rho(T, \langle c \rangle) = \rho_{\text{residual}}(\langle c \rangle) + \rho_{\text{lattice}}(T) \quad (3.2)$$

where ρ is the total resistivity of the alloy, $\rho_{\text{residual}}(\langle c \rangle)$ is the contribution to residual resistivity from alloying elements and $\rho_{\text{lattice}}(T)$ is the temperature dependent resistivity from lattice vibration. This relationship, along with Debye temperature, T_D , is shown schematically in Figure 3.1.

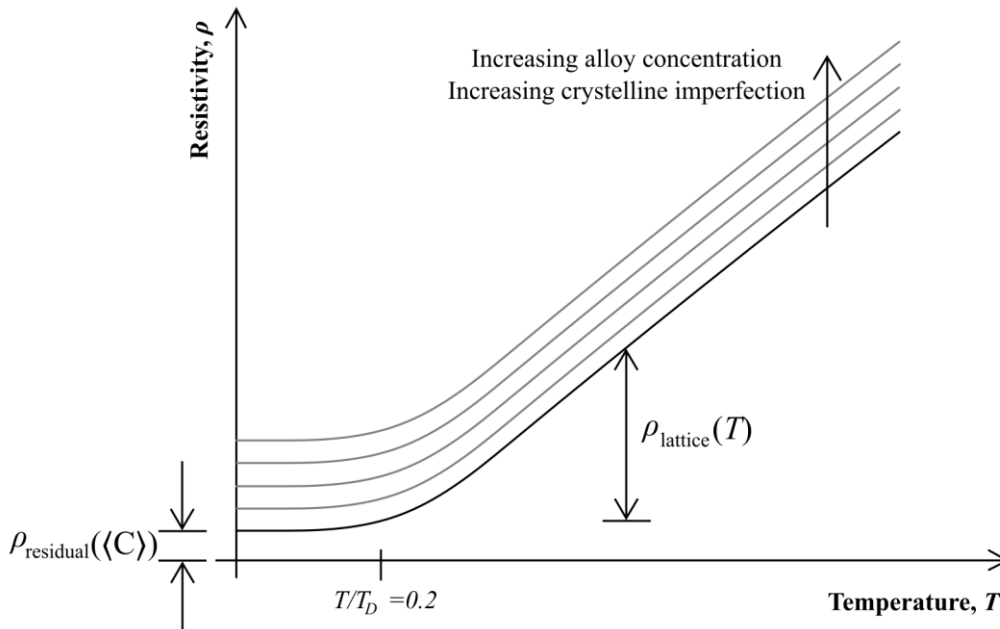


Figure 3.1: Schematic illustrating the linear temperature dependency above 20% of the Debye temperature. The increase in residual resistivity is a function of lattice impurity and approximately a linear function of alloy concentration.

Of course, the residual resistivity term should not be considered truly temperature independent but rather not have an intrinsic temperature dependency (Rossiter, 1991). It will be shown in this chapter that for example thermally activated microstructural changes can cause irreversible changes in residual resistivity.

The situation is further complicated in the ferromagnetic materials common in power station applications. In ferromagnetic materials additional scattering occurs in the electrons carrying the

magnetic moment as a result of magnetic disorder (Rossiter, 1991). As the temperature is increased the magnetic resistivity rises at an increased rate reflecting the increase in disorder. At the Curie temperature where disorder is complete there is a change in the temperature - resistivity curve (Dyos & Farrell, 1992). The temperature dependent magnetic contribution resulting from spin-disorder, $\rho_{mag}(T)$, is often added to Matthiessen's rule giving (Pepperhoff & Acet, 2001; Rossiter, 1991),

$$\rho_T(T, \langle c \rangle) = \rho_{residual}(\langle c \rangle) + \rho_{lattice}(T) + \rho_{mag}(T) . \quad (3.3)$$

This trend is used in the experimental observations in iron of Weiss and Marotta reproduced in Figure 3.2 (Weiss & Marotta, 1959). The reader is referred to The Electrical Resistivity Handbook (Dyos & Farrell, 1992) for further experimental results from a wide selection of alloys at a range of temperatures.

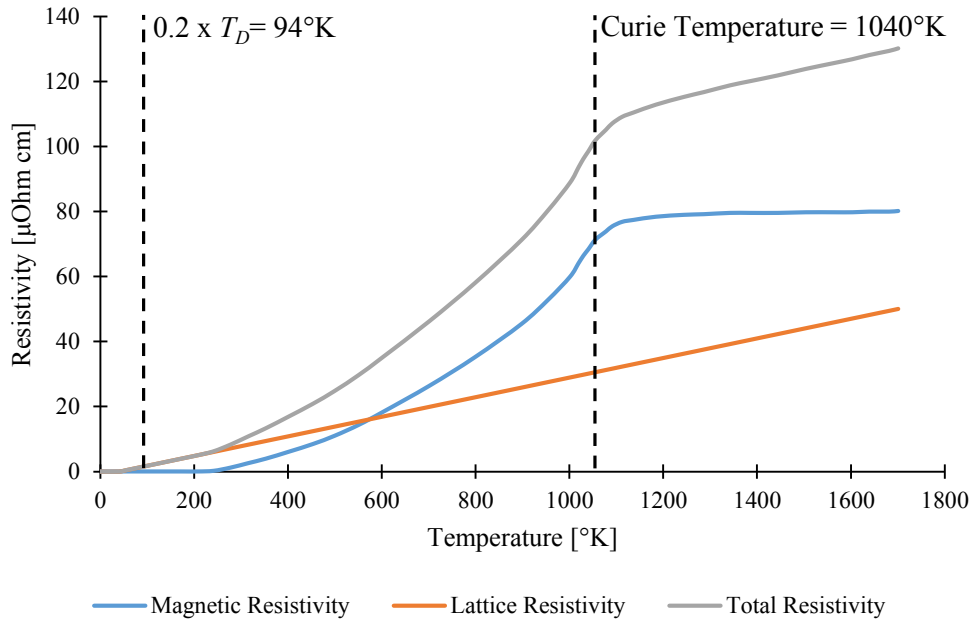


Figure 3.2: Lattice and magnetic resistivity of iron. Data read from graphs in (Weiss & Marotta, 1959)

Again the framework of Equation 3.3 is a simplification. Irreversible, thermally activated microstructural changes may alter the magnetic state of the component and change the shape of the resistivity - temperature relationship. Further, for high concentration alloys and magnetic materials it is reasonable to expect interaction of different phenomena and deviation from simple additivity (Dyos & Farrell, 1992; Pollock, 1993; Rossiter, 1991). Nevertheless, it will be used as a starting point for assessing the likely effect of the microstructural evolution associated with creep exposure.

Macroscopic defects such as grain boundary separation and cracking should be considered a geometric impediment, acting by limiting the area available for current flow. It is expected that the resistivity

contribution is likely to have significant anisotropy associated with the orientation of the defects. The macrodefects will be included as a multiplicative factor to the otherwise undamaged resistivity.

$$\rho(\omega, T, \langle c \rangle) = G[\rho_{residual}(\langle c \rangle) + \rho_{lattice}(T) + \rho_{mag}(T)] \quad (3.4)$$

where G is the additional resistivity provided by a given defect state.

3.4 Dislocations

Dislocations disrupt the crystalline structure and therefore contribute to the residual resistivity of the component. In comparison to alloy concentration, the influence of crystalline imperfection is considered to be much less significant (Pollock, 1993). Further, due to the temperature independence of the residual resistivity, at high temperature the resistivity is further dominated by phonon scattering from lattice vibrations and the effect of dislocations are said to be negligible (Dyos & Farrell, 1992). For this reason, the influence of dislocations will not be further considered in this thesis.

3.5 Carbide Evolution

It is expected that the reduction in alloy solute concentration during precipitate nucleation and growth will improve the lattice regularity and reduce resistivity. Further, in keeping with Matthiessen's rule, it is expected that the reduction in resistivity will be approximately linear with the number of solute atoms depleted from the matrix and therefore relate to precipitate growth. The linear dependence of resistivity on solute depletion is exploited in numerous studies by utilising 'resistometric' measurements as a tool to study precipitate evolution and kinematics (Ceresara & Fiorini, 1972; Lasek, 1976; Oh et al., 1997; Servi & Turnbull, 1966) and potentially heat treatment monitoring and control (Tan et al., 2015).

The transformation fraction, χ , is defined here to be the number of transformed atoms divided by those that will eventually transform to reach the equilibrium condition, or in terms of solute concentration,

$$\chi = \frac{\langle c \rangle_0 - \langle c \rangle}{\langle c \rangle_0 - \langle c \rangle_\infty} \quad (3.5)$$

where $\langle c \rangle$ is solute concentration, $\langle c \rangle_0$ is the initial concentration, $\langle c \rangle_\infty$ is the concentration of the fully transformed equilibrium state. Following Mattheisen's rule, in resistometric measurements the transformation fraction is measured as,

$$\chi = \frac{\rho_0 - \rho}{\rho_0 - \rho_\infty} \quad (3.6)$$

where ρ is resistivity, ρ_0 is the initial resistivity, ρ_∞ is the resistivity of the fully transformed equilibrium state (Ceresara & Fiorini, 1972; Lasek, 1976; Oh et al., 1997; Servi & Turnbull, 1966). The kinematics of solute depletion are considered to follow the Wert-Zener equation (Dyson, 2000; Wert & Zener, 1950; Yin & Faulkner, 2005b),

$$\tau \frac{d\chi}{dt} = \frac{3}{2} \left[\chi^{\frac{1}{3}} (1 - \chi) \right] \quad (3.7)$$

where t is the time and τ is a characteristic time constant obtained experimentally. When solved and rearranged following the work of Oh (Oh et al., 1997) gives,

$$\chi = 1 - 0.699e^{-1.5\left(\frac{t}{\tau}\right)}, \quad (3.8)$$

or more conveniently the Avrami-Johnson-Mehl equations (Oh et al., 1997),

$$\chi = 1 - e^{-\left(\frac{t}{\tau}\right)^\zeta}. \quad (3.9)$$

where, again τ is a characteristic time constant and ζ is an exponent usually assumed to be constant and found experimentally. These functions are plotted in Figure 3.3. They show that the rate of nucleation, growth and associated solute depletion is expected to reduce with time due to the availability of rate controlling atoms (Yin & Faulkner, 2005a). The reduction in resistivity due to solute depletion is therefore expected to follow a similar exponentially decreasing pattern, tending to an equilibrium resistivity.

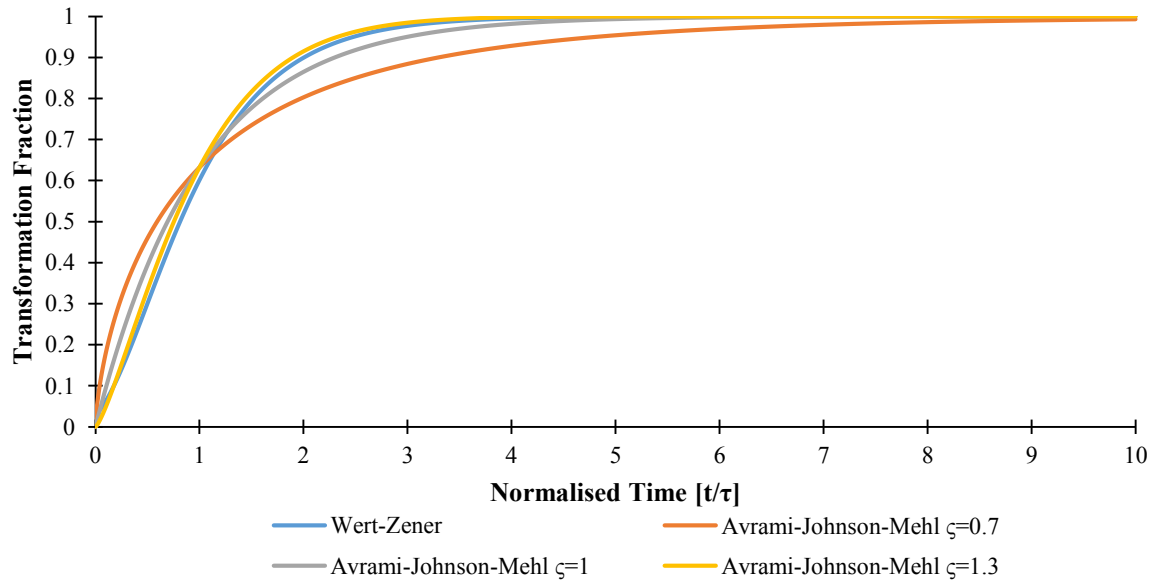


Figure 3.3: Transformation fraction against normalised time for Wert-Zener and Avrami-Johnson-Mehl precipitation rate equations. The range of Avrami-Johnson-Mehl exponent values, ζ , chosen following (Oh et al., 1997).

The presence of new phases will also influence the resistivity, the extent of which is difficult to predict and will depend on the exact nature of the precipitate and the host lattice (Pollock, 1993) but it is expected that the effect of solute depletion will dominate the formation of relatively low volume fraction secondary phases.

At elevated temperatures the precipitates can coarsen, compromising their effectiveness at impeding dislocation movement and promoting grain boundary decohesion (Taplin, 2013; Viswanathan, 1989; Webster & Ainsworth, 1994). The coarsening is not expected to have a substantial effect on the solute concentration as it is considered a constant volume fraction process with coarsening occurring as a result of the preferential growth of larger particles at the expense of smaller particles with negligible net transfer of solute atoms to the matrix; the equations quantifying the rate of coarsening is said to be well understood (Dyson, 2000). It is therefore hypothesised that the only effect of coarsening on electrical conductivity is the effect of the changing configuration of the constant volume fraction of secondary phases. This problem is discussed in detail by Rossiter (Rossiter, 1991) but will not be given further consideration here.

3.5.1 Experiment Results on the Influence of Carbide Evolution from Literature

The use of electrical resistance measurements to infer thermally activated microstructural degradation has been previously studied in literature. Byeon and Kwun (Byeon & Kwun, 2003) investigated 2.25Cr-1Mo steel while Seok, Bae and Koo (Seok et al., 2004) and Yu, Nahm and Kim (Yu et al., 1999) studied 1Cr-1Mo-0.25V steels. In all studies microstructural degradation was accelerated by continued exposure to 630°C. Ageing was periodically interrupted allowing four-point DC resistance measurements to be taken from machined specimens of controlled geometries at near ambient conditions. In all cases the resistance measurements were compared to mechanical properties also dependent on solute concentration.

The resistivity results are summarised in Figure 3.4. As solute depletion is diffusion controlled the Arrhenius rate law can be used to interchange time, t_1 , at elevated temperature, T_1 , to extended exposure time, t_2 , at lower temperature, T_2 (Seok et al., 2004).

$$t_2 = t_1 \exp \left[-\frac{Q}{R} \left(\frac{1}{T_2} - \frac{1}{T_1} \right) \right] \quad (3.10)$$

where Q is the activation energy for the self-diffusion of iron, 272 kJ/mol and R is the universal gas constant, 8.314 kJ/kmolK. This allows the scaling of 630°C exposure times to effective 550°C exposure times, a temperature which better represents the operational conditions of a power station. Additionally, the reported resistivities have been normalised to their initial values.

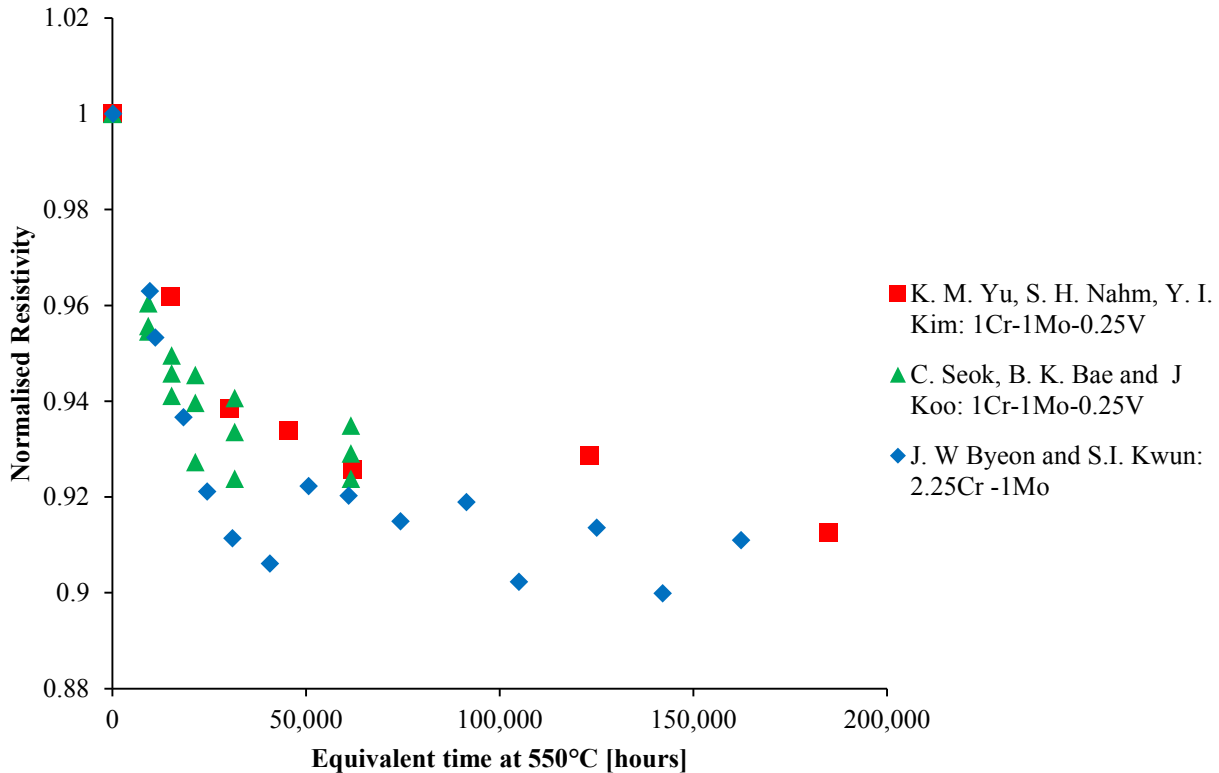


Figure 3.4: Reported reduction in resistivity against equivalent ageing time at 550°C (Byeon & Kwun, 2003; Seok et al., 2004; Yu et al., 1999). Data read from graphs, resistances normalised to initial conditions and time scaled to equivalent 550°C ageing time using Equation 3.10.

As anticipated, the resistivity exponentially decreases towards an equilibrium value, reflecting the solute depletion as solute atoms leave the matrix to form carbide precipitates. Equilibrium appears to be reached after approximately 50,000 hours of service conditions. The magnitude of the resistivity change of Figure 3.4 however is misleading as the readings were taken and normalised at room temperature. According to Matthiessen's rule the absolute decrease in resistivity due to changes in solute concentration is expected to be nominally temperature independent. Therefore, if the resistance measurements were conducted at operational temperature the total resistivity would increase due to lattice vibration and the temperature independent drop in resistivity becomes comparatively small. It will be shown in the following section that for 2.25Cr-1Mo steel increasing the temperature from room temperature to 550°C roughly doubles the resistivity. The resistivity change due to solute depletion shown in Figure 3.4 would therefore be approximately halved if measured at that temperature.

3.5.2 Continuous Measurement of the Influence of Carbide Evolution

To illustrate the influence of carbide evolution and solute depletion using in-situ PD measurements an accelerated thermal ageing experiment was undertaken using virgin 2.25Cr-1Mo material provided by E.ON. The experiment was conducted with assistance from Wayne Hosein, a MEng student supervised as part of this project. Ageing was accelerated using a furnace at 630°C. Four square configuration,

5 mm electrode separation sensors were permanently installed on segments of material following the method described in Chapter 2. Only one of the two orthogonal directions was measured at each location and 200 mA inspection current was used. A thermocouple was also installed to measure the local temperature at each potential drop measurement point. PD measurements were taken continuously but thermal ageing was occasionally interrupted to take ‘low temperature’ (30°C) readings. Resistances were normalised to their initial value at 630°C. The average normalised resistance and average temperature of the four samples are shown in Figure 3.5.

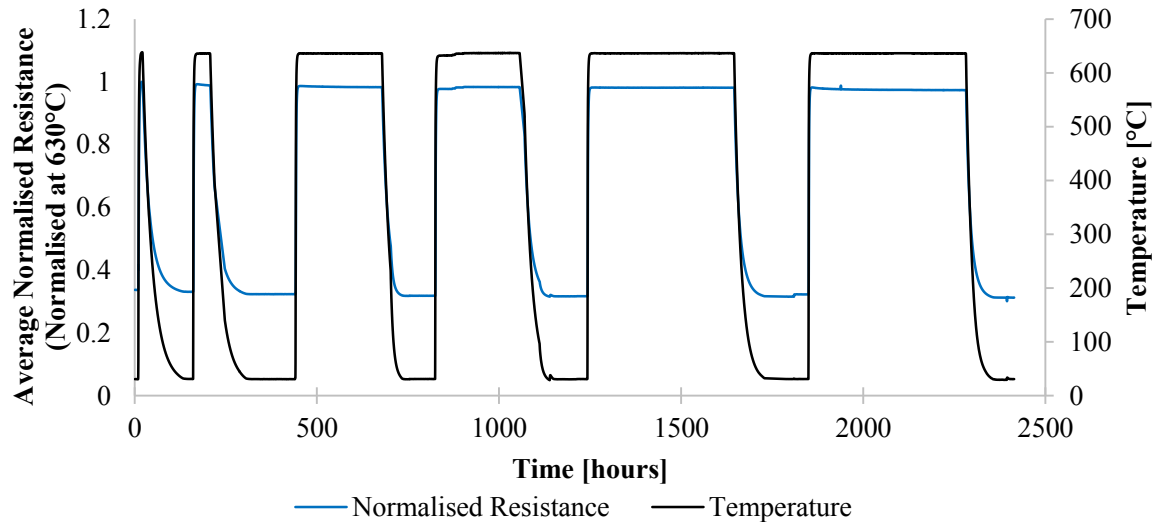


Figure 3.5: Temperature and average resistance of four 2.25Cr-1Mo samples taken using the square electrode configuration, permanently installed potential drop measurement, normalised at 630°C. Spread in resistance data evident in following figure.

The raw resistance data was then processed to produce Figure 3.6. Each sensor was temperature compensated to account for minor deviations from the set point. Secondly, the Arrhenius rate law was adopted to calculate the equivalent time at 550°C based on individual thermocouple readings to better reflect the expected time scales in power station components. The four measurements are shown in Figure 3.6; only data within 5°C of the set point temperature was included. The discontinuities observed account for time while the specimens were heating and cooling where data has been filtered out; ageing may continue during the cooling periods, especially during the initial high rate of resistivity change. The exponentially decreasing resistivity is consistent with the trends predicted by the theory of Wert-Zener and Avrami-Johnson-Mehl and the previous empirical results reported in Figure 3.4.

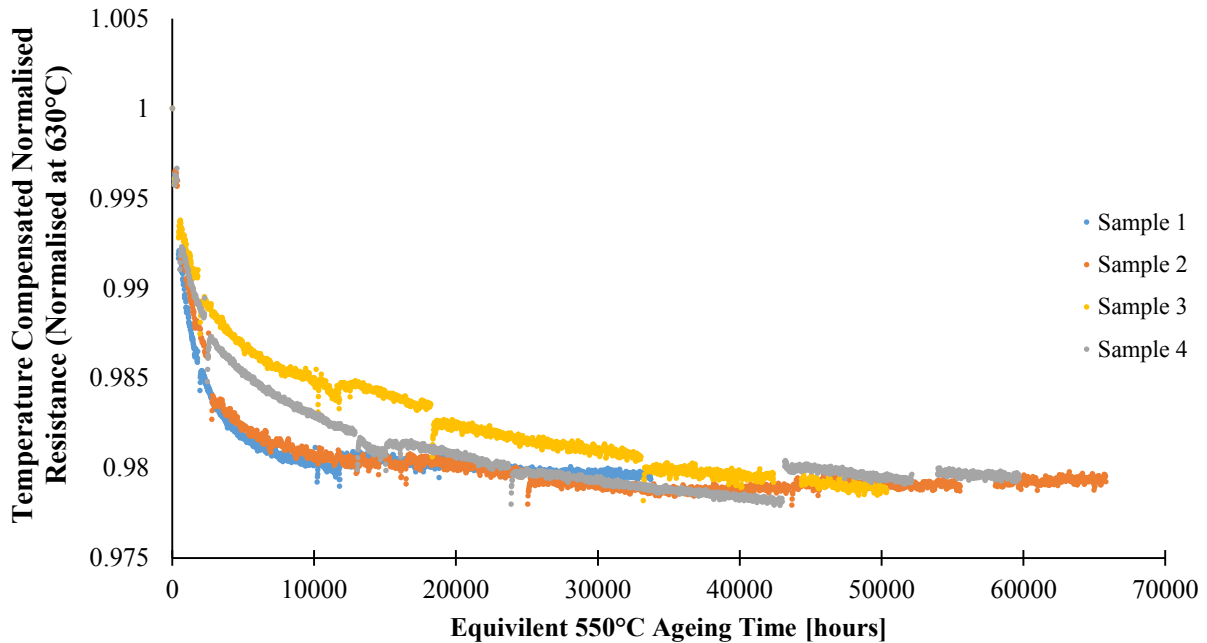


Figure 3.6: Temperature compensated resistance of 2.25Cr-1Mo steel normalised at 630°C for experiment shown in Figure 3.5. Equivalent ageing times have been calculated using Equation 3.10 and thermocouple data local to each measurement location.

The time scale observed in the exponential decay of Figure 3.6 is however much shorter than Figure 3.4, perhaps suggesting a different starting point for the measurement. Again, the change in resistivity attributed to solute depletion should be considered in the context of the normalisation temperature. According to Matthiessen's rule the resistivity change is expected to be temperature independent, therefore, the increased resistivity due to the elevated temperature of this experiment will result in a smaller percentage change in resistivity. The percentage change when normalised at room temperature is observed to be 6%, again consistent with Figure 3.4.

The substantial resistivity decrease appears to be complete in approximately 10,000 hours (of equivalent 550°C ageing time). Following this the resistivity reaches a steady state within the time frame of the experiment. No long term change in resistivity as a result of carbide coarsening is evident.

Figure 3.7 shows the resistance data for each successive cooling cycle. The resistance data is normalised to the 550°C point on the first cooling cycle. The initial drop in resistivity from the first heating cycle is therefore not included. This provides evidence for agreement with Matthiessen's rule, echoing the schematic shown in Figure 3.1. Thermal ageing reduces the resistivity as solute atoms are depleted from the matrix to form precipitates; the reduction in resistivity is seen to be temperature independent.

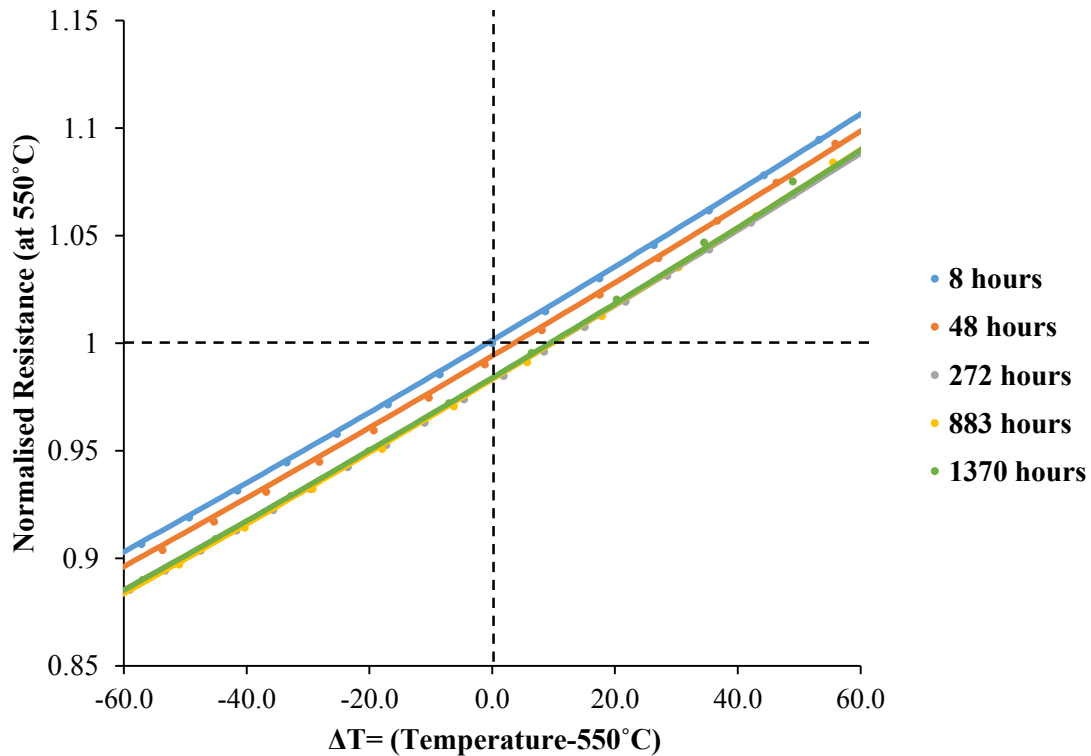


Figure 3.7: Normalised Resistance against temperature for each successive cooling cycle shown in Figure 1.5. The linear approximation is a least-squares fit for $550 \pm 70^\circ\text{C}$

It can be concluded that solute depletion is easily detectable using electrical resistivity measurements. Despite the additional complexity of the ferromagnetic host material, the small changes in solute concentration appear to have a temperature independent additive contribution to resistivity in accordance with Matthiessen's rule. With additional prior knowledge of the composition of the phases of the initial and equilibrium state it may be possible to be quantitative about the concentration of each element depleted from the matrix. Solute depletion is seen to occur immediately and the rate decreases with time. This isolates the effect from other damage mechanisms which occur gradually over time or accelerate towards failure. Following the initial resistivity decrease attributed to solute depletion the resistivity appears to be stable with no evidence of the influence of carbide coarsening.

Though it is understood that strain can accelerate carbide coarsening, solute depletion and carbide coarsening are predominantly functions of temperature (Dyson, 2000; Yin & Faulkner, 2005a). Further, the kinetics of solute depletion and growth are thought to be well understood (Dyson, 2000) and so it is suggested that analytical predictions, coupled with simple temperature monitoring, may be adequate to approximate the thermally activated material damage.

The approximation that the resistivity change will be temperature independent provides a measurement strategy. The temperature dependent lattice resistivity will reduce at lower temperatures and therefore



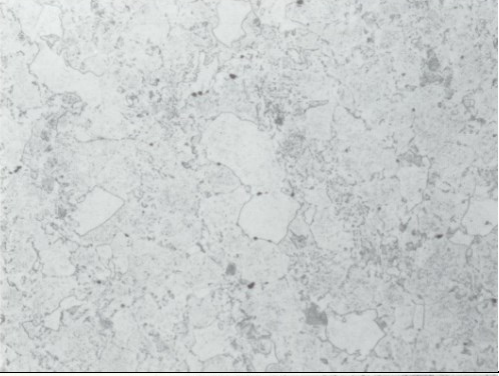
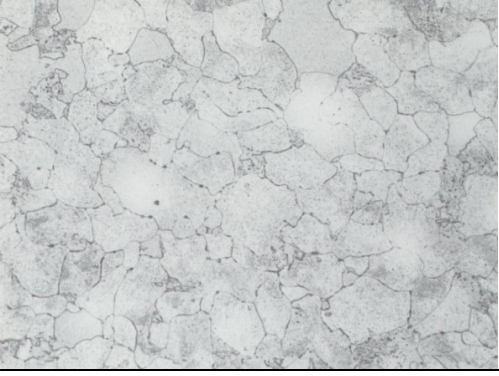
the percentage change caused by solute depletion will be greater, therefore measuring at ambient (or even sub-ambient) conditions is recommended as it is the remnant resistivity that is of interest. Conversely, as is evident from the accelerated elevated temperature results of Figure 3.6, if it is beneficial to suppress these changes, measurement at high temperature is recommended. Alternatively, as there is no reason to believe that solute depletion will have anisotropic influence on resistivity, the isotropic effect of solute depletion can be suppressed in the resistance ratio.

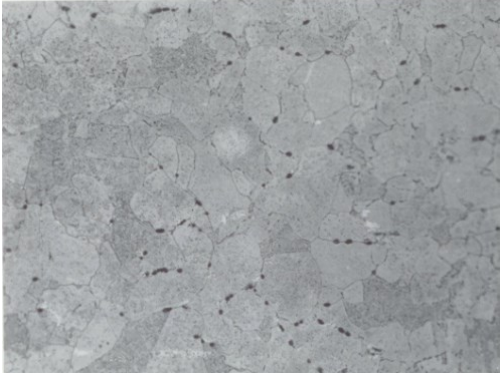


3.6 Grain Boundary Separation

The VGB criteria for assessing the creep state of components based on visual inspection of grain boundary separation was introduced in Section 1.2.1. Table 3.1 shows micrographs of components exposed to at least 100,000 hours of service conditions taken from report VGB TW507. Of particular interest in the context of this thesis is the aligned cavities that are seen to form during the 3B, advanced creep damage, condition. Intuitively, the alignment of the inclusions will form a greater ‘barrier’ to current flow in certain directions (here top to bottom) than others. The proposed potential drop sensor has sensitivity to directional variations in resistivity and is therefore able to detect anisotropy; by utilising the Normalised Resistance Ratio, isotropic changes in resistivity may be suppressed whilst maintaining sensitivity to anisotropic resistivity changes caused by aligned cavitation.

It has proved difficult to recreate grain boundary separation in accelerated laboratory tests and it has not been possible to obtain sufficiently large samples to measure the effect of grain boundary separation experimentally. Instead, an analytical model has been adopted to estimate the likely electrical anisotropy associated with grain boundary separation. The analysis presented here will model the damaged material state as an equivalent effective resistivity tensor which acts to reduce the conductivity of the initial undamaged material.

Table 3.1: VGB assessment criteria based on the state of grain boundary separation including example micrographs of each damage level from (VGB-Kraftwerkstechnik GmbH, 1992).

Assessment Class	Structural and Damage Conditions	Example Microstructure from (VGB-Kraftwerkstechnik GmbH, 1992)
0	As received, without thermal service load.	
1	Creep exposed, without cavities.	
2A	Advanced creep exposure, numerous cavities without preferred orientation.	
2B	More advanced creep exposure, numerous cavities without preferred orientation.	

3A	Creep damage, numerous orientated cavities.	 Micrograph showing a polycrystalline metal structure with numerous small, dark, elongated cavities oriented along grain boundaries. A scale bar in the bottom right corner indicates 50 μm.
3B	Advanced creep damage, chains of cavities and/or grain boundary separations.	 Micrograph showing advanced creep damage with chains of dark, elongated cavities and some grain boundary separations. A scale bar in the bottom right corner indicates 50 μm.
4	Advances creep damage, microcracks.	 Micrograph showing advanced creep damage with visible microcracks. A scale bar in the bottom right corner indicates 100 μm.
5	Large creep damage, macrocracks.	-

The effective conductivity of an inhomogeneous material with inclusions of differing conductivity has been addressed by a number of authors. The most comprehensive publication on the topic, extending to crack like defects, is provided by Shafiro and Kachanov (Shafiro & Kachanov, 2000). In the study inclusions are modelled as ellipsoids which may have eccentricity and may be inclined at an angle. It is then possible to calculate the effective conductivity of a mixture of inclusions with size, eccentricity and direction on the assumption that they are non-interacting.

The primary difficulty in estimating the conductivity tensors associated with the images of Table 3.1 is that we only have access to a 2D representation of the material state. The micrographs conceal the number density of inclusions below the surface and also the true size and morphology of the inclusions. Gross approximations must then be made regarding the geometry of the inclusions, so it is appropriate to use a simplified model. Conservative values will be adopted to arrive at an extreme case of maximum influence on conductivity. A model is used where each cavity is approximated as a ‘penny shaped crack’: an extreme oblate ellipsoid that has one axis negligible in length compared to the remaining two. It will further be assumed that all cavities are perfectly aligned; grain boundary separation is usually observed on boundaries perpendicular to the maximum principal tensile stress axis. A schematic representation of this model is provided for illustrative purposes in Figure 3.8. This simplification gives the extreme case of totally anisotropic conductivity. The aligned, two-dimensional inclusions will have no influence on conductivity in the plane to which the inclusions are aligned, but will reduce conductivity in the direction normal to this plane (here, left to right). The reduction of conductivity in this direction will therefore be an overestimate and provide an upper limit not only to absolute increase in resistivity but also the likely influence of anisotropy.

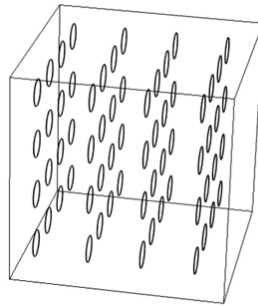


Figure 3.8: Schematic illustrating the aligned penny-shaped crack model of grain boundary separation. Each cavity is modelled as a two dimensional insulating inclusion.

Shafiro and Kachanov (Shafiro & Kachanov, 2000) details an analytical method to assess the contribution of such an inclusion, $\mathbf{H}^{(i)}$, to the conductivity matrix, $\boldsymbol{\sigma}$ so that:

$$\boldsymbol{\sigma} = \sigma_0 \mathbf{I} + \sum_i \mathbf{H}^{(i)}, \quad (3.11)$$

where σ_0 is the initial isotropic conductivity of the material and we sum the contribution of many inclusions using a non-interaction approximation. Each inclusion is shown to have a contribution equal to Equation 3.12 where d is the inclusion radius, V is the volume of the material and the short axis of the ellipsoid is aligned with the unit vector, \mathbf{s} .

$$\mathbf{H} = -\sigma_0 \frac{d^3}{3V} \mathbf{s}\mathbf{s}. \quad (3.12)$$

In order to extrapolate the information we have from the two dimensional micrograph into the third spatial dimension we must make some assumptions. As we are viewing only a cross section through each inclusion we do not necessarily know the true length; to obtain an upper limit we must therefore assume that all of the inclusions are of the same size equal to the longest inclusion viewed. Further to this we also assume that all cavities whose centre is \pm half a diameter from the plane of cross section will be visible and the cavitated state is homogeneous in the third dimension. The volumetric number density of inclusions, N , and area density of inclusions, n , will therefore be related by the assumed cavity length, $N = n/d$. Combining Equations 3.10 and 3.11, and converting some of these terms into a form that will allow us to make an estimate from a given micrograph we arrive at,

$$\boldsymbol{\sigma} = \sigma_0 \begin{pmatrix} 1 & 0 & 0 \\ 0 & \left(1 - n \frac{d^2}{3}\right) & 0 \\ 0 & 0 & 1 \end{pmatrix}. \quad (3.13)$$

In this case we have arbitrarily assumed that all the cavities are aligned in the x_2 direction.

The micrographs of advanced creep damage, level 3B, from Table 3.1 will be used as illustrative examples. Clearly, there is a great difference in the two micrographs given as level 3B; it is understood that these represent minimum and maximum boundaries to the advanced creep damage level and therefore form a range of states where component retirement is likely.

The number area density, n , and maximum crack length, d , of Equation 3.13 will be obtained from measurement of the micrographs. Figure 3.9 (a) shows 10 features identified as aligned cavitation; from the scale of the micrographs, this is equivalent to ~ 64 per mm^2 . One of these has been measured as $16 \mu\text{m}$. Inserting these values into Equation 3.13 gives an anticipated reduction in conductivity of 0.55% in the direction normal to alignment (here, left to right). Equivalent measurements for Figure 3.9 (b) are harder to reach, but as an example, if the cluster of cavities identified is treated as a single $100 \mu\text{m}$ crack, then each such crack per mm^2 will reduce the conductivity by $\sim 2\%$ in the normal direction; it is therefore believed that an anisotropic conductivity decrease of the order of 10% may be possible by the end of level 3B damage; representing a substantial increase in resistivity during advanced creep.

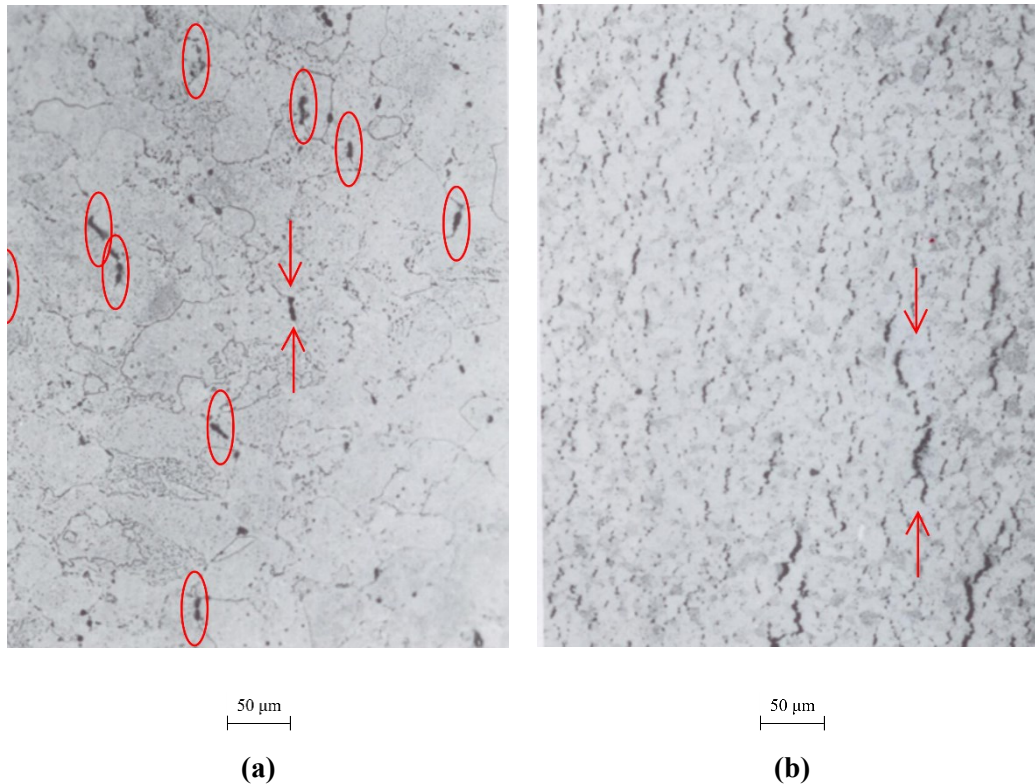


Figure 3.9: Example images of advanced, level 3B, microstructures from (VGB-Kraftwerkstechnik GmbH, 1992). Marked on to the images are features that have been used to approximate the number density and size of inclusions to approximate the influence of grain boundary separation on electrical resistivity using Equation 3.13.

It may be concluded therefore that the resistivity changes associated with grain boundary separation are small until the advanced stages of creep damage, with a conservative upper limit of 0.5% conductivity decrease. A significant anisotropic conductivity drop of the order of 10% is expected in the latter stages of advanced creep as creep cracks start to initiate, though this may be too late in life to be of practical use. The Normalised Resistance Ratio offers a means to separate the anisotropic resistivity changes from isotropic changes; however, it may be a challenge to separate the effect of strain that is also associated with advanced creep when using a permanently installed sensor.

There is concern over the reliability of monitoring grain boundary separation as an indication of creep. Cr-Mo steels may show little, if any, void formation at failure (Furtado & May, 2004). This observation is supported by reports such as the NIMS Metallographic Atlas of Long-Term Crept Materials; in this comprehensive summary of microstructure from creep tests, many in excess of 100,000 hours, there is little-to-no evidence of any grain boundary separation. Monitoring grain boundary separation will therefore fail to indicate proximity to failure.

3.7 Discussion

It was concluded in sections 3.4 to 3.6 that,

- Dislocation development will have negligible influence on resistivity at elevated measurement temperatures
- Solute depletion will decrease the resistivity of the material by of the order of 2% at 550°C, but the rate of change will decrease rapidly as equilibrium is approached. The vast majority of resistivity change will be complete after 10,000 hours of 550°C exposure. The design life of a component, which is often extended, is typically 100,000 hours.
- The influence of carbide coarsening was not observed.
- The influence of grain boundary separation is expected to be anisotropic and be <0.5% until the advanced stages of creep damage. The increase in grain boundary separation is thought to occur very late in life, possibly after decommissioning would normally have occurred.

The implications of these resistivity changes will be discussed in relation to the possible monitoring strategies.

3.7.1 Monitoring Strategies

3.7.1.1 Assessing Creep State using Resistivity

Creep State from Resistivity Changes - Normalised Resistance

Normalised Resistance measurements will be sensitive to all resistivity changes and additionally the sensitivity to strain caused by electrode migration. If sensors are installed on virgin material then initially resistance changes are likely to be dominated by the effect of solute depletion on isotropic resistivity. It is unlikely to be of great practical importance as a stable state is reached after a relatively short amount of time and will not be a direct cause of failure. Following this, resistivity is expected to be stable until the very advanced stages of creep damage as grain boundary separation and crack initiation become a significant influence. The use of Normalised Resistance in isolation is not well suited to monitor grain boundary separation as it will be difficult to separate the influence from the effect of strain or other isotropic resistivity changes; it is suggested that the Normalised Resistance Ratio is better suited to monitoring grain boundary separation.

Creep State from Resistivity Changes - Normalised Resistance Ratio

The Normalised Resistance Ratio suppresses changes in isotropic resistivity and will only be sensitive to changes in anisotropic resistivity and, when using permanently installed electrodes, strain. In Section 3.6 it was concluded that in very advanced stages of creep there may be significant changes in electrical

anisotropy. The effect may be isolated from strain using spring loaded electrodes and used in an inspection manner, however this will undermine the use as a monitoring tool. The primary issue with monitoring creep state using changes in electrical anisotropy is that changes are very modest until damage is very advanced, prohibiting its use as a predictive tool throughout the full life of the component.

3.7.1.2 Assessing Creep State using Strain

Creep State using Strain - Normalised Resistance

As described in Chapter 1, strain and strain rate can provide a wealth of information on creep state. As the proposed resistance measurements are dependent both on resistivity and strain, in order to infer accurate strain information the influence of resistivity will need to be compensated, suppressed or be negligibly small. Referring forwards to the biaxial strain inversion of Equation 4.15 Chapter 4, each percentage change in resistivity will have an approximately equal effect to a percent of strain. For example, the 1.75% reduction in resistivity observed as a result of solute depletion in Figure 3.6 would be interpreted as 1.75% biaxial strain. In uniaxial laboratory experiments strain at failure is typically in excess of 10% (see for example Figure 4.15 and Figure 4.17 of Chapter 4), therefore, following the initial effect of solute depletion, the modest changes in resistivity are likely to be negligible compared to the effects of strain and can be simply neglected. In power station components however, design stresses allow for 1% creep strain over 100,000 hours of service (EPRI, 2007); in order to accurately resolve this strain rate the resistivity stability must be much less than 1% per 100,000 hours, a demanding target which is unlikely to be achieved.

One strategy for accounting for long term drift is the adoption of ‘dummy sensors’. A sample of material of the same cast, which is then thermally but not mechanically coupled to the component under test will experience the same thermally activated microstructural evolution. A sensor attached to this material will then provide a baseline drift which can then be subtracted from readings, compensating the resistivity changes and additionally instrument drift as will further be discussed in Chapter 5.

Creep State using Strain - Normalised Resistance Ratio

The use of the Normalised Resistance Ratio has the benefit that isotropic resistivity changes and instrument drift are suppressed, therefore only the anisotropic resistivity changes resulting from advanced grain boundary separation will interfere with interpretation. As even very conservative estimates of electrical anisotropy resulting from grain boundary separation are limited to 0.5% up until advanced creep then it is not expected to be a practical concern.

Unfortunately, biaxial strain information is lost in adopting the Normalised Resistance Ratio, preserving only information on strain ratio. Chapters 4 and 5 will investigate the interpretation of the Normalised Resistance Ratio as an indicator of creep state through strain.

3.8 Conclusions

Though the effects of solute depletion and grain boundary separation are expected to have an influence on resistivity comfortably within the sensitivity capabilities of potential drop measurements, the effects are believed to be limited to the initial and final stages of creep life. For the majority of the life of power station components the resistivity is expected to be relatively stable. Strain then becomes the preferred indicator of creep state as it is known to develop throughout the entirety of component life. Resistivity changes then become problematic, interfering with the interpretation of resistance as a purely strain sensitive measurement.

In accelerated laboratory creep tests the large strain rate and modest resistivity changes suggest that the effect of resistivity is likely to be negligible compared to the effects of strain and can be simply neglected, allowing the interpretation of resistance as purely a strain sensitive measurement.

The low strain rates expected in power station components, combined with the length of time monitoring must be conducted over, suggests that appropriate measures must be considered to account for the potential for long term resistivity drift. The Normalised Resistance Ratio therefore provides a strain sensitive metric which is inherently stable through the suppression of isotropic resistivity and instrument drift and is recommended as the most suitable means of providing stable strain sensitive data.

Chapter 4

Strain Inversion of Potential Drop Measurements

4.1 Introduction

The previous chapter opened with the simple expression,

$$R = \rho\Lambda \quad (4.1)$$

where R is the transfer resistance to be measured, ρ is the resistivity and Λ is a geometric coefficient with units of inverse length. Expected resistivity changes in creep exposed components were investigated and it was concluded that, with the exception of very early and late in the creep life, irreversible resistivity changes are expected to be modest, predominantly isotropic and likely to be of limited use for creep monitoring; instead the geometric effect of strain becomes the preferred indicator. In the present case, where electrodes are permanently attached to the surface of the component, the distortion of the initial electrode positions as a result of the accumulation of creep strain will affect the resistance. This chapter will provide and demonstrate the relationship between strain and resistance allowing the appropriate interpretation of data. Further, if resistivity changes can be suppressed, compensated or are negligibly small then it will be possible to invert strain from resistance, resulting in a robust and simple sensor suitable for continuous use at high temperature. The applicability of the inversions to power stations will be discussed in light of the anticipated creep strain and resistivity change in power station components.

4.2 Creep Strain in Power Station Components

It is necessary to consider the nature of creep strain accumulation in power station components as background to this chapter. Unlike the uniaxially stressed creep samples commonly tested in the laboratory, it must be assumed that real components are multiaxially stressed. Two important considerations in this thesis concern the expected magnitude of creep strain rate and also the strain tensor arising from the multiaxial stress state of a component.

It has proved challenging to find direct answers to these questions from literature, instead it is necessary to infer the information from design codes and standards for the design of pressure piping such as BS EN 13480-3 (*BS EN 13480-3*, 2012) or ASME B31.1 (*B31.1*, 2007).

The design of a component is based on the comparison of a calculated stress to a limit imposed by a designated maximum allowable stress. For pipes operating under creep conditions, design stresses are limited to the lower of either a secondary creep rate of 1% per 100,000 hours or 80% of the 100,000 hour creep rupture stress (EPRI, 2007). This is consistent with reports of expected strain of ~3% at 80% life (Parker, 1986) and the European Creep Collaborative Committee (ECCC) suggesting 1% and 2% as thresholds for increased inspection (Auerkari et al., 2005). It will be assumed throughout this thesis that a secondary strain rate of 1% per 100,000 service hours and a maximum strain of ~5% is possible for power station components.

In order to establish the strain tensor for a given location on a power station component it is first necessary to understand the stress state; to do so it is again useful to review the design methodology and established theory; a brief, simplified overview from the aforementioned standards (*B31.1*, 2007, *BS EN 13480-3*, 2012, EPRI, 2007) will be given here.

An underlying assumption in the design of power station pipelines is that, with the exception of expansion joints, they are considered ‘closed-ended’ and so the internal pressure is able to exert stress in the axial direction. For cylindrical components the ratio of circumferential to axial stress resulting from internal pressure is 2:1. The radial stress is considered to be much smaller than both the circumferential or axial stresses.

Given the functional requirements of flow and pressure of the component the pipeline diameter is chosen. The pipe wall thickness is then chosen so that the circumferential stress is within the maximum allowable design stress. As already stated, typically this results in main steam lines that are around 350 mm outside diameter with a wall thickness of around 65 mm.

In addition to the axial stress produced from internal pressure, assumed to be half that of the circumferential stress, there are also other sustained loads that need to be accommodated; most notably the dead weight load. Due to the thick pipe walls required to sustain the circumferential pressure loads the pipes can weigh in the region of 500 kg/m, producing considerable bending stresses. The piping support structure must then be designed to limit the total axial stress to below the maximum allowable design stress whilst also accommodating other sustained or occasional loads, such as those arising from thermal expansion.

It can then be concluded that the stress state of a given point on a component is not likely to be well known, and will be very dependent on the pipe hanger configuration, and the location on the pipe. In a

perfectly supported pipe the ratio of circumferential to hoop stress will be 2:1 due to internal pressure alone. Bending loads may then increase the axial stress so that it reaches approximately the circumferential stress to form an ‘equibiaxial’ stress state. Equally, the bending load may add a compressive component to the axial stress which may counteract the axial stress from pressure, in this case the total axial stress may reduce to zero.

Given this multiaxial stress state, it is then necessary to consider the resulting strain. The following concepts are well established and taken from the following references (Naumenko & Altenbach, 2007; Penny & Marriott, 1995; Viswanathan, 1989; Webster & Ainsworth, 1994). The creep strain resulting from a given stress state behaves in an analogous way to plasticity, governed by conservation of volume and the resulting ‘flow rules’. There are two questions of interest; the magnitude of strain and the distribution of deformation between the three directions.

Creep is a shear dominated process and so when considering the magnitude it must be considered in terms of the equivalent stress, σ_e , in a similar way to the Von Mises yielding criterion for plasticity.

$$\sigma_e = \frac{1}{\sqrt{2}} [(\sigma_1 - \sigma_2)^2 + (\sigma_2 - \sigma_3)^2 + (\sigma_1 - \sigma_3)^2]^{1/2} \quad (4.2)$$

Equation 4.2 reveals the volume conserving nature of creep, if all principal stresses are equal then there is no driving force for deformation as volume cannot change. It is rather the discrepancy between stresses that provides the shear stress driving deformation. The resulting strain rate obeys the Norton power law (Equation 1.3).

$$\dot{\varepsilon}_e = f(\sigma_e) \propto \sigma_e^n \quad (4.3)$$

In order to consider the distribution of deformation we should consider the flow rules that govern plasticity where the deviatoric stress governs deformation; the difference between a stress component and the average, or ‘hydrostatic’, stress.

$$\begin{pmatrix} \sigma_{11} & \sigma_{12} & \sigma_{13} \\ \sigma_{21} & \sigma_{22} & \sigma_{23} \\ \sigma_{31} & \sigma_{32} & \sigma_{33} \end{pmatrix} = \begin{pmatrix} \sigma_H & 0 & 0 \\ 0 & \sigma_H & 0 \\ 0 & 0 & \sigma_H \end{pmatrix} + \begin{pmatrix} \sigma_{11} - \sigma_H & \sigma_{12} & \sigma_{13} \\ \sigma_{21} & \sigma_{22} - \sigma_H & \sigma_{23} \\ \sigma_{31} & \sigma_{32} & \sigma_{33} - \sigma_H \end{pmatrix} \quad (4.4)$$

$$\text{Stress Tensor} = \text{Hydrostatic Stress Tensor} + \text{Deviatoric Stress Tensor}$$

where $\sigma_H = (\sigma_{11} + \sigma_{22} + \sigma_{33})/3$. The hydrostatic stress acts only to change the volume of the component which of course it cannot; the deviatoric stress must drive deformation. In plastic deformation the time independent strain is proportional to the deviatoric stress but in creep the strain rate is proportional to the deviatoric stress. Combining the magnitude and distribution arguments yields,

$$\begin{aligned}\dot{\varepsilon}_1 &= \frac{f(\sigma_e)}{\sigma_e} \left[\sigma_1 - \frac{(\sigma_1 + \sigma_2 + \sigma_3)}{3} \right] \\ \dot{\varepsilon}_2 &= \frac{f(\sigma_e)}{\sigma_e} \left[\sigma_2 - \frac{(\sigma_1 + \sigma_2 + \sigma_3)}{3} \right] \\ \dot{\varepsilon}_3 &= \frac{f(\sigma_e)}{\sigma_e} \left[\sigma_3 - \frac{(\sigma_1 + \sigma_2 + \sigma_3)}{3} \right]\end{aligned}\tag{4.5}$$

The first term on the right hand side provides the magnitude of the strain rate while the second term describes how that strain is distributed across the three principal directions.

Equation 4.5 illustrates the challenge of estimating the creep strain rate; in addition to temperature, material properties and damage state, the three dimensional stress state is required to estimate strain rate. Additionally, stress uncertainties in any direction will be amplified by the stress exponent. Estimates of strain rate are therefore to be treated with caution. Further, even estimating the distribution of strain will not be possible without knowledge of all three stress components. In order to obtain accurate strain or strain rate information from power station components it must therefore be measured directly and biaxially.

4.3 Inversion

4.3.1 Electrode Configurations

It was stated in Chapter 2 that in-line electrode configurations are more usual in potential drop techniques but a square electrode configuration has been adopted in this project due to its enhanced sensitivity to strain. Additionally, it was mentioned that an electrode separation will be chosen so that the current penetration is not limited by the component thickness but rather the electrode separation to remove dependency on thickness changes not associated with strain. These concepts will be explored in more detail in this section to provide background to the reasoning behind the selection of this particular measurement configuration.

Potential drop measurements will tend to exhibit either ‘thick’ or ‘thin’ behaviour depending on the component thickness in relation to the current injecting electrodes. If the component is much thinner than the electrode separation then the current will fill the depth of the component and an effectively 2D current distribution will result. On the other hand, if the electrode separation is much smaller than the component thickness then the current distribution from a point source will be spherical and the majority will not penetrate beyond one electrode separation; as an approximation the current will therefore not be influenced by the back wall. In reality, measurements will behave between the ‘thin’ and ‘thick’

asymptotic behaviours but measurements should be conducted with the aim of reproducing one or other so that results may be accurately interpreted.

Figure 4.1 shows five possible resistance measurements from different electrode configurations. By using an electrode separation that is either much smaller or much larger than the component thickness the measurements may be implemented as a ‘thick’ or ‘thin’ measurement; ten possible implementations are therefore discussed.

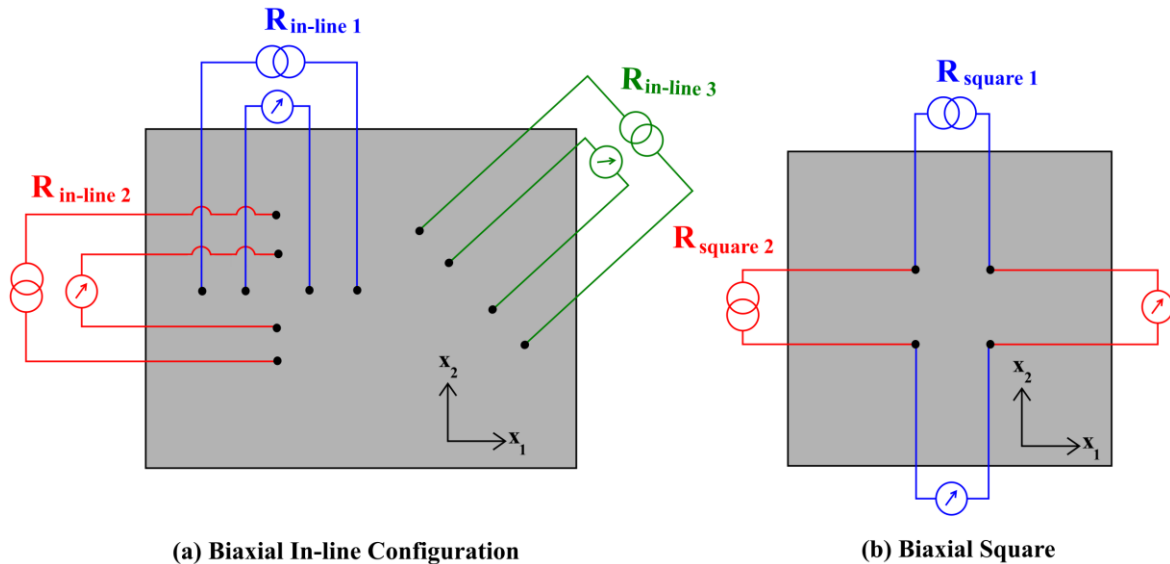


Figure 4.1: Five possible implementations of the potential drop measurement.

Madhi (Madhi, 2010) provides analytical solutions for resistances based on the electric potential of point current sources in either half-space or thin plate components. In-line and square arrangements were considered and expressed in terms of component thickness and initial electrode separation. The change in Normalised Resistance as a result of strain was then calculated using the general relation $d = d_0(1 + \varepsilon)$ where d is an initial dimension and ε is the strain in the direction of the displacement. A summary of the solutions is displayed in Table 4.1.

Some important characteristics may be deduced from the equations in Table 4.1. In the ‘thin’ measurements the current penetration is limited by the back wall; all measurements must therefore be dependent on the component thickness and therefore the strain in the thickness direction, ε_3 . On the other hand, measurements on ‘thick’ components are independent of the thickness and therefore insensitive to strain in that direction.

Clearly, due to the inherently biaxial nature of the square electrode configurations the measurements must be sensitive to strain in both orthogonal surface plane directions. In ‘thick’ components the in-line measurement will only be sensitive to strain in the direction which electrodes are aligned; clearly strain orthogonal to their direction will not distort the electrode configuration directly. ‘Thick’, in-line resistances are seen to decrease with increasing strain; the increasing electrode separation increases

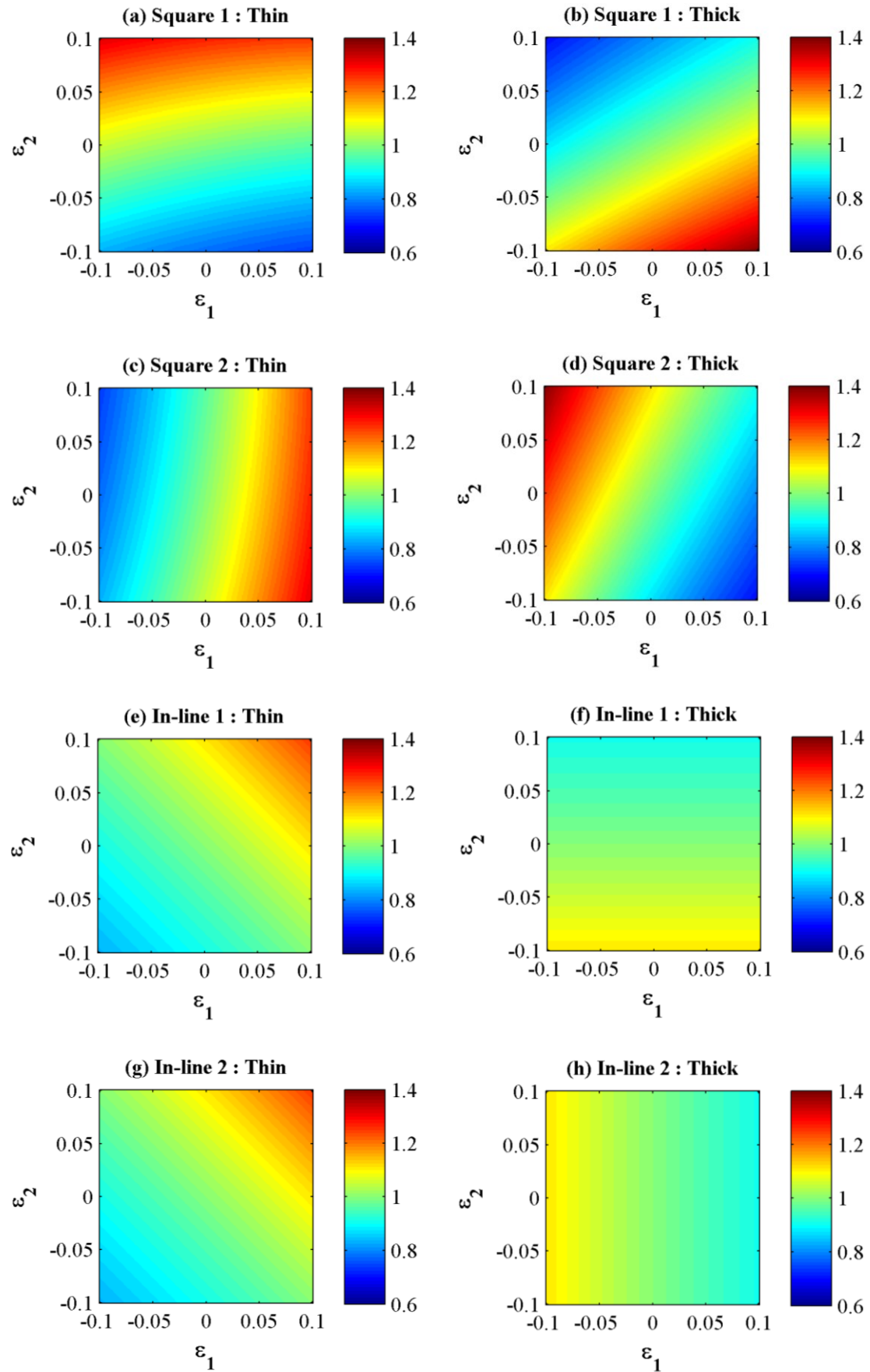
resistance but is dominated by the greater area available to current flow both laterally and through the depth of the component. An unintuitive result is evident in the in-line measurements of ‘thin’ components; there is no sensitivity to strain in the surface plane directions. This is due to the fact that the increase in resistance from the increased distance between electrodes is exactly compensated by the increasing area available to current flow as it is able to extend laterally.

Table 4.1: Analytical solutions relating resistance change to strain and resistivity. Root equations from (Madhi, 2010). ‘Thin’ measurements are those where the electrode separation is much greater than the component thickness, ‘thick’ measurements are those where the electrode separation is much smaller than the component thickness. Configurations follow the labelling given in Figure 4.1. s is the constant introduced in Chapter 2, $2+\sqrt{2}$.

	Thin	Thick
Square 1	$\frac{R}{R_0} = \frac{\rho}{\rho_0} \frac{1}{(1 + \varepsilon_3)} \frac{1}{\ln 2} \ln \left[\frac{(1 + \varepsilon_1)^2}{(1 + \varepsilon_2)^2} + 1 \right]$	$\frac{R}{R_0} = \frac{\rho}{\rho_0} s \left(\frac{1}{(1 + \varepsilon_2)} - \frac{1}{\sqrt{(1 + \varepsilon_1)^2 + (1 + \varepsilon_2)^2}} \right)$
Square 2	$\frac{R}{R_0} = \frac{\rho}{\rho_0} \frac{1}{(1 + \varepsilon_3)} \frac{1}{\ln 2} \ln \left[\frac{(1 + \varepsilon_2)^2}{(1 + \varepsilon_1)^2} + 1 \right]$	$\frac{R}{R_0} = \frac{\rho}{\rho_0} s \left(\frac{1}{(1 + \varepsilon_1)} - \frac{1}{\sqrt{(1 + \varepsilon_1)^2 + (1 + \varepsilon_2)^2}} \right)$
In-line 1	$\frac{R}{R_0} = \frac{\rho}{\rho_0} \frac{1}{(1 + \varepsilon_3)}$	$\frac{R}{R_0} = \frac{\rho}{\rho_0} \frac{1}{(1 + \varepsilon_1)}$
In-line 2	$\frac{R}{R_0} = \frac{\rho}{\rho_0} \frac{1}{(1 + \varepsilon_3)}$	$\frac{R}{R_0} = \frac{\rho}{\rho_0} \frac{1}{(1 + \varepsilon_2)}$
In-line 3	$\frac{R}{R_0} = \frac{\rho}{\rho_0} \frac{1}{(1 + \varepsilon_3)}$	$\frac{R}{R_0} = \frac{\rho}{\rho_0} \frac{s}{2} \frac{1}{\sqrt{(1 + \varepsilon_1)^2 + (1 + \varepsilon_2)^2}}$

To illustrate the resistance behaviour of the different electrode configurations more clearly, resistance plots have been produced for a range of ε_1 and ε_2 strains as shown in Figure 4.2. The requirement of conservation of volume can be used to infer the value of ε_3 ,

$$\varepsilon_1 + \varepsilon_2 + \varepsilon_3 = 0. \quad (4.6)$$



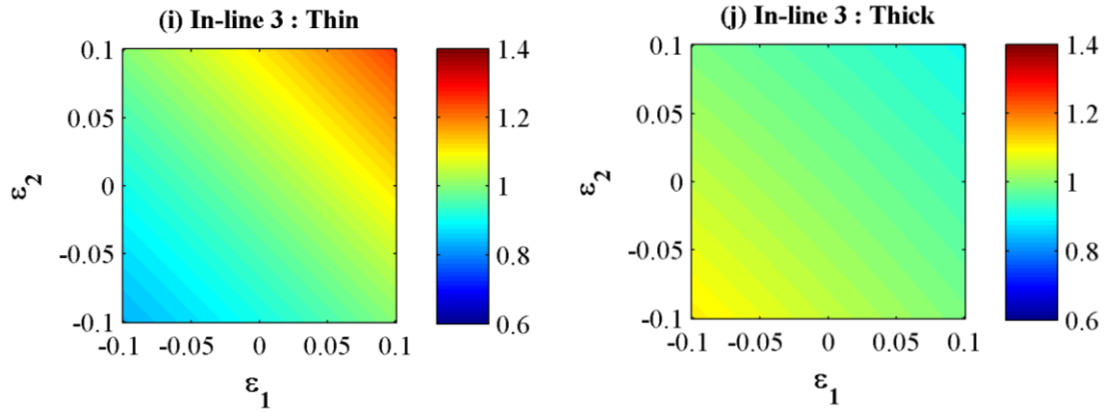


Figure 4.2: Normalised Resistances for a range of different biaxial strain combinations. In the ‘thin’ measurements, where a value for ϵ_3 is required, conservation of volume is assumed through Equation 4.6.

The critical result from Figure 4.2 is the enhanced strain sensitivity that results from the square electrode configuration over the in-line arrangement. The square electrode configuration is therefore more suited to strain measurements and will be adopted going forward, however this comes at the expense of a more complex strain inversion.

All the resistances of Table 4.1 are a function of resistivity. All resistances will therefore strongly depend on component temperature and will be susceptible to the effect of long term microstructural degradation. It would be a very significant attribute to be able to combine resistance readings in such a way that would suppress the effect of resistivity while maintaining sensitivity to both surface strain directions independently. In principle it is possible to combine ‘thick’ and ‘thin’ measurements with the assumption of constant volume (Equation 4.6) to result in a strain independent resistivity measurement; practically speaking however this is not straightforward to implement on power station components. Moreover, the constant volume assumption may not be reliable; oxidation, corrosion or spallation will cause an additional change in component thickness not attributable to strain. Terms including $1 + \epsilon_3$ will therefore be susceptible to errors and so a ‘thick’ arrangement is preferable which is independent of changes in component thickness. The square and in-line ‘thick’ measurements are not sufficiently independent to allow them to be combined to cancel out resistivity whilst maintaining sensitivity to both independent orthogonal surface strains; however, information on strain aspect ratio may be preserved as will be discussed in the following section.

4.3.2 Strain Inversion of a Square Electrode Potential Drop Sensor on a Thick Walled Component

4.3.2.1 Normalised Resistance Ratio Inversion

The simplest means of suppressing the resistivity using the two ‘thick’ square electrode expressions,

$$\frac{R_1}{R_{10}} = s \frac{\rho}{\rho_0} \left(\frac{1}{(1 + \varepsilon_2)} - \frac{1}{\sqrt{(1 + \varepsilon_1)^2 + (1 + \varepsilon_2)^2}} \right) \quad (4.7)$$

$$\frac{R_2}{R_{20}} = s \frac{\rho}{\rho_0} \left(\frac{1}{(1 + \varepsilon_1)} - \frac{1}{\sqrt{(1 + \varepsilon_1)^2 + (1 + \varepsilon_2)^2}} \right)$$

is to divide the two expressions to result in the previously introduced Normalised Resistance Ratio. It is described in (Madhi & Nagy, 2011b) that dividing the two equations and following some algebra the Normalised Resistance Ratio can be approximated using the ‘power approximation’,

$$NRR = \frac{\frac{R_1}{R_{10}}}{\frac{R_2}{R_{20}}} = \left(\frac{1 + \varepsilon_1}{1 + \varepsilon_2} \right)^s, \quad (4.8)$$

where, again, s is the constant $2+\sqrt{2}$.

It is worth pointing out that the term $(1 + \varepsilon_1)/(1 + \varepsilon_2)$ is equivalent to the aspect ratio of the initially square electrode configuration. While the effect of isotropic resistivity has been suppressed, a biaxial inversion is not possible as there is only one equation and two unknown variables. However, ε_1 and ε_2 are not truly independent as they are linked by the ‘flow rules’ of deformation; from Equation 4.5,

$$\frac{\varepsilon_1}{\varepsilon_2} = \frac{\frac{f(\sigma_e)}{\sigma_e} \left[\sigma_1 - \frac{(\sigma_1 + \sigma_2 + \sigma_3)}{3} \right]}{\frac{f(\sigma_e)}{\sigma_e} \left[\sigma_2 - \frac{(\sigma_1 + \sigma_2 + \sigma_3)}{3} \right]} \quad (4.9)$$

and therefore by assuming a constant stress state,

$$\frac{\varepsilon_1}{\varepsilon_2} = \frac{\left[\sigma_1 - \frac{(\sigma_1 + \sigma_2 + \sigma_3)}{3} \right]}{\left[\sigma_2 - \frac{(\sigma_1 + \sigma_2 + \sigma_3)}{3} \right]}. \quad (4.10)$$

If the stress state is known then the expected distribution of strain can be predicted. For example in the case of uniaxial loading in the x_1 direction,

$$\frac{\varepsilon_1}{\varepsilon_2} = -2 \quad (4.11)$$

and Equation 4.8 can be written,

$$NRR = \left(\frac{1 + \varepsilon_{1 \text{ uniaxial}}}{1 - 0.5\varepsilon_{1 \text{ uniaxial}}} \right)^s \quad (4.12)$$

or,

$$\varepsilon_{1 \text{ uniaxial}} = \frac{NRR^{1/s} - 1}{0.5 NRR^{1/s} + 1}, \quad (4.13)$$

allowing for strain in uniaxial stress conditions to be obtained.

In general, however, in power station components the stress state is not well known and therefore such assumptions cannot be made. The Normalised Resistance Ratio may still be of use however as the rate of change of aspect ratio may be used as an indicative metric of rate of change of strain and therefore provide information on damage state; this concept will be discussed in detail in Chapter 5.

4.3.2.2 Normalised Resistance Inversion

In cases where the stress state is not well defined then ε_1 and ε_2 must be treated as independent. It is not possible to obtain a resistivity independent inversion to recover both strain components. A resistivity coupled Normalised Resistance inversion is possible on this basis by combining Equations 4.7 and 4.8 yielding,

$$\frac{1 + \varepsilon_1}{\rho/\rho_0} = s \frac{NRR^{1/s} - 1}{\frac{R_1}{R_{10}} - \frac{R_2}{R_{20}}} \quad (4.14)$$

$$\frac{1 + \varepsilon_2}{\rho/\rho_0} = s \frac{\left(\frac{1}{NRR} \right)^{1/s} - 1}{\frac{R_2}{R_{20}} - \frac{R_1}{R_{10}}}$$

In order to make use of this inversion it is necessary to address the resistivity dependence of Equation 4.14. The resistivity will change substantially with temperature and, to a lesser extent, is expected to change with extended time in creep conditions as was discussed in Chapter 3. In certain situations, such as constant temperature, short duration accelerated creep tests, the resistivity may be sufficiently stable so that it may be neglected. In power station conditions however it must be somehow assessed and compensated for. Strategies for doing so will follow in the next section. The estimated resistivity change will be denoted as r/r_0 allowing for the Normalised Resistance strain inversion,

$$\varepsilon_1 = \frac{r}{r_0} s \frac{NRR^{1/s} - 1}{\frac{R_1}{R_{10}} - \frac{R_2}{R_{20}}} - 1 \quad (4.15)$$

$$\varepsilon_2 = \frac{r}{r_0} s \frac{NRR^{-1/s} - 1}{\frac{R_2}{R_{20}} - \frac{R_1}{R_{10}}} - 1$$

Imperfect resistivity compensation will provide a source of error in the inversion of resistance data. Another equivalent effect results from the measurement system where gain drift or instability would have a similar scaling effect as resistivity change.

Resistivity Changes and the Influence on Measurement Uncertainty

A simple illustration of the sensitivity of the Normalised Resistance Inversion to resistivity changes comes from an alternative formulation of Equation 4.15,

$$\begin{aligned}\varepsilon_1 &\approx s \frac{r}{r_0} \frac{1}{\frac{R_1}{R_{10}}} \left((NRR)^{\frac{1}{s}} - \frac{1}{\sqrt{1 + (NRR)^{-\frac{2}{n}}}} \right) - 1 \\ \varepsilon_2 &\approx s \frac{r}{r_0} \frac{1}{\frac{R_2}{R_{20}}} \left((NRR)^{-\frac{1}{s}} - \frac{1}{\sqrt{1 + (NRR)^{\frac{2}{s}}}} \right) - 1\end{aligned}\quad (4.16)$$

In order to find the apparent strain from the imperfect compensation of resistivity changes it will be assumed that there has been no attempt at compensation (*i.e.* $r/r_0=1$) and no strain has occurred so that the Normalised Resistance Ratio is 1. This gives,

$$\varepsilon_{\text{apparent } 1} \approx \varepsilon_{\text{apparent } 2} \approx \frac{R_{10}}{R_1} - 1 \approx \frac{\rho_0}{\rho} - 1 \approx \frac{-\Delta\rho}{\rho_0}\quad (4.17)$$

Where the subscript ‘apparent’ indicates that this is the erroneous strain resulting from resistivity change and not truly strain. This shows that, approximately, a given fractional change in resistivity will be interpreted directly as strain; a 1% increase in resistivity will be interpreted as \approx -1% strain.

Equation 4.18 gives a simplified expression for the expected change in resistivity of a power station component, separating the reversible temperature dependency from the irreversible material changes resulting from creep exposure,

$$\frac{\rho}{\rho_0} \approx 1 + \frac{\Delta\rho_{\text{rev}}(T)}{\rho_0} + \frac{\Delta\rho_{\text{irr}}}{\rho_0} .\quad (4.18)$$

Overwhelmingly, the variations in component resistivity will be a result of temperature changes. A 10 °C temperature uncertainty will therefore cause a strain uncertainty of 2.2% strain in CMV material according to the temperature coefficient that will be calculated from data in Chapter 7, Figure 7.6. Fortunately, the temperature-resistivity relationship is repeatable, monotonic and may be approximated as linear over a limited range. Further, the temperature can be directly measured using a thermocouple and therefore it is believed that the temperature dependency can be effectively compensated using the approximation,

$$\frac{\Delta\rho_{\text{rev}}(T)}{\rho_0} \approx \alpha(T - T_0)\quad (4.19)$$

where the temperature coefficient, α , is estimated empirically. Temperature correction in this fashion is usually implemented as a simple automated learning process. By monitoring both the temperature and the transfer resistance over a relatively short period simple regression analysis can accurately determine, α , separating the long term monotonic changes from short term non-monotonic variations. Additionally, assuming that temperature fluctuations are random about a fixed set point then imperfect temperature compensation will simply provide a random baseline uncertainty that will be averaged out over successive readings.

Chapter 3 discussed the long term resistivity changes that occur from exposure to creep conditions or thermal exposure, changes that will be harder to predict than those caused by temperature fluctuations. Over the limited time scale of accelerated laboratory tests the resistivity change may be sufficiently small so that, in comparison to the large resistance changes that occur with strain, it can be neglected. In power station components however, resistivity ‘drift’ may occur over tens of hundreds of hours and must be kept much smaller than the expected strain rate of 1% over 100,000 hours as to not introduce significant error. Additionally, uncertainty originating from measurement instrumentation will have an equivalent effect on the strain inversion. If, for example, the instrument gain is unstable then the measured resistances will change proportionally; both resistivity and instrument drift will be indistinguishable from the effects of strain.

It may be possible to compensate such changes by obtaining a measurement that is sensitive to resistivity but not strain using a ‘dummy sensor’, one that is thermally but not mechanically coupled to the component under test or otherwise. Otherwise it will be necessary to use only the Normalised Resistance Ratio for interpretation which inherently suppresses multiplicative changes common to both orthogonal resistance measurements but only maintains information on aspect ratio.

4.4 Small Component Considerations

In order for the inversions suggested in this chapter to be successful it must be assumed that all resistance changes can be attributed to electrode migration. Other sources of resistance change must either be negligibly small to not interfere with the inversion or can be accurately predicted and compensated for. Before the inversions are demonstrated experimentally it is necessary to account for the effects of two potential sources of error which arise as a result of testing on small samples. As these issues are not present in large power station components then they will only be discussed briefly here.

4.4.1 Edge Effects

The majority of injected current penetrates less than one electrode separation depth into the component and will also extend laterally with a comparable length scale; however, the current distribution rapidly decays and the influence extends much further. Therefore, if a sensor is placed close to the edge of a

component then the current path is constricted and the resulting potential field is distorted. In the uniaxial creep tests to be discussed in Section 4.5.2, the components must be suitably small in order to fit them into conventional creep testing machines; the component cross section used was 24 mm x 10 mm. It is then necessary to reduce the electrode separation to scale down the sensor geometry and reduce the influence of edges; there is, however, a practical limit to what can easily be achieved and from experience this is approximately an electrode separation of 4-5 mm. The influence of edges on components of this size will be significant.

It is not trivial to quantify the influence of edges on the resistance measurement, especially considering the influence of deformation on electrode position and component constriction. A Comsol (“Comsol,” 2012) model was used to investigate the likely influence of edges so that the effect can be compensated for when inverting data. A conducting block was modelled with dimensions 24 mm x 10 mm x 80 mm to replicate the gauge section of a uniaxial creep test specimen. DC point current sources were used and the potential predicted at two remote points to replicate a potential drop measurement with 5 mm electrode separation. The component was then deformed; strain was imposed by extending the component in the loading direction while contracting in the orthogonal directions with a strain ratio of $\varepsilon_1 = -2\varepsilon_2 = -2\varepsilon_3$ to imitate a uniaxial load; the electrode geometry was deformed in the same fashion as shown in Figure 4.3. The resistances were then calculated based on the difference of the two potentials.

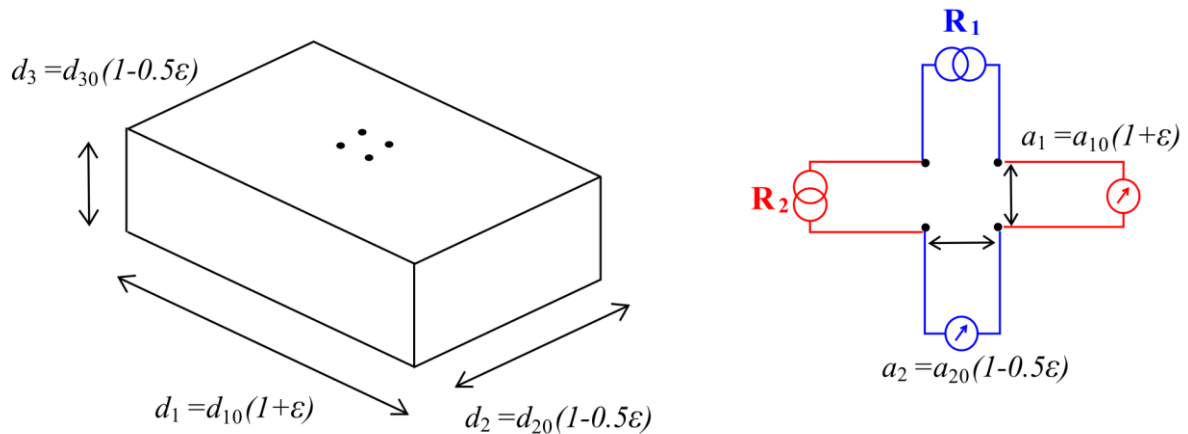


Figure 4.3: Schematic showing how uniaxial strain is imposed on simulations.

Figure 4.4 shows the outcome of this process over a range of 0 – 10% strain. Equivalent results obtained neglecting any edge effects are calculated using Equation 4.7; the Comsol model was verified by repeating the process on a 80 mm x 80 mm x 80 mm component where edges were found to have negligible effect and values in agreement with theory. Figure 4.4 shows that the resistances in both orthogonal directions were found to increase in the presence of edges. By normalising the resistances, as shown in Figure 4.5, it can be seen that the sensitivity to strain also increases.

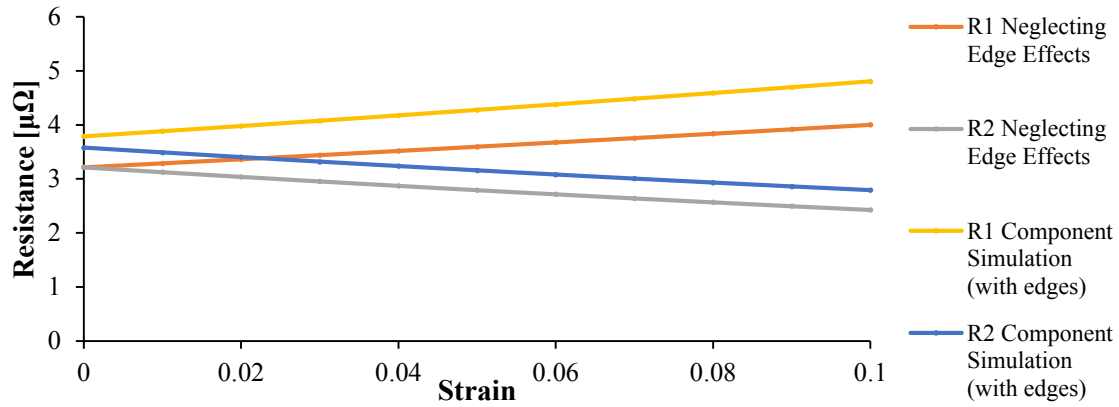


Figure 4.4: Resistances obtained from a simulation of a 24 mm x 10 mm x 80 mm component of arbitrary conductivity of 10 %IACS and a 5 mm electrode separation potential drop sensor. Strain imposed as illustrated in Figure 4.3. Values neglecting edge effects are obtained using Equation 4.7.

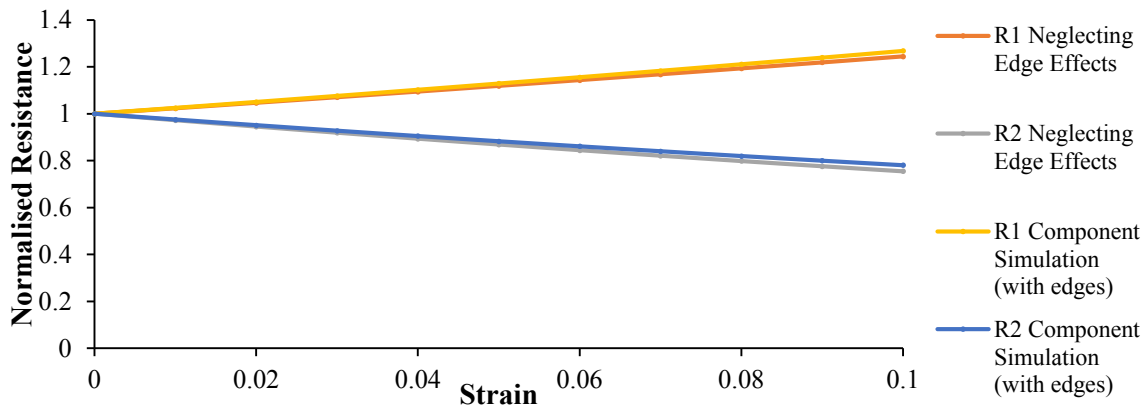


Figure 4.5: Normalised Resistances; all resistances in Figure 4.4 are normalised to their initial no strain value.

Interpreting these Normalised Resistances according to the Normalised Resistance and Normalised Resistance Ratio inversions gives the result in Figure 4.6. Strain orthogonal to the loading direction was multiplied by -2 to allow for comparison. Unfortunately the apparently modest looking effect on the Normalised Resistance propagates to a substantial error in the Normalised Resistance strain inversion. Fortunately however, the error is linear and therefore compensation is trivial given a good estimate of electrode separation component dimensions and a single simulation, the result of which is shown in Figure 4.7. It is important to note that the Normalised Resistance Ratio inversion is much less affected but requires the assumption of uniaxial loading.

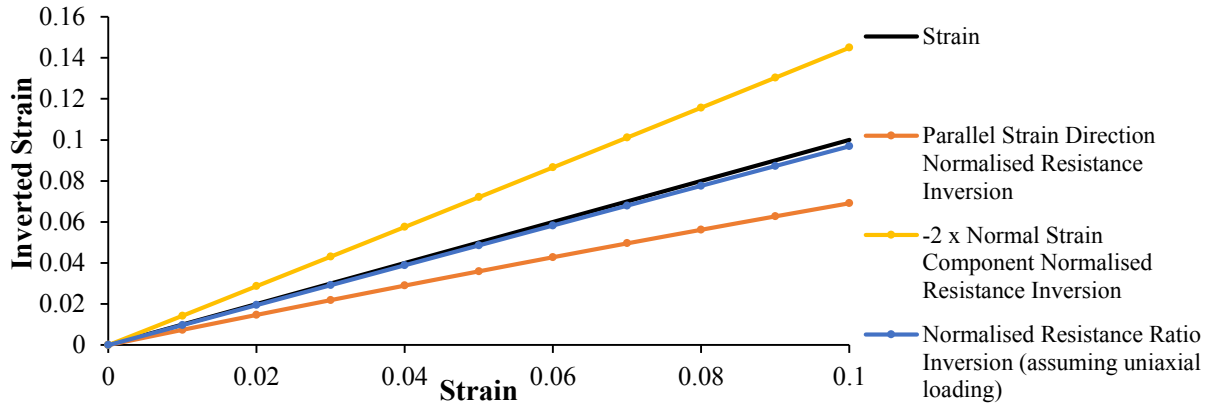


Figure 4.6: Strain inverted from the Normalised Resistances of Figure 4.5 and the Normalised Resistance and Normalised Resistance Ratio inversions. The strain component normal to the direction of loading is multiplied by -2 so that it can be included in the comparison.

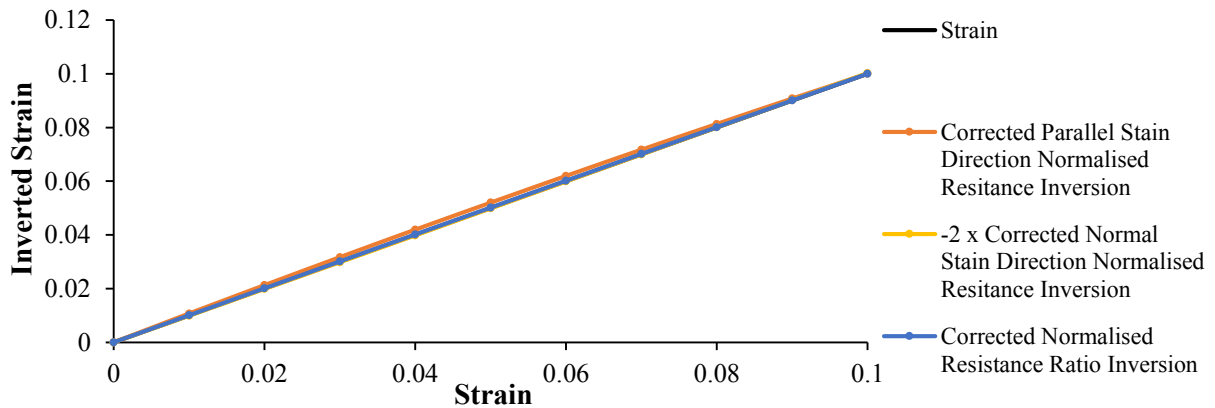


Figure 4.7: Corrected strain inversion, obtained by dividing the results of the strain inversion in Figure 4.6 by the error predicted using simulated model at 10% strain.

4.4.2 Imperfect Electrode Placement

Implicit in the formulation of the equations in Table 4.1 is the assumption that the initial electrode geometry is square, see Equation 2.9 to 2.10 of Chapter 2. In practice this will certainly be violated to some degree and the random or systematic nature of the uncertainty will depend on the electrode attachment process. This assumption will lead to errors in the inversion of strain. It is possible to correct for this error using the initial resistances to indicate the effective initial aspect ratio; however, this can only be achieved if the initial resistances are not affected by edges and the initial resistance ratio is purely a result of imperfect electrode placement. This cannot be assumed in small geometry components with edge effects present and therefore imperfect electrode placement must be conceded as a source of error.

The symptom of initial electrode placement error on inverted strain will be shown here as an illustration of the error bounds that may result in the testing of small components. Equation 2.7 of Chapter 2 was used to calculate the resistances that would result from imperfect electrode placement and the subsequent influence on the strain inversion. For a given electrode placement uncertainty, here a separation error of $\pm 10\%$, the two configurations shown in Figure 4.8 are known to give the greatest error in the subsequent strain inversion; they are characterised by a large initial aspect ratio. Following this, the electrode positions were artificially strained in a similar fashion to the previous Comsol model using a programme written in Matlab (“Matlab,” 2014); electrodes were separated in the y-direction and brought together in the x-direction. Again a $\varepsilon_1 = -2\varepsilon_2$ ratio of y to x deformation was chosen to replicate deformation by uniaxial stress. The resistances were then inverted to strain using Equations 4.13 and 4.15. Figure 4.9 shows the apparent strain from the inversions against the strain imposed on the model.

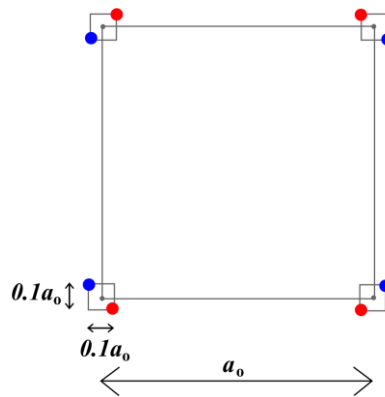


Figure 4.8: Illustration showing imperfect initial electrode placements that give the greatest error in the subsequent strain inversion for a given electrode placement uncertainty. Impact on strain inversion is shown in Figure 4.9.

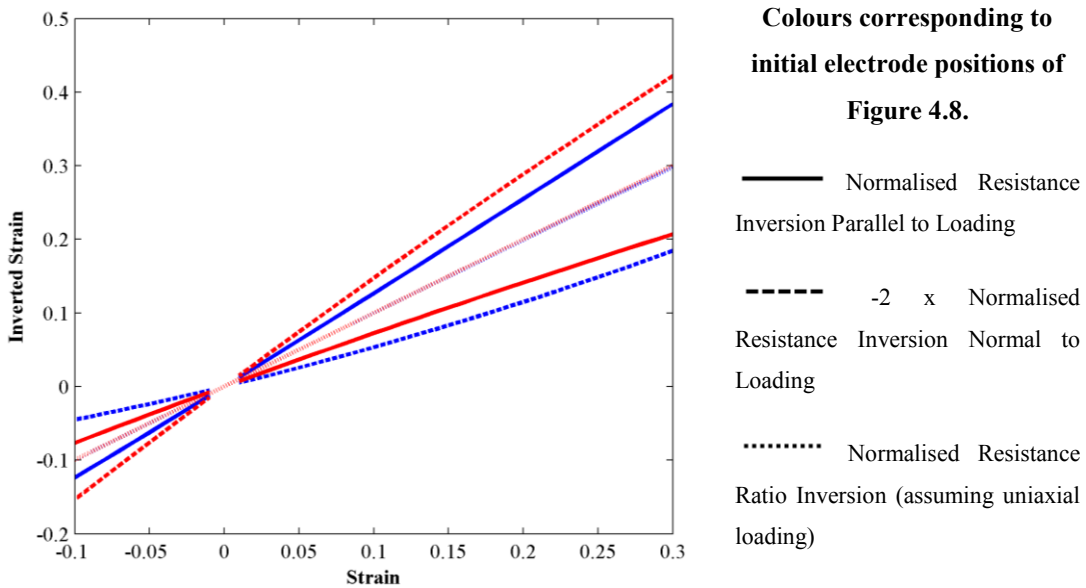


Figure 4.9: Strain inversion results from two cases of imperfect initial electrode placement. Colours correspond to the electrode configurations shown in Figure 4.8.

Figure 4.9 shows that the symptom of imperfect electrode placement on Normalised Resistance inversion is that one strain component will be underestimated while the orthogonal strain component will be overestimated. The Normalised Resistance Ratio inversion however is relatively unaffected.

It is important to remember that on large components such as that described in Section 4.5.1 the influence of imperfect electrode can be effectively suppressed with an analytical correction. On the small uniaxial component tests discussed in Section 4.5.2, the Normalised Resistance Ratio inversion can be used without significant error from electrode placement, however, errors consistent with Figure 4.9 are expected when using the Normalised Resistance inversion.

4.5 Experimental Demonstration

In order to demonstrate the ability of the potential drop technique to successfully invert strain, two sets of experiments were conducted. The first experiment was a large tensile test specimen designed to remove edge effects; it was plastically deformed at room temperature so that detailed independent strain measurements could be easily taken. Second, a series of accelerated creep tests were conducted to demonstrate the ability of strain inversion in creep conditions.

4.5.1 Room Temperature Tensile Test

The experiment described in this section was introduced in Chapter 2.8 as a means of demonstrating some of the core principles of the potential drop technique, including strain sensitivity. The experiment was conducted with help from Dr. Paul Hooper. For ease of reference a brief overview will be repeated here.

A S275 mild steel tensile specimen with a gauge cross section of 75 mm x 24 mm and gauge length 150 mm was produced, as shown in Figure 4.10. To one side of the specimen a random speckle pattern was painted for the purpose of taking an independent strain measurement using digital image correlation (DIC). On the reverse side of the specimen, a 10-element array of 5 mm electrode separation potential drop sensors was installed. The sample was tested using a 2.5 MN Instron tensile test machine. A Stanford Research SR830 Lock-in amplifier was used with a 1 Hz, 300 mA inspection current.

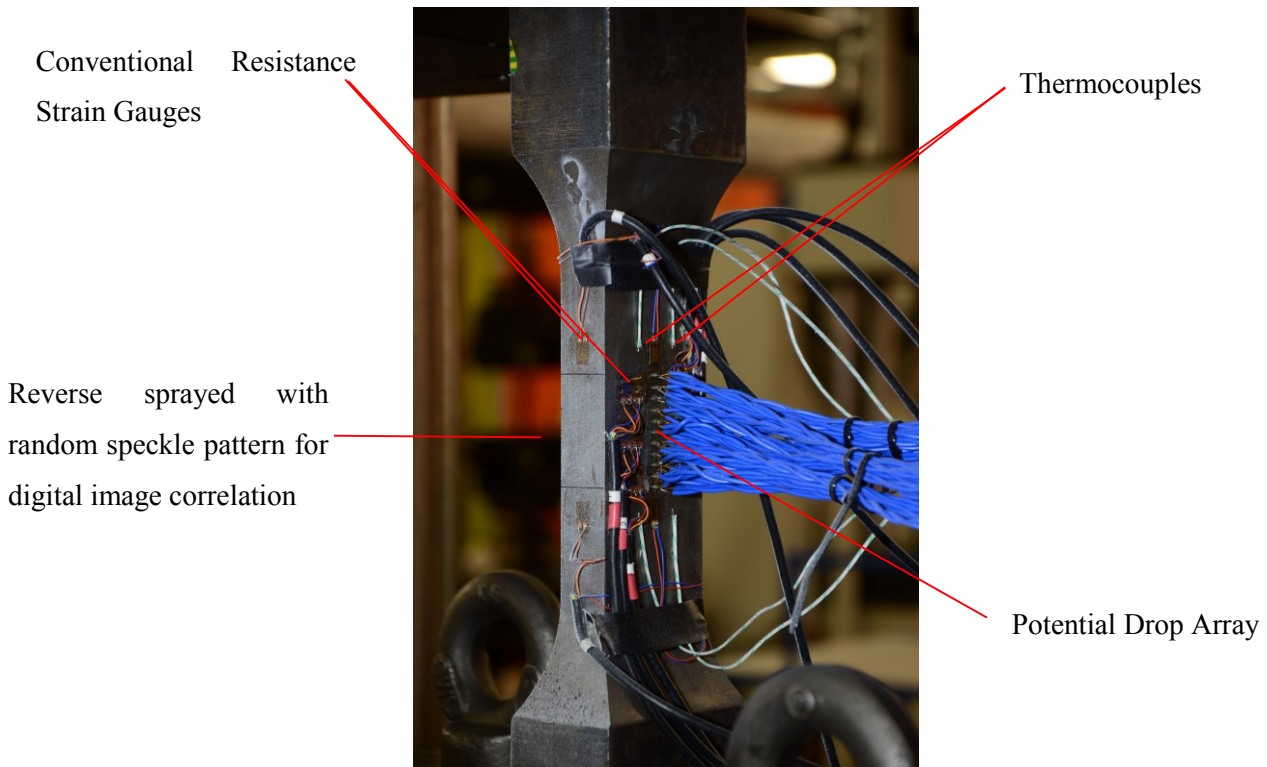


Figure 4.10: Annotated photograph of room temperature tensile test specimen. For scale the component cross section dimensions are 50 mm x 25 mm in the gauge length.

The component was quasi-statically deformed with a constant displacement rate of 0.2 mm/hour, equivalent to a strain rate of ~ 0.0013 /hour. Figure 4.11 shows the numbering and direction convention for the array elements and each of the two orthogonal Normalised Resistances. Normalised Resistances for the 10 elements, in the two orthogonal directions (20 readings in total) are shown in Figure 4.12. As this was a uniaxial stress test the component is expected to deform with constant volume; contracting with a strain of half that of the extension in the loading direction ($\varepsilon_{normal} = -0.5\varepsilon_{loading}$) prior to necking. In this case resistances are expected to increase in the direction of loading and decrease in the normal direction.

Superimposed onto the graph is the engineering stress as monitored by the load cell of the tensile test machine; as the experiment was conducted at a constant displacement rate this stress is expected to reflect a conventional stress-strain curve. The maximum of the engineering stress curve coincides with the point of strain localisation. This is evident in the Normalised Resistance values; the strain increases linearly and uniformly up until this point; following this strain preferentially accumulates in the central elements of the array where necking occurs.

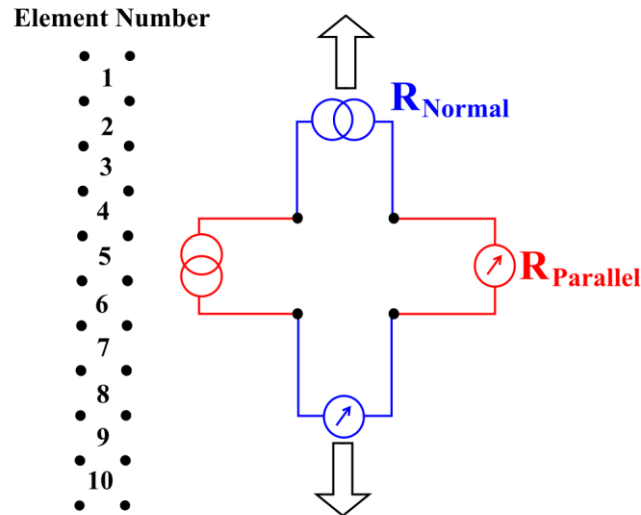


Figure 4.11: Array numbering and direction convention.

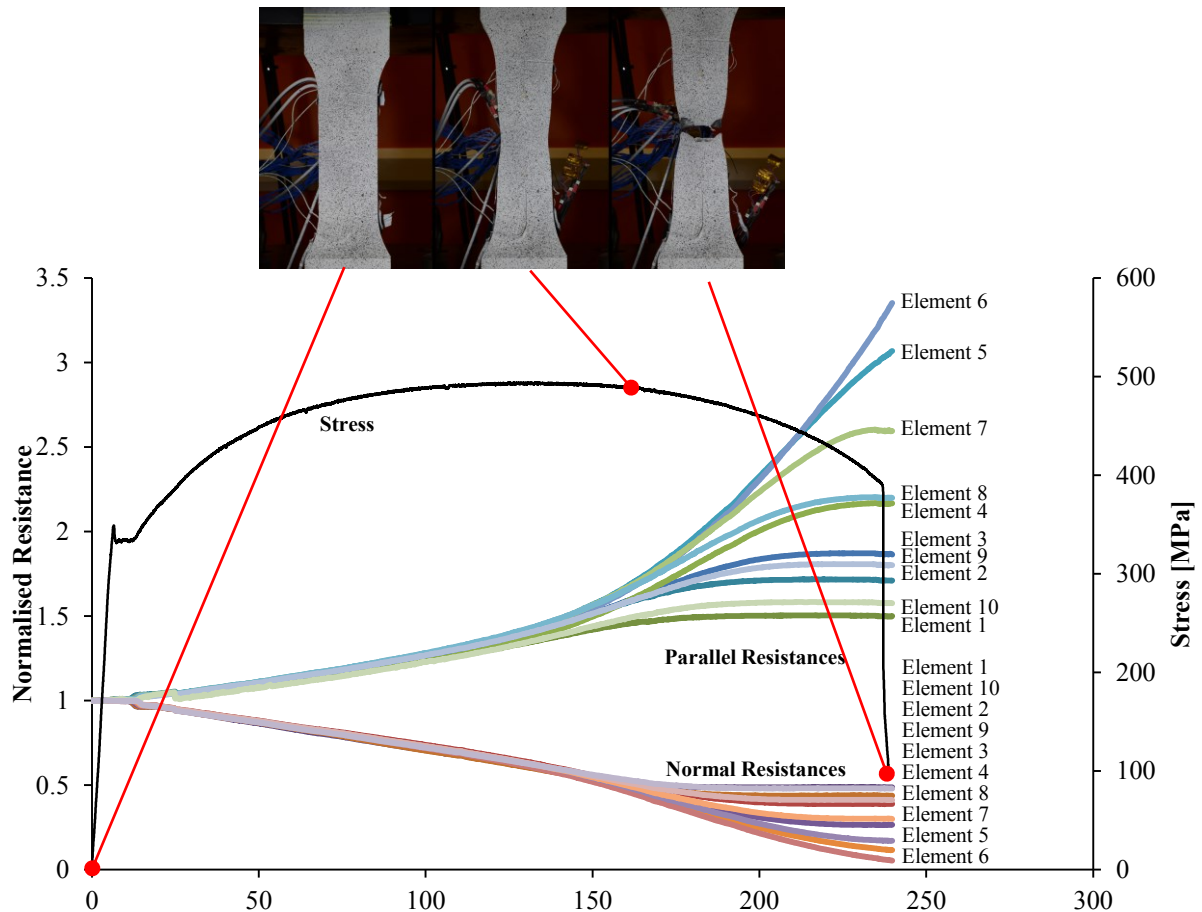


Figure 4.12: Normalised Resistance against time. 10 array elements are shown, resistances parallel to the direction of loading increase, while those normal decrease. Following the onset of necking (at the maximum engineering stress) strain begins to accumulate preferentially in the central elements at the expense of those at either end.

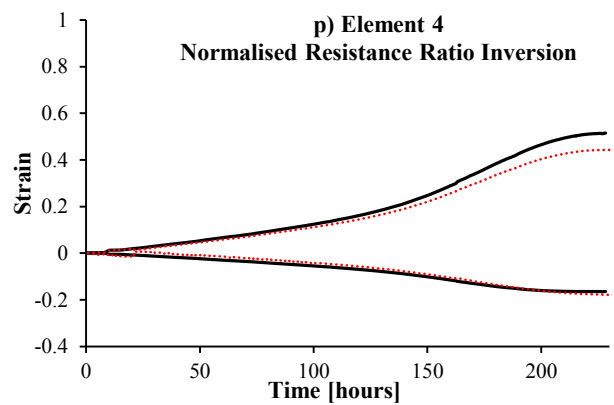
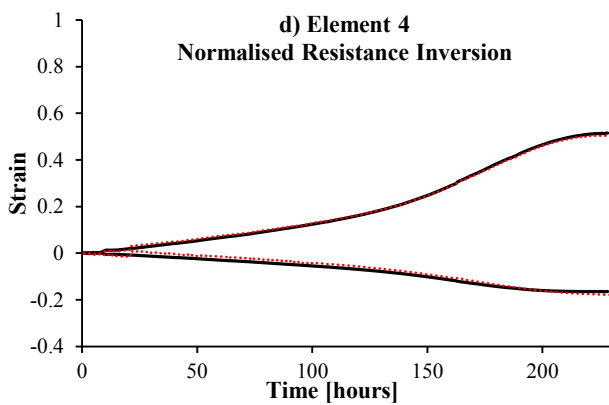
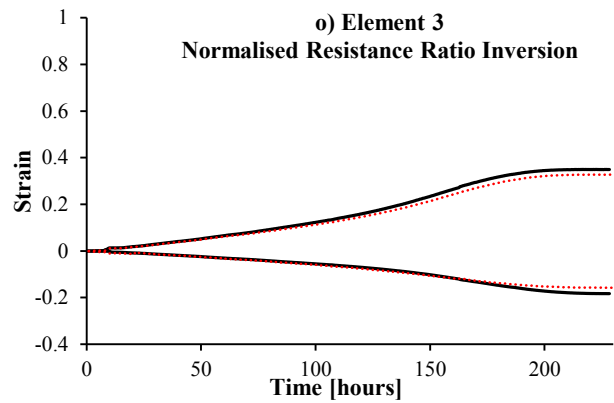
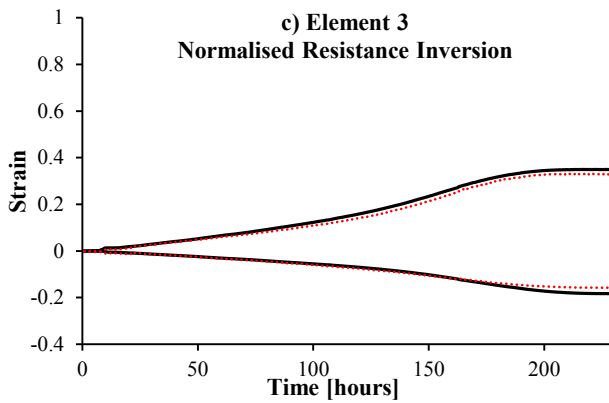
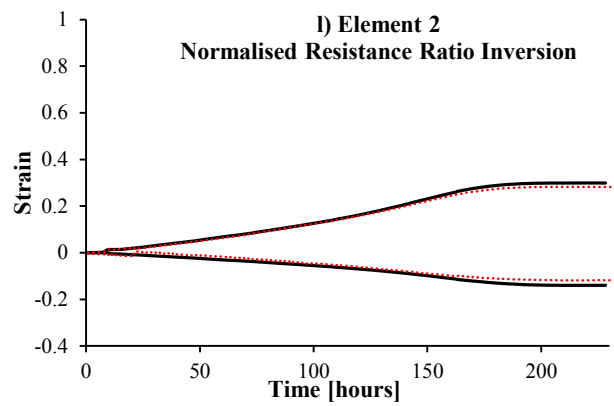
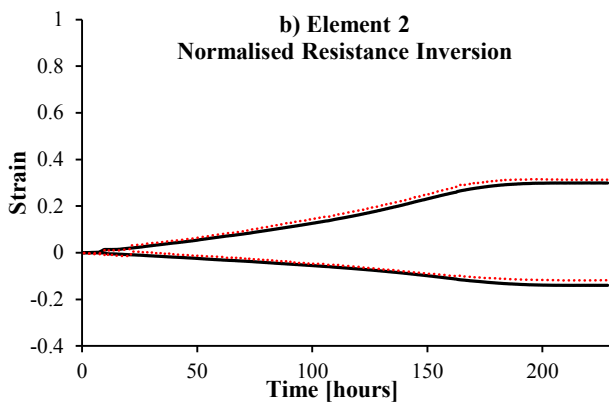
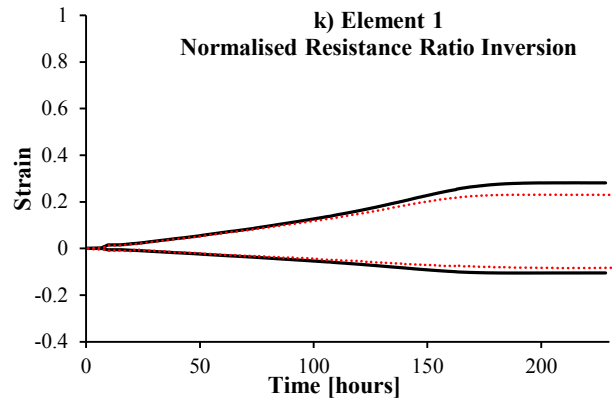
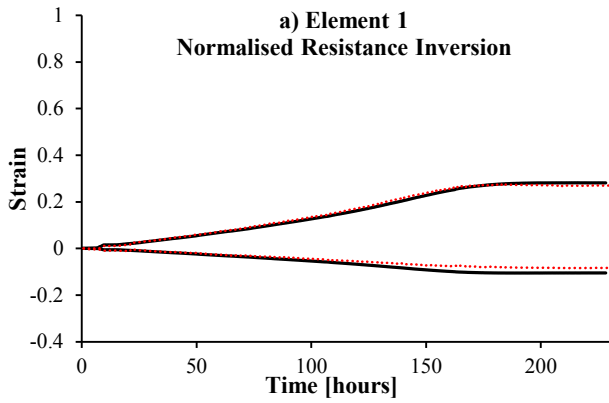
Two small but distinct steps in resistance can be seen at ~10 and ~20 hours. The first is indeed a true result of strain occurring in the transition from elastic to plastic strain; localised bands of plastic deformation known as Lüders bands occur, as confirmed by examination of the DIC strain field data. The second discontinuity is not believed to be strain but rather an experimental error.

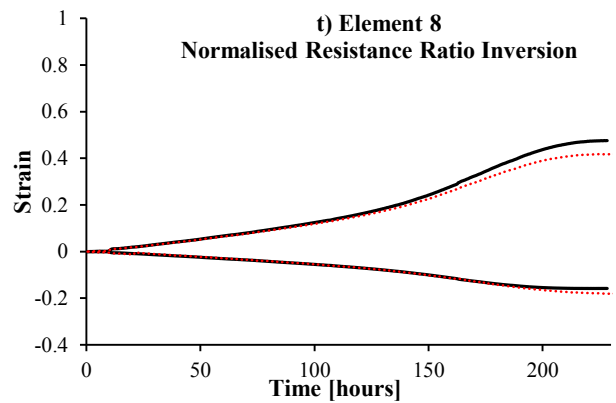
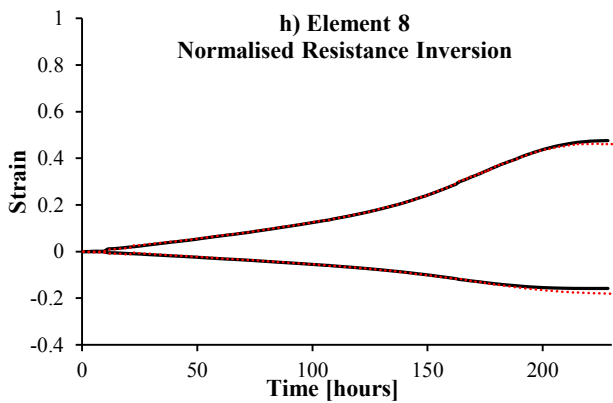
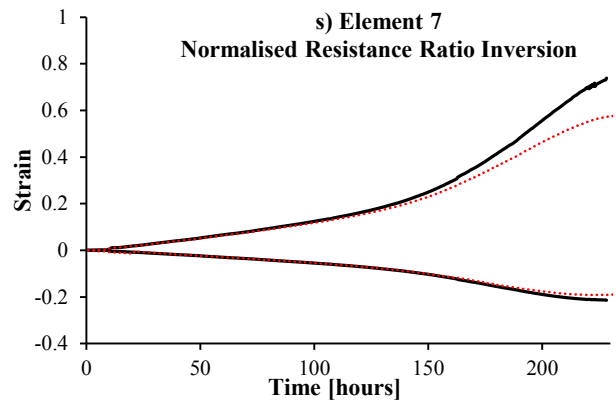
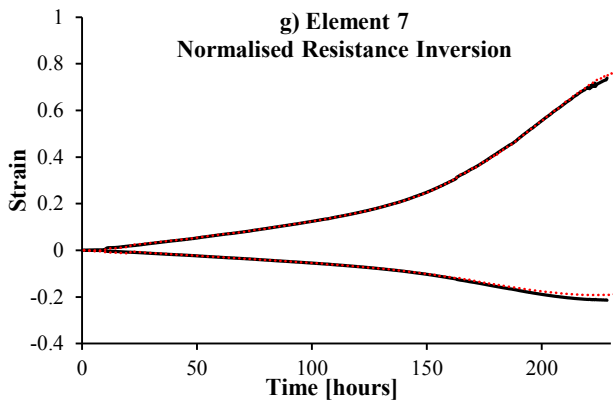
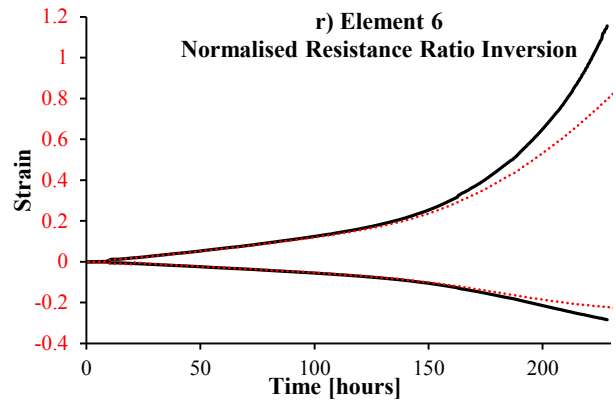
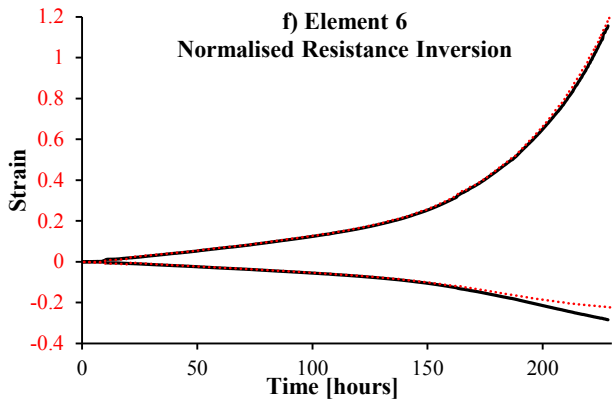
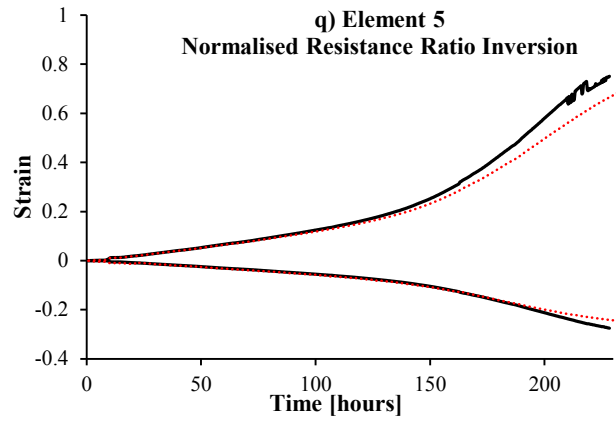
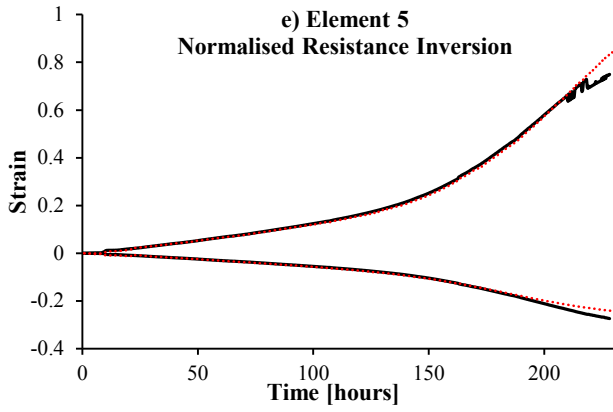
The Normalised Resistances shown in Figure 4.12 are interpreted according to the Normalised Resistance Ratio and Normalised Resistance inversions, Equations 4.13 and 4.15 respectively, and shown in Figure 4.13. Recall that the Normalised Resistance Ratio inversion requires an assumption about the strain ratio in orthogonal directions which may be obtained in this case of uniaxial stress as $\epsilon_{normal} = -0.5\epsilon_{loading}$ due to conservation of volume. The Normalised Resistance Inversion requires no assumption about the strain ratio, however, is sensitive to changes in resistivity. No temperature compensation is required in this case however as the experiment is conducted under nominally constant room temperature conditions and there is not expected to be any other resistivity change.

Each element of the PD array can be compared to the strain field as measured by DIC in the corresponding region on the reverse side of the component. A single Nikon D7000 with Nikkor 200 mm macro lens was used giving 4,928 x 3,264 pixels, out of plane movement is assumed to be zero. A stochastic speckle pattern was applied with acrylic spray paint to ensure good adhesion to the steel sample. An image is divided into facets which contain enough features (speckle pattern) to allow the position of those facets to be identified in subsequent images (Sutton et al., 2009). The images were processed using commercial DIC software Aramis (“Aramis,” 2012).

The two inversions are in very good agreement with each other and the DIC strain measurements up until necking at about ~130 hours. Following this point the assumption of uniaxial stress is violated locally, undermining the assumed strain ratio of $\epsilon_{normal} = -0.5\epsilon_{loading}$; this is seen to cause substantial error in the Normalised Resistance Ratio inversion in the central elements (4-8) towards failure. It is important to note the extreme strain that has accumulated by this stage and such problems are not expected in the creep of power station components where strain of <10% is anticipated. Excellent agreement can be seen between the Normalised Resistance inversion and the DIC measurement well beyond the initiation of necking as there is no required assumption about the stress state. Only results up to 230 hours are shown as following this the painted speckle pattern which provides the reference points for the DIC algorithm disintegrated from the large strain, as can be seen occurring prematurely in element 5.

Legend: Potential Drop Strain **————** DIC Strain





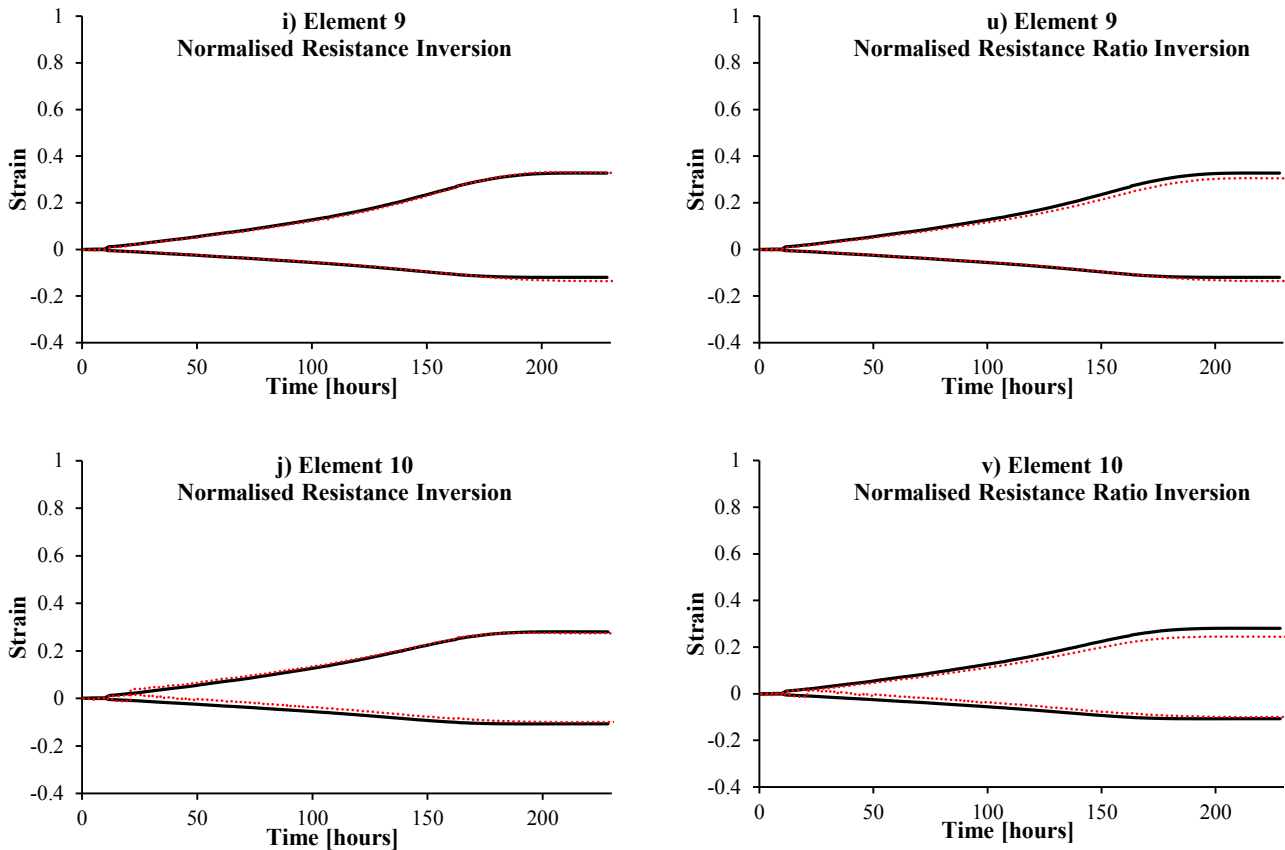


Figure 4.13: Result of the Normalised Resistance (a-j) and Normalised Resistance Ratio (k-v) strain inversions of potential drop data for each element of the potential drop array. DIC measured strain from the opposite side of the sample is included for comparison; the area of interest of the DIC calculated strain field was matched to the gauge length of each potential drop array element on the reverse side of the component.

This experiment demonstrates the ability of the Potential Drop measurement to measure strain and has verified the Normalised Resistance and Normalised Resistance Ratio inversion. The use of a room temperature test has enabled a relatively simple independent strain measurement to be carried out with confidence.

4.5.2 High Temperature Creep Tests

A number of experiments on uniaxial creep specimens were conducted over the course of the project. Demonstrating the strain inversion in creep conditions poses numerous practical difficulties and the experimental procedure was iteratively improved, therefore only the most recent batch of measurements will be included. The experiments were prepared and managed by Pakorn Nimityont, a MSc student supervised as part of this project. A background to the high temperature testing completed in this thesis was given in Chapter 2.9. Creep samples of 24 mm x 10 mm gauge cross section were produced and an 8 element 5 mm PD array installed. Three creep tests on virgin P91 material were conducted at 620 °C and stresses of 115 MPa, 130 MPa and 160 MPa.

A motivation for the present work is the lack of technology to provide a robust, high temperature strain measurement. As a consequence the greatest difficulty in demonstrating the strain inversion was providing an independent strain measurement to verify the results obtained by PD. A number of technologies and techniques were attempted but were found to be prohibitively unreliable. An additional complication was that, due to the large stress and temperature dependency of creep, the strain along the gauge length of the uniaxial creep specimens was found to be highly non-uniform. The independent strain measurement would therefore have to match the gauge length of the PD measurement. A set of extensometry was produced that would be mounted to the rear of the creep specimen by M3 spot welded studs which would transfer the displacement outside of the furnace where it could be measured using a linear variable differential transformer (LVDT). The studs would initially be separated to cover an integer number of PD elements (either 4 or 6); in this way a larger gauge length could be used which is easier to implement. The strain measured by extensometry should match the average strain of the encompassed PD elements. In the schematic of Figure 4.14 the studs used for mounting the extensometry cover the central 4 PD elements; the strain as measured by the LVDT, ϵ_{LVDT} , should match the average of the strain as measured by the PD elements 3-6, $\epsilon_{PD3} - \epsilon_{PD6}$.

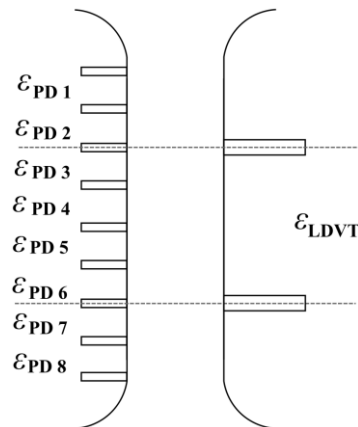


Figure 4.14: Illustration of the gauge length matching of the potential drop array and the mounting of the extensometry for the LVDT.

Results from these three experiments will be discussed in sequence from highest to lowest stress. In order to invert the resistance data to find strain the edge effects must be compensated for using the multiplicative factor derived from simulation as explained in Section 4.4.1; the Normalised Resistance inversion will be compensated by a factor of 1.45 and the Normalised Resistance Ratio inversion will be compensated by a factor of 1.03. For the purpose of the Normalised Resistance Ratio inversion a strain ratio of $\epsilon_{normal} = -0.5\epsilon_{loading}$ was again assumed from uniaxial loading.

4.5.2.1 Uniaxial Creep Test 1: P91, 620 °C, 160 MPa

The temperature distribution along the gauge section was 621.25 ± 0.5 °C and was stable to <0.2 °C over the duration of the experiment. Figure 4.15 shows the result of the Normalised Resistance Ratio

inversion for each element of the PD array. Elements 7 and 8 are seen to be temperamental, dropping in and out of service; element 3 is also seen to drop out approaching failure. Despite this the strain distribution across the specimen is evident. Strains at elements 1 and 8 are seen to be notably lower than the rest with maximum strain rates being observed towards the centre of the component; this is believed to be a consequence of the increasing cross section at the end of the gauge section. Further variation may result from the temperature dependence of creep strain rate meaning that even a modest temperature variation along the length of the component will result in a significant influence on strain rate.

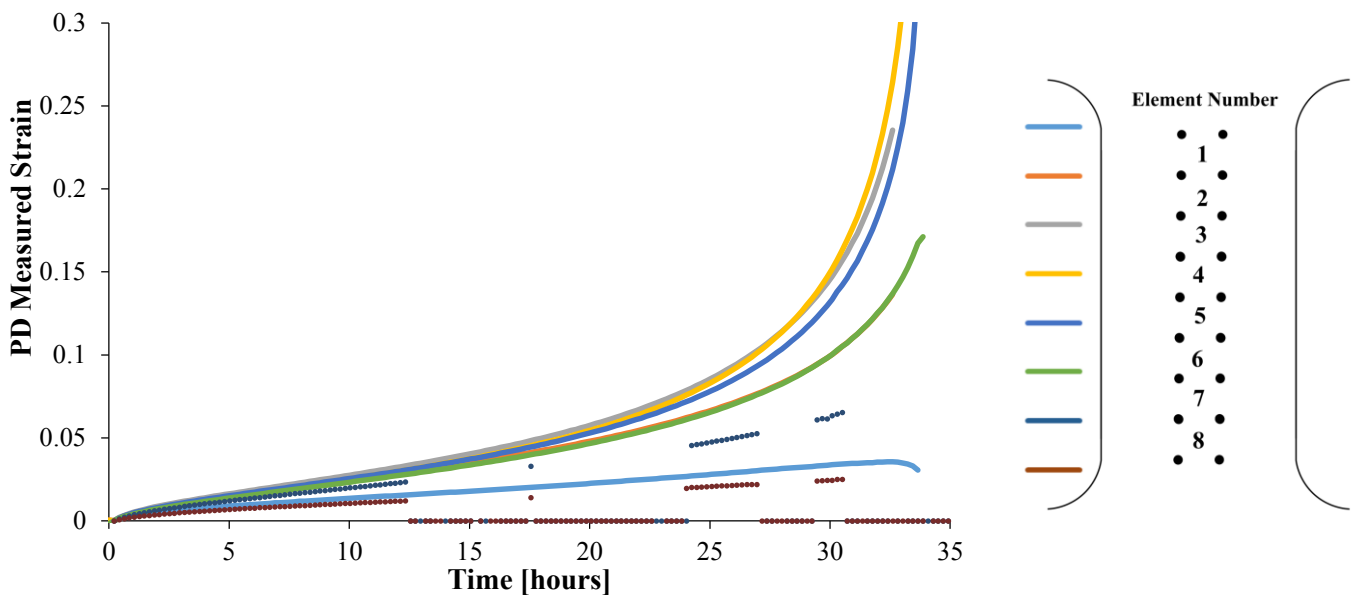


Figure 4.15: Uniaxial Creep Test 1: P91, 620 °C, 160 MPa. Result of the Normalised Resistance Ratio strain inversion for each of the 8 elements of the potential drop array.

The extensometry was installed to cover the central 6 elements of this experiment. The strain as measured by the LVDT should therefore be compared to the average of the inverted strain over elements 2-7. The results of the strain inversions are shown in Figure 4.16 alongside the LVDT measured strain. The strain component normal to the direction of loading from the Normalised Resistance inversion has been multiplied by -2 so that it can be included in the comparison.

As element 7 was found to be temperamental, this unfortunately has the effect of undermining the average of elements 2-7. For the readings where the full set of elements were functional there is good agreement between the LVDT and PD measured strain. The Normalised Resistance Ratio inversion is seen to agree best, recall from section 4.4.1 and 4.4.2 that the Normalised Resistance Ratio is less affected by edge effects and imperfect initial electrode placement. Unlike the larger component described in Section 4.5.1, it was not possible to account for imperfect initial electrode placement. The two orthogonal strain components of the Normalised Resistance inversion are seen to be straddling either side of the Normalised Resistance Ratio inverted strain; this is consistent with the anticipated

effect of imperfect electrode placement which must be accepted as a limitation of small sample testing. By averaging the result of a number of array elements the influence of random error in electrode placement is reduced but systematic errors common to all elements will remain.

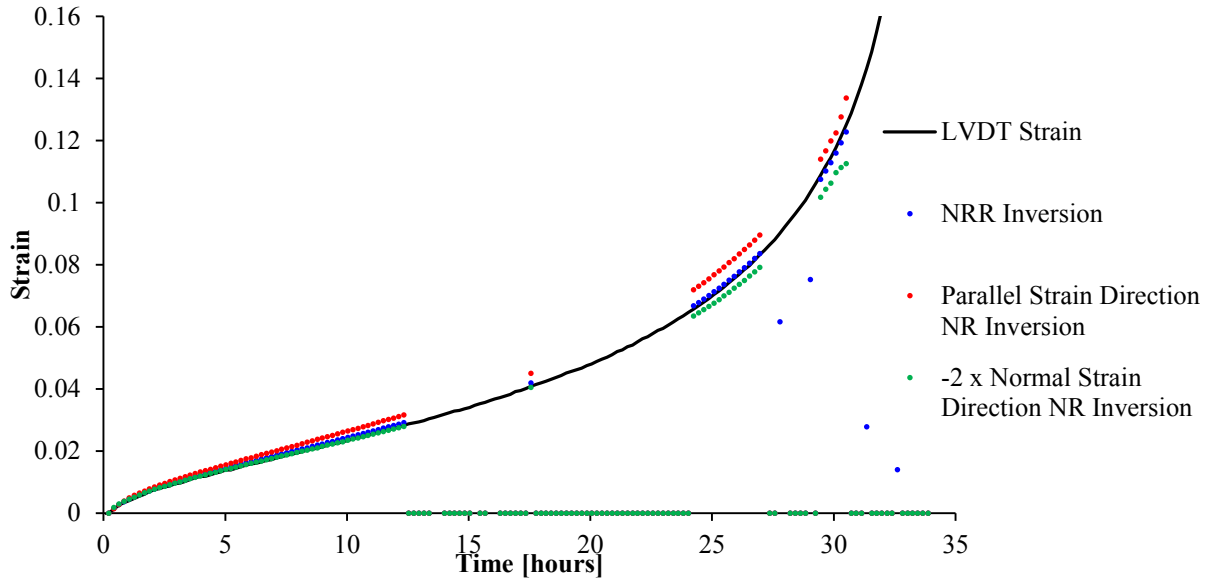


Figure 4.16: Uniaxial Creep Test 1: P91, 620 °C, 160 MPa. Comparison of the strain measured by LVDT and the potential drop inversions. Central 6 elements of the potential drop array were averaged to match gauge length of the extensometry.

4.5.2.2 Uniaxial Creep Test 2: P91, 620 °C, 130 MPa

The temperature distribution along the gauge section was at worst 622.25 ± 3 °C and drift of up to 4 °C was observed over the duration of the experiment. Figure 4.17 shows the result of the Normalised Resistance Ratio inversion for each element of the PD array. On this occasion all PD elements were functioning well throughout the creep test. Good strain symmetry is observed with $\varepsilon_1 \approx \varepsilon_8$, $\varepsilon_2 \approx \varepsilon_7$ and the central four elements behaving similarly. Failure finally occurred in element 5.

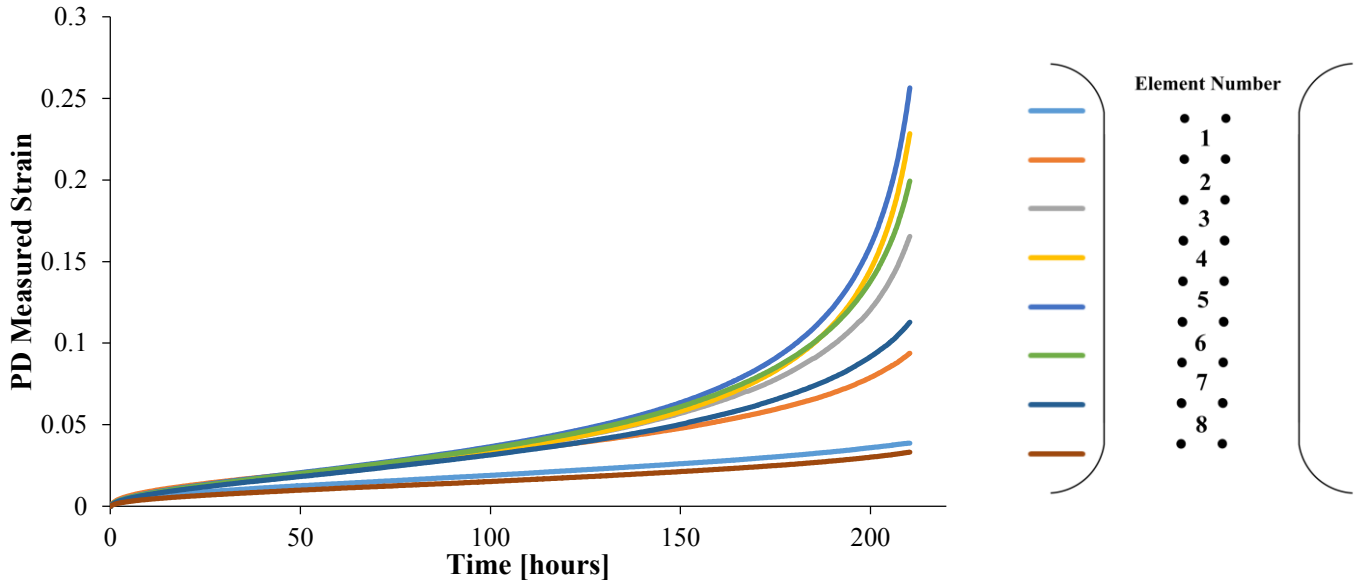


Figure 4.17: Uniaxial Creep Test 2: P91, 620 °C, 130 MPa. Result of the Normalised Resistance Ratio strain inversion for each of the 8 elements of the potential drop array.

Unfortunately, although the PD readings were apparently problem free on this occasion, the extensometry jammed on loading. Attempts were made to free the mechanism and eventually a strain rate was measured. It can be seen in Figure 4.18 that the strain rate as measured by the LVDT through the extensometry is lower than the Normalised Resistance Ratio inversion which is believed to be most accurate. It is possible that the extensometry, which was found not to be free moving in this experiment, caused the strain as measured by LVDT to be underestimated. The inconsistency between the strains reported by the different inversions is again believed to be a result of the imperfect initial electrode placement which cannot be accounted for on these small geometry components.

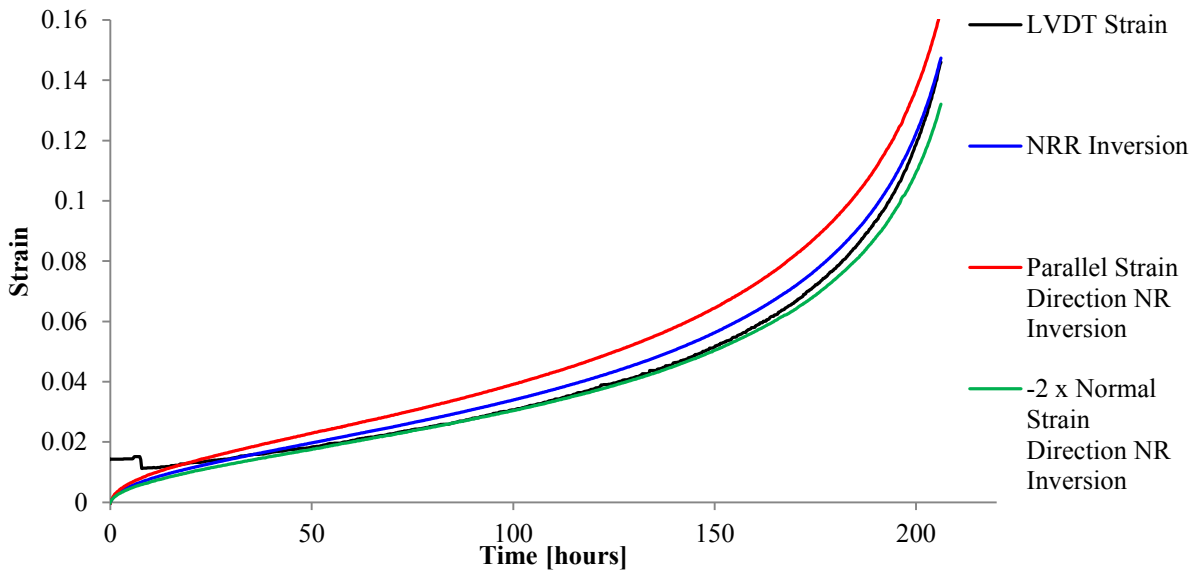


Figure 4.18: Uniaxial Creep Test 2: P91, 620 °C, 130 MPa. Comparison of the strain measured by LVDT and the potential drop inversions. Central 6 elements of the potential drop array were averaged to match gauge length of the extensometry.

4.5.2.3 Uniaxial Creep Test 3: P91, 620 °C, 115 MPa

All array elements appear to be functioning well, with the exception of element 1 which failed prior to loading and is not shown; a computer failure resulted in missing data at around 1200 hours. In this experiment the extensometry was placed over the central four elements (3-6) with the aim to measure the strain over a gauge length with a more uniform strain distribution; this is evident in Figure 4.19.

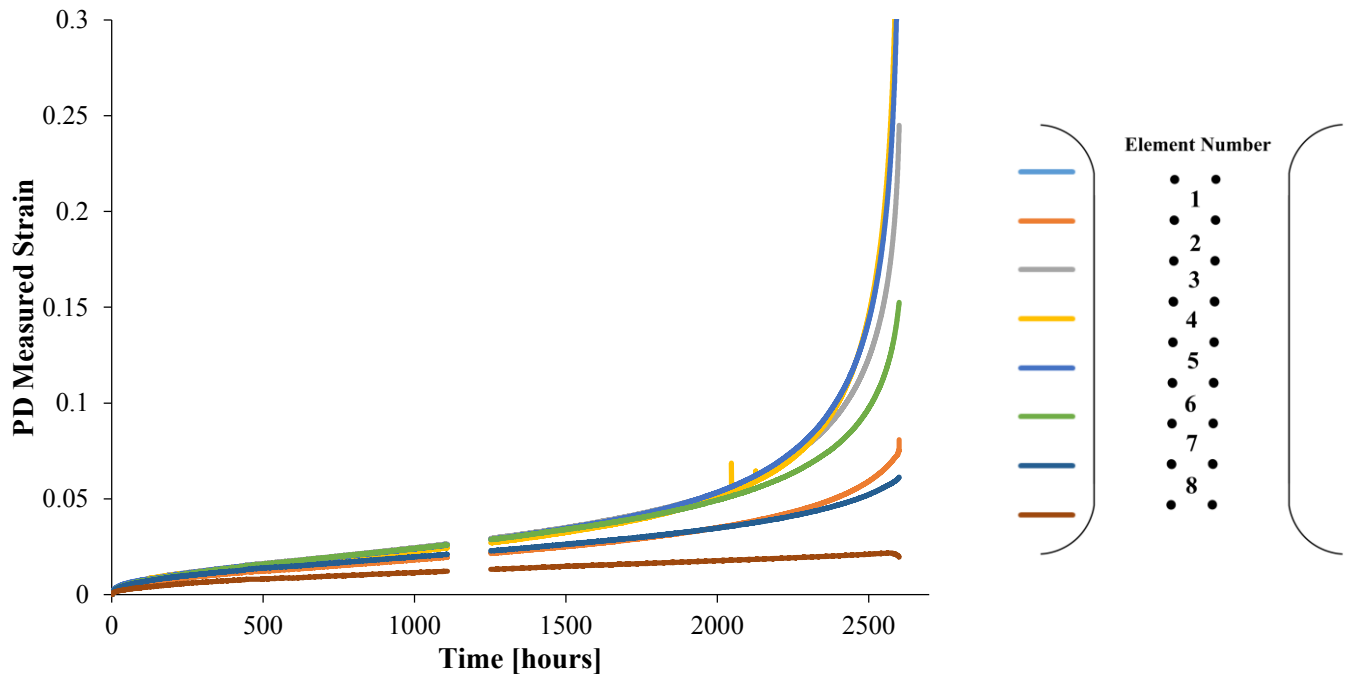


Figure 4.19: Uniaxial Creep Test 3: P91, 620 °C, 115 MPa. Result of the Normalised Resistance Ratio strain inversion for each of elements of the potential drop array, with the exception of element 1 which failed prior to loading. The missing data is a result of a computer failure.

Figure 4.20 shows a comparison between the Normalised Resistance Ratio inversion, the Normalised Resistance Inversion and the strain measured through extensometry and an LVDT. Consistent with previous results and the expected behaviour due to edge effects, the Normalised Resistance Ratio inversion shows good agreement with the strain measured by the LVDT, while the orthogonal strain measurement from the Normalised Resistance inversion straddle what is expected to be the correct strain value.

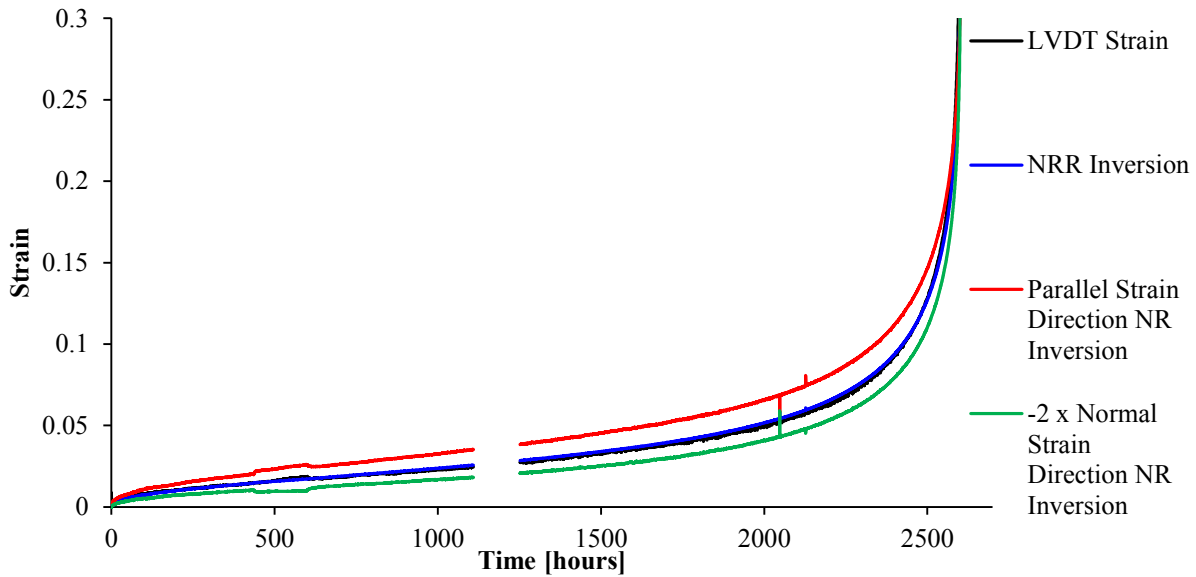


Figure 4.20: Uniaxial Creep Test 3: P91, 620 °C, 115 MPa. Comparison of the strain measured by LVDT and the potential drop inversions. Central 4 elements of the potential drop array were averaged to match gauge length of the extensometry.

Some interesting observations are possible as a result of the unfortunately poor temperature control experienced in this experiment; probably a result of inadequate insulation of the furnace. Figure 4.21 shows the first 1000 hours of the experiment in detail while Figure 4.22 shows the temperature of 7 thermocouples attached to the test component and one measuring the ambient lab temperature over the same time for comparison. The obvious feature of this graph is the air conditioning failure between ~430 hours and 600 hours, which had a notable effect on the temperature inside the furnace. Aside from this, the ambient lab temperature and the component temperature are also well correlated resulting in larger than usual short term temperature fluctuations with a range of up to 1 °C.

Due to the resistivity dependence of the Normalised Resistance inversion the temperature fluctuations of the component result in errors in the calculated strain. On the other hand, the Normalised Resistance Ratio suppresses isotropic resistivity changes and therefore the resulting calculated strain is insensitive to the temperature changes resulting in the far smoother curve; the perturbations evident in Figure 4.19 are a result of the slight discrepancy between orthogonal readings separated by ~1 minute. Temperature sensitivity is common across many measurements, as clearly evident here in the strain measured through extensometry. Again, the fluctuation in readings are well correlated with both the component and lab ambient temperature. The temperature sensitivity could conceivably be a result of thermal expansion of the extensometry but is more likely to be a result of temperature sensitivity of the LVDT itself, which is sufficiently close to the furnace to be heated by it. In this regard the Normalised Resistance Ratio inverted strain appears to outperform the extensometry.

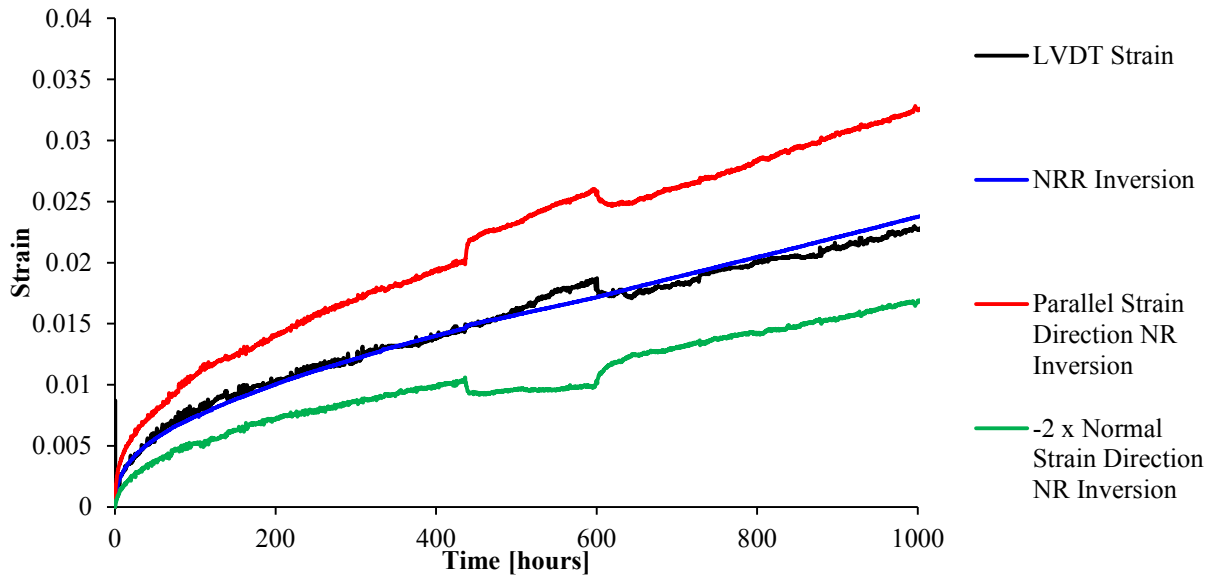


Figure 4.21: Detail showing first 1000 hours of Figure 4.20.

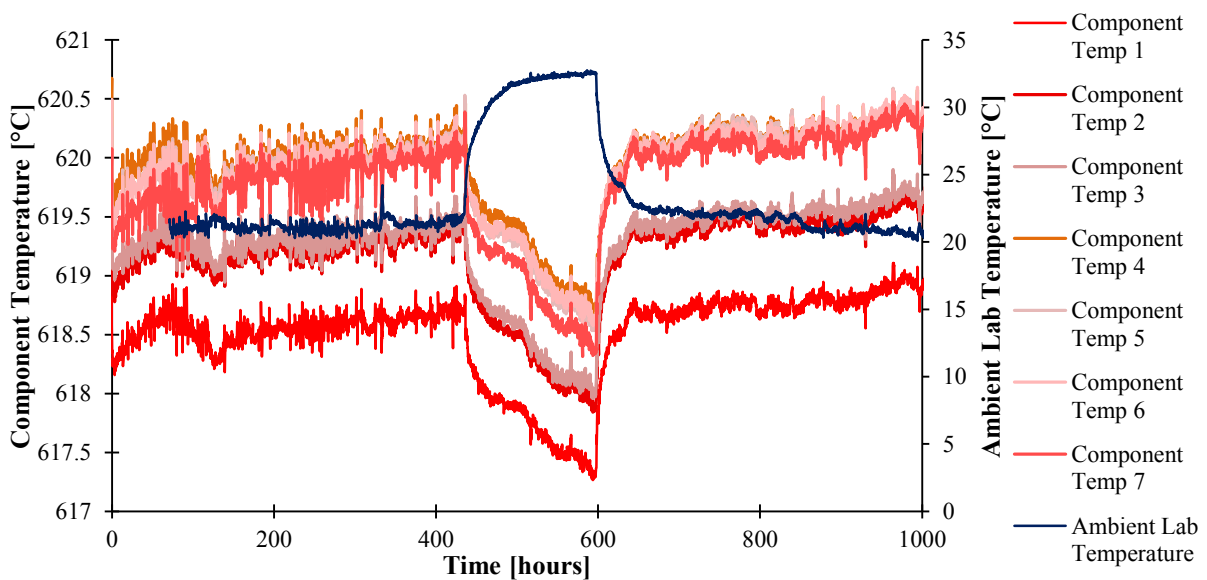


Figure 4.22: Temperature of the component and the ambient lab temperature for comparison with Figure 4.21.

4.6 Discussion

The strain inversions presented in Equations 4.13 and 4.15 have been verified experimentally through the room temperature tensile test. Although there are experimental limitations in high temperature demonstration, the inversion is seen to be successful with discrepancy occurring as a consequence of the small creep samples and difficulties in implementing an independent strain reading.

It is noteworthy that there does not appear to be a substantial error in the results of the strain inversion approaching failure. This suggests that in these accelerated lab tests the influence of grain boundary separation is negligible in comparison to the effect of strain.

The two different options for strain inversion will be discussed separately; the Normalised Resistance inversion and the Normalised Resistance Ratio inversion.

4.6.1 The Normalised Resistance Inversion

It is useful to revisit Equation 4.17 when evaluating the Normalised Resistance strain inversion; the inversion relies on the resistance change caused by geometry and the suppression or compensation of resistivity change which would otherwise cause an erroneous apparent strain,

$$\varepsilon_{\text{apparent } 1} \approx \varepsilon_{\text{apparent } 2} \approx \frac{R_{10}}{R_1} - 1 \approx \frac{\rho_0}{\rho} - 1 \approx \frac{-\Delta\rho}{\rho_0} . \quad (4.20)$$

For accelerated component tests we find failure strain in the region of 20% which occurs in the order of tens or hundreds of hours; there is therefore a significant amount of strain without a long time period for resistivity changes to occur. In power station conditions however the strain to failure is expected to be much smaller (Parker, 1986) and to occur over decades; design stresses for power station components typically allow a secondary creep rate of 1% per 100,000 hours of service. The resistivity change must therefore be stable to the order of 10^{-8} /hour in order for it not to compete with the magnitude of resistance change attributed to strain; in light of Chapter 3 this demanding target is unlikely to be met. In addition, measurement drift and instability will also have to be more consistent than the rate of change associated with the strain measurement to not cause significant error.

In the uniaxial creep tests reported in this chapter the samples were held at nominally constant temperature and therefore reversible temperature dependency is negated. In a power station context temperature must be monitored and compensated for. Temperature compensation is demonstrated in Chapter 7 for power station data.

The following chapter discusses the uncertainty in strain rate measurements in more detail and offers strategies to deal with resistivity change and instrument drift in the Normalised Resistance inversion. The Normalised Resistance Ratio is however inherently protected from such issues.

4.6.2 The Normalised Resistance Ratio Inversion

The Normalised Resistance Ratio suppresses the influence of resistivity common to both orthogonal measurements. It also has the same effect on measurement gain drift or instability as the multiplicative influence will be cancelled when taking the ratio. It is therefore recommended that the Normalised Resistance Ratio is used where possible.

The challenge of using the Normalised Resistance Ratio inversion is that only information on strain ratio or aspect ratio is preserved. In order to use the Normalised Resistance Ratio for strain inversion the orthogonal strain components will need to be coupled which requires knowledge of the stress state for a given position; information which is unlikely to be available for a given position on a power station component. The strain ratio must therefore be used to indicate creep state without an explicit biaxial strain inversion. This may be done by using the rate of change of aspect ratio as will be discussed in the following chapter.

4.7 Conclusion

It was shown that the square electrode arrangement provides greater strain sensitivity than the in-line arrangement. An electrode separation that is smaller than the component thickness is required so that the resistance measurement is not affected by thickness changes not associated with strain.

Two strain inversions have been presented. The first uses only the Normalised Resistance Ratio and is therefore insensitive to isotropic resistivity changes or instrument instability; this inversion however only provides a strain ratio and therefore requires an assumption about the strain distribution to provide absolute strain values. The Normalised Resistance Inversion provides a biaxial strain measurement but is susceptible to errors introduced by resistivity change and instrument drift and instability.

Both inversions have been successfully demonstrated experimentally in the lab. The ability to measure strain over local gauge lengths has proved difficult to achieve by other means and therefore the potential drop technique may offer useful possibilities for high temperature strain monitoring in the lab. In a power station context however the challenge becomes much more demanding. The strain rate to be measured is naturally very much smaller and must be monitored over decades. For the Normalised Resistance inversion to be successful the resistivity and instrument stability is required to be near perfect, which is not expected to be possible based on the findings of the previous chapter.

It is recommended that the Normalised Resistance Ratio and the now established strain relationship can be used to provide creep information. As the stress state is unlikely to be reliably known then it can only provide information on orthogonal strain ratio. The following chapter presents a case on how this metric, or rather the rate of change of aspect ratio, can be used to indicate creep state.

Chapter 5

Interpretation of Potential Drop Data for the Creep State Assessment of Power Station Components

5.1 Introduction

Chapters 1-4 present a potential drop measurement that is sensitive to geometry changes and component resistivity. Chapter 4 concludes that there are two options for utilising resistance data for obtaining strain information; the Normalised Resistance inversion or the Normalised Resistance Ratio inversion. It has been demonstrated that in a lab environment and over relatively short time scales it is possible to invert Normalised Resistance measurements to obtain a biaxial strain measurement on the basis that resistivity and instrument instability are negligible in comparison to the effect of accelerated creep strain and therefore all resistance changes can be attributed to strain. Alternatively, it is possible to use the Normalised Resistance Ratio, which inherently suppresses isotropic resistivity and gain changes common to both orthogonal measurements. It can be used to invert strain provided that it is possible to couple orthogonal strain components; for example, under uniaxial loading conditions. Both routes therefore have limitations when applying the technique to power station components. While changes in resistivity and instrument stability may be modest over the accelerated time scale of lab tests, in the harsh power station environment where measurements may be taken over decades, instability may begin to dominate over the influence of the very low strain rate. On the other hand, the Normalised Resistance Ratio, which is insensitive to such changes, cannot be used to invert strain unless the stress state is known for the given location; information which is unlikely to be known, as discussed in Section 4.2.

It was suggested in Chapter 1 that, rather than using absolute strain values, the *increase in strain rate* may provide valuable information on the damage state of the component. This is an important concept in this chapter and will be revisited in this introduction.

This chapter investigates the problem of random and systematic uncertainty in monitoring rates based on amplitude measurements such as resistance, themes which are common across many monitoring

applications and so in the first instance will be discussed in a general sense, providing a framework for evaluating and developing monitoring strategies.

The use of *increase in strain rate* to infer creep state is a subtle but important distinction as it circumvents the requirement to accurately determine strain but allows the use of relative changes in strain sensitive analogues which may be easier to accurately determine. In this case, the Normalised Resistance Ratio provides the strain rate sensitive metric, negating many sources of systematic uncertainty.

This chapter aims to demonstrate the PD strain monitoring method as a suitable tool for providing information on increased strain rate. As a result of the large stress sensitivity of strain rate, even small changes in internal and external damage will result in large, often order of magnitude, changes in strain rate. This dramatic increase in strain rate offers an indicator of proximity to failure. In order to demonstrate the broad utility of strain rate based measurements the simple relation of proportionality between remaining life and inverse (true) strain rate,

$$(t_f - t) \propto \frac{1}{\dot{\epsilon}} \quad (5.1)$$

This relationship is included in the API 579-1/ASME FFS-1 §10.5.2 (*API 579-1/ASME FFS-1*, 2007) Fitness for Service standard for the assessment of components operating in the creep regime. These ideas will be demonstrated using the accelerated uniaxial lab tests from Chapter 4.

5.1.1 Use of Strain Rate to Infer Creep Damage

For convenience, in the first instance the concepts and methodology will be discussed in terms of a uniaxial creep test and strain in the loading direction. Revisiting Section 1.1.2.1, a model of the creep strain – time curve was presented where a minimum strain rate was reached at the end of primary creep as strain hardening and softening processes balance out in an equilibrium (Callister, 2006; Evans & Wilshire, 1993; Viswanathan, 1989; Webster & Ainsworth, 1994). The minimum creep strain rate, $\dot{\epsilon}_{min}$, which is not a function of time, is understood to be described by the well documented Norton power law, $v(\sigma)$, and Arrhenius's Law, $u(T)$, which are considered to be independent (Evans & Wilshire, 1993).

$$\dot{\epsilon}_{min} = u(T) v(\sigma) \quad (5.22)$$

Following this point 'external' damage mechanisms reduce the load bearing cross section, such as the loss of cross section from conservation of volume, whilst 'internal' damage mechanisms, such as grain boundary separation and carbide coarsening, reduce the strength of the remaining area. Due to the increase in damage there must be a symptomatic increase in the rate of strain accumulation leading to

the characteristic ‘tertiary’ appearance of the curve. Clearly, the reverse argument must also hold, that creep damage may also be inferred from the increase in strain rate.

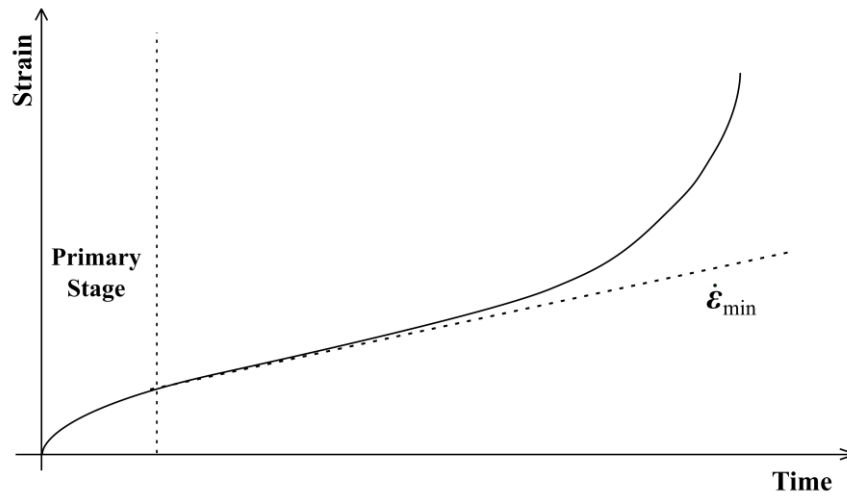


Figure 5.1: Illustration of the strain - time creep curve. A minimum creep rate, $\dot{\epsilon}_{min}$, is established at the end of primary creep. Following this point damage accumulates in the component and a symptomatic increase in strain rate results.

It is intuitively apparent that it is not the time scale or absolute strain value that gives an impression of proximity to failure but the *shape* of the curve; notably the rapidly increasing strain rate relative to the minimum strain rate approaching failure. It is this idea that can be exploited to inform creep state according to the following concepts.

Following the minimum creep rate, internal and external damage accumulates causing an increase in strain rate; the following simplification can be inferred from the continuum damage approaches first established by Rabotnov and Kachanov (Kachanov, 1986; Rabotnov, 1969),

$$\dot{\epsilon} = u(T) v(\sigma) w(\Psi) = \dot{\epsilon}_{min} w(\Psi) \quad (5.3)$$

This allows separation of the different functions and the description of tertiary creep in terms of minimum strain rate and the increase in strain rate resulting from the accumulation of internal and external damage, written here to be $w(\Psi)$. Following Equation 5.3, the strain rate encompasses two useful pieces of information for life assessment: 1) the minimum strain rate, which describes the response of the undamaged component to the operational conditions in accordance to the Norton and Arrhenius laws and 2) the increase in strain rate from the minimum resulting from the accumulation of damage. The former is understood to provide estimates of creep life through the long-established Monkman-Grant relationship, while the latter provides a continuous indicator of damage and, with an interpretive framework, time to failure.

The damage state can then be inferred by the relative increase in strain rate,

$$\frac{\dot{\epsilon}}{\dot{\epsilon}_{min}} = w(\Psi), \quad (5.4)$$

but in order to do so, the form of $w(\Psi)$ will need to be assumed. The function $w(\Psi)$ is discussed in Appendix B. It concludes that a suitable form for the function is,

$$\frac{\dot{\epsilon}}{\dot{\epsilon}_0} = e^{\Omega\epsilon} \quad (5.5)$$

where the use of true strain, ϵ , has been adopted as more suitable due to the possibility of large strains; a reference strain, denoted by the subscript zero, is used instead of the requirement of identifying the minimum strain rate. Ω is a material and situation dependent constant relating total damage to strain, again discussed in Appendix B.

It is worth pointing out that Equation 5.5 must be a result of a grossly simplified model. Clearly, the simple strain dependence implies that many of the internal and external damage models are neglected or simplified. However, in a power station context, where periphery information may be limited or poorly defined there is a distinct benefit to use only the information is being monitored; in this case strain. Further, to use the methodology for remnant life calculations the equation must be of a suitable form to enable extrapolation into the future; Equation 5.5 is well suited to this. Integration with the condition that the time and strain rate at failure is t_f and $\dot{\epsilon}_f$ respectively yields,

$$(t_f - t) = \frac{1}{\Omega} \left[\frac{1}{\dot{\epsilon}} - \frac{1}{\dot{\epsilon}_f} \right]. \quad (5.6)$$

This can be further simplified on the assumption that the strain rate at failure will be large to give,

$$(t_f - t) = \frac{1}{\Omega\dot{\epsilon}} \quad (5.7)$$

In order to demonstrate the broad utility of strain rate based measurements the simple relation of proportionality between remaining life and inverse (true) strain rate will be adopted. The above model is intended as a basis for the demonstration of 1) the suitability of the PD technique to provide strain-rate information in a power station context and 2) the utility of rate-based information for remnant life calculations. It has been chosen for this purpose as it is dependent only on strain and requires no further information. It is possible to estimate a value of Ω based on in-situ measurements by rearranging Equation 5.5,

$$\ln\left(\frac{\dot{\epsilon}}{\dot{\epsilon}_{min}}\right) = \Omega\epsilon \quad (5.8)$$

By plotting $\ln(\dot{\epsilon}/\dot{\epsilon}_{min})$ against ϵ then the gradient of the best fitting linear fit will provide Ω .

5.2 Creep Rate Measurement Uncertainty

Typical creep strain behaviour was investigated in Chapter 1 and it was concluded that strain rates of less than 1% per 100,000 hours will need to be monitored to accurately characterise ‘secondary’ creep. Maharaj *et al.* (Maharaj et al., 2009) claim that a secondary creep rate of 2×10^{-8} /hour is typical, equating to 0.5% strain in approximately 30 years of service. We will consider this the target ‘base rate’ to be measured.

The uncertainty associated with a rate measurement will either be systematic, arising from the measurement principle, or random, dictated by the repeatability of the measurement system independent of systematic changes. Both sources of uncertainty will be investigated to evaluate monitoring procedure and inform appropriate measurement strategies.

5.2.1 Rate Uncertainty Associated with Random Errors

In order to establish a means of comparing and evaluating strain rate monitoring strategies it is necessary to formulate the uncertainty associated with a rate calculated from a series of individual measurements. Each individual measurement, in this case strain, will be assumed to be randomly distributed around a mean. The analysis is included in Appendix C concluding with Equation 5.9. Assuming that the creep rate is nominally constant and that individual readings are taken at regular intervals then the confidence interval ($\dot{\epsilon} \pm \Delta\dot{\epsilon}$) is:

$$\Delta\dot{\epsilon} = \frac{\sigma_{\epsilon} P \sqrt{12}}{t_m \frac{3}{2} f_m \frac{1}{2}} \quad (5.9)$$

where σ_{ϵ} is the standard deviation of each reading of strain, t_m is the length of time the component is monitored over and f_m measurement repetition frequency. The value of P corresponds to the chosen confidence level according to Table 5.1.

Table 5.1: P values for given confidence levels.

Confidence Level (%)	P
90	1.645
95	1.960
99	2.576

As an example, in order to measure the previously suggested ‘base rate’ of 2×10^{-8} /hour to within 10% (*i.e.* to be 95% confident that our estimate is to within $\pm 0.2 \times 10^{-8}$ /hour) over a four year period of taking measurements once a day an individual measurement standard deviation of 0.0395% strain would be required, a demanding requirement even at this relatively high measurement repetition frequency.

Equation 5.9 presents possible strategies for achieving the required confidence in strain rate. Rate uncertainty can be increased by reducing the individual measurement uncertainty, increasing the sample frequency or duration over which measurements are taken. The decision on how to improve rate uncertainty will depend on design parameters for the particular technique, for example, in the present case of a remotely powered sensor powered by a finite battery supply the compromise will be to maximise battery life.

An important conclusion to draw from this analysis is the benefit of monitoring over periodic inspection. Statutory outages typically occur every four years in the UK, thus providing a practical limit to the frequency of measurements which require direct access to the component. In order to obtain the same strain rate uncertainty by taking one strain measurement every 4 years versus one strain measurement per day the inspection method would have to be 38 times more accurate. For direct length measurement, for example from creep pips, such accuracy is unlikely to be achieved from a practical perspective due to build-up of oxidation products, temperature effects, potentially prohibitive access requirements and changes in technical staff (Maharaj et al., 2009). In contrast, the individual measurement uncertainty is expected to be improved by permanently attaching sensors, ensuring positional variability is eliminated.

5.2.2 Rate Uncertainty Associated with Systematic Errors

The increased volume of data collected in continuous monitoring and the elimination of positional variability can often reveal systematic errors in the measurement procedure which may not be identifiable in the sparse data obtained through inspection. It is also possible that monitoring systems are more prone to systematic errors as instrumentation is left in-situ, often in harsh environments for extended periods and measurements are taken over a range of conditions. Systematic errors are therefore an important consideration.

Systematic errors will come from both the stability of the measurement electronics and also the sensing principle. The resistance measurement described in this thesis is an example of an amplitude measurement; the resistance is calculated from the amplitude of the potential difference created by a controlled current. The description in this section is common to all amplitude based measurements and so will be described in general terms.

5.2.2.1 Measurement Electronics Drift and Stability

For strain monitoring a quantity, θ , that is a function of the desired length scale, l , is sampled through some signal conditioning electronics to provide a measurement, θ_m . The measurement equipment, operating in a harsh environment over many years, is susceptible to instability issues which will lead to changes in the measurement, regardless of the real quantity.

Temporal instability is the error in the measurement as a function of time, t , that leads to drift. Thermal instability is the error in the measurement as a function of instrument temperature, T_{inst} , that leads to reversible variations in the measurement. In both cases the error may be an offset or gain error (Wheeler & Ganji, 2010). In the following, θ_m is the measured signal, $\theta(l)$ is the desired quantity which is a function of the desired length scale, $F(t)$ is the gain time stability and $f(t)$ is the offset time stability, $G(T_{inst})$ is the gain temperature stability and $g(T_{inst})$ is the offset temperature stability. n is additive random noise.

$$\theta_m = \theta(l) F(t)G(T_{inst}) + f(t) + g(T_{inst}) + n \quad (5.10)$$

The random incoherent noise has been discussed as random error. The gain drift and thermal stability will however cause a systematic apparent change in the measured quantity which will be interpreted as strain. As time progresses and instrument temperature changes the measured quantity will be erroneously scaled by a factor of $F(t)G(T_{inst})/F(t_0)G(T_{inst_0})$ relative to the initial reference measurement meaning that this factor will be interpreted as strain.

Gain time stability is usually given in ppm/year and gain temperature stability in ppm/°C. Although individual components can be specified to very high tolerances, typical temperature drift of measurement instruments are of the order of 100 ppm/°C (SR830 50 ppm/°C amplitude stability (Stanford Research Systems Inc., 2011)). In a power station environment, depending on the geographic location, the measurement electronics may go through daily cycles of ~10 °C and yearly cycles of ~30 °C. Compounded with heating from the power station itself a range of 50 °C may be expected.

With an instrument with a specification of 100 ppm/°C a 50 °C temperature change would result in a 0.5% change in the measured quantity which would then propagate through the strain inversion to be interpreted as strain. In linear relationships between strain and the measured quantity the error will equate to the instability divided by the ‘gauge factor’. In the case of the Normalised Resistance inversion (see Chapter 4 Equation 4.15) the gain instability would have an approximately 1:1 relationship with the apparent strain, therefore a gain error of 0.5% would be interpreted directly as strain. Equally, the inherently long measurement times required in creep measurements mean that even modest gain time stability can become significant when considered over decades.

The instability of the measurement electronics are therefore expected to be of an equal magnitude to the changes in measurement resulting from strain, undermining the use of the Normalised Resistance inversion unless the measurement system is carefully designed to minimise such issues. Moreover, it is likely to be necessary to build in self-calibration functionality by taking measurements of extremely high stability reference components which on an individual basis can be specified down to ~1ppm/°C.

5.2.2.2 Sensor Drift and Stability

Equivalent stability arguments can additionally be made for the sensors, the nature of which will be specific to the sensing principle and sensor design. There may be inherent temperature dependence in the measured quantity or thermal ageing of the sensor itself. In the case of inferring strain information from potential drop readings the dependence on component resistivity provides the primary cause of drift and instability. Chapter 4.3.2.2 gives the approximate strain error of the Normalised Resistance strain inversion as,

$$\varepsilon_{\text{apparent}} \approx \frac{-\Delta\rho}{\rho_0} \quad (5.11)$$

and that the resistivity changes can be separated into reversible temperature dependency, a function of component temperature, T_{comp} , and the irreversible resistivity material changes resulting from creep exposure.

$$\frac{\rho}{\rho_0} \approx 1 + \frac{\Delta\rho_{\text{rev}}(T_{\text{comp}})}{\rho_0} + \frac{\Delta\rho_{\text{irr}}}{\rho_0} . \quad (5.12)$$

The systematic error caused by resistivity change is therefore analogous to that from measurement electronics. Measurements of resistance are erroneously scaled by temperature fluctuations and long term ageing. Though the influence of reversible temperature dependency is expected to be much greater than irreversible material degradation, it is expected to be very predictable and repeatable. It can therefore be effectively suppressed by measurement of component temperature, but importantly, the operational temperature is expected to be anchored to a set-point temperature and therefore fluctuations from this can be considered a random error. The effect of long term material degradation, explored in Chapter 3, is anticipated to be harder to compensate for. The implied requirement for resistivity stability for the use of the Normalised Resistance inversion is greater than 0.5% over 30 years, a demanding requirement that is not expected to be achievable.

It may be possible to correct for sensor instability by obtaining an independent reading indicative of sensor drift, in this case an indicator of resistivity change. A common approach is the use of a ‘dummy’ sensor; one that is thermally but not mechanically coupled to the test component, providing a resistance measurement indicative of resistivity but not strain.

5.2.3 Creep Rate Measurement Uncertainty Conclusions

The analysis of the uncertainty of rate calculations from random errors provides a framework for the assessment of monitoring techniques but also provides a basis for informing monitoring strategies. One important insight comes from comparing infrequent inspection type measurements to continuous monitoring, the increased measurement repetition frequency provides improved rate uncertainty. Further, the individual measurement uncertainty is expected to be improved by permanently attaching

sensors, ensuring positional variability is eliminated. Systematic errors are an important consideration in monitoring systems as there may be considerable long and short term variability in the measurement conditions with instrumentation operating in-situ for extended periods.

Drift and instability of measurement electronics and the reversible and irreversible effect of resistivity are expected to have analogous effects on the systematic error of strain measurements, erroneously scaling the measurements. Due to the low strain rates in power station components the required stability of measurements must be excellent in order to use the Normalised Resistance inversion to obtain biaxial strain measurements; much smaller than the 2×10^{-8} /hour effects of strain. It may be possible to compensate for measurement system drift by the use of calibration routines, taking measurements from high stability components which allow the changes in the measurement system to be tracked. Likewise, it may be possible to compensate resistivity changes by the use of a 'dummy' sensor by assuming that resistivity drift in the dummy sensor is common to the other sensors.

An alternative approach which inherently suppresses systematic uncertainty is to use the Normalised Resistance Ratio. As the signal conditioning electronics and material inspected will be common to both orthogonal resistance measurements, the scaling uncertainty will be cancelled out by dividing the two. All that remains then is the random uncertainty which can be improved using the framework of Equation 5.9. The remainder of this chapter is dedicated to utilising the Normalised Resistance Ratio to infer creep state.

5.3 Normalised Resistance Ratio as a Metric for Strain Rate

The introduction of this chapter explained that the relative increase in strain rate could be used for remnant life calculation and creep state assessment using the relations,

$$(t_f - t) = \frac{1}{\Omega \dot{\epsilon}} \quad (5.13)$$

and

$$\frac{\dot{\epsilon}}{\dot{\epsilon}_0} = e^{\Omega \epsilon} \quad (5.14)$$

This section will describe the use of the Normalised Resistance Ratio as a metric for strain rate and therefore how it can be applied to Equation 5.13 and 5.14 to provide information on creep state. In order to do so, several arguments will need to be considered. These include:

- The Normalised Resistance Ratio is a function of aspect ratio.
- Aspect ratio is a linear function of strain.
- Incorporation of the Normalised Resistance Ratio into remnant life calculation.

Each of these stages will be addressed in turn.

5.3.1 The Normalised Resistance Ratio is a Function of Aspect Ratio

A useful approximation for the relationship between the Normalised Resistance Ratio and strain was introduced in Section 4.3.2.1 following the work of Madhi and Nagy (Madhi & Nagy, 2011b),

$$NRR = \frac{R_1/R_{10}}{R_2/R_{20}} \approx \left(\frac{1 + \varepsilon_1}{1 + \varepsilon_2} \right)^s = \gamma^s, \quad (5.15)$$

where, s is the constant $2+\sqrt{2}$ and γ is the aspect ratio of the initially square electrode configuration. It is not possible to invert biaxial strain information from Equation 5.15 as there are two unknown variables and one equation. It is therefore necessary to use the aspect ratio, or rather, rate of change of aspect ratio to provide the information on strain rate.

5.3.2 Aspect ratio is a Linear Function of Strain

It was described in Section 4.2 that ε_1 and ε_2 are not truly independent as they are linked by the ‘flow rules’ of deformation, a result of which is

$$\frac{\dot{\varepsilon}_1}{\dot{\varepsilon}_2} = \frac{[\sigma_1 - \frac{(\sigma_1 + \sigma_2 + \sigma_3)}{3}]}{[\sigma_2 - \frac{(\sigma_1 + \sigma_2 + \sigma_3)}{3}]} . \quad (5.16)$$

In certain situations this allows for strain inversion, for example in the uniaxial creep tests of the previous chapter. In generic power station components the stress state is not expected to be known and therefore such an inversion is not possible. An alternative approach is to assume that the stress state is constant over time and deformation is sufficiently small so that the true stress state is not significantly altered, integrating gives,

$$\frac{\varepsilon_1}{\varepsilon_2} = \frac{[\sigma_1 - \frac{(\sigma_1 + \sigma_2 + \sigma_3)}{3}]}{[\sigma_2 - \frac{(\sigma_1 + \sigma_2 + \sigma_3)}{3}]} . \quad (5.17)$$

and further,

$$\frac{\varepsilon_1}{\varepsilon_2} = \frac{1}{k} . \quad (5.18)$$

The aspect ratio can then be written in terms of a single strain component and the value of k ,

$$\gamma = \left(\frac{1 + \varepsilon_1}{1 + \varepsilon_2} \right) = \frac{1 + \varepsilon_1(t)}{1 + k\varepsilon_1(t)} \quad (5.19)$$

This formulation reveals that for a given stress state the aspect ratio will deform approximately linearly with strain.

$$\frac{\partial \gamma}{\partial \varepsilon} = \frac{k + 1}{(k\varepsilon_1 - 1)^2} \quad (5.20)$$

Therefore for small strains (up to 20%) γ can be approximated to be a linear function of ϵ , which will now be taken as the strain in the direction of maximum principal stress. The equivalent can also be shown for true strain, ϵ , as will be used from this point. κ is a best fitting constant $\approx (1 - k)$ as shown in Figure 5.2.

$$\gamma \approx 1 + \kappa\epsilon \approx 1 + \kappa\epsilon \quad (5.21)$$

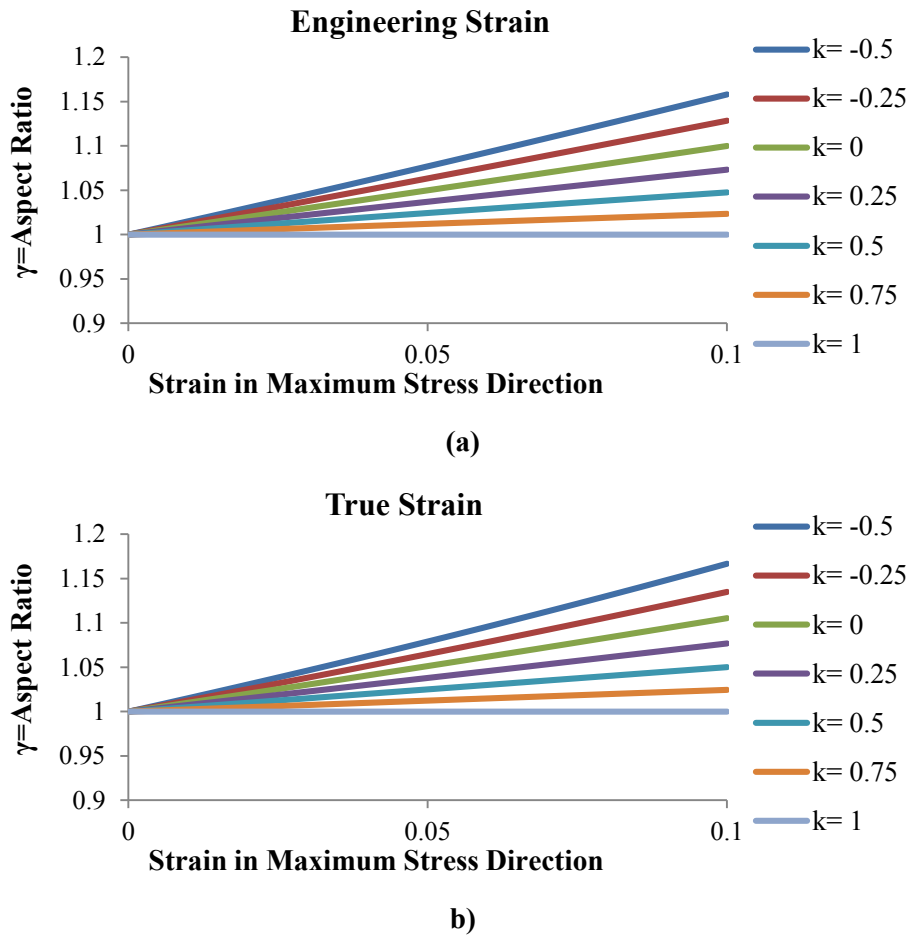


Figure 5.2: Figure showing approximately linear relationship between aspect ratio and (a) Engineering and (b) True strain for a range of stress states denoted by the value of k .

This implies that,

$$\frac{\partial\gamma}{\partial t} \approx \kappa \frac{\partial\epsilon}{\partial t} \quad (5.22)$$

i.e. for a given stress state the rate of change of aspect ratio is an approximately linear function of the rate of change of strain. The other important conclusion is regarding the sensitivity: the κ value. A physical insight into how this value will change can be gained by considering different states of stress triaxiality.

The expected stress state for power station components was described in Chapter 4.2. It was concluded that the radial stress would be small and for closed ended power station components the ratio of circumferential to axial stress resulting from internal pressure is 2:1, corresponding to a k of 0. An additional axial stress originating from bending may act to reduce the axial stress, if the axial stress was to become zero a k of -0.5 would result. However, if the bending stress would add to the axial stress an ‘equibiaxial’ state may arise where, despite the accumulation of strain, the aspect ratio will not change, the square arrangement of electrodes will simply get bigger. In this case $k = 1$ and there is no sensitivity to strain. It is however believed that this state is unlikely and the axial stresses will be smaller than the hoop stresses. A range of values of κ for an anticipated range of stress states for power station components is shown by Figure 5.3,

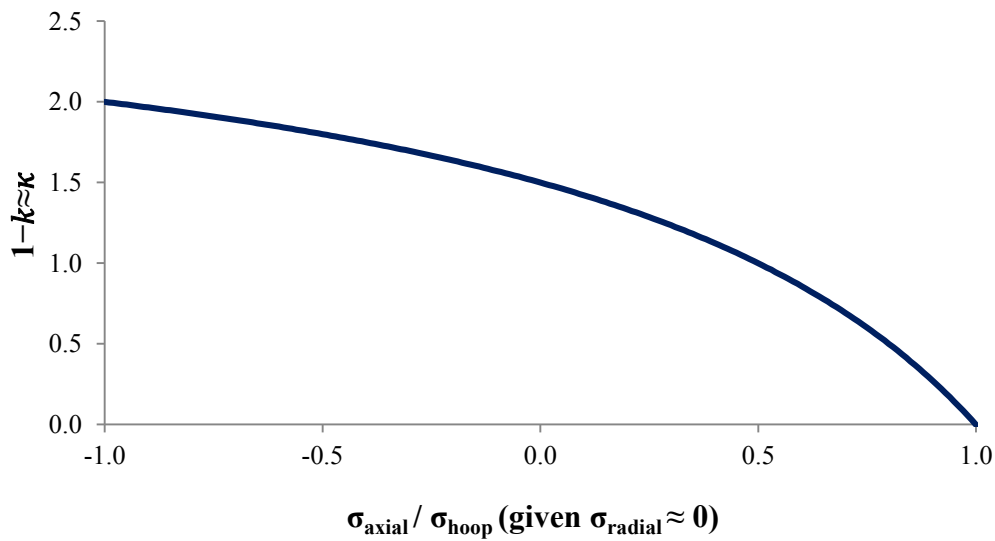


Figure 5.3: Approximate sensitivity of change of aspect ratio for a range of stress states.

It can therefore be concluded that the aspect ratio is a linear function of strain for constant stress state conditions, or more importantly the rate of change of aspect ratio is a linear function of strain rate. Recall that it is the *relative increase in strain rate* that provides strain information, therefore the constant of proportionality between aspect ratio and strain is unimportant as when normalising the aspect ratio it simply cancels,

$$\frac{\dot{\epsilon}}{\dot{\epsilon}_0} \approx \frac{\dot{\gamma}/\kappa}{\dot{\gamma}_0/\kappa} \approx w(\Psi). \quad (5.23)$$

The stress state does not therefore need to be known. The significance of the constant of proportionality only extends to the sensitivity of the aspect ratio to strain, with lower sensitivity making measurement more challenging. The linear sensitivity of the aspect ratio to strain is dependent on stress state with a point of zero sensitivity occurring under perfect ‘equi-biaxial’ stress conditions.

The Normalised Resistance Ratio, which is a known function of aspect ratio, will now be incorporated into remnant life calculations.

5.3.3 Incorporation of the Normalised Resistance Ratio into Remnant Life Calculations

Equations 5.13 and 5.14 are written again for convenience,

$$\frac{\dot{\epsilon}}{\dot{\epsilon}_0} = e^{\Omega\epsilon} \quad (5.24)$$

$$(t_f - t) = \frac{1}{\Omega} \left[\frac{1}{\dot{\epsilon}} - \frac{1}{\dot{\epsilon}_f} \right] \quad (5.25)$$

As it has been shown that aspect ratio and rate of change of aspect ratio are linear functions of strain and strain rate, these equations can be written in terms of aspect ratio. First, Equations 5.21 and 5.22 will be rearranged to give strain and strain rate as a function of aspect ratio,

$$\dot{\epsilon} \approx \frac{1}{\kappa} \frac{\partial \gamma}{\partial t} \quad (5.26)$$

$$\dot{\epsilon}_0 \approx \frac{1}{\kappa} \frac{\partial \gamma}{\partial t_0} \quad (5.27)$$

$$\epsilon \approx \frac{\gamma - 1}{\kappa} \quad (5.28)$$

These can be substituted into Equation 5.24.

$$\frac{1}{\kappa} \frac{\partial \gamma}{\partial t} = \frac{1}{\kappa} \frac{\partial \gamma}{\partial t_0} e^{\Omega \frac{\gamma-1}{\kappa}} \quad (5.29)$$

or:

$$\dot{\gamma} = \dot{\gamma}_0 e^{\frac{\Omega}{\kappa}(\gamma-1)} \quad (5.30)$$

And the time to failure is given by,

$$(t_f - t) = \frac{1}{\dot{\gamma} \frac{\Omega}{\kappa}} \quad (5.31)$$

Ω/κ is found by plotting and finding the gradient of,

$$\ln\left(\frac{\dot{\gamma}}{\dot{\gamma}_0}\right) = \frac{\Omega}{\kappa}(\gamma - 1) \quad (5.32)$$

It can therefore be seen that the value of κ which is determined by the stress state of the component is lumped with the value Ω and can be found empirically. Again, this is an important outcome as it means that the stress state does not need to be known but must be constant over time.

The significance is that the aspect ratio can be determined using the Normalised Resistance Ratio alone. As discussed previously the Normalised Resistance ratio is inherently stable due to the cancelling of thermal and temporal instability of electronics and sensors.

For completeness, the aspect ratio and rate of change of aspect ratio will now be written in terms of the Normalised Resistance Ratio, from Equation 5.15,

$$\gamma = NRR^{1/s} \quad (5.33)$$

Using the chain rule,

$$\frac{d\gamma}{dt} = \frac{d NRR}{dt} / \frac{d NRR}{d\gamma} \quad (5.34)$$

Differentiating Equation 5.15 gives,

$$\frac{d NRR}{d\gamma} = s NRR^{\frac{s-1}{s}} \quad (5.35)$$

And therefore,

$$\frac{d\gamma}{dt} = \frac{N\dot{R}R}{s NRR^{\frac{s-1}{s}}} \quad (5.36)$$

5.3.4 Experimental Demonstration

This section will demonstrate the use of potential drop measurements and in particular the Normalised Resistance Ratio for strain rate based remnant life calculations. To do so, the three uniaxial creep experiments already shown in Section 4.5.2 will be used. The three experiments will be discussed in parallel.

The Normalised Resistance Ratio data from the two experiments is shown in Figure 5.4. This is the data which was used in the Normalised Resistance Ratio inversions to produce the strain results in Chapter 4, for more information on the experiments please revisit that section. Absolute strain values will not be explicitly calculated in this chapter but instead the creep strain rate information will be inferred from Normalised Resistance Ratio data. Again, the colouring of the two figures corresponds to the sample schematic also included in the Figure. As previously described, element 1 of the 115 MPa experiment and elements 7 and 8 of the 160 MPa experiment experienced difficulty and therefore data has been excluded.

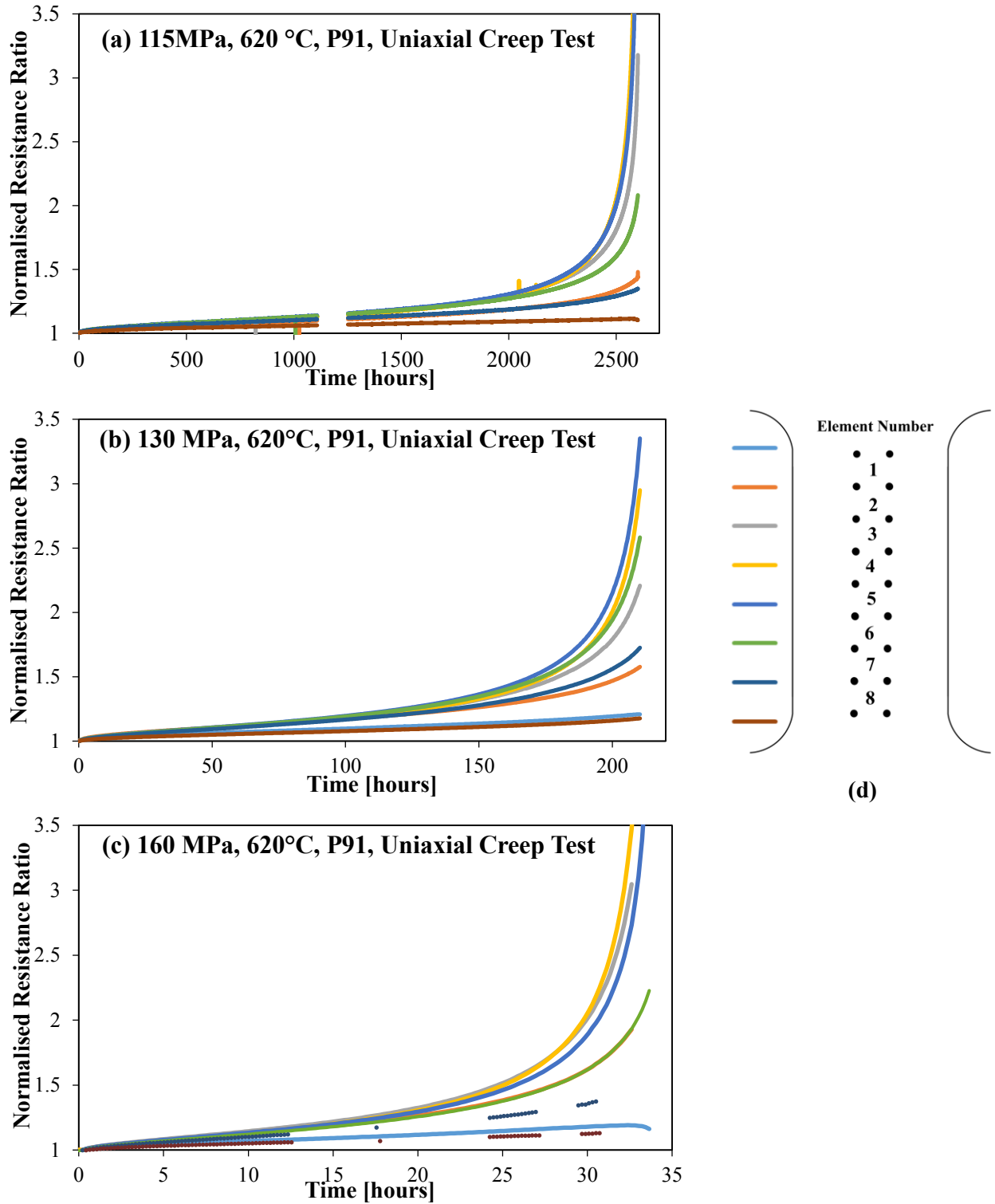


Figure 5.4: Normalised Resistance Ratio against time for three accelerated uniaxial creep of P91 material at 620°C and loads of (a) 115 MPa (b) 130 MPa and (c) 160 MPa. (d) shows a schematic of the test component with potential drop array numbering convention and colours forming the legend.

The data displayed was collected at a rate of one reading every ~12.5 minutes. In order to calculate the rate of change of the Normalised Resistance Ratio smoothing was first applied to the resistance data to

suppress random fluctuations. In the case of the 130 MPa experiment the mean of the past 10 data points was used; the use of past data replicating a process that could be carried out in real time. *i.e.*

$$R_{smoothed_i} = \frac{\sum_{i-10}^i R_i}{10} \quad (5.37)$$

A linear fit was assumed over the previous 10 data points and the gradient found by least squares regression. Again, 10 data points were used to calculate each rate value. 10 data points with a 12.5 minute separation gives a time scale of ~2 hours which in this case was equal to ~1% of life. The same process was applied to the data from the 115 MPa and 160 MPa experiment, except due to the differing time scale the last 50 and 3 data points were used respectively. It is worth noting that in power station conditions 1-2% of life may represent many weeks of service and therefore it is possible to accumulate much more data, however the standard error of the data is expected to be larger due to the unfavourable measurement environment and the creep strain rate will of course be much smaller. The results of the discrete time derivative calculation are shown in Figure 5.5. The log-y axis indicates the scale of the changes in the strain rate present.

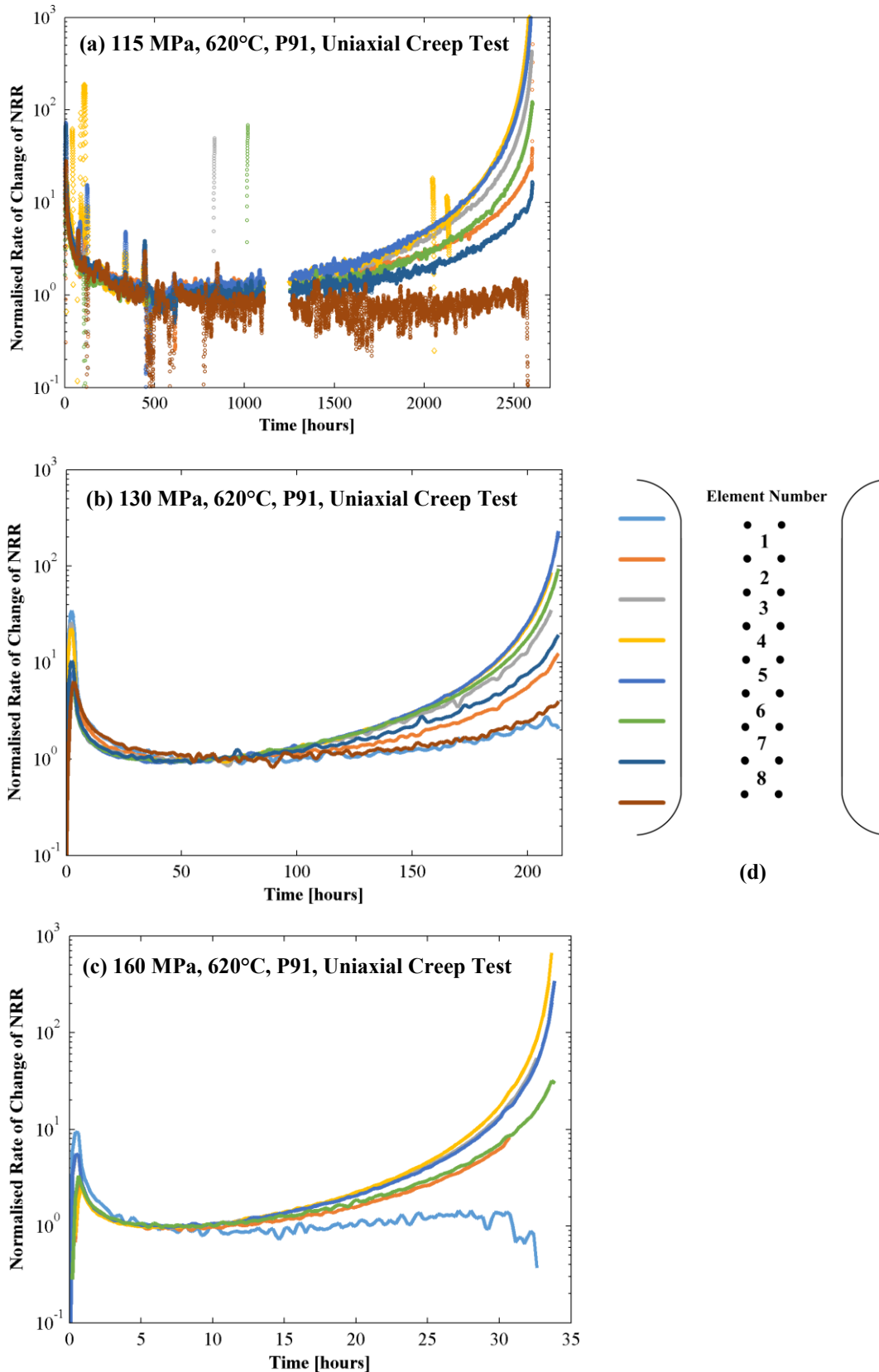


Figure 5.5: Rate of change of Normalised Resistance Ratio (NRR) normalised to the minimum rate of change for two accelerated uniaxial creep of P91 material at 620°C and loads of (a) 115 MPa (b) 130 MPa and (c) 160 MPa. (d) shows a schematic of the test component with potential drop array numbering convention and colours forming the legend.

In Figure 5.4 the rate of change appears nominally constant for much of the life, hence the terminology of ‘steady-state’ creep. In reality however, following primary creep, the strain rate increases as damage accumulates as is evident in Figure 5.5. Towards failure the strain rate can be seen to increase by orders of magnitude; it is suggested that this is a consequence of the high stress sensitivity of creep strain rate as evident from the Norton creep law. Regardless of the interpretation, the strain rate clearly provides information on component integrity throughout life and particularly approaching failure.

From the Normalised Resistance Ratio and the rate of change of Normalised Resistance Ratio the aspect ratio and its time derivative can be calculated and used for remnant life estimate calculations. As previously explained Ω/κ can be found by plotting and finding gradient of Equation 5.32,

$$\ln\left(\frac{\dot{\gamma}}{\dot{\gamma}_{min}}\right) = \frac{\Omega}{\kappa}(\gamma - 1) \quad (5.38)$$

This process is illustrated in Figure 5.6 for the fifth and fourth elements of the sensor array for the 130 MPa and 160 MPa experiment respectively; the location where failure occurred. If the accumulation of damage is truly strain controlled according to the Equation 5.24 then the gradient should be constant. Examining Figure 5.6 shows this is a reasonable approximation for much of the component life. The rate of strain accumulation accelerates with proximity to the end of life, therefore the majority of what is seen as the substantial deviation from the linear occurs in the final hours of the experiment. In these final stages approaching failure necking may have occurred, violating the constant stress state assumption.

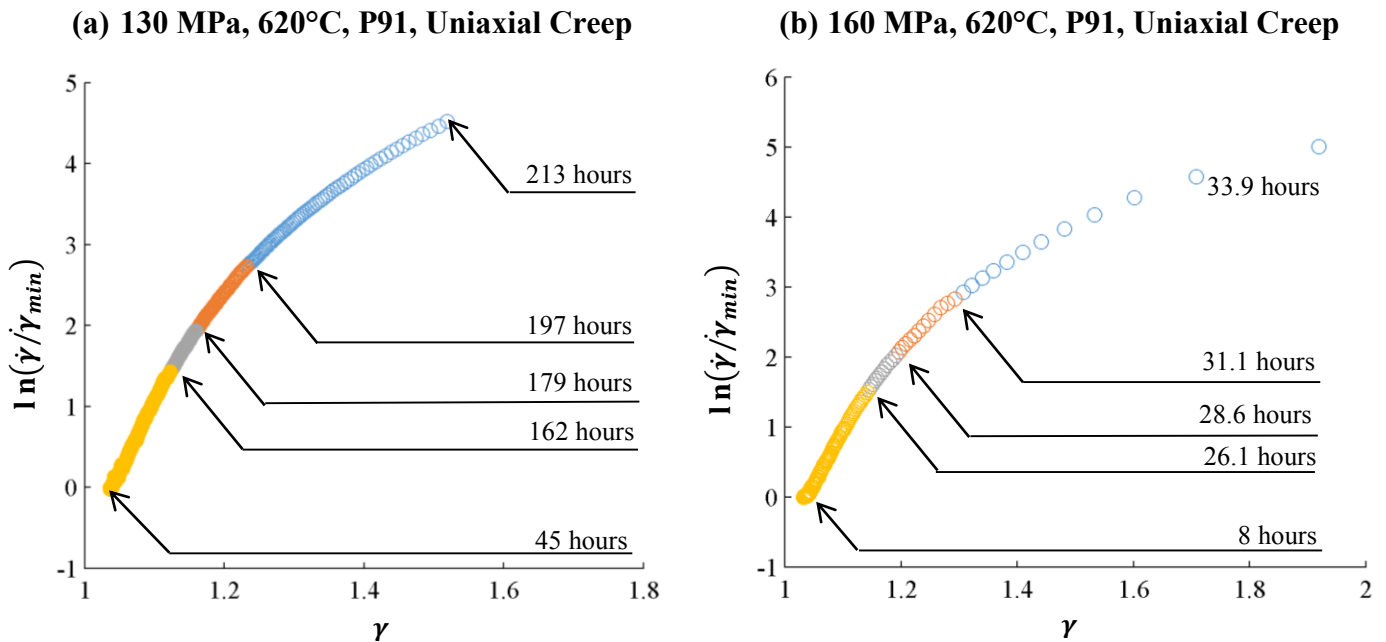


Figure 5.6: $\ln(\dot{\gamma}/\dot{\gamma}_{min})$ against γ . The gradient of this graph indicates the value of Ω/κ . Data shown begins at the point of minimum creep rate at (a) 45 and (b) 8 hours. The yellow region is the first 70% of the minimum creep rate to failure data, grey is 70-80%, orange is 80-90% and blue is the final 10% of data.

Figure 5.7 shows the estimated time of failure, calculated using,

$$(t_f - t) = \frac{1}{\dot{\gamma} \frac{\Omega}{\kappa}}, \quad (5.39)$$

the estimated time to failure is re-evaluated at each data point based on the data accumulated so far. The estimate is therefore refined as time progresses and failure approaches. It is only possible to begin the remnant life calculation once the minimum creep rate has been achieved, in this case at 550 hours, 45 hours and 8 hours for the 115 MPa, 130 MPa and 160 MPa experiment respectively. Following the point of minimum rate comes a period of extreme uncertainty as the value of $\frac{\Omega}{\kappa}$ is estimated from the growing pool of strain and strain rate data.

The life estimate is evaluated for each element on the array, except the failed elements 1 from the 115 MPa experiment and elements 7 and 8 from the 160 MPa experiment. Evidently, creep is not entirely uniform across the entire gauge length of the component; the central four elements have similar strain rate responses while moving away from the centre of the gauge section the strain rate is seen to decrease. Notably, the top and bottom elements have markedly lower strain rates as a result of the altered stress state in the proximity of the wider gripped region. It is therefore expected that the damage accumulation is slower and the life expectation longer. The central elements have a very similar life expectancy therefore damage is well distributed across this portion of the gauge length. This highlights an inherent limitation of point measurements; it is necessary to be inspecting an area where damage accumulation is expected to be high.

The red arrow annotations are included to allow easier comparison between the calculated estimates and the true failure time. It can be seen that, for estimates from elements in the region of failure, following the point of minimum creep rate accurate estimates of the time of failure are quickly established. In all experiments the estimate is found to be within ~10% from ~40% of life onwards; the missing data of the 115 MPa experiment at around 1100 hours increases the time until a stable estimate is established. The minimum creep rates were at 15-20% of life, marking the earliest point life estimates could be calculated.

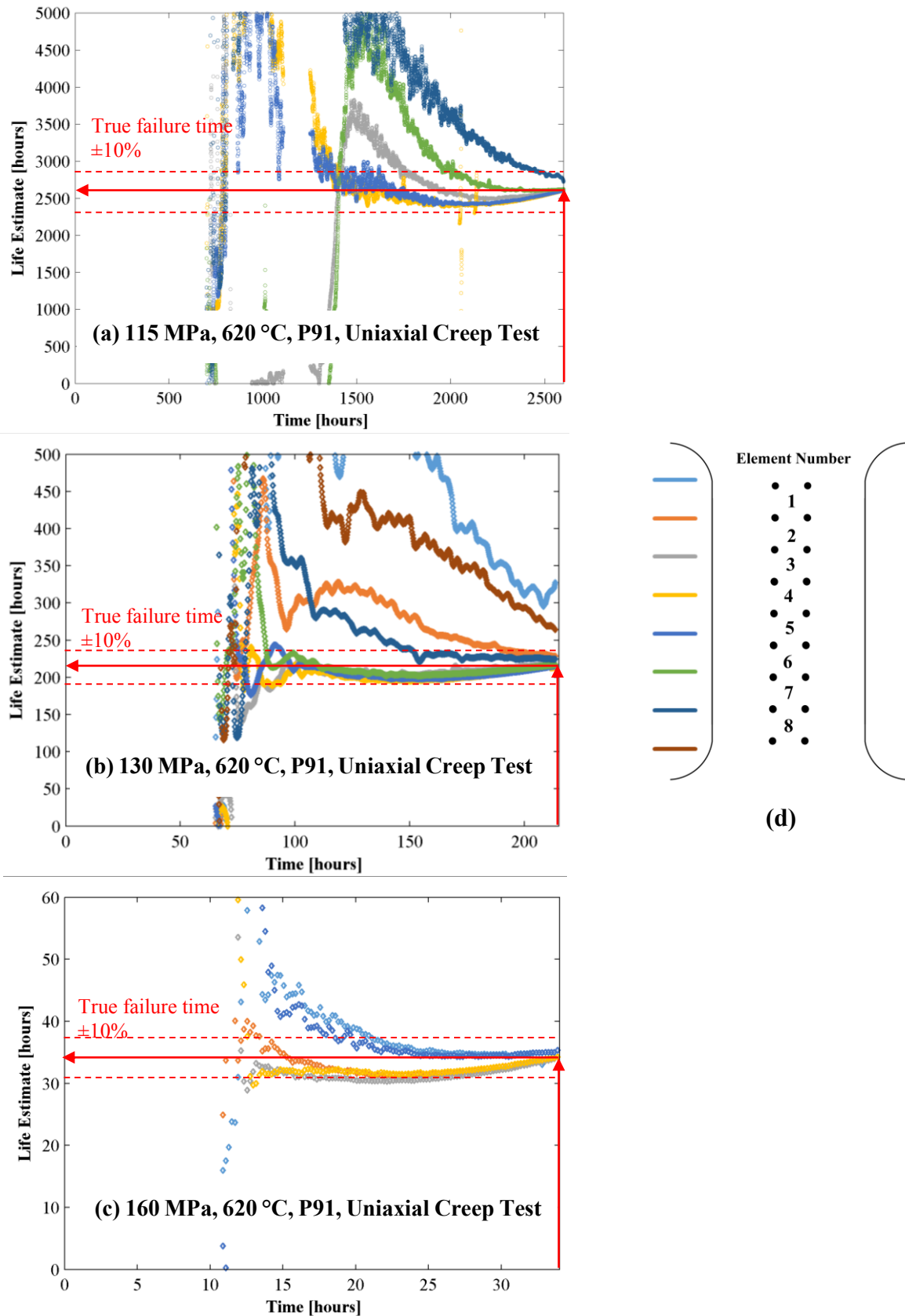


Figure 5.7: Running estimate of failure time for two accelerated uniaxial creep of P91 material at 620°C and loads of (a) 115 MPa, (b) 130 MPa and (b) 160 MPa. Red annotation shows the true failure time and $\pm 10\%$ bounds. (d) shows a schematic of the test component with potential drop array numbering convention and colours forming the legend.

It can also be shown that it is not necessary for all of the data to be present; for example it is not required that the minimum creep rate is captured as the initial strain rate can be chosen arbitrarily as shown in Figure 5.8 where the sensors were assumed to be installed at 70% life and data before that time discarded. The relationship between strain and strain rate is quickly determined due to the increasing rate at end of life and it can be seen that a good estimate of remnant life is achieved.

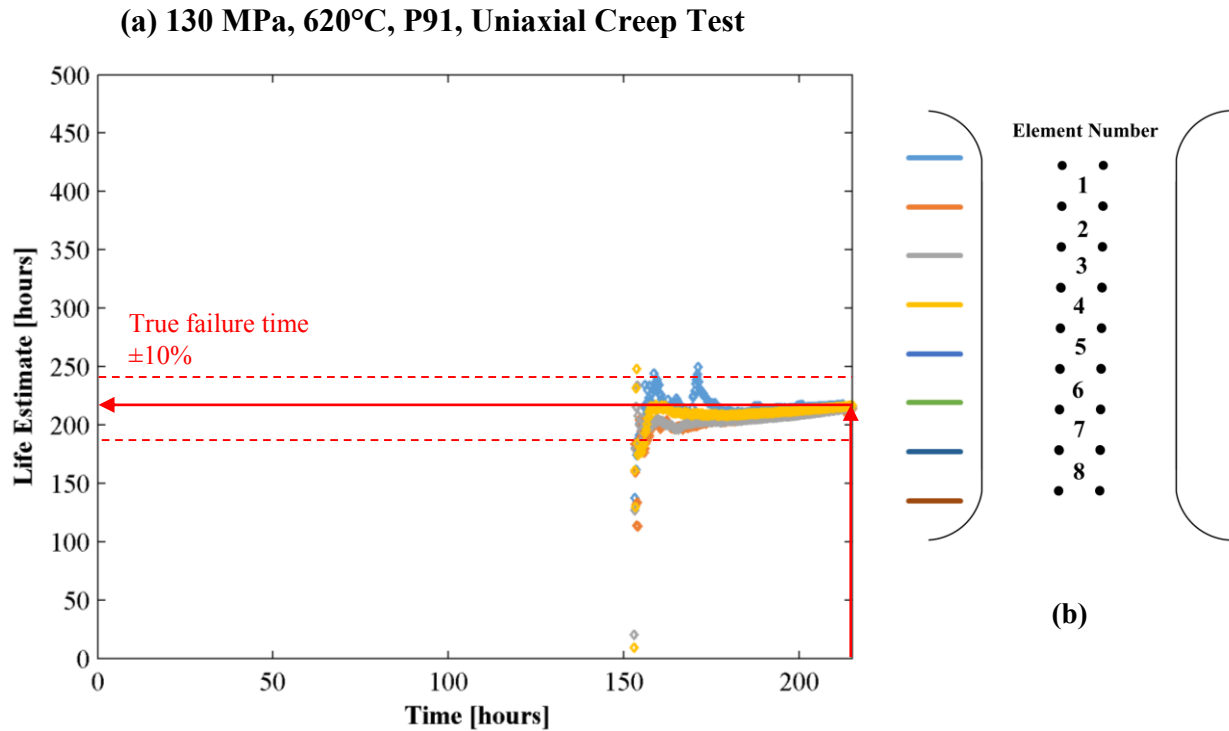


Figure 5.8: Running estimate of failure time for accelerated uniaxial creep of P91 material at 620°C and loads of 130 MPa. Only data from the last 30% of life is used to imitate a sensor being installed on a component late in life. Red annotation shows the true failure time and $\pm 10\%$ bounds. (b) shows a schematic of the test component with potential drop array numbering convention and colours forming the legend.

5.3.5 Application to Power Station Conditions

It is important to consider the likely success of this scheme in a power station operation conditions. The form of the creep curve is expected to be less favourable to the proposed time to failure calculations. It is the value of Ω that dictates the ‘shape’ of the strain-time curve. The gradient of Figure 5.6 (a) was found to be 17.6 at 162 hours (*i.e.* the yellow portion of the graph). In this uniaxially stressed case the value of κ is known to be 1.5 (see Figure 5.3) so the value of Ω can therefore be inferred to be 26.4. Prager (Prager, 1995, 2000) states the value of Ω is expected to increase with decreasing stress, decreasing temperature and stress multiaxiality. It can therefore be assumed that in power station conditions the Ω/κ value will be much higher than that of this experiment. An increase in Ω suggests that a greater portion of the strain rate acceleration is a result of material degradation as opposed to loss of cross section through deformation. Figure 5.9 shows the form of a selection of curves with a range

of Ω values that have been suggested as realistic (Prager, 1995, 2000). As conditions become more representative of power station conditions the strain rate will be much lower for much of the component life and begin to accelerate closer to failure. The result will be that it will become more challenging to establish a relationship between strain and strain rate and therefore Ω/κ will be harder to estimate.

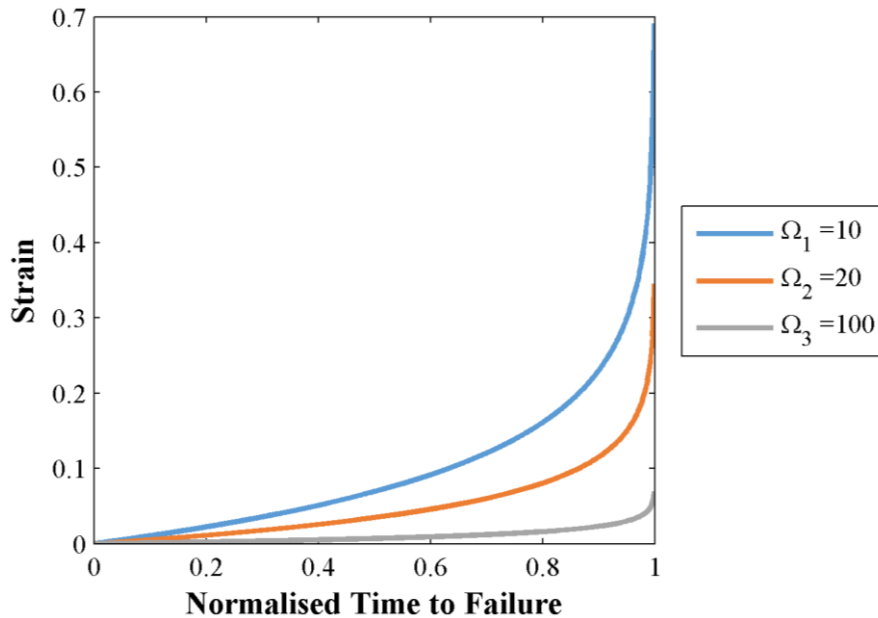


Figure 5.9: Creep strain curves for a range of values of Ω .

Of course, the real challenge for remnant life prediction is dealing with changes in operating conditions; strategic changes in operating pressure, temperature, pipe supports etc.. At each change in operating condition the process of remnant life prediction will have to be restarted. Fortunately, as shown in Figure 5.8, new estimates of the component remnant life can be quickly established regardless of prior history.

5.4 Conclusion

The secondary creep rate of power station components is expected to be of the order of 10^{-8} /hour and it may be of necessary to monitor the component over decades. In order to monitor this strain rate in the unfavourable measurement environment of a power station the stability of the measurement electronics and sensor hardware must be excellent. It likely to be necessary to employ dummy gauges and instrument calibration to provide baseline measurements that can be used to compensate for measurement instability. It is suggested in this chapter that instead of using a dummy gauge two perpendicular gauges may be used; when dividing the two measurements, instability of the sensor and electronics will be cancelled out and a measure of the strain (or aspect) ratio will be preserved. In the case of PD measurements, the Normalised Resistance Ratio serves this purpose.

It is shown that for constant stress state conditions the aspect ratio and rate of change of aspect ratio is an approximately linear function of strain and strain rate. Although without knowledge of the stress state the constant of proportionality is not known, the aspect ratio will still provide a relative change in strain rate. The increase in strain rate from the minimum strain is known to be a symptomatic indicator of creep damage and therefore the rate of change of aspect ratio will still provide valuable information.

The proportionality between inverse true strain rate and remnant life has been concluded from a number of continuum damage approaches. This method offers a means of evaluating the constant of proportionality from strain data collected in-situ by establishing a relationship between strain rate and strain. This process is possible using measurements of aspect ratio alone and hence can be achieved using Normalised Resistance Ratio data. This process has been demonstrated using accelerated uniaxial test data.

Chapter 6

Potential Drop Monitoring of Weldments

6.1 Introduction

Creep failure at welds will often be the life limiting factor for pressurised power station components, offering a site for local damage accumulation. Monitoring the creep state of welds will be of great value to power station management and potential drop monitoring may provide a useful tool. This chapter provides a preliminary study of potential drop monitoring of creep damage at a weldment, investigating some of the challenges associated with interpreting potential drop measurements at an interface between different materials and considers the influence of macroscopic damage. Finally, an accelerated creep experiment is conducted using a cross-weld specimen, demonstrating the promise of potential drop monitoring for welds.

6.1.1 Industrial Background

Weldments in high temperature, high pressure, power station components can be generally categorised as girth or seam welds. Girth welds are those made circumferentially around the pipe and may be used to join lengths of pipe end to end or onto a header. Seam welds are made axially along the length of a component and exist to form components out of plate material. Both types have specific failure characteristics and should be considered separately.

The significant difference between the two welds is of course orientation. In girth welds the cross-weld load is axial, provided predominantly by self-weight, while in seam welds the cross-weld load is circumferential, provided by internal pressure. As the axial stresses are considered to be smaller than the hoop stresses girth welds tend to fail by a ‘leak before break’ mechanism whereas failures in seam welds can be catastrophic (Cerjak & Mayr, 2008; Ellis, 1997).

Concern about the two classes of welds differ in the UK and the US based on a legacy of policy in the use of seam welded components. In the US the seam welded pipes are used to connect the steam header to main steam pipes and also in hot reheat piping (Viswanathan & Stringer, 2000). In the UK however the Central Electricity Generating Board (CEGB) only used seamless pipes for high temperature, high pressure applications and this practice is maintained today (Dean, 2014). EPRI documented 27

incidences of seam weld failure and major cracking by 2003 (EPRI, 2003) but it is known that this number continues to rise (Parker, 2014a). The most well-known are the 1985 Mohave Power Station disaster which caused 6 fatalities and the Monroe catastrophic failure in 1986 (Cerjak & Mayr, 2008; EPRI, 2003); both are shown in Figure 6.1. It is claimed that premature seam weld failures cannot be predicted based on simple life-fraction rule calculations but rather occur due to a unique combination of operating and metallurgical variables (Viswanathan & Stringer, 2000). A combination of the severe and unpredictable nature of potential failure results in the requirement that seam welded components are extensively inspected for signs of damage. Conversely, damage in girth welds has been a matter of great concern in Europe for many years but until recently less so in the US, possibly as a result of the use of different steels and lower operational temperatures (Ellis, 1997). Catastrophic failure of girth welds is not expected (Viswanathan & Stringer, 2000), however, in general the life of a component is limited by the weld (Cerjak & Mayr, 2008; Perrin & Hayhurst, 1996). In both cases there is a clear motive for the adoption of on-load monitoring techniques.

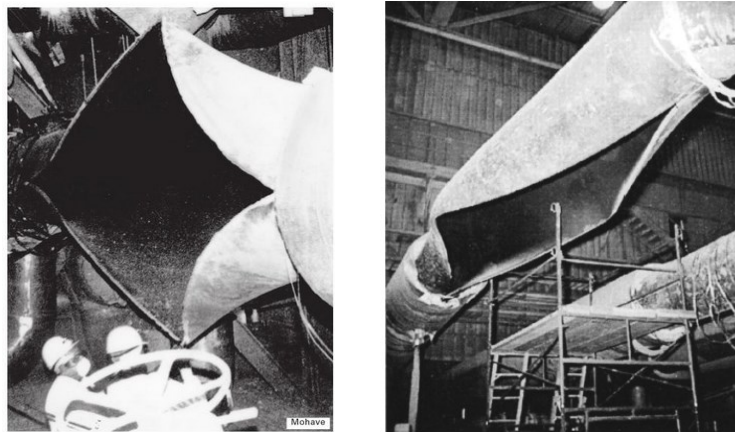


Figure 6.1: Photographs of seam weld failures at (left) the 1985 Mohave power station resulting in six fatalities and ten further injuries (Cerjak & Mayr, 2008) and (right) the 1986 Monroe seam weld failure (Viswanathan & Stringer, 2000).

Cracking in the vicinity of a weld can be classified according to the scheme by Schüller (Schüller et al., 1974) illustrated in Figure 6.2 (a). In seam weld failures a variety of cracking modes, including Type I, Type III and Type IV have been observed. In most cases in hot reheat pipes the crack initiates at the cusp of the weld geometry and propagates along the fusion line, while in main steam lines failures are more likely to occur in the fine grained weld centre line. A range of different failure characteristics and causes have been reported and it has therefore been difficult to define an ‘at risk’ condition. Instead, failures are considered very situational and may be caused by any one of a number of different causes including excess temperature or stress, pre-existing defects, impurity segregation and particularly ‘sharp’ weld cusps. (EPRI, 2003)

Concern around girth weld failure is overwhelmingly associated with Type IV failure (Abson & Rothwell, 2013; Cerjak & Mayr, 2008; Ellis, 1997; Perrin & Hayhurst, 1999; Viswanathan & Stringer, 2000). As mentioned in Chapter 1, high chrome steels are known to be particularly susceptible and the widespread adoption of P91 material means that there is considerable concern in the power industry at present (Abson & Rothwell, 2013; Cerjak & Mayr, 2008; I. A. Shibli & Coleman, 2006; TWI Ltd., 2008). Type IV damage accumulates in the intercritical heat-affected zone (ICHAZ) of a weld, a narrow band of material located at the edge of the HAZ adjacent to the parent material as shown in Figure 6.2 (b). The ICHAZ is rendered creep 'soft' by the prior thermal exposure of the welding process; the 850-900 °C temperature at that location is such that the grain structure is refined and carbides are significantly coarsened (Perrin & Hayhurst, 1999).

The likely depth of crack initiation is an important consideration in implementing a suitable measurement arrangement; sensitivity of the quasi-DC potential drop measurement is limited to the current penetration depth, approximately one electrode separation deep. According to EPRI evaluation guidelines (EPRI, 2003) in most cases the point of initiation in seam welds is the weld cusp of the double-V weld geometry shown in Figure 6.2 c). The crack is reported to propagate first to the inside surface and then to the outside. Although Type IV cracking in girth welds is associated with bending stresses that are higher at the pipe outside surface, crack initiation is believed to initiate sub-surface at the near outer diameter region. Specifically, cracks are expected to initiate at a depth of the first weld bead below the surface weld pass; this is a result of the surface temper bead and the tendency for cavitation to occur on the more radially orientated interface (S. Brett, 1994; Ellis, 1997). It is understood that the approximate depth of the second weld bead is ~2-10 mm depending on the preparation of the weld cap (Yaghi et al., 2011); indeed it is common for the surface temper beads to be ground off so that damage becomes surface breaking and evident in surface inspection techniques (Ellis, 1997). Potential drop monitoring is therefore expected to be well suited to detecting Type IV damage in girth welds as the crack is expected to occur within its field of sensitivity while it may remain undetected by conventional surface inspection methods.

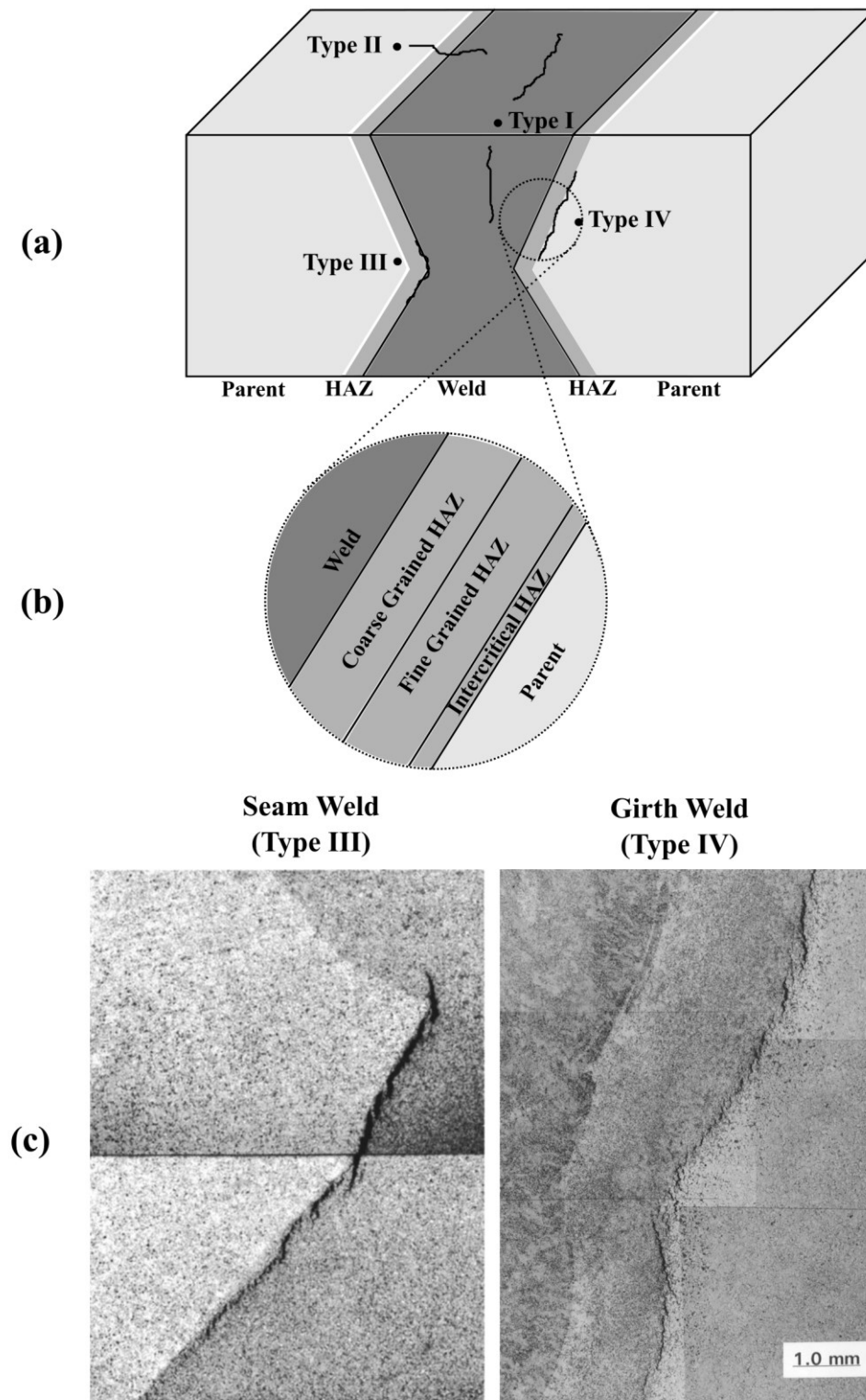


Figure 6.2: (a) The weld damage classification scheme as suggest by Schüller. (b) The macrostructure of the HAZ showing the position of the Intercritical HAZ (ICHAZ) where Type IV failure occurs. (c) Examples of (left) typical seam weld failure initiating at the cusp of a double-V joint (Viswanathan, 2000) and (right) Type IV failure which is a common issue in girth welds (Sposito, Ward, et al., 2010).

6.1.2 PD Measurements at a Weld

Potential drop measurements may be applicable to both seam and girth welds and much of the underlying theory and practical considerations will be common to both situations. However, for the purpose of this thesis it will be assumed that we are examining girth welds. Seam welds exist over long lengths and the location of crack initiation is unpredictable (EPRI, 2003) suggesting that it will be necessary to install very many sensors to ensure that damage is captured. Girth weld failure is understood to occur as a result of axial bending loads and therefore likely initiation sites can be more accurately identified, lending itself to the point inspection technique previously described.

Potential drop measurements of creep damage in the vicinity of a weld differ in nature to measurements of volumetric creep. In addition to the influence of strain and bulk resistivity changes there is also expected to be an additional contribution from localised damage accumulation and cracking; the macroscopic impediment to current flow will clearly influence the resistance. It is therefore believed that a potential drop method may be well suited to monitoring the accumulation and growth of creep damage at a weld. Additionally, the creep strain behaviour of the different weld domains is expected to be quite distinct with strain particularly accumulating in the ICHAZ (Parker & Parsons, 1995). This has led to attempts to measure strain very locally at welds as an indicator of creep state (Cerjak & Mayr, 2008; Maharaj et al., 2009).

Unfortunately, contrary to the additional promise of detection of macro-damage, comes the considerable additional complexity of taking potential drop measurements in the vicinity of the weld. The different domains of the weld will be composed of different materials of different electrical properties; potential drop measurements in the vicinity of a weld interface will be influenced by the conductivity of both domains; this may prove to be problematic and limit the sensitivity.

The problem of potential drop monitoring at the interface of different materials will be explored analytically and the implications to monitoring explored. Finite element simulations will then be shown as a means to understand the likely influence of cracking on the potential drop measurement. Finally, an accelerated creep test will be presented as a demonstration of the promise for potential drop measurements of creep damage at a weld.

6.2 Potential Drop Monitoring at the Interface of Material Domains

Prajapati et.al. (Prajapati et al., 2012) have explored the issue of taking measurements in the vicinity of a weld. An analytical solution was presented for the resistance measured using a square electrode configuration on a ‘thick’ component, the standard measurement adopted in this thesis. The solution is

divided into three separate conditions depending on the sensor position relative to the weld as indicated by the superscripts ‘Side 1’ (all electrodes on material 1), ‘straddle’ (half on material 1 and half on 2) and ‘Side 2’ (all electrodes on 2). There will be a resistance taken ‘parallel’ and ‘normal’ to the weld seam making 6 possible resistances to be calculated in total. The distance from the centre line of the square of electrodes to the weld interface is denoted as h and the electrode separation will continue to be denoted as a , σ_1 and σ_2 are the electrical conductivities of the two material domains; terminology is shown in Figure 6.3 for clarity.

1) All electrodes are placed on the first side of the weld interface: $h/a < -0.5$

$$R_{Parallel}^{Side\ 1} = \frac{1}{\pi\sigma_1 a} \left[\left(1 - \frac{1}{\sqrt{2}}\right) + \frac{\sigma_1 - \sigma_2}{\sigma_1 + \sigma_2} \left(-\frac{1}{\frac{2h}{a}} - \frac{1}{\sqrt{1 + \left(\frac{2h}{a}\right)^2}} \right) \right] \quad (6.1)$$

$$R_{Normal}^{Side\ 1} = \frac{1}{2\pi\sigma_1 a} \left[2 \left(1 - \frac{1}{\sqrt{2}}\right) \dots \right. \\ \left. + \frac{\sigma_1 - \sigma_2}{\sigma_1 + \sigma_2} \left(\frac{1}{\sqrt{1 + \left(1 + \frac{2h}{a}\right)^2}} + \frac{1}{\sqrt{1 + \left(1 - \frac{2h}{a}\right)^2}} - \frac{1}{\sqrt{1 + \left(\frac{2h}{a}\right)^2}} \right) \right] \quad (6.2)$$

2) Two electrodes are one side of the weld interface and the other two are on the second side: $-0.5 < h/a < 0.5$

$$R_{Parallel}^{Straddle} = \frac{2}{\pi(\sigma_1 + \sigma_2)a} \left(1 - \frac{1}{\sqrt{2}}\right) \quad (6.3)$$

$$R_{Normal}^{Straddle} = \frac{1}{2\pi(\sigma_1 + \sigma_2)a} \left\{ 4 - \frac{4}{\sqrt{2}} \dots \right. \\ \left. - (\sigma_1 + \sigma_2) \left[\frac{1}{\sigma_1} \left(1 - \frac{1}{\sqrt{1 + \left(1 + \frac{2h}{a}\right)^2}}\right) - \frac{1}{\sigma_2} \left(1 - \frac{1}{\sqrt{1 + \left(1 - \frac{2h}{a}\right)^2}}\right) \right] \right\} \quad (6.4)$$

3) All electrodes are placed on the second side of the weld interface: $h/a > 0.5$

$$R_{Parallel}^{Side\ 2} = \frac{1}{\pi\sigma_2 a} \left[\left(1 - \frac{1}{\sqrt{2}}\right) + \frac{\sigma_1 - \sigma_2}{\sigma_1 + \sigma_2} \left(\frac{1}{\frac{2h}{a}} - \frac{1}{\sqrt{1 + \left(\frac{2h}{a}\right)^2}} \right) \right] \quad (6.5)$$

$$R_{Normal}^{Side\ 2} = \frac{1}{2\pi\sigma_2 a} \left[2 \left(1 - \frac{1}{\sqrt{2}} \right) \dots \right. \\ \left. + \frac{\sigma_2 - \sigma_1}{\sigma_2 + \sigma_1} \left(\frac{1}{\sqrt{1 + \left(1 + \frac{2h}{a} \right)^2}} + \frac{1}{\sqrt{1 + \left(1 - \frac{2h}{a} \right)^2}} - \frac{1}{\sqrt{1 + \left(\frac{2h}{a} \right)^2}} \right) \right] \quad (6.6)$$

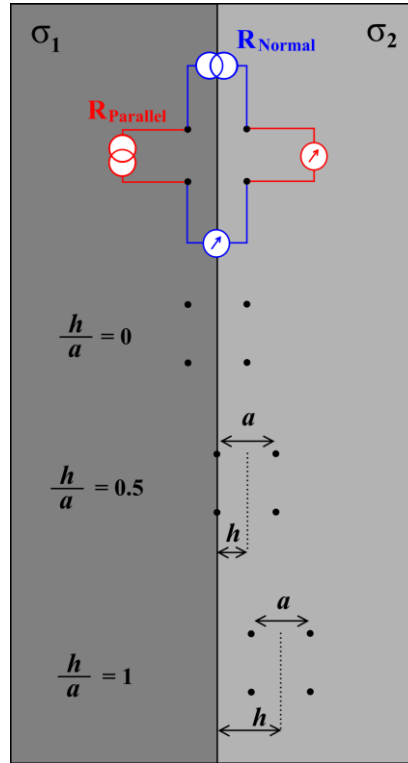


Figure 6.3: Schematic showing the notation used in describing square electrode configuration potential drop measurements in the vicinity of an interface between two materials of different conductivities. In the case of a weld the two materials will be the weld and parent material of conductivity σ_1 and σ_2 respectively.

The outcome of Equations 6.1 - 6.6 are shown in Figure 6.4 for a range of possible h/a values and conductivity ratios. Following Prajapati (Prajapati et al., 2012) and for convenience of presentation resistances are normalised to a reference resistance, a theoretical value that would result from a measurement of material that had the conductivity of the arithmetic mean of the two domains $\sigma_{ref} = (\sigma_1 + \sigma_2)/2$;

$$R_{ref} = \frac{1}{\pi\sigma_{ref}a} \left(1 - \frac{1}{\sqrt{2}} \right) \quad (6.7)$$

The Resistance Ratio is simply the ratio of the normal and parallel resistances.

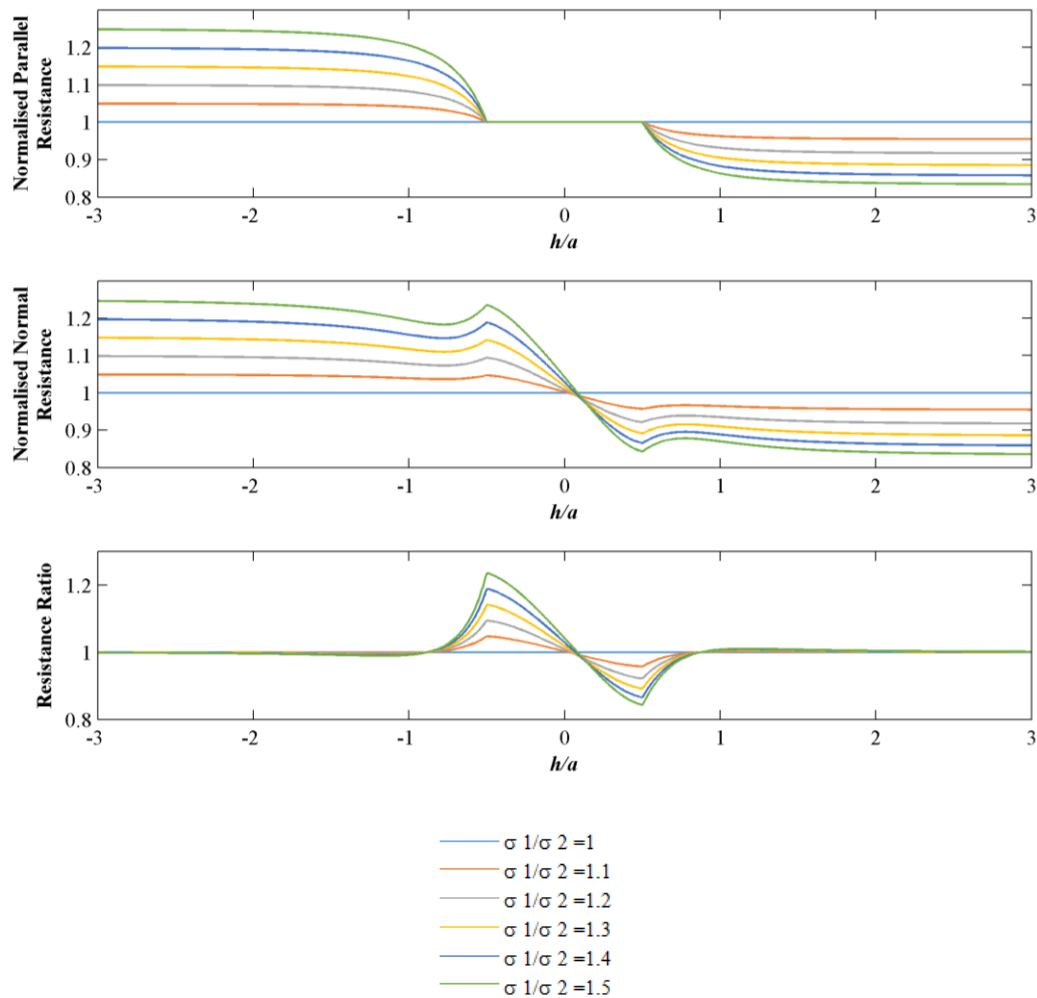


Figure 6.4: Resistances calculated parallel and normal to the weld/parent interface according to the notation shown in Figure 6.3. Resistances are normalised to a theoretical reference resistance as described by Equation 6.7. The resistance ratio is simply the normal resistance divided by the parallel. After (Prajapati *et al.*, 2012).

The Resistance Ratio in the vicinity of the weld interface is described in terms of an ‘apparent anisotropy’ by Prajapati *et al.* (Prajapati *et al.*, 2012); the differing sensitivity of the normal and parallel resistance readings to the interface produces a discrepancy in the orthogonal resistances which may be interpreted as anisotropy. The apparent anisotropy is a function of location, h/a , and conductivity ratio, σ_1/σ_2 . In an inspection capacity, where electrodes are applied to the component by spring loaded pins, the apparent anisotropy may mask the presence of damage. This chapter will continue the work of Prajapati *et al.*, extending the analysis to a monitoring capacity. The electrodes are permanently attached to the component, and so h/a is nominally fixed, the apparent anisotropy can be normalised out and only *changes* in conductivity ratio will act to limit sensitivity.

Consider the case where one pair of electrodes is installed on the weld interface ($h/a=-0.5$), the point of maximum apparent anisotropy. Providing the ratio of the conductivity of the two materials stays the same then the Normalised Resistance Ratio will not deviate. However, if for example, over time the

conductivity of one material changes relative to the other by 50% then the Normalised Resistance Ratio will increase by over 20% as shown in Figure 6.4, masking the influence of any damage that may be occurring. The effect of apparent anisotropy expected in a monitoring context is therefore an important consideration that will limit the sensitivity of a measurement in the vicinity of a weld.

From Figure 6.4 there are clearly some positions that are more sensitive to changes in conductivity ratio than others. A sensor installed perfectly straddling the weld face ($h/a = 0$) is seen to have very little sensitivity to changes in conductivity ratio. As previously mentioned it is evident that the largest sensitivity to changes in conductivity ratio is at position $h/a = \pm 0.5$. From Equations 6.3 and 6.4 the Normalised Resistance Ratio can be calculated for this condition, here assuming the absence of strain.

$$NRR_{\frac{h}{a}=-0.5} = \frac{4 - 2\sqrt{2} + \left(\frac{\sigma_1}{\sigma_2} - 1\right) \left(1 - \frac{1}{\sqrt{5}}\right)}{4 - 2\sqrt{2} + \left(\frac{\sigma_{10}}{\sigma_{20}} - 1\right) \left(1 - \frac{1}{\sqrt{5}}\right)} \quad (6.8)$$

For consistency with the rest of the thesis this can be written instead in terms of resistivity,

$$NRR_{\frac{h}{a}=-0.5} = \frac{4 - 2\sqrt{2} + \left(\frac{\rho_2}{\rho_1} - 1\right) \left(1 - \frac{1}{\sqrt{5}}\right)}{4 - 2\sqrt{2} + \left(\frac{\rho_{20}}{\rho_{10}} - 1\right) \left(1 - \frac{1}{\sqrt{5}}\right)} \quad (6.9)$$

As it is the change in conductivity ratio that is of interest, it is suitable to rewrite,

$$\frac{\rho_2}{\rho_1} = \frac{\rho_{20} \left(1 + \frac{\Delta\rho_2}{\rho_{20}}\right)}{\rho_{10} \left(1 + \frac{\Delta\rho_1}{\rho_{10}}\right)} = \frac{\rho_{20}}{\rho_{10}} (1 + \delta) \quad (6.10)$$

where δ is a perturbation to the initial resistivity ratio $\frac{\rho_{20}}{\rho_{10}}$. Therefore,

$$NRR_{\frac{h}{a}=-0.5} = \frac{4 - 2\sqrt{2} + \left(\frac{\rho_{20}}{\rho_{10}} (1 + \delta) - 1\right) \left(1 - \frac{1}{\sqrt{5}}\right)}{4 - 2\sqrt{2} + \left(\frac{\rho_{20}}{\rho_{10}} - 1\right) \left(1 - \frac{1}{\sqrt{5}}\right)} \quad (6.11)$$

Equation 6.11 provides a basis for assessing the sensitivity of the Normalised Resistance Ratio to changes in resistivity ratio. Two primary sources of change in resistivity ratio will be considered; reversible temperature dependency and thermal ageing.

6.2.1 Typical Weld/Parent Combinations

Typical parent/weld filler material combinations exist to provide optimal mechanical properties for a weld. For high chrome materials, including P22, P91 and P92 (see Table 1.1 for compositions) this is achieved by creating a weld deposit that is similar in chemical composition and mechanical properties to the base material (Coleman & Newell, 2007; Packard & Morrett, 2008; Tanner et al., 2013). Clearly, matching the chemical compositions of the weld and parent material will act to minimise differences in

conductivity. An exception is 0.5Cr-0.5Mo-0.25V steel common in the UK which is typically welded with 2.25Cr-1Mo filler material, similar in composition to P22 material (BOC, 2007; Tanner et al., 2013). It is therefore expected that welds in 0.5Cr-0.5Mo-0.25V component will have particularly contrasting conductivity ratios and will be used as an example of a particularly problematic case.

A virgin girth weld was provided by E.ON for use in testing. The weld consists of 0.5Cr-0.5Mo-0.25V parent material welded with 2.25Cr-1Mo weld filler material. The pipe outer diameter was 320 mm, the inner diameter was 210 mm and contained a ‘single- J’ configuration weld. The experimental results in this chapter have all been obtained using this component.

6.2.2 Reversible Temperature Dependency

A sample was cut from the aforementioned weld component and a potential drop sensor was installed on the weld material and another in the parent material. The component was heated to 620 °C and allowed to cool while readings were taken. The resistances are shown in Figure 6.5. As expected from Chapter 3, the higher alloy content of the filler material results in a higher resistivity. It is also worth noting that the absolute temperature dependencies of the two materials are approximately equal (again, in agreement with Matthiessens’ Rule) and approximately linear over a limited temperature range. The net result is that the relative conductivity of the two materials converge and the conductivity ratio moves increasingly towards unity. The apparent anisotropy that results is therefore a function of temperature and will act to mask any change in the Normalised Resistance Ratio as a result of creep damage.

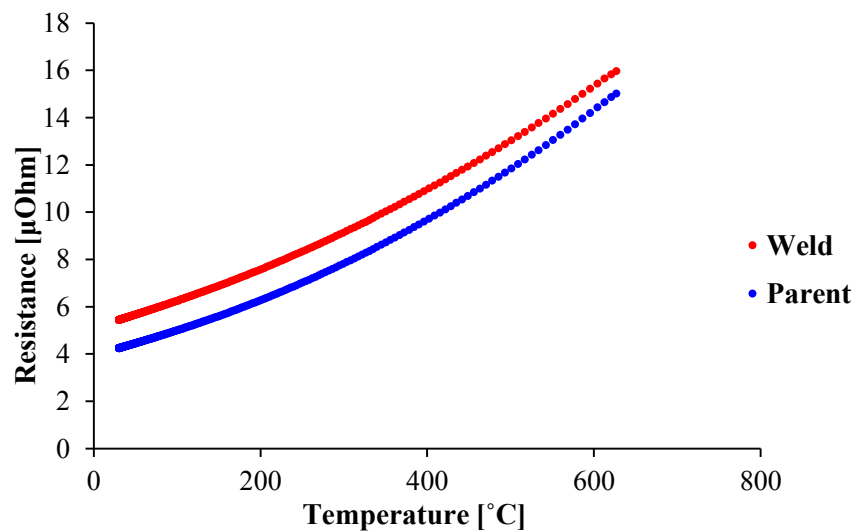


Figure 6.5: Resistance for the weld (2.25Cr-1Mo filler) and parent (0.5Cr-0.5Mo-0.25V) material. Each reading is the average of the two orthogonal resistances from a given sensor. It is worth noting that although the electrodes were nominally separated by 4 mm some systematic error from the electrode placement will be present – the temperature dependency will however be unaffected. Expected room temperature resistances based on experience are 4.27 μΩ and 5.50 μΩ for a 4 mm separation in the parent and weld material respectively.

Figure 6.5 also illustrates the benefit of high temperature monitoring, as the conductivity ratio is reduced at high temperature. From Equation 6.11 it can be shown that a reduction in the initial resistivity ratio will reduce the sensitivity of apparent anisotropy to perturbations in resistivity.

Additionally, recall that the reversible temperature dependency can be approximated using a linear approximation described by the resistivity temperature coefficient, α , which describes the fractional resistivity change,

$$\rho_T = \rho_{T=T_0} \left(1 + \alpha_{T=T_0} (T - T_0) \right) \quad (6.12)$$

$$\alpha_{T=T_0} \equiv \frac{1}{\rho_{T=T_0}} \left(\frac{\Delta\rho}{\Delta T} \right)_{T=T_0} \quad (6.13)$$

Equation 6.13 shows explicitly the benefit of monitoring at a high temperature or more specifically at a higher normalisation resistivity. Normalising at a larger resistivity will reduce the fractional change in resistivity for a given temperature change. Figure 6.6 shows the resistances of Figure 6.5 normalised to their 550 °C values. Recall from Equation 6.9 that it is the term,

$$\frac{\left(1 + \frac{\Delta\rho_2}{\rho_{20}} \right)}{\left(1 + \frac{\Delta\rho_1}{\rho_{10}} \right)} \quad (6.14)$$

that produces the spurious change in Normalised Resistance Ratio. Using Equation 6.12 this becomes,

$$\frac{1 + \alpha_{weld, T_0=550} (T - 550)}{1 + \alpha_{parent, T_0=550} (T - 550)} \quad (6.15)$$

From the data of Figure 6.6 the temperature coefficients are calculated by least squares regression to be $\alpha_{parent, T_0=550} = 0.00191 / ^\circ\text{C}$ and $\alpha_{weld, T_0=550} = 0.00164 / ^\circ\text{C}$. This equates to a modest uncertainty in the Normalised Resistance Ratio of 0.0013 for a 10 °C change.

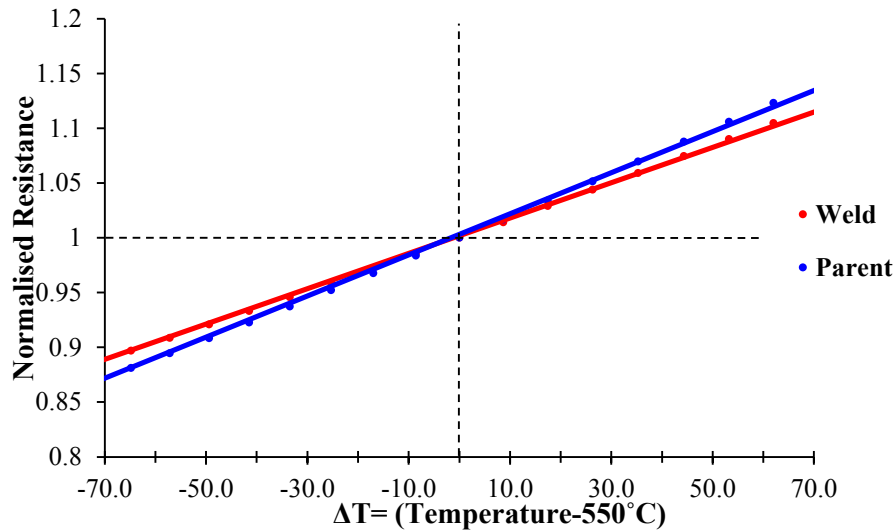


Figure 6.6: Resistances measured in weld and parent material normalised to their values at 550 °C. Despite the similar temperature dependency of the two materials the higher resistivity of the weld material results in a lower temperature coefficient. At higher temperatures the relative resistivities become more similar and the temperature coefficients therefore become more similar.

6.2.3 Irreversible Thermally Activated Resistivity Change

It was concluded from Chapter 3 that an important cause of resistivity change is the result of solute depletion on precipitate formation. It was explained and demonstrated that the resistivity change associated with changing alloy concentration is expected to be additive in nature and temperature independent in accordance to Matthiessen's Rule; this provides further support for the benefit of high temperature measurements. As the resistivity is considerably larger at power station operational temperatures then the fractional change resulting from a given resistivity decrease will be considerably smaller. From Figure 3.6 of Chapter 3 it was shown experimentally that virgin 2.25Cr-1Mo material may show up to 2% resistivity change when aged at 630 °C. To put an expected bound to the possible effect of thermal ageing, if the resistivity of one or other of the weld or parent material was to reduce by 3% then the maximum expected change to the Normalised Resistance Ratio would be ~1.5%. This is expected to be a gross overestimation; as discussed in Chapter 3 the influence of solute depletion is expected to occur at an exponentially decreasing rate and may be normalised out after a relatively short time. Further, following the production of a weld it is necessary to undertake a post-weld heat treatment (PWHT). The PWHT serves to relieve residual stresses and temper the material, this requires heat treatment at 650 °C+ and will cause the desired precipitation of carbides that may have been dissolved during welding (Bailey, 1994; Cerjak & Mayr, 2008). This suggests that the previously observed rapid decrease in solute concentration (and therefore resistivity) may already have occurred prior to service and a more stable state be present. Finally, the effect is significantly reduced if the sensor is not installed at $h/a \pm 0.5$. The effect of long-term ageing on the Normalised Resistance Ratio is therefore expected to be small.

6.2.4 Summary of Potential Drop Monitoring at the Interface of Material Domains

The apparent anisotropy caused by the differing sensitivity of the normal and parallel resistance readings in the vicinity of a weld is likely to have an overwhelming effect over the influence of creep damage if measurements are taken in an inspection type manner; small measurement position uncertainty over repeat measurements will result in substantial uncertainty. However, permanently installing electrodes allows the apparent anisotropy to be normalised and only changes in the conductivity of the weld domains will result in uncertainty.

Operation at high temperature has the fortunate benefit of stabilising the relative conductivities of the weld and parent material, a result of Matthiessen's Rule. The temperature sensitivity of the conductivity ratio will reduce as the resistivity of both materials will be greatly increased but the temperature dependency will not; the result is that a given temperature change will reduce the fractional resistivity change of both materials. The effect of temperature fluctuations on the Normalised Resistance Ratio becomes negligibly small over a limited range; further, assuming that the temperature fluctuations are symmetric about a set point then the remnant effect is expected to be suppressed with temporal averaging.

Conductivity changes associated with creep exposure were investigated in Chapter 3. It was concluded that the dominant mechanism responsible for conductivity change is expected to be solute depletion and may cause, conservatively, up to a 1.5% change in Normalised Resistance Ratio. Fortunately this effect becomes exponentially smaller with time and after ~2 years in service or after suitable post weld heat treatment (PWHT) it is unlikely to be problematic.

Taking measurements at high temperature therefore alleviates many of the problems associated with potential drop measurements in the vicinity of different material domains. Following the initial result of solute depletion, the conductivity ratio of the domains should remain stable, enabling good sensitivity to strain and cracking.

6.3 Influence of Cracking on Potential Drop Measurements

The influence of cracking on DC or quasi-DC potential drop measurements acts by reduction of available area for current flow and the resulting distortion of the potential field. It will be a function of crack size, geometry, orientation and position and therefore inversion of crack geometry is not trivial. Two examples will be presented in order to illustrate the likely influence of cracking on the potential drop measurement and the importance of crack position on sensitivity. The results will inform future optimisation for on-site applications.

Figure 6.7 shows schematics of two models studied using Comsol. A conducting cube of 80 mm x 80 mm x 80 mm was created with a 5 mm square electrode configuration on the centre of one face, ensuring the measurements were negligibly affected by the cube edges and so the component would behave as if it were infinitely large. Point current sources and point potential probes were used to replicate a DC potential drop measurement. The two orthogonal resistances were simulated while a crack of increasing size was imposed on the model, as illustrated. The crack extends through the length of the conducting block and intersects the centre line of the electrodes; it is acknowledged that this may not be realistic but allows an investigation into two cases of crack growth. The distinction between the two models is that in Simulation 1 the crack initiates from the top surface and grows down through the component, while in Simulation 2 the crack initiates at the bottom surface and grows towards the electrodes on the top surface. Resistance values are normalised to their values with no crack present and in (1) the crack lengths, d_a , were normalised to the electrode separation, a , and in (2) the remaining intact length d_b (component thickness - crack length) was normalised to the electrode separation.

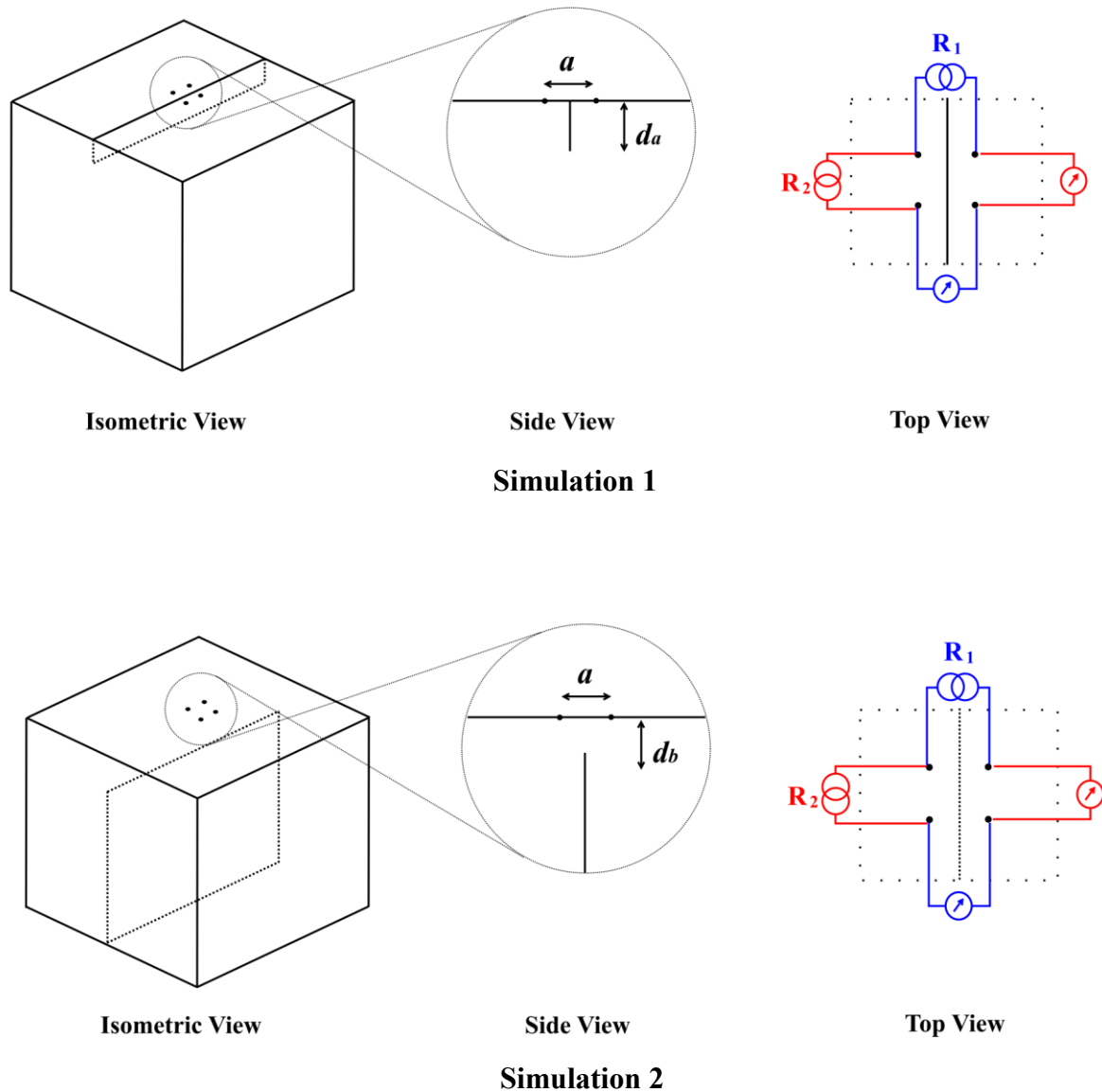
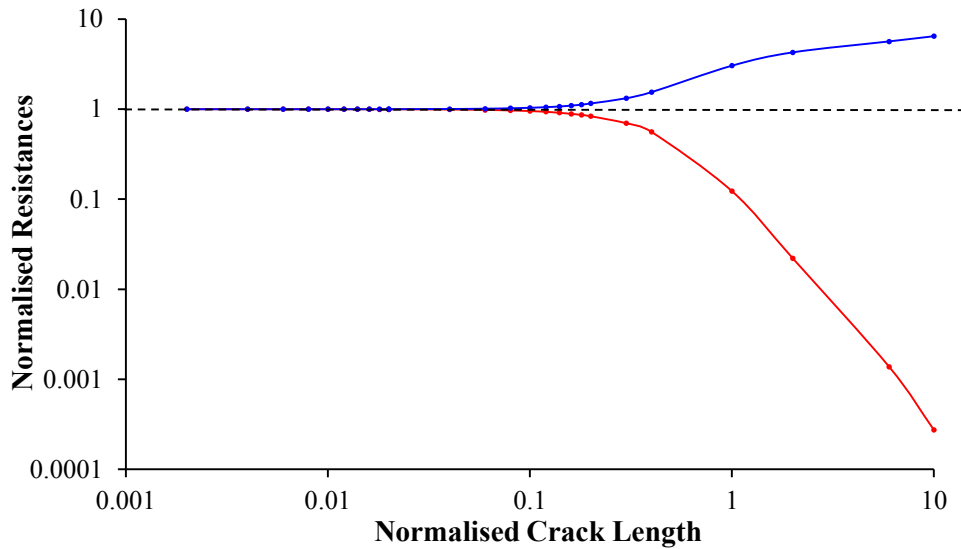


Figure 6.7: Schematics showing illustrations of the two models simulated. A 80 mm x 80 mm x 80 mm conducting block with a sensor of 5 mm electrode separation placed on the top surface. In both cases the crack extends across the entire width of the specimen. In Simulation 1 the crack initiates on the top surface and propagates down through the specimen. In Simulation 2 the crack initiates at the bottom of the specimen and propagates towards the top surface of the component where the sensor is placed. Resistances are described with subscript 1 and 2 indicating the orientation with respect to the crack as shown.

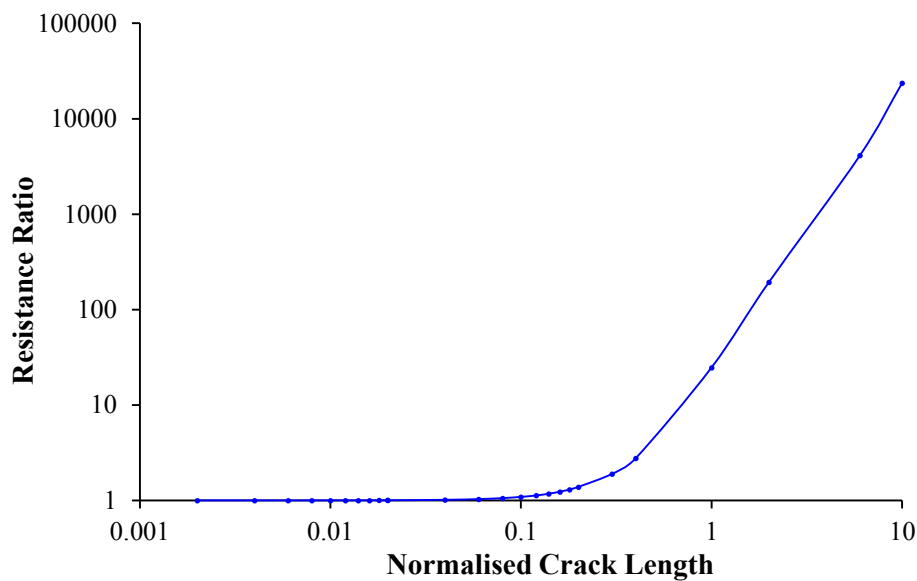
6.3.1 Simulation 1

Figure 6.8 shows the results from Simulation 1, the crack growing from the top surface. Initially it can be seen that there is very little sensitivity to crack growth until the crack size reaches approximately one tenth of the electrode separation with a maximum sensitivity when the crack length is approximately half the length scale of the electrode separation. The resistances taken orthogonal to the crack (in blue) will increase with crack length as the current is forced around the crack. In the parallel direction

however the apparent resistance will decrease as the increasing crack depth separates the potential measuring electrodes from the current path, the potential difference and therefore the inferred transfer resistance must then decrease.



(a)



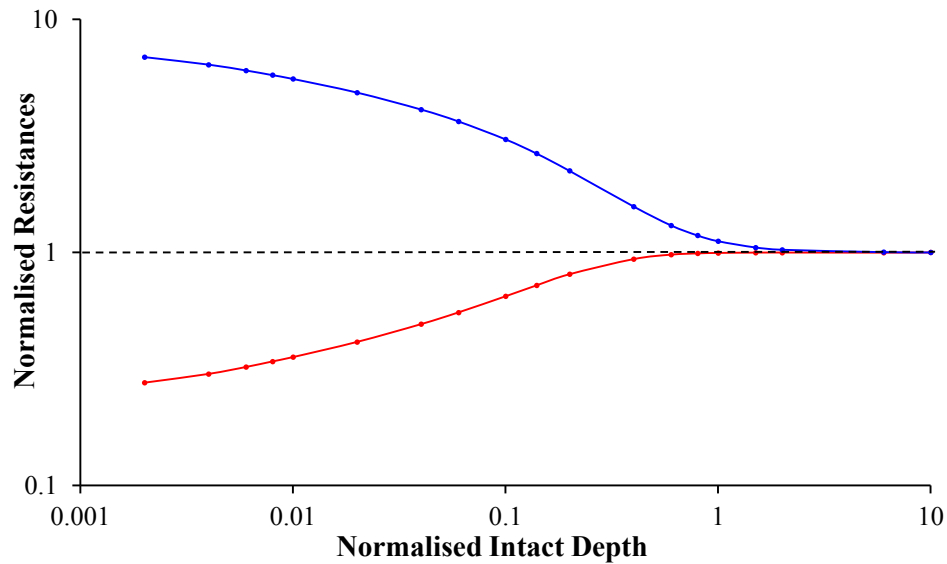
(b)

Figure 6.8: Results of Simulation 1: (a) Resistances normal and parallel to the weld/parent interface with colours according to Figure 6.7. (b) The ratio of the normal and parallel resistances. The normalised crack length is the depth of the crack divided by the electrode separation.

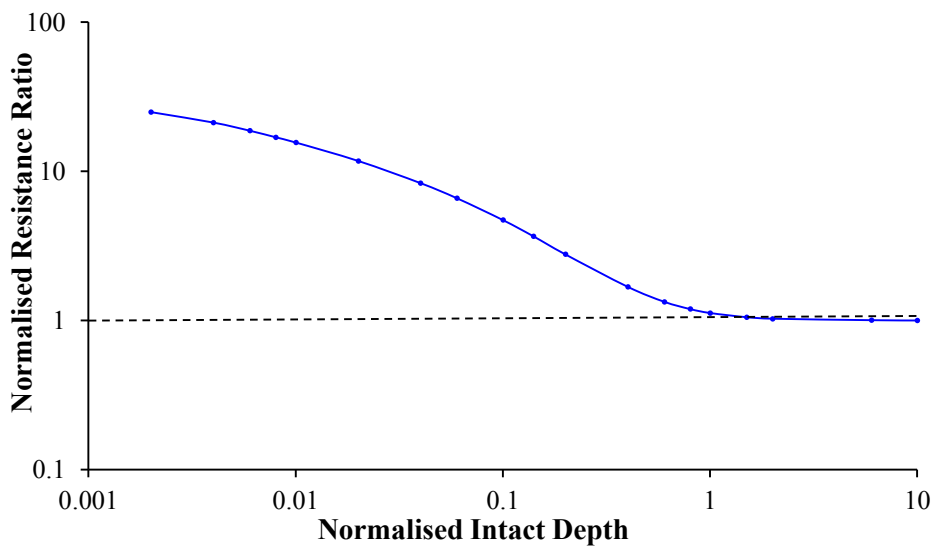
6.3.2 Simulation 2

In Simulation 2 the crack is growing from the bottom of the component and the intact remaining depth normalised to the electrode separation is plotted. Figure 6.9 shows that sensitivity to changes in intact depth are diminishingly small at values greater than 1; as the current penetration depth is limited to

approximately the electrode separation the current will not interact with a crack deeper than this. As the crack grows the resistance measured orthogonal to the crack must asymptote to infinity as the remaining available area decreases, eventually there will be no available cross section for current to pass. Similarly, the apparent resistance measured parallel to the crack will asymptote to zero as the injecting and sensing electrodes become increasingly isolated from each other.



(a)



(b)

Figure 6.9: Results of Simulation 2: (a) Resistances normal and parallel to the weld/parent interface with colours according to Figure 6.7. (b) The ratio of the normal and parallel resistances. The normalised intact depth is the remaining depth below the surface before the crack tip.

6.3.3 Summary

In both cases of crack propagation the contrasting influence on orthogonal resistances acts to amplify the sensitivity of the resistance ratio. With the previously discussed exception of the slight influence of changing conductivities of different material domains of a weld, the resistance ratio is nominally temperature independent and therefore may provide a robust indicator of crack growth. Clearly the magnitude of resistance ratio change caused by a crack infringing on even a fraction of the current penetration depth will be apparent above the sensitivity floor provided by the presence of the weld interface suggesting good sensitivity.

These simulations present the compromise required in optimising the application of potential drop measurements for monitoring macro-defects. A larger electrode separation will increase the penetration depth and therefore the depth at which cracks may be detected. Conversely, the larger the electrode separation the smaller the defects will be relative to the measurement geometry and so sensitivity is decreased.

The two simple models are used to broadly illustrate the sensitivity of the potential drop method to macroscopic damage. In reality the cracks will grow laterally as well as through the depth of the component and will not necessarily occur along the centre line of a sensor. A more in depth study of the influence of crack growth is to be completed.

6.4 Cross-weld Uniaxial Creep Test

An accelerated creep test was conducted in order to demonstrate the use of the potential drop technique for monitoring creep damage. A cross-weld uniaxial creep specimen was manufactured from the previously described 0.5Cr-0.5Mo-0.25V component with 2.25Cr-1Mo weld material. The specimen was the same geometry as the uniaxial creep tests detailed in Section 4.5.2; 24 mm x 10 mm cross section and gauge length 40 mm.

In order to identify the different domains, one surface of the cross-weld specimen was polished and a Vickers Hardness test was conducted along the length of the specimen; it was then etched to reveal microscopic features. The results of both procedures are combined in Figure 6.10. The macrograph reveals the weld parent interface and clearly shows the extent of the HAZ; also visible are the Vickers Hardness indentations. The Vickers hardness results are superimposed on to the image with a scale matching the macrographs and so values are aligned with the indentations. As expected the weld material is harder than the parent material, hardness values reach a peak in the coarse grained HAZ and reduces moving through the HAZ. It can be assumed therefore that the ICHAZ is approximately 3.5 mm from the weld face.

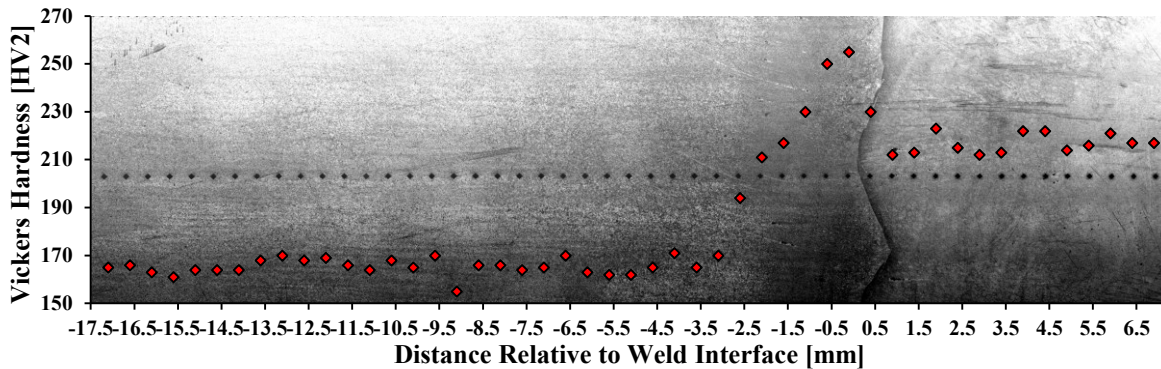


Figure 6.10: Vickers Hardness against distance along specimen. In the background a micrograph of the etched material is shown with a scale matching the x-axis of the graph. The indentations from the Vickers Hardness can be seen aligned to their respective data points. The HAZ can be seen to extend from ~ -3.5 mm up to the weld face.

An array of potential drop sensors was used in order to compare the creep behaviour in the different domains and help identify localised accumulation of damage. It was decided to centre the potential drop array approximately around the ICHAZ as shown in Figure 6.11. A 9-element array of 5 mm electrode separation was used with 100 mA inspection current. The sample was crept at 625 °C and 80 MPa using a lever arm creep machine with furnace. Thermocouples were installed along the gauge length and the temperature distribution was measured to be ± 1 °C, however the temperature control appeared to exhibit approximately 1 °C fluctuations with a period of ~ 5 hours which contributed to the minimum sensitivity of this experiment. Figure 6.11 (b) shows a schematic of the sample, the relative positions of the different weld domains and a legend relating to Figure 6.12 and Figure 6.13.

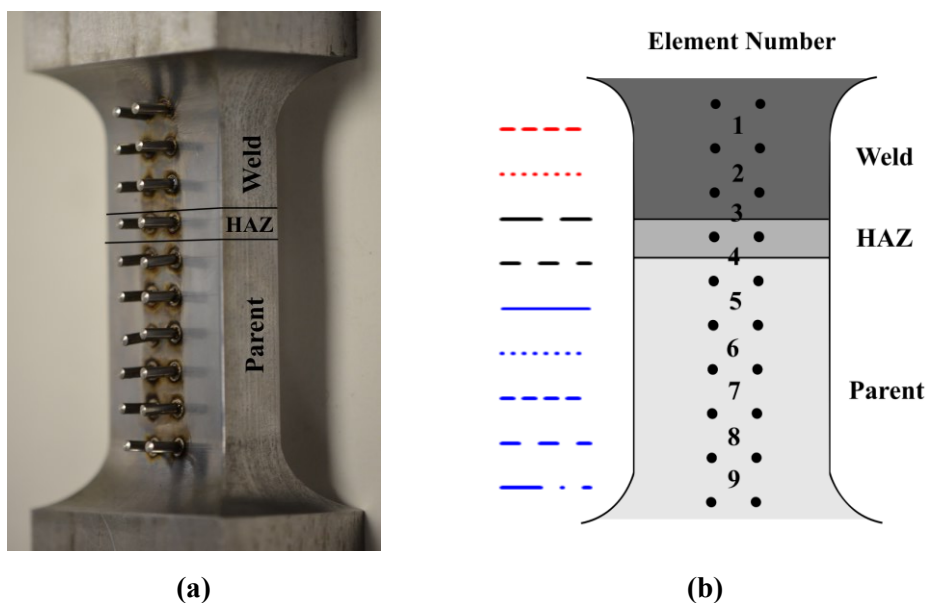


Figure 6.11: (a) Photograph of cross-weld specimen with 9-element potential drop array and approximate locations of weld domains marked. (b) Schematic of the cross-weld sample showing potential drop array, weld domains and the legend for the graphs in Figure 6.12 and Figure 6.13.

Figure 6.12 shows the Normalised Resistance Ratio over time for the experiment. Recall that due to the combined effect of strain and cracking in this case an inversion is not straightforward and so will not be attempted. Instead, it is intended that the Normalised Resistance Ratio and rate of change of Normalised Resistance Ratio will provide a compound indicator of creep state. Firstly, on loading it can be seen that there is initially unusual behaviour of the array elements in the vicinity of the weld; elements 3 and 4. This is believed to be the influence of microstructural evolution changing the apparent anisotropy, as discussed in Section 6.2.3, and the result of slight changes in geometry moving the h/a values. For much of the remainder of the experiment resistance changes are expected to be overwhelmingly attributed to strain accumulation. Although there will be different strain behaviour in the different material domains, it is important to recall that there will also be a ‘background’ strain distribution as evident in the volumetric creep tests on samples of the same geometry in Chapter 4. The key feature of Figure 6.12 is the rapid increase in the rate of change of Normalised Resistance Ratio in the vicinity of the weld interface approaching failure. It was discussed throughout Chapter 5 that the increase in strain rate is a good indicator of proximity to failure. Likewise, clearly the rapid and substantial increase in resistance due to the presence of a crack will provide useful information on the proximity to failure.

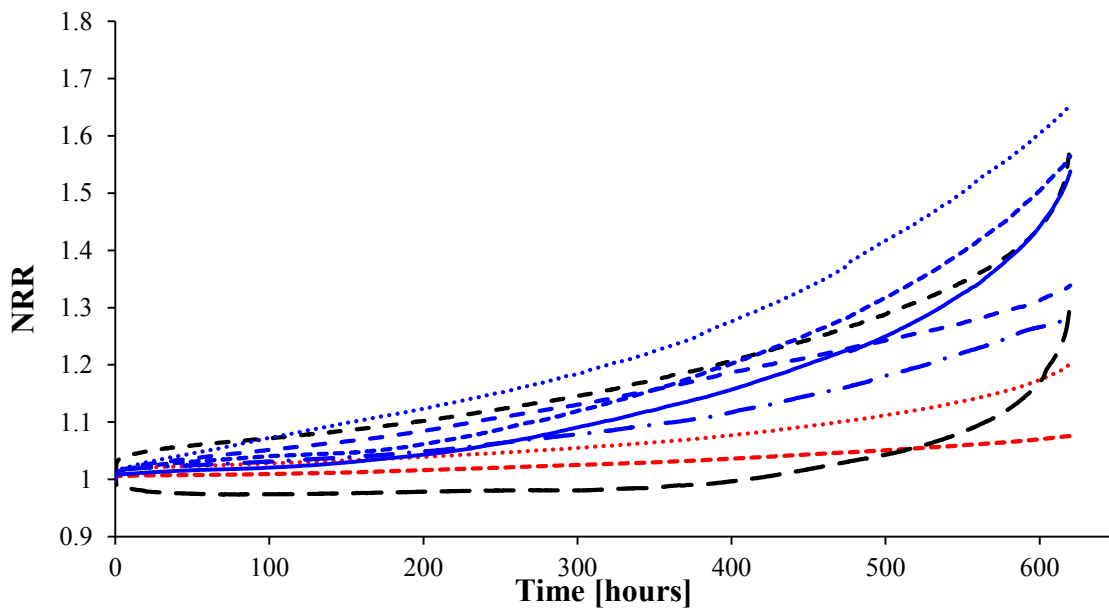


Figure 6.12: Normalised Resistance Ratio against time for cross-weld creep specimen. Normalisation was made immediately prior to loading. Legend according to Figure 6.11; blue measurements are of parent material, red are weld material and black include HAZ.

To illustrate this more clearly Figure 6.13 shows the rate of change of Normalised Resistance Ratio against time. The dashes indicating the element location have been removed as it was not possible or necessary to display them clearly. It is shown however that the measurements in the vicinity of the weld interface show a very dramatic increase towards failure. The test was aborted just before failure and indeed a macro-crack was clearly evident in the vicinity of the HAZ, as shown in Figure 6.14.

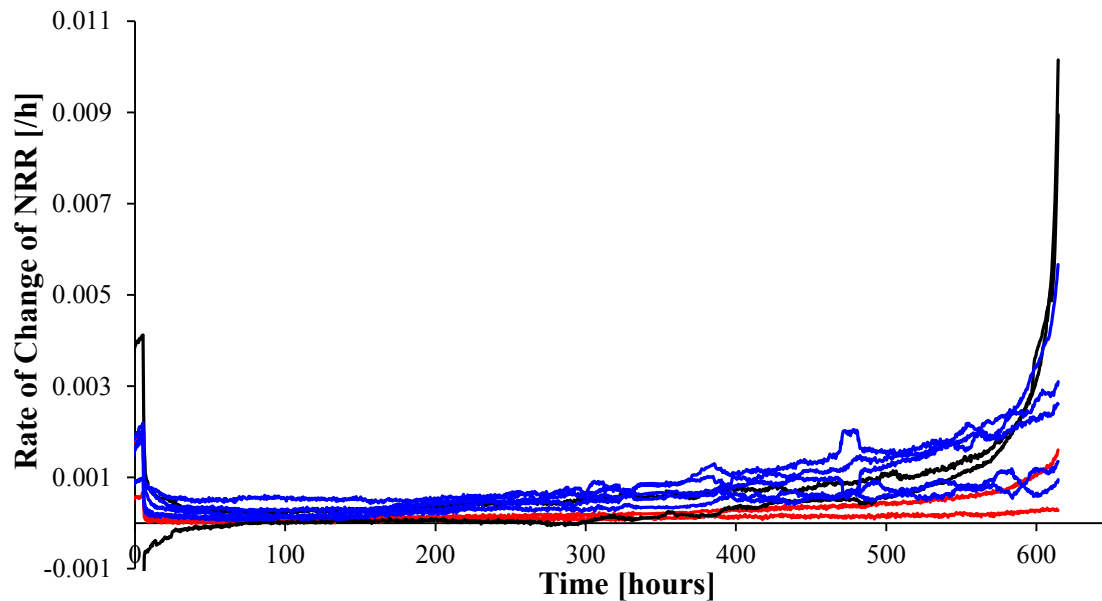


Figure 6.13: Rate of Change of Normalised Resistance Ratio against time for cross-weld creep test. Legend according to Figure 6.11 but dashes have been omitted for simplicity; blue measurements are of parent material, red are weld material and black include HAZ. Rate calculated by central finite difference method with a time step of 10 hours.



Figure 6.14: Photograph of specimen after experiment was concluded. A crack can clearly be seen in the vicinity of the HAZ.

This experiment demonstrates the sensitivity of potential drop methods to the macroscopic creep damage associated with weld failure. The limitation of this experiment, however, is that the component thickness was only twice the electrode separation; the crack is therefore constrained to grow within the field of sensitivity of the potential drop measurement. In thicker components it is possible, though unexpected, for a crack to initiate below the penetration depth of the potential drop measurement and considerable growth may occur before detection. Investigating the risk of this situation arising and optimising the electrode separation to account for variability in the depth of initiation is future work.

6.5 Conclusions

Creep failure at welds will often be the life limiting mechanism of pressurised power station components and so monitoring their integrity will be of great value to power station management. It is suggested here that potential drop methods are particularly well suited to monitoring weld failures due to their sensitivity to localised accumulation of strain and also cracking.

The presence of the distinct material domains of different electrical properties presents a challenge in the interpretation of potential drop data. It has been shown that when taking square electrode configuration resistance readings an apparent anisotropy is observed in the vicinity of the weld/parent interface. With respect to continuous monitoring, the particular issue of concern is the effect of changes in the ratio of the weld and parent resistivity, particularly as a result of thermal ageing and reversible temperature dependency. Fortunately, sensitivity to such changes is reduced as the ratio of conductivities will reduce at high operating temperatures. Further, the temperature coefficient will be reduced and the relative effect of solute depletion will be diminished as the total resistivity is increased with temperature. Taking measurements at high temperature will therefore significantly reduce the uncertainty in resistance ratio measurements.

It has been shown through simulations of two representative cases how cracking will influence resistance measurements. It can be seen in the two cases that cracking initiating from either within the component or from the surface of the component has a substantial effect on the resistance ratio. Cracks infringing on even 10% of the penetrations depth are seen to have a significant effect on the measured resistance ratio.

The question of optimising the measurement procedure is not straightforward. Some points to consider are:

- Increased electrode separation increases penetration depth and therefore ability to detect subsurface cracking.
- Increasing electrode separation reduces the relative size of a given crack, reducing the sensitivity.
- Reducing electrode separation reduces the gauge length of strain measurements which may provide useful information on very local variations in strain which may act as a precursor to crack initiation.
- It has not yet been established whether it is more beneficial to centre the sensor around the weld/parent interface in an attempt to reduce the effect of apparent anisotropy or around the ICHAZ which may improve sensitivity to Type IV damage.

- If attempting to install sensors centred about the weld/parent interface, h/a will be minimised to reduce the effect of apparent anisotropy. Increasing electrode separation, a , may help to ease this task as the effect of uncertain h placement will be reduced.

Finally, a cross-weld uniaxial creep test was conducted to show how potential drop measurements may be implemented to monitor weld damage. The rapid increase in the rate of change of Normalised Resistance Ratio shows promise as a useful indicator of proximity to failure.

Chapter 7

Implementation of Potential Drop Creep Sensors in a Power Station Environment

7.1 Introduction

Two site trials have been conducted throughout the course of this project to demonstrate the performance of the potential drop creep measurement system on operational components in a power station environment. A total of 32 sensors were installed; 20 at Ratcliffe and 12 at West Burton power stations, owned by E.ON and EDF respectively.

In order for the trials to be completed the measurement procedure that had been successfully demonstrated in the laboratory environment with mostly research grade, commercially available measurement equipment had to be developed into a system with hardware that was sufficiently robust and electronics that were designed to deal with the unique challenges of the power station environment. The equipment and procedures have been successively improved in parallel with the development of the lab measurement system. As with the results from the laboratory already presented in this thesis emphasis and results will be placed on current capabilities.

This chapter will detail the potential drop system developed in order to take measurements in the demanding power station environment. A background to the installations and the work conducted at both power stations will be provided with some data to demonstrate current performance.

7.2 Sensor Hardware

A high temperature sensor comprising of electrodes, a thermocouple, strain relief and associated cabling had to be designed. It had to be capable of withstanding a number of years at operational conditions of 550-600 °C in an environment of continuous vibration and possible major mechanical disturbances.

Electrodes were formed from 3 mm diameter stainless steel studs that could be stud welded to the components using a commercially available capacitance discharge welder; the result is an electrode that forms a robust galvanic connection to the component. Due to the increased scale of the electrodes an

increased electrode separation of 10 mm was adopted. Wires were then welded to the end of the studs and a strain relief installed to protect the electrodes and wires. Finally, a k-type thermocouple is installed in the vicinity of the potential drop sensor for the purpose of temperature compensation. The sensor can be seen in Figure 7.1.

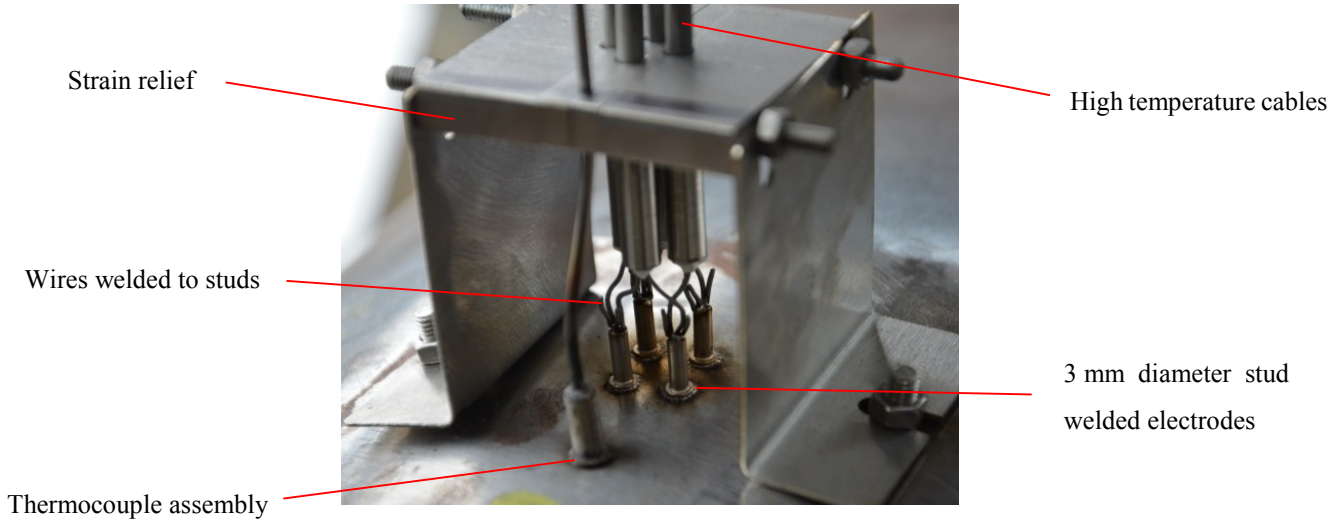


Figure 7.1: Labelled photograph of potential drop sensor design

The cables used to connect to electrodes are a bespoke design and are specially manufactured for this application. The current design is rated for use up to 800 °C and the whole system including cabling is designed to minimise inductive cross-talk. The component is wrapped in thermally insulating material and cladding (~200 mm thick), the high temperature cabling extends out normal to the surface and is sufficiently long (500 mm) so that it is sufficiently clear of the high temperature of the pipe before connecting with a lower temperature cabling seen in blue in Figure 7.2 (a). All of the sensors have been installed on pipe components and have been installed in a cross formation at 90° intervals around the circumference, as seen in Figure 7.2 (b).



Figure 7.2: Photographs of potential drop sensors installed at West Burton power station.

7.3 Measurement System

A prototype automated measurement system was developed under license by TSK Solutions Ltd. with assistance from Prof. Challis and further developed at Imperial College. The measurement system is designed to replicate the measurement equipment described in Section 2.7.2, and incorporates key components designed by Prof. Nagy for the lab system. The electronics had to be designed to accommodate unique challenges presented by the power station environment. A selection of key measurement specifications as measured in the laboratory are given in Table 7.1. Where there is a selectable range of values (for example inspection frequency) the typical value used on site will be given.

Table 7.1: Key measurement parameters for the automated potential drop measurement system.

Parameter	Typical Value
Inspection Frequency	1 Hz
Inspection Current	100 mA (RMS)
Measurement Noise	1.4 nV/ $\sqrt{\text{Hz}}$ (at 1 Hz)
Relative Accuracy	$\pm 0.1\%$ (for 10 $\mu\Omega$ measurement load)
Common Mode Rejection	126 dB -142 dB
Measurement Length	16 Seconds/Channel

The measurement system is battery powered, removing the necessity to install mains power cables and making it easy to install. It is programmable to service up to 4 sensors and to take measurements at user

defined intervals. Data is stored locally and can be downloaded by USB connection to a laptop at intervals.

The prototype measurement system can be seen being installed in Figure 7.3. The high temperature cables can be seen protruding out of the insulation where they are connected to the low temperature cables which are then wired into the measurement system.



Figure 7.3: Photograph showing sensors and measurement system installed at West Burton power station.

7.4 E.ON Ratcliffe-On-Soar

Five sets of four sensors were installed on main steam and hot-reheat pipes at straight and bend locations in August 2012. Both Ratcliffe and West Burton are conventional coal-fired plants. The pipes were being replaced and therefore sensors were installed on virgin CMV material. Following a small number of sensor failures the high temperature sensor design was completely redesigned to the version that has been described and installed in West Burton.

Initially a Stanford Research Systems SIM based system similar to that described in Chapter 2 was used to collect single measurements approximately monthly. A measurement system was brought into the power station with a laptop computer and connected to each sensor successively in order to take a measurement. Over this time the difficulties in taking measurements on site were established and instrumentation and measurement procedures were improved. This formed the basis of the prototype automated system that has been described and was eventually installed at both sites.

The automated measurement system was installed at West Burton first and has the benefit of improved hardware design. The remainder of the chapter will therefore focus on the West Burton installation.

7.5 EDF West Burton

Three sets of four sensors were installed with three prototype measurement systems in August 2014. As with the previous installation at Ratcliffe, sensors were installed on main steam lines and hot reheat pipes both at straight sections and bends. This time however the pipes are near the end of life and are scheduled to come out of service three years after sensors were installed; it is therefore expected that measurable creep strain will occur over this period. All photographs in this chapter are from the West Burton installation, along with example data.

The following data will show the present quality of data obtained with the current measurement instrumentation. Particular emphasis will be placed on addressing the influence of the temperature fluctuations inherent in operational power station components and in the ambient power station environment.

7.5.1 Normalised Resistance

A sensor has been selected to demonstrate representative power station conditions and show the performance that is currently achieved.

7.5.1.1 Temperature Compensation

Figure 7.4 shows the data currently collected from a single sensor. For the first ~500 hours measurements were taken at an interval of one reading per hour and following this every four hours. Each reading contains the two orthogonal resistance measurements taken over 16 seconds each and a single associated thermocouple reading. Figure 7.4 shows the overall trend in typical power station operation. Long periods of operation fluctuating about a set point temperature with periods of shut down at intervals. It is beneficial to minimise the influence of reversible temperature dependency which can be seen to have a very substantial impact on the measured resistances. Only measurements taken at the nominal operational condition, as indicated by the measured temperature will be considered; all measurements taken at less than 550 °C will therefore be discarded.

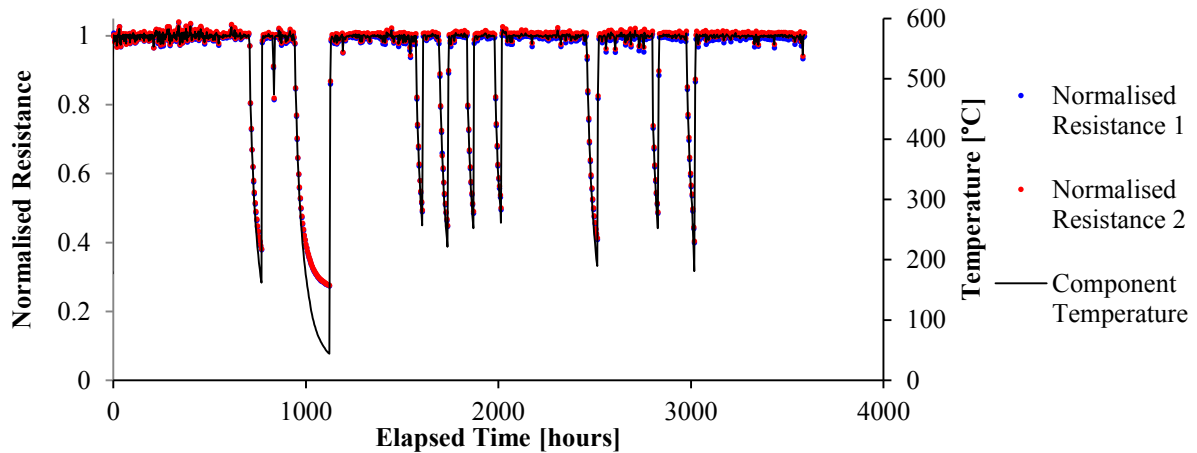


Figure 7.4: Normalised Resistances and temperature associated with a single sensor at West Burton power station.

Figure 7.5 shows 150 hours of data taken from Figure 7.4. On closer inspection the temperature fluctuations and the impact on the measured resistances is much clearer. Even at the constant nominal operational temperature, a range of tens of degrees is evident, the time scale of the temperature change is not yet established.

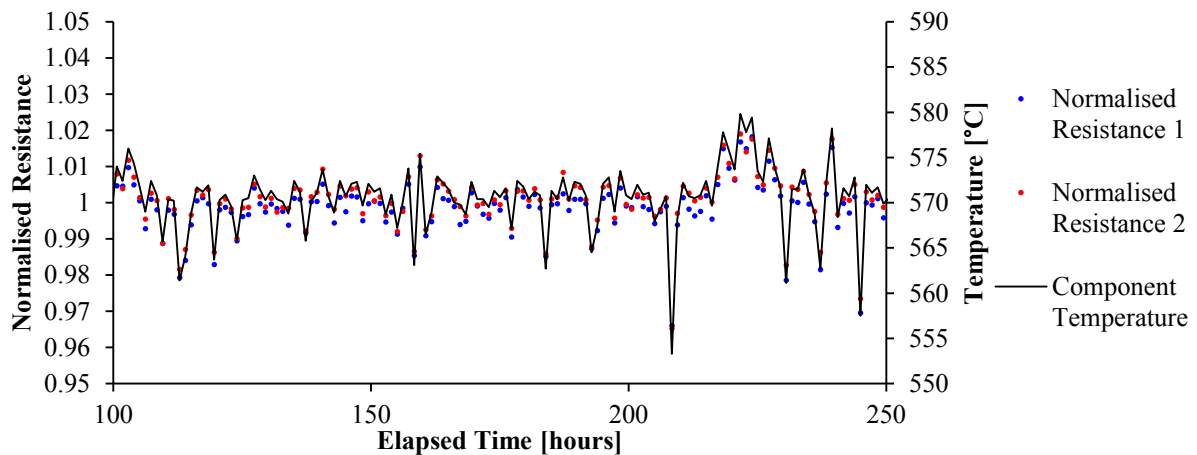


Figure 7.5: Normalised Resistances and temperature associated with a single sensor at West Burton power station. The data is the same as Figure 7.4 with a short duration selected for clarity.

Clearly, from Figure 7.5, the measured resistances and temperature are well correlated. This is shown again in Figure 7.6. The correlation is clear and easily measured allowing for a simple, linear temperature compensation to be applied. The temperature coefficient is measured to be $0.0022/^\circ\text{C}$ at this temperature.

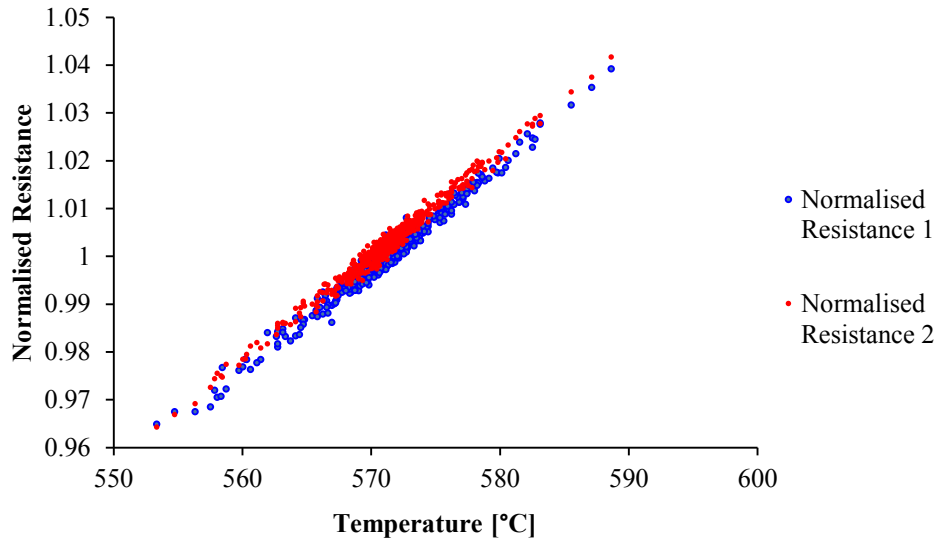


Figure 7.6: Scatter graph showing the approximately linear temperature dependence of resistance. Data for the first 600 hours is displayed.

The data from Figure 7.5 can then be temperature corrected as shown in Figure 7.7. Comparing the two figures shows how effective the simple temperature compensation is; the $\pm 5\%$ variation in resistance is suppressed to a fraction of a percent. Further improvement may be possible by more temperature sampling.

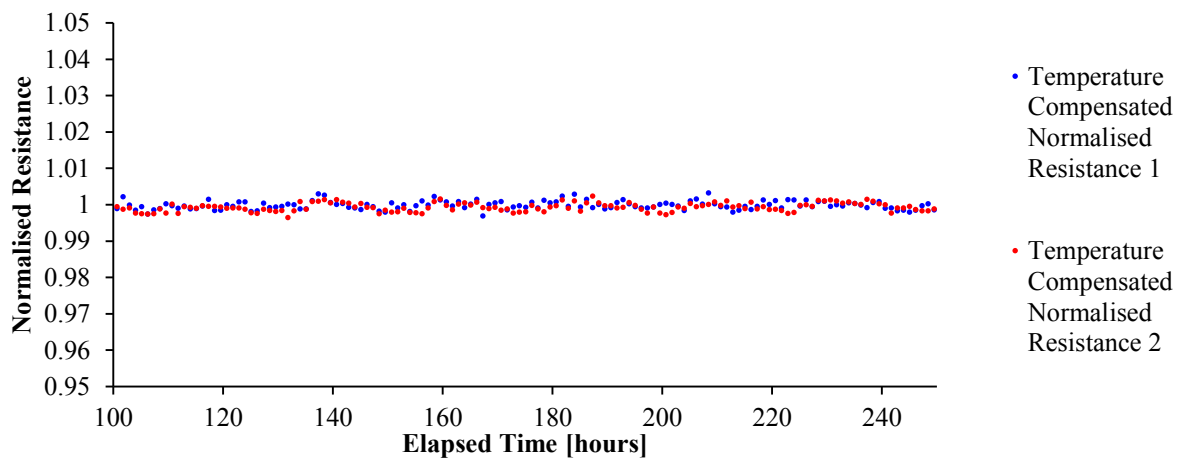


Figure 7.7: Temperature compensated Normalised Resistance. The original Normalised Resistance data is that from Figure 7.5.

The initial filtering out of data from shut down periods and the additional temperature compensation provides the results of Figure 7.8. The rate of resistance change observed is in line with what might be expected as a result of creep strain from a component towards the end of life. The result is encouraging as the repeatability of results is clearly sufficient to identify the presence of strain.

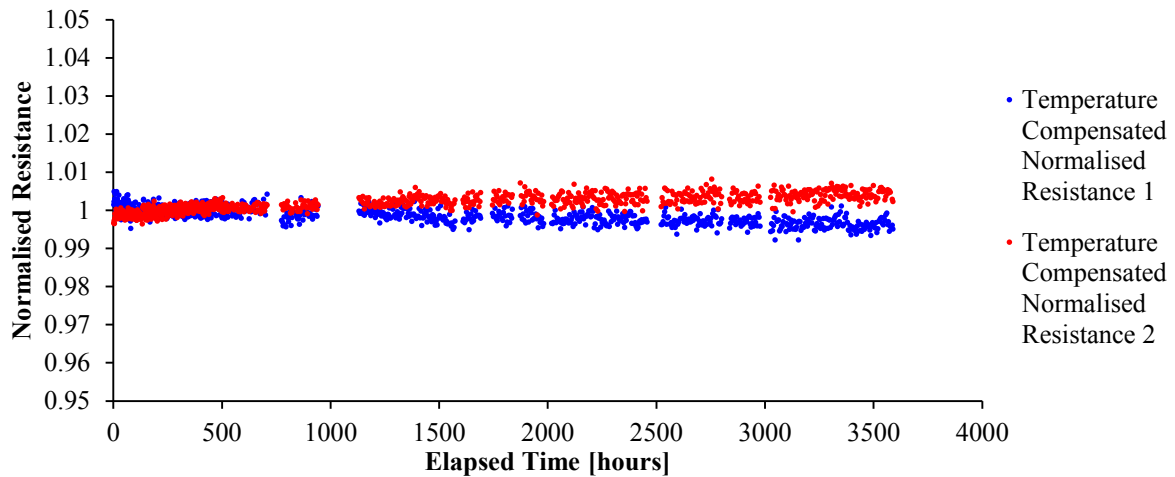


Figure 7.8: Temperature compensated Normalised Resistance. The original Normalised Resistance data is that from Figure 7.4.

The measurement equipment had the addition of an inbuilt precision resistor network that could be used to monitor the measurement system stability. At each sensor measurement cycle an equivalent measurement was taken from the resistor network. The resistor network has an effective value of $10\ \mu\Omega$ and thermal stability of $\pm 5\ \text{ppm}/^\circ\text{C}$. The measurements taken from this resistor network together with an associated temperature reading of the measurement equipment is shown in Figure 7.9. The daily temperature cycle of the power station environment is seen to have a notable effect on the measurements, far in excess of the $\pm 5\ \text{ppm}/^\circ\text{C}$ of the measured load. Evidently, the performance limiting parameter for measurement variability is the thermal stability of the measurement system which from Figure 7.9 is calculated to be $\sim 200\ \text{ppm}/^\circ\text{C}$. An equivalent uncertainty from measurement system thermal instability must also be present in the sensor readings and therefore may be assumed to be responsible for much of the uncertainty of Figure 7.7 and Figure 7.8. Improving the thermal stability of the measurement system can be achieved by improving the electronic design and specification of components which is the focus of current efforts, a substantial improvement is expected.

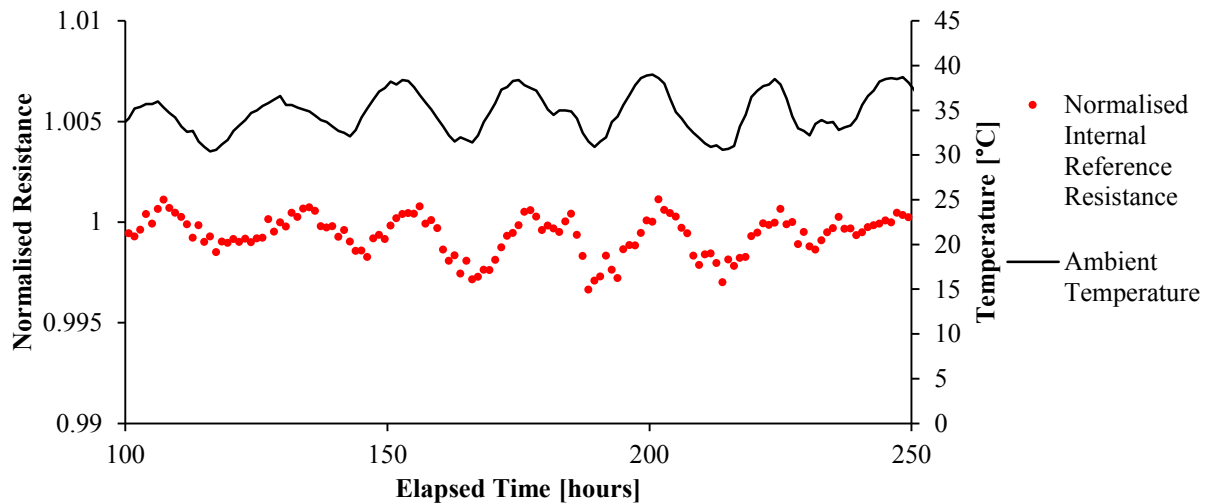


Figure 7.9: Normalised Resistance readings of a $10 \mu\Omega \pm 5 \text{ ppm}/^\circ\text{C}$ resistor network situated inside the measurement equipment together with an associated temperature measurement of the ambient measurement equipment condition.

7.5.2 Normalised Resistance Ratio

An alternative approach to the suppression of temperature dependence of both the component under test and the measurement electronics is the use of the Normalised Resistance Ratio. By dividing the two orthogonal readings taken in succession over a relatively short period of time any variation that is common to both readings is suppressed. Importantly, this also extends to time dependent isotropic resistivity changes and instrument drift that may become apparent after longer testing duration.

For consistency with the previous figures the same data from the same sensor has been used. The temperature dependency seen previously for the Normalised Resistance data in Figure 7.5 is effectively removed without any temperature compensation and therefore no requirement to install a thermocouple.

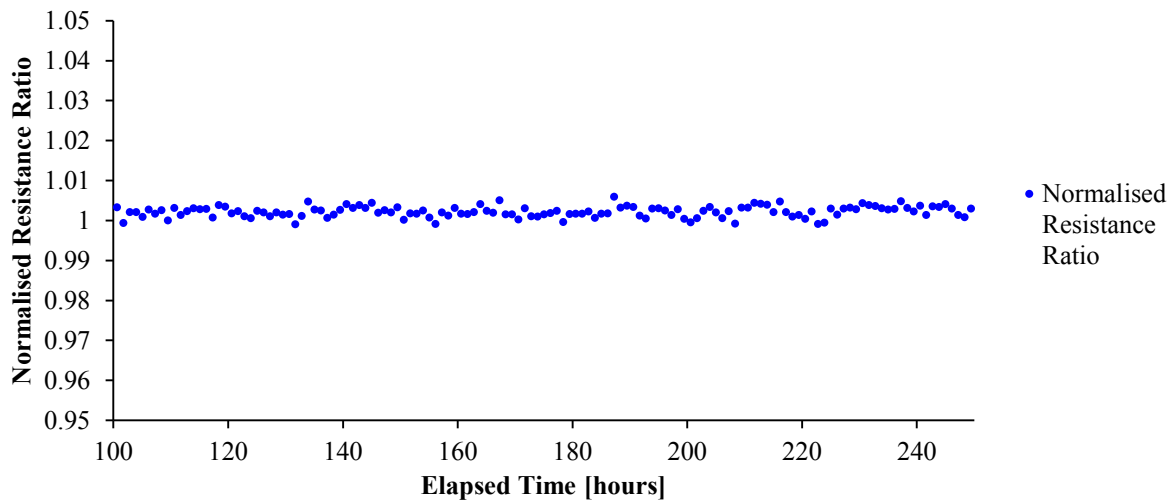


Figure 7.10: Normalised Resistance Ratio calculated from the data displayed in Figure 7.5. Normalised Resistance 2 is divided by Normalised Resistance 1. No temperature compensation is carried out.

Examining the data over a longer period again shows a change in resistance ratio that is in line with the expected strain rate of a component approaching the end of life, again the gradient of this rate of change is clearly discernible from the measurement variation.

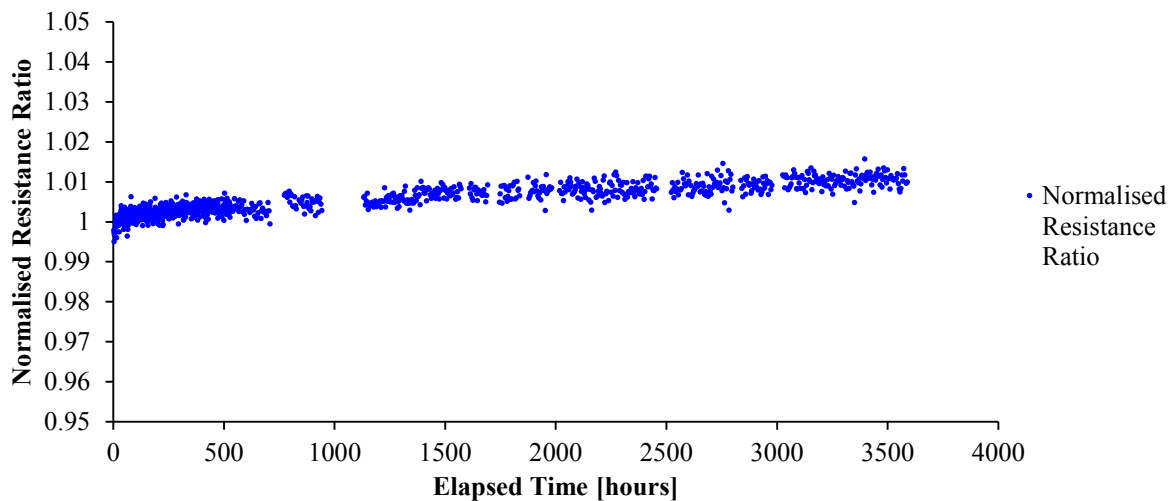


Figure 7.11: Normalised Resistance Ratio calculated from the data displayed in Figure 7.4. Normalised Resistance 2 is divided by Normalised Resistance 1. No temperature compensation is carried out but measurements taken at less than 550 °C are discarded.

The success of the Normalised Resistance Ratio is dependent on the assumption that the measurement conditions are common to both orthogonal measurements. Between the two measurements, each of which constitutes a 16 second record length, there is an extended delay of 25 seconds for housekeeping and settling of the electronics. This provides a maximum time scale of approximately 1 minute between the beginning of the first measurement and the end of the second. Changes in conditions of the

component under test and ambient environment over this time scale will not be suppressed; it is believed that it this may result in much of the uncertainty evident in Figure 7.10 and Figure 7.11. It is possible to reduce the delay between orthogonal measurements by improvement of the electronic design, which again is currently underway. The length of time of the measurement is to be optimised to minimise the random measurement uncertainty, maximise battery life and reduce the time scale of the total measurement.

7.6 Conclusions

A potential drop system, including high temperature sensor hardware and automated measurement electronics, has been developed that is sufficiently mechanically and electronically robust to take in-situ potential drop measurements of power station components. Two site trials in coal fired power stations are being conducted. A total of 32 sensors have been installed in a range of locations on main steam and hot reheat pipework.

Measurements gathered using the potential drop system show stable and repeatable readings in the data gathered to date. Resistivity fluctuations caused from the temperature variation of the component can be effectively suppressed using thermocouple readings and simple temperature compensation. Further improvement is expected to be easily realised by increased temperature sampling. The effect of ambient temperature fluctuations on measurement stability is apparent and it is believed that this is currently the performance limiting parameter on Normalised Resistance measurement variation. Improving the thermal stability of the measurement is the focus of current efforts. The results gathered at the site trials show excellent promise for the use of potential drop measurements in creep strain monitoring, with repeatability of individual resistance readings being adequate to discern the influence of resistance change resulting from creep strain.

As discussed throughout this thesis the Normalised Resistance Ratio offers the considerable advantage of suppressing all multiplicative effects common to both orthogonal resistance measurements which are taken in quick succession. This includes isotropic resistivity changes associated with temperature dependency and long term creep, and drift and instability of measurement instrument gain. The effectiveness of the Normalised Resistance Ratio in suppressing reversible temperature dependent fluctuations has been demonstrated and it is assumed that this success may be extrapolated to long term drift. Further work is to be undertaken in optimising the measurement protocol so that orthogonal measurements are taken over a shorter time scale so that it may be assumed that conditions are more similar and therefore suppression improved. The interpretive frame work for Normalised Resistance Ratio data suggested in Chapter 5 may be adopted to provide information on creep state and remnant life based on increase in strain rate.

Chapter 8

Conclusions

Progress towards a monitoring technique that is capable of the on-load monitoring of creep damage in power station components has been presented in this thesis. In this concluding chapter, a review of the thesis is presented together with a summary of the main academic and industrial contributions and suggestions for future work.

8.1 Thesis Review

Chapter 1 provided a background to the nature of creep in static power station components and the significant economic benefit that an improved and continuous awareness of creep state would bring in the way of increased power generation availability. The capability of on-line monitoring of creep state has yet to be satisfactorily realised and forms the motivation for this thesis. Current evaluation practices were reviewed in addition to the current state of the art of emerging techniques.

A challenging aspect of the problem of evaluating creep damage is that there are a number of different mechanisms that act to reduce the integrity of the component. Many evaluation techniques are dedicated to grain boundary separation, which is understood to usually be the ultimate cause of failure. Adequate evaluation of sparse cavity formation and growth can be technologically challenging and difficult to isolate in the presence of a number of other evolving microstructural features, moreover, significant creep damage may not develop until prohibitively late in life to act as a useful indicator of creep life. A monitoring technique must be sufficiently encompassing to gain an adequate representation of a number of damage mechanisms. Alternatively, it is suggested here that monitoring *the relative increase in strain rate* may act as a ‘holistic’ indicator of creep state. Creep strain rate acts as an expression for the creep sustaining integrity of the component, monitoring the increase in strain rate therefore acts as a symptomatic expression of the damage state.

Potential drop methods have been suggested as having particular promise for the evaluation of creep damage as electrical resistivity has been reported to be sensitive to various damage mechanisms including grain boundary separation, carbide evolution, and dislocations. Additionally, by permanently attaching electrodes a strain sensitive technique can be realised.

Chapter 2 presents a novel potential drop measurement technique that has been previously developed. Permanently installing electrodes provides a robust galvanic connection enabling on-load measurements; additionally, in doing so the measurement becomes sensitive to strain through the separation of electrodes. A quasi-DC approach has been adopted to suppress the influence of the electromagnetic skin effect that would otherwise undermine the stability of the measurement in the ferromagnetic materials of interest; the use of even low frequency measurements allows phase sensitive detection and greatly enhanced noise performance. A square electrode configuration has been adopted due to its directional sensitivity to anisotropic resistivity and enhanced strain sensitivity.

Chapter 3 details the three most significant microstructural mechanisms associated with exposure to creep conditions and extended thermal ageing; dislocations, carbide evolution and grain boundary separation. The influence of these mechanisms on the electrical conductivity is of dual interest, on one hand it is possible that electrical resistivity changes can provide information on the creep state of the component. Alternatively, as strain provides valuable information on the creep state of components, resistivity changes may act to mask the influence of strain, limiting the effectiveness of a resistance-strain inversion.

It was concluded from established theory that the influence of dislocation density changes will be negligible, especially at elevated operational temperatures. The effect of solute depletion on conductivity has been previously reported in literature and experimental results corroborating these findings were obtained in this project; a significant decrease in resistivity was observed in the early stages of thermal exposure of virgin material. While this is known to have a significant effect on mechanical properties it is likely to be of little practical interest to monitor a short lived transition to a more stable state.

It was hypothesised that due to the alignment of grain boundary defects the effect on the conductivity tensor may be anisotropic. An analytical model was adopted to evaluate the likely influence of grain boundary separation on electrical conductivity. Estimates were obtained using the proposed analytical model and example images of grain boundary separation. These were necessarily very conservative due to the limitation of using two dimensional images and therefore a worst case would be assumed extrapolating to the third dimension. The inclusion length squared dependence of resistivity resulted in very little influence until the very advanced stages of creep damage where grain boundary separation reaches a stage of micro-cracking. It was therefore concluded that using conductivity to monitor the development of grain boundary separation is unlikely to be effective until prohibitively late in life.

It was concluded therefore that resistivity changes are expected to be very modest, with the exception of very early and late in life, and therefore would be of little practical use for creep monitoring. In the

context of accelerated laboratory tests, it could be inferred that the effect of irreversible resistivity changes from microstructural evolution is likely to be small in comparison to the effect of the substantial strain that is expected; resistance could then be attributed overwhelmingly to strain. This was supported by the successful strain inversions of accelerated uniaxial tests in the following chapter. When applied to power station conditions however, where the strain rate is of course orders of magnitude lower, the stability of resistivity must be near perfect; a requirement that is not expected to be achieved. By utilising the Normalised Resistance Ratio sensitivity to isotropic conductivity changes may be suppressed.

Chapter 4 explores the relationship between potential drop measurements and the effect of strain. A square electrode configuration with electrode separation smaller than the component thickness was selected due to the large sensitivity to strain in the surface plane and insensitivity to thickness changes which may not necessarily be attributable to strain.

Two strain inversions have been presented. The first uses only the Normalised Resistance Ratio and is therefore insensitive to isotropic resistivity changes or instrument instability; this inversion however only provides a strain ratio and therefore requires an assumption about the strain distribution to provide absolute strain values. The Normalised Resistance Inversion provides a biaxial strain measurement but is susceptible to errors introduced by resistivity change and instrument drift and instability. Both inversions have been demonstrated in laboratory tests with due consideration for the effects and limitations of using small components.

It was previously concluded that the stability of resistivity must be near perfect so that it does not interfere with the detection of slight resistance changes resulting from strain. Additionally, even very minor instrumentation drift or instability caused by either changes in operating conditions or ageing will erroneously scale the desired measurement. By utilising the Normalised Resistance Ratio sensitivity to isotropic conductivity changes and instrument drift and instability may be suppressed. Unfortunately, it is not possible to invert absolute biaxial strain values from the Normalised Resistance Ratio without knowledge of the stress state; only information on aspect ratio is preserved which cannot be interpreted without coupling the orthogonal stress directions.

In order to make use of the information on aspect ratio provided by the Normalised Resistance Ratio the concept of using the relative increase in strain rate as an indicator of creep state was revisited. It was shown (with the exception of a perfect 'equibiaxial' stress state) that aspect ratio and the rate of change of aspect ratio are approximately proportional to strain and strain rate respectively. Therefore the *relative increase in rate of change of strain* is equivalent to the *relative increase in rate of change of*

aspect ratio and therefore information on creep strain can be inferred from the Normalised Resistance Ratio.

In order to demonstrate the use of strain rate measurements for the evaluation of creep state, remnant life calculations were demonstrated on accelerated uniaxial creep specimens. Proportionality between remnant life and inverse true strain rate was assumed. Additionally, the constant of proportionality was calculated from the in-situ measurements and so would be accurate for the particular test condition.

Creep failure at welds will often be the life limiting mechanism of pressurised power station components and so monitoring their integrity will be of great value to power station management. It is suggested that the potential drop technique described in this thesis is particularly well suited to monitoring weld failures due to their sensitivity to localised accumulation of strain and also cracking. Chapter 6 provides a preliminary study into the possibilities of potential drop monitoring at a weld as well as the associated challenges.

A weld is composed of distinct material domains which will have different electrical conductivity. A potential drop measurement in the vicinity of a weld will be dependent on the resistivity of both materials. The capacity of the Normalised Resistance Ratio to suppress resistivity changes is based on the assumption of a homogeneous material and therefore will be compromised at a weld. It was found, however, that at elevated temperature the relative conductivities between the weld and parent material will be more similar and less sensitive to temperature changes.

It was shown through two initial simulations that the presence of cracks much smaller than the electrode separation would cause significant influence on resistance measurements which are expected to be detectable.

An accelerated uniaxial creep test was conducted on a cross-weld specimen with a potential drop array installed. The initiation and rapid growth of a crack in the vicinity of the HAZ was clearly detectable. Building on the previous chapter, the rate of change of the Normalised Resistance Ratio in particular proved a clear indication of proximity to failure.

Two site trials have been conducted during this project, hosted by E.ON and EDF. The aim of the trials was to demonstrate the use of the potential drop creep monitoring technique and as an opportunity to develop and improve the system. To carry out the installations, high temperature hardware that is sufficiently robust for the power station environment was developed. Additionally, a bespoke measurement system was developed externally and further developed at Imperial College.

Data collected from the site trials show stable results with evidence of strain accumulation. Suppression of the effect of temperature changes that are a feature of power station operation has been shown to be possible by compensation using thermocouple data and also by using the Normalised Resistance Ratio.

8.2 Summary of Main Contributions

In working towards the aim of developing an on-load creep monitoring technique a number of novel academic and industrial contributions have been made. These will be summarised and grouped according to their broader context.

Measurement Capability

Throughout the course of this project the capability and quality of the previously established measurement technique has been significantly improved. The measurement electronics have been substantially improved, thanks to the considerable assistance of Prof. Peter B. Nagy, in addition to the development of the practical execution of the technique. While this is not explicitly detailed in this thesis the quality of the results throughout would not have been achievable without this development.

Electrical Conductivity Changes

A review of the conductivity changes that might be expected in power station steels has been completed. Aside from the direct implications for this thesis it may also inform the use of ACPD and DCPD for high temperature testing in the laboratory, both very frequently used techniques. Continuous resistance measurements have been made of the effect of solute depletion. An analytical model of the influence of inclusions in a conducting material has been applied to the case of grain boundary separation.

Interpretation of Potential Drop Measurements as Strain

A novel potential drop array measurement has been developed to increase the spatial strain information that can be collected from high temperature component tests. Strain inversions for square configuration thick walled components have been developed and demonstrated experimentally.

Strain Rate Based Creep Damage Assessment

A methodology for inferring creep state from measurements of aspect ratio has been presented and demonstrated using experimental data. This method may be applicable to a range of sensor types. The main benefits of this method are:

- Creep strain rate is an expression of the total creep state of the component encompassing all damage mechanisms.
- Drift and instability of electronics are inherently suppressed provided that they are common to both orthogonal measurements.

- Only information on strain is used in the remnant life calculation and therefore no periphery measurements are required. The parameters governing the remnant life calculation can be continually updated representing the true situation at hand.

Potential Drop Measurements at a Weld

A potential drop array technique has been developed to identify the localised creep damage expected at weld. Key issues associated with taking measurements in the vicinity of two different materials have been explored. It has been concluded that significant improvement is expected from taking measurements at high temperature. The ability to detect creep damage at a weld has been successfully demonstrated experimentally.

Practical Implementation in Power Stations

The first use of the potential drop creep monitoring technique in a power station environment has been achieved. The data collected so far looks promising for the use of the technique to infer creep damage.

8.3 Future Work

Throughout this project a number of opportunities for further research have arisen, these may compliment or build upon the work in this thesis or may have application outside this particular research aim.

Although the reported influence of solute depletion on resistivity has been shown experimentally and is consistent with the expected theory, an independent measurement of solute concentration has not been made to further support this hypothesis; although it is believed to be possible if there is sufficient interest.

An analytical model was adopted to infer the likely influence of grain boundary separation on conductivity. It has not yet been possible to support this result experimentally due to the difficulty in obtaining or creating a sample with sufficiently extensive grain boundary separation to measure. Such a sample is sought and measurements can then be completed.

The creep tests used to validate the strain inversions have all been greatly accelerated uniaxial creep tests. The strain rates are therefore orders of magnitude higher than those expected in power station components and the time scale of the experiments are of the order of 10's or 100's of hours as opposed to >100,000 hours. A useful demonstration of the reliability of the technique would be to undertake long term stability tests in the absence of strain to provide a baseline below which strain would not be reliably detectable.

The strain rate based creep state assessment methodology should be tested in more realistic conditions, most notably in a range of biaxial stress states as increasing stress triaxiality will both limit the realised strain and also the sensitivity of the aspect ratio to strain. Additionally, the 'shape' of the creep curve is expected to be altered by moving to longer term creep tests more representative of power station conditions; increases in strain rate are not expected until nearer failure making strain rate based remnant life calculations more challenging.

The work applying the potential drop technique to welds was intended only as a preliminary study and therefore there is a good deal of further work required in this area. Attention should be given to the most effective electrode separation or even arrangement. A compromise between penetration depth, sensitivity to cracking and gauge length of strain measurement will need to be considered in the first instance. Consideration should be given to the optimal electrode placement relative to the weld. The negative effect of the differing conductivity of the material domains is minimised by centering the sensor around the weld interface. On the other hand, creep damage is expected to accumulate on the edge of the HAZ and therefore the sensor should be centered about this point to increase sensitivity to cracking. Further trials should be completed on thicker components to investigate the possibility of cracking occurring subsurface or below the sensors field of sensitivity.

Although the measurement system has been demonstrated on-site, there is much development to be done before the technique can be adopted more widely. It is intended that a new generation of measurement equipment and hardware be developed for this purpose building in improved reliability, performance and capability.

Appendix A

An Analytical Solution for Square Electrode Configuration Potential Drop Measurements

This Appendix provides an analytical solution for the impedance measured from a square-electrode configuration using DC to AC frequencies.

Bowler (Bowler, 2006) provides an analytical solution for the potential difference between two points on a conducting surface resulting from the injected current at two other points. This analysis is easily applied to the proposed square electrode configuration measurement shown Figure A.1 with the coordinate convention to be employed.

The potential difference between two points on a conducting surface resulting from the injected current at two other points is given by Bowler (Bowler, 2006). In the case of the square electrode configuration the potential difference, v , is simplified to,

$$v = \frac{I}{\pi\sigma} [F_i(r_1) - F_i(r_2)] \quad (\text{A.1})$$

where F_i is a function to be discussed, r_1 and r_2 are the dimensions labelled in Figure A.1, σ is the conductivity and I is the injected current.

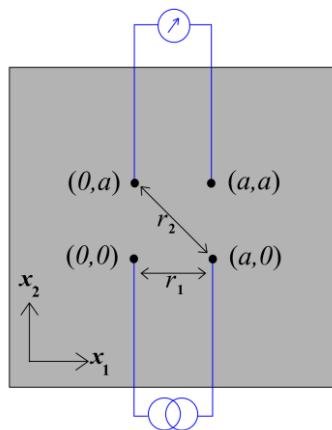


Figure A.1: Square electrode arrangement labelled to show geometry convention.

Bowler provides the following solution to the function, F_i .

$$F_{exact}(r) = -ik[\gamma_e + \ln(-ik) - 1] + F_{series}(r), \quad (\text{A.2})$$

where γ_e is Euler's constant (0.577216...) and

$$k = \frac{1+i}{\delta}. \quad (\text{A.3})$$

The series term is given as:

$$F_{series}(r) = \frac{1}{r} \left[1 - \sum_{n=1}^{\infty} \frac{(ikr)^{n+1}}{n(n+1)!} \right]. \quad (\text{A.4})$$

Note that it is only the series term in Equation A.2 that is a function of r . Therefore the other terms will cancel when we now apply to Equation A.1.

$$v = \frac{I}{\pi\sigma} \left\{ \frac{1}{r_1} \left[1 - \sum_{n=1}^{\infty} \frac{(ikr_1)^{n+1}}{n(n+1)!} \right] - \frac{1}{r_2} \left[1 - \sum_{n=1}^{\infty} \frac{(ikr_2)^{n+1}}{n(n+1)!} \right] \right\} \quad (\text{A.5})$$

The DC asymptotic value which can be found taking $k \rightarrow 0$.

$$v_{dc} = \frac{I}{\pi\sigma} \left\{ \frac{1}{r_1} - \frac{1}{r_2} \right\} \quad (\text{A.6})$$

Therefore,

$$\frac{v}{v_{DC}} = \frac{\frac{I}{\pi\sigma} \left\{ \frac{1}{r_1} \left[1 - \sum_{n=1}^{\infty} \frac{(ikr_1)^{n+1}}{n(n+1)!} \right] - \frac{1}{r_2} \left[1 - \sum_{n=1}^{\infty} \frac{(ikr_2)^{n+1}}{n(n+1)!} \right] \right\}}{\frac{I}{\pi\sigma} \left\{ \frac{1}{r_1} - \frac{1}{r_2} \right\}} \quad (\text{A.7})$$

Simplifying and by recalling from Figure 1 that $r_1 = a\sqrt{2}$ and $r_2 = a$

$$\frac{v}{v_{DC}} = 1 + \frac{\frac{1}{\sqrt{2}} \sum_{n=1}^{\infty} \frac{(ika\sqrt{2})^{n+1}}{n(n+1)!} - \sum_{n=1}^{\infty} \frac{(ika)^{n+1}}{n(n+1)!}}{\left(1 - \frac{1}{\sqrt{2}} \right)} \quad (\text{A.8})$$

In Chapter 2 we introduced the transition frequency where the skin depth is equal to the smaller of the component thickness or electrode separation. In the case of a conducting half space the limiting dimension is the electrode separation, a , leading to the condition that

$$a = \frac{1}{\sqrt{(f_T \pi \mu \sigma)}}. \quad (\text{A.9})$$

It therefore also follows that,

$$\frac{a}{\delta} = \sqrt{\frac{f}{f_T}}. \quad (\text{A.10})$$

The term ka in Equation A.8 can then be considered as the complex normalised dimension.

$$\kappa = ka = \frac{a}{\delta}(1+i) = \sqrt{\frac{f}{f_T}}(1+i) \quad (\text{A.11})$$

This allows us to rewrite Equation A.8 in terms of normalised dimensions and, assuming constant injected current, infer the measured resistance.

$$\frac{R}{R_{DC}} = 1 + \frac{\frac{1}{\sqrt{2}} \sum_{n=1}^{\infty} \frac{(i\kappa\sqrt{2})^{n+1}}{n(n+1)!} - \sum_{n=1}^{\infty} \frac{(i\kappa)^{n+1}}{n(n+1)!}}{\left(1 - \frac{1}{\sqrt{2}}\right)} \quad (\text{A.12})$$

Equation A.12 allows the evaluation of impedance for a range of frequencies as shown in Figure A.2. The resistance and reactance are normalised by the DC magnitude $|R|$, and the frequency is normalised by the transition frequency.

This result is included in Chapter 2.

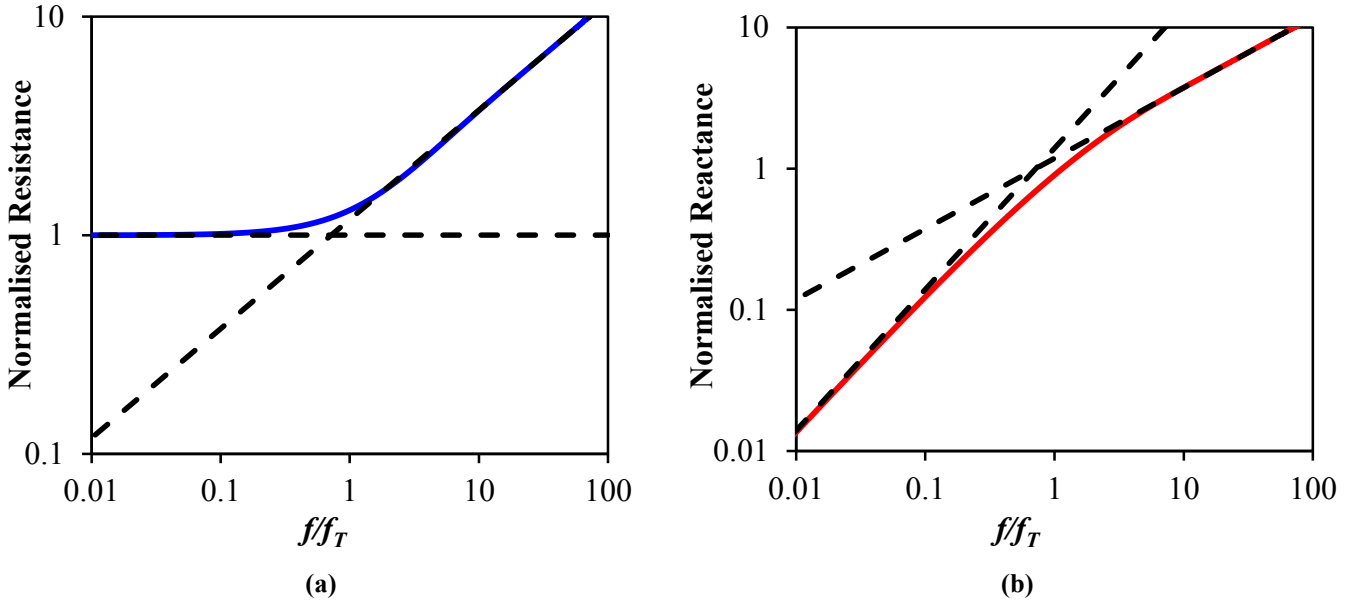


Figure A.2: Impedance resulting from a square electrode configuration. Resistance and reactance normalised to the DC resistance magnitude. First 100 terms in the series of Equation A.12 were evaluated.

Appendix B

Remnant Life Predictions from Strain Rate Measurements

B.1 Introduction

The creep state of a component and therefore the proximity to failure is governed by a number of damage mechanisms; either external, reducing the physical component cross section, or internal, reducing the creep strength of the remaining geometry (see Section 1.1.2.1). Measurements of any one mechanism may not provide a complete picture of creep state. Strain rate provides a symptomatic indicator of creep state encompassing all creep mechanisms. In order to extrapolate current information to provide estimates of remnant life a simplified model is required as measureable parameters will be limited and it is not possible to accommodate for the behaviour of damage mechanisms that are yet to materialise.

Chapter 5 is dedicated to demonstrating the use of relative changes in strain rate to infer creep damage. In order to illustrate this, proportionality between inverse true strain rate and remnant life is assumed;

$$(t_f - t) = \frac{1}{\Omega \dot{\epsilon}} \quad (\text{B.1})$$

where, Ω , may be found assuming,

$$\frac{\dot{\epsilon}}{\dot{\epsilon}_0} = e^{\Omega \epsilon} \quad (\text{B.2})$$

This appendix will give some background to these equations and discuss the limitations. For convenience and clarity, uniaxial loading will be assumed in the first instance.

B.2 Kachanov & Rabotnov, Creep Damage Parameters

The work of Rabotnov, which was then extended by Kachanov forms the basis of the continuum damage mechanics descriptions of tertiary creep damage (Kachanov, 1986; Rabotnov, 1969). They described a ‘damage parameter’, ω , which equates internal damage mechanisms to a loss in *effective* load carrying area, \tilde{A} . Considering also the loss in cross section resulting from conservation of volume and strain accumulation, $e^{-\epsilon}$, gives,

$$\tilde{A} = A_0 e^{-\epsilon} (1 - \omega) \quad (\text{B.3})$$

\tilde{A} is related to the initial, undamaged area A_0 to form the definition of the damage parameter. It must be stressed that the effective area is not meant as a physical area but rather an analogue for loss of strength.

The effective stress can then be described by the relation given by Rabotnov (Rabotnov, 1969) and Kachanov (Kachanov, 1986).

$$\tilde{\sigma} = \frac{\sigma_0 e^{\epsilon}}{(1 - \omega)} \quad (\text{B.4})$$

Putting Equation B.4 into the Norton power law, $\dot{\epsilon} = C \tilde{\sigma}^n$

$$\dot{\epsilon} = C \left(\frac{\sigma_0 e^{\epsilon}}{(1 - \omega)} \right)^n = \frac{\dot{\epsilon}_0 e^{n\epsilon}}{(1 - \omega)^n} \quad (\text{B.5})$$

This description is modified to the more general constitutive equation which accounts for embrittlement to produce the constitutive equations provided by Leckie and Hayhurst (Leckie & Hayhurst, 1977).

$$\dot{\epsilon} = \frac{\dot{\epsilon}_0 e^{n\epsilon}}{(1 - \omega)^v} \quad (\text{B.6})$$

where v is a parameter which is constant for given test conditions. Frequently this is paired with a second constitutive equation,

$$\dot{\omega} = \frac{\dot{\omega}_0 e^{k\epsilon}}{(1 - \omega)^r} \quad (\text{B.7})$$

k and r are considered constants for the given conditions. These equations are given as Equation 89.1 by Rabotnov (Rabotnov, 1969) and Equation 2.61 by Kachanov (Kachanov, 1986). The equations are not conveniently integrated to give the functions of time and strain necessary for remnant life calculations (Prager, 1995, 2000). It is widely remarked that insufficient attention to the interpretation of the damage parameter, discrepancies in engineering and true strain, and unrealistic boundary conditions provide unsatisfying time to failure calculations.

B.3 Voight, A Relation to Describe Rate-Dependent Material Behaviour

The work of Voight provides a simple mathematical proposition that relates the rate of change of measured quantity to the measured quantity (Voight, 1989). Voight's proposition is significant as it allows the formulation of predictive time to failure calculations by its integration and application of appropriate initial conditions. His proposition is the terminal stages of rate-dependent material failure obey:

$$\dot{\Gamma}^{-\alpha}\ddot{\Gamma} - A = 0 \quad (\text{B.8})$$

where Γ is a measurable quantity, in this case strain, and α and A are 'constants of experience'. The simple relation has been demonstrated in a range of different rate dependent failure mechanisms extending most notably to geophysics and the prediction of volcanic eruptions, earthquakes and other structural failures (Cornelius & Scott, 1993; Voight, 1989). Even in this very diverse set of processes, the constant α frequently approaches 2 as is the case with creep. To demonstrate how creep strain agrees with Voight's proposition he considers only the effect of cross section loss due to deformation. He starts with the familiar Norton power law,

$$\dot{\epsilon} = C\sigma^n \quad (\text{B.9})$$

where in this case ϵ is true strain and σ is true stress defined by the ratio of instantaneous load, P and area, A . The instantaneous cross section is related to the true strain by $e^\epsilon = \frac{A}{A_0}$ and by consequence $\sigma = \sigma_0 e^\epsilon$. Therefore relating the true stress to the initial stress, σ_0 ,

$$\dot{\epsilon} = C\sigma_0^n e^{n\epsilon} = \dot{\epsilon}_0 e^{n\epsilon} \quad (\text{B.10})$$

Differentiating gives the Voight formulation,

$$\dot{\epsilon}^{-2}\ddot{\epsilon} - n = 0 \quad (\text{B.11})$$

Voight's proposition is significant as it allows the formulation of predictive time to failure calculations by its integration and application of appropriate boundary conditions. Such calculations have been demonstrated across numerous subject areas.

Integration of Equation B.11 with the condition that at the time of failure, t_f , the strain rate is $\dot{\epsilon}_f$ gives

$$(t_f - t) = \frac{1}{n} \left[\frac{1}{\dot{\epsilon}} - \frac{1}{\dot{\epsilon}_f} \right] \quad (\text{B.12})$$

Assuming that the strain rate at failure is very large, the final term can be neglected, providing the key result that time to failure can be extrapolated from inverse rate versus time data.

The limitation of the formulation provided by Voight is that it is assumed that deformation is the only damage mechanism. It is realised that the reduction in cross sectional area alone cannot account for all of the increase in strain rate (Leckie & Hayhurst, 1977; Prager, 1995). Following from the definitions and work already described in Section B.2 it is also necessary to account for the loss in strength of the remaining area by including the damage parameter.

B.4 Materials Testing Council –The Omega Method

The Omega method, developed by the Materials Testing Council offers a bridge between the damage parameter concepts of Kachanov and Rabotnov and the predictive formulation of Voight’s postulation.

Starting from Equation B.6, repeated here,

$$\dot{\epsilon} = \frac{C\sigma_0^n e^{n\epsilon}}{(1-\omega)^v} = \frac{\dot{\epsilon}_0 e^{n\epsilon}}{(1-\omega)^v} . \quad (\text{B.13})$$

Prager notes that this is not conveniently integrated. Rather than using the above power function, the damage is assumed to be strain controlled (Evans & Wilshire, 1993; Prager, 1995, 2000; Wilshire & Burt, 2005). Clearly, for some damage mechanisms this is a significant over simplification but it has the distinct benefit that it includes only the measured parameter, strain, and therefore does not rely on periphery measurements. It was suggested that creep rate acceleration during service could be viewed as a result of three or more separate factors, deformation, increasing damage and ‘other microstructural changes not associated with damage’ (Prager, 1995, 2000).

$$\dot{\epsilon} = \dot{\epsilon}_0 e^{n\epsilon} \times \frac{1}{e^{-p\epsilon}} \times \frac{1}{e^{-c\epsilon}} \quad (\text{B.14})$$

where n remains the Norton’s stress exponent to account for changes in cross section, p corresponds to strain controlled damage and c is explained to be used to account for deficiencies in Norton’s exponent. Equation B.14 can be rewritten,

$$\dot{\epsilon} = \dot{\epsilon}_0 e^{(n+p+c)\epsilon} \quad (\text{B.15})$$

Prager uses the notation $\Omega = n + p + c$. It is explained that Ω defines the rate at which strain accelerates as a result of creep strain. It is described as a ‘total damage coefficient’ which quantitatively describes the ability of a material to tolerate strain. Equation B.15 is exactly comparable to Equation B.10 and it therefore follows that,

$$(t_f - t) = \frac{1}{\Omega} \left[\frac{1}{\dot{\epsilon}} - \frac{1}{\dot{\epsilon}_f} \right] \quad (\text{B.16})$$

As before, assuming the strain rate at failure is large then we arrive at the result:

$$(t_f - t) = \frac{1}{\dot{\epsilon}\Omega} \quad (\text{B.17})$$

It is also worth noting that the well-known simplified Monkman-Grant relation (Monkman & Grant, 1956) is a compatible with Equation B.17,

$$t_f = \frac{M}{\dot{\epsilon}} \quad (\text{B.18})$$

where M is a constant.

B.5 Discussion

The work of Prager therefore provides the required proportionality between remnant life and inverse true strain rate and, importantly, does so by including both area loss through deformation and internal damage mechanisms. It is appropriate to dedicate the discussion of this Appendix to the consideration of the approximations and assumptions necessary fulfil Equations B.1 and B.2.

1) Constant Load and Constant Temperature

Inferring component state from strain rate must rely on the assumption of nominally constant load and temperature; the increase in strain rate must be attributable to changes in the component as opposed to changes in conditions. It is considered that this assumption is reasonable as the components will be exposed to a target operating pressure and temperature. As creep is highly stress and temperature sensitive (Evans & Wilshire, 1993) it is reasonable to assume that creep during shut downs or reduced load operation can be neglected. Long term, ‘strategic’, changes in operating conditions (for example switching to a different pressure) are believed to be infrequent in the majority of stations. At each long-term change in operating condition the remnant life estimation procedure will have to be restarted.

It is also worth noting that any prediction will be better informed by the collection of numerous data sources, for example stress and temperature.

2) Influence of Multiaxial Stress State

The final form of Equation B.15 relies on the assumption of uniaxial loading. As revealed by Equation 4.5 of Chapter 4 the strain rate is actually shear dominated and is therefore a function of the equivalent stress as opposed to the individual stress components. For situations where deformation is considered to be a dominant damage mechanism Equation B.15 will have to be slightly modified

accordingly. However, for real power station components the increase in strain rate is believed to be overwhelmingly attributed to internal damage mechanisms and the influence of deformation becomes diminishingly small. As internal damage accumulates the effective equivalent stress will increase, causing a symptomatic increase in strain rate in each direction; consistent with Equation B.15.

3) Isotropic Damage

There is a tendency for grain boundary separation to occur predominantly on boundaries normal to the maximum stress direction (Evans & Wilshire, 1993). This observation undermines the assumption from a microstructural perspective. However, it is noted by Naumenko and Altenbach (Naumenko & Altenbach, 2007) that if an initially isotropic material is subjected to constant or monotonic loading the influence of the damage anisotropy on the strain-time response is not significant.

4) Constant Volume

The constriction of the cross-sectional area is equal to $e^{-\epsilon}$. The resulting increase in strain rate is equal to $e^{n\epsilon}$ following the Norton power law.

5) The increase in strain rate as a result of microstructural evolution is strain controlled.

The assumed form of the increase in strain rate resulting from microstructural evolution (not constriction) obeys the following relation.

$$\frac{\dot{\epsilon}}{\dot{\epsilon}_0 e^{n\epsilon}} = \frac{1}{(1 - \omega)^v} = (e^\epsilon)^{(\Omega - n)} \quad (\text{B.19})$$

This is a reasonable approximation for cavitation. The area fraction of intergranular cavities has been observed to increase uniformly with accumulated creep strain (Cane, 1981). It is however conceded that otherwise a microstructurally stable material is assumed and that this is a deficiency in the approach of Prager (Prager, 1995, 2000). With reference to micromechanically-consistent models (Ashby & Dyson, 1984; Dyson, 2000; Perrin & Hayhurst, 1996), cavitation is the only damage mechanism that is considered to be a function of strain. Carbide coarsening for example is considered to be predominantly a function of temperature and may occur in the absence of strain. While this is seen as a limitation, it is inherent in any purely strain based model. As the relationship between strain and strain rate is being constantly evaluated it is possible to reevaluate Ω which may help take into account the effect of ageing.

6) $\frac{1}{\dot{\epsilon}_f}$ is negligible.

The error in remnant life estimation associated with this assumption is proportional to the ratio of current strain rate and failure strain rate. There is little available direct evidence to indicate what the failure strain rate would be in power station conditions; to obtain this data would require running

representative creep tests to failure which may take decades. The work of Penny is noteworthy here (Penny & Marriott, 1995; Penny, 1996). It is suggested that failure does not occur when there is no remaining effective cross sectional area with an infinite strain rate but rather at some earlier point where the remaining cross section can no longer sustain the applied load. This failure criterion is a function of the fraction of the initial nominal stress to failure stress; much more damage or loss of area can be sustained before the effective stress reaches the failure stress if the initial stress is low. The failure stress is dictated by how brittle the material is but is assumed to be bound by the yield and ultimate tensile stress at that temperature. The relatively low stresses in power station components (compared to accelerated tests) suggest that a good deal of damage may be sustained before failure and therefore strain rate at failure will be large.

B.6 Conclusion

The reliability of the remnant life calculations is to be considered in the context of these assumptions. The simple relationships of Equations B.1 and B.2 are intended as a limited scope illustration of the potential utility of strain rate based measurements. The relations have been selected as are dependent purely on strain information and rely on no periphery information. It is intended however that strain based measurements may be accommodated into multi-parameter models which may account for many of the assumptions discussed.

Appendix C

Uncertainty of Linear Rate Estimates

Calculated from a Series of Measurements

This appendix presents the analysis required to calculate the expected uncertainty of a rate estimate calculated from a series of points, each with an associated random uncertainty. This is crucial in order to evaluate the expected performance of rate measurement systems and also to inform measurement strategy. The theory in this Appendix is the work of Prof. Peter Cawley.

The objective of this Appendix is to derive an expression for the uncertainty of the gradient estimate for a given confidence level; for example $b \pm \Delta b$ at 95% confidence interval. To do so we start with the model that N measurements are taken at a measurement repetition frequency of f_m over a total length of time, t_m , each measurement has a standard error of σ as shown in Figure C.1.

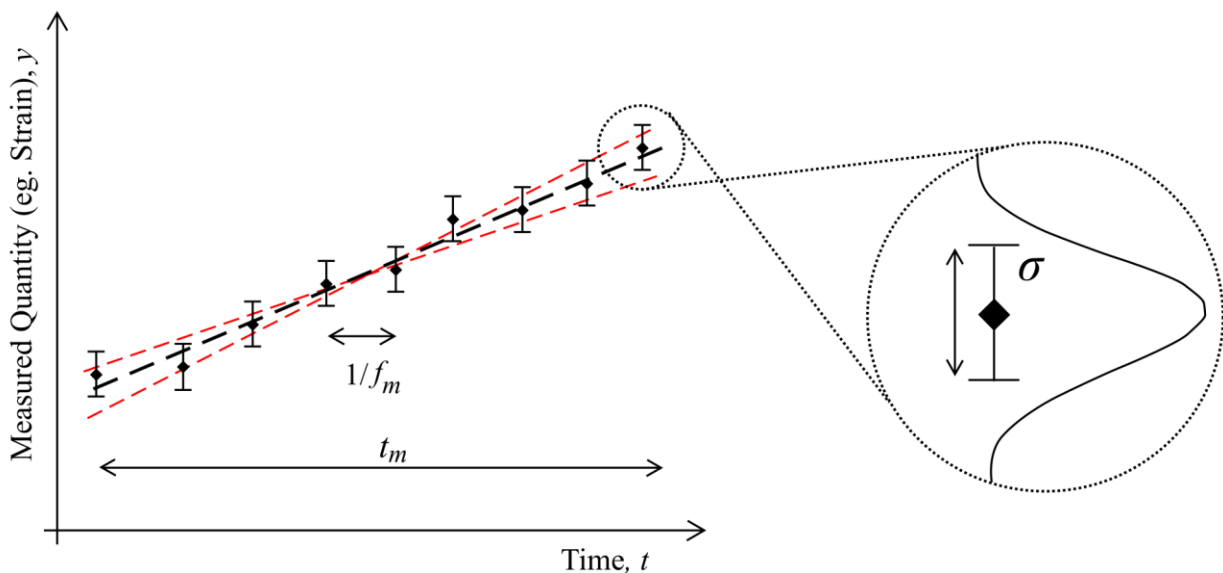


Figure C.1: Schematic showing an estimate of a gradient from a series of measurements, each with a given uncertainty. This Appendix is dedicated to evaluating the uncertainty of the gradient estimate, illustrated by the red dashed lines.

The standard error, S , of the straight line fit is the square root of the sum of the squares of the deviations from the straight line,

$$S^2 = \sum_{i=1}^N (y_i - a - bt_i)^2 \quad (C.1)$$

where (t_i, y_i) are measurement pairs. The standard error of the gradient is related to the individual measurement standard deviation, σ , according to,

$$S^2 = (N - 2)\sigma^2 \quad (C.2)$$

It can be shown (Bulmer, 1979) that the variance of the gradient estimate is given by,

$$\sigma_{grad}^2 = \frac{S^2}{(N - 2) \sum_{i=1}^N (t_i - \bar{t})^2} = \frac{\sigma^2}{\sum_{i=1}^N (t_i - \bar{t})^2} \quad (C.3)$$

where \bar{t} is the mean time of the measurement $\approx t_m/2$. If the individual thickness readings are normally distributed, the slope follows a 't' distribution with $(N - 2)$ degrees of freedom. However, we are interested in large numbers of readings so the 't' distribution is approximately normal (for $N > 25$, the error is under 10%). Therefore,

$$\Delta b = \sigma_{grad} P \quad (C.4)$$

P is the 't score' which is a function of N and the desired level of confidence. However, if N is large then P becomes independent of N (the distribution becomes normal as discussed above) and P is as given in Table C.1.

Table C.1: Values of P for at different confidence levels.

Confidence Level (%)	P
90	1.645
95	1.960
99	2.576

Now,

$$t_i = (i - 1)\Delta t \quad (C.5)$$

and,

$$\bar{t} = \frac{(N - 1) \Delta t}{2} \quad (C.6)$$

so,

$$\sum_{i=1}^N (t_i - \bar{t})^2 = \Delta t^2 \sum_{i=1}^N \left((i-1) - \frac{(N+1)^2}{2} \right)^2. \quad (\text{C.7})$$

Expanding gives,

$$\sum_{i=1}^N (t_i - \bar{t})^2 = \Delta t^2 \sum_{i=1}^N \left(i^2 - (N+1)i + \frac{(N+1)^2}{4} \right)^2. \quad (\text{C.8})$$

Using standard expressions for sums of series in i^2 and i gives,

$$\sum_{i=1}^N (t_i - \bar{t})^2 = \Delta t^2 \left(\frac{2N^3 + 3N^2 + N}{6} - \frac{N(N+1)^2}{2} + \frac{N(N+1)^2}{4} \right) \quad (\text{C.9})$$

which reduces to,

$$\sum_{i=1}^N (t_i - \bar{t})^2 = \frac{\Delta t^2}{12} (N^3 - N) \quad (\text{C.10})$$

Equation C.3 into Equation C.4 gives,

$$\Delta b = \sigma_{grad P} = \frac{\sigma P}{\sqrt{\sum_{i=1}^N (t_i - \bar{t})^2}} \quad (\text{C.11})$$

And then Equation C.10 into C.11 gives,

$$\Delta b = \frac{\sigma P \sqrt{12}}{\Delta t \sqrt{N^3 - N}} \approx \frac{\sigma P \sqrt{12}}{\Delta t N^{3/2}} \quad (\text{C.12})$$

as N is large. Using the terms introduced in Figure C.1, $\Delta t = 1/f_m$ and $N = T f_m$ so,

$$\Delta b = \frac{\sigma P \sqrt{12}}{T \sqrt{N}} \quad (\text{C.13})$$

This result is used in Section 5.2.1.

References

- Abe, F. Grade 91 heat-resistant martensitic steel. In A. Shibli (Ed.), *Coal Power Plant Materials and Life Assessment* (pp. 3–51). Woodhead Publishing Limited., 2014
- Abe, F. Introduction. In F. Abe, T. Kern, & R. Viswanathan (Eds.), *Creep-Resistant Steels* (p. 700). Elsevier., 2008
- Abson, D. J., & Rothwell, J. S. Review of type IV cracking of weldments in 9–12%Cr creep strength enhanced ferritic steels. *International Materials Reviews*, **58**(8), 437–473., 2013
- Allwood, F. P., & Wilson, J. D. Creep strain management of power plant components. In F. S. Chau & C. T. Lim (Eds.), *Intl. Conf. on Experimental Mechanics: Advances and Applications* (pp. 238–243). International Society for Optics and Photonics., 1997
- API 579-1/ASME FFS-1 (2007). API/ASME., 2007
- Aramis. GOM mbH., 2012
- Ashby, M. F., & Dyson, B. F. Creep Damage Mechanics and Micromechanisms. In *Proceedings of International Congress on Fracture.*, 1984
- ASTM. E1319 – 98, Standard Guide for High-Temperature Static Strain Measurement (Vol. 88, pp. 2010–2012)., 2012
- Auerkari, P., Brown, T. B., Dean, D. W., Dogan, B., Hales, R., Holdsworth, S. R., ... Vilhelmsen, T. *ECCC Recommendations, High Temperature Component Analysis Overview of Assessment & Design Procedures.*, 2005
- B31.1 (2007). ASME., 2007
- Bailey, N. *Weldability of Ferritic Steels*. Woodhead Publishing., 1994
- Balandin, A. Low-frequency 1/f noise in graphene devices. *Nature Nanotechnology*, **8**(8), 549–55., 2013
- Baumann, B., & Schulz, M. Long-time high-temperature strain gauge measurements on pipes and dissimilar welds for residual lifetime evaluation. *Nuclear Engineering and Design*, **130**(3), 383–388., 1991
- BOC. IPRM 2007, Consumables (pp. 373–387)., 2007
- Bowler, N. Theory of four-point alternating current potential drop measurements on a metal half-space. *Journal of Physics D: Applied Physics*, **39**, 584–589., 2006
- Brett, C. Personal Communication. E.ON., 2015
- Brett, S. Cracking Experience in Steam Pipework Welds in National Power. In *Conference Proceeding on Materials and Welding Technology in Power Plants*. VGB, Essen, Germany., 1994

-
- Brett, S., Buchanan, L. W., Concari, S., Cosso, G. L., Fenton, S., Fleming, A., ... Seliger, P. *ECCC Recommendations, Residual Life Assessment and Microstructure.*, 2005
- British Energy Generation. R5: Assessment procedure for the high temperature response of structures. Gloucester, UK., 1999
- BS EN 13480-3 (2012). BSI Standards Ltd., 2012
- Bulmer, M. G. *Principles of Statistics*. Dover Publications, Inc., 1979
- Byeon, J. W., & Kwun, S. I. Nondestructive Evaluation of Thermally Degraded 2 . 25Cr – 1Mo Steel by Electrical Resistivity Measurement, **44(6)**, 1204–1208., 2003
- Callister, W. D. *Materials Science and Engineering: An Introduction* (7th ed.). John Wiley & Sons, Inc., 2006
- Cane, B. J. Creep fracture of dispersion strengthened low alloy ferritic steels. *Acta Metallurgica*, **29(9)**, 1581–1591., 1981
- Cane, B. J. Remaining creep life estimation by strain assessment on plant. *International Journal of Pressure Vessels and Piping*, **10**, 11–30., 1982
- Cane, B. J., & Williams, J. Remaining life prediction of high temperature materials. *International Materials Reviews.*, 1987
- Cegla, F. B., Cawley, P., Allin, J., & Davies, J. High-temperature (>500°C) wall thickness monitoring using dry-coupled ultrasonic waveguide transducers. *IEEE Transactions on Ultrasonics, Ferroelectrics, and Frequency Control*, **58(1)**, 156–167., 2011
- Ceresara, S., & Fiorini, P. Resistometric investigation of the ageing process after quenching and cold-work in Al-Zn-Mg alloys. *Materials Science and Engineering*, **10(1)**, 205–210., 1972
- Cerjak, H., & Mayr, P. Creep Strength of Welded Joints of Ferritic Steels. In F. Abe, T.-U. Kern, & R. Viswanathan (Eds.), *Creep Resistant Steels* (pp. 472–503). Cambridge: Woodhead Publishing Limited., 2008
- Chen, Z. J., Govindaraju, M. R., Jiles, D. C., & Biner, S. B. Assessment of creep damage of ferromagnetic material using magnetic inspection. *IEEE Transactions on Magnetics*, **30(6)**, 4596–4598., 1994
- Coleman, K., & Newell, W. F. P91 and Beyond, Welding the new-generation Cr-Mo alloys for high-temperature service. *Welding Journal.*, 2007
- Comsol. Comsol Inc., 2012
- Cornelius, R. R., & Scott, P. a. A materials failure relation of accelerating creep as empirical description of damage accumulation. *Rock Mechanics and Rock Engineering*, **26**, 233–252., 1993
- CSNDT/Eddy Current Technology. Conductivity Of Metals Sorted By Resistivity. In www.eddy-current.com/conductivity-of-metals-sorted-by-resistivity/, 2015
-

-
- Dean, D. W. Personal Communication. EDF., 2014
- Devine, M. K., & Jiles, D. C. Effects of high temperature creep on magnetic properties of steels. *1992. Digests of InterMag. International Magnetism Conference*, **28**(5), 2465–2466., 1992
- Dyos, G. T., & Farrell, T. *Electrical Resistivity Handbook*. Peter Peregrinus Ltd., 1992
- Dyson, B. Use of CDM in Materials Modeling and Component Creep Life Prediction. *Journal of Pressure Vessel Technology*, **122**(3), 281., 2000
- Ellis, F. V. EPRI TR-108971, Review of Type IV Cracking in Piping Welds., 1997
- Ennis, P. J., & Czyrska-Filemonowicz, A. Recent advances in creep-resistant steels for power plant applications. *Sadhana*, **28**, 709–730., 2003
- EPRI. Fossil Plant High-Energy Piping Damage: Theory and Practice, Volume 1: Piping Fundamentals (Vol. 1)., 2007
- EPRI. *Guidelines for the Evaluation of Seam-Welded High-Energy Piping, CS-4774.*, 2003
- Evans, R. W., & Wilshire, B. *Introduction to creep*. Institute of Materials., 1993
- Fidler, R. The calibration of CERL-Planer capacitance strain gauges. *Strain*, **22**(4), 171–177., 1986
- Fortmann, M. D.-I. Vorrichtung zur Dehnungsmessung. Germany: European Patent Office., 1983
- Furtado, H. C., & May, I. Le. High temperature degradation in power plants and refineries. *Materials Research*, **7**(1), 103–110., 2004
- Ghia, S., Certo, M., De Michelis, C., & Rizzi, L. On-line monitoring and non destructive techniques for measurement of creep deformation. In A. Bicego, A. Nitta, & R. Viswanathan (Eds.), *Materials Ageing and Component Life Extension.*, 1995
- Gooch, D. J. Remnant Creep Life Prediction in Ferritic Materials. In I. Milne, R. O. Ritchie, & B. L. Karihaloo (Eds.), *Comprehensive Structural Integrity* (Vol. 5, pp. 309–359). Newnes., 2007
- Govindaraju, M. R., Kaminski, D. a., Devine, M. K., Biner, S. B., & Jiles, D. C. Nondestructive evaluation of creep damage in power-plant steam generators and piping by magnetic measurements. *NDT & E International*, **30**(1), 11–17., 1997
- Hoffmann, K. An Introduction to Stress Analysis and Transducer Design using Strain Gauges. HBM Test and Measurement., 1987
- Jiles, D. C. *Introduction to Magnetism and Magnetic Materials, Second Edition*. CRC Press., 1998
- Johnson, J. B. The Schottky effect in low frequency circuits. *Physical Review*, **26**(1), 71–85., 1925
- Kachanov, L. *Introduction to continuum damage mechanics*. Springer Science & Business Media., 1986

- Karimian, N., Wilson, J. W., Peyton, A. J., Yin, W., Liu, J., & Davis, C. L. Differential permeability behaviour of P9 and T22 power station Steels. *Journal of Magnetism and Magnetic Materials*, **352**(1), 81–90., 2014
- Karimian, N., Yin, W., Liu, J., Hao, X. J., Strangwood, M., Davis, C. L., & Peyton, A. J. Non-contact em measurement of the properties of power station steels taken from service. *IEEE Instrumentation and Measurement Technology Conference*, 1573–1578., 2013
- Kassner, M. E., & Hayes, T. a. Creep cavitation in metals. *International Journal of Plasticity*, **19**(10), 1715–1748., 2003
- Kittel, C. *Introduction to Solid State Physics* (Vol. 11). Wiley., 2004
- Lasek, J. A resistometric investigation of the decomposition kinetics of Al-21·8 at.% Zn solid solution at 276 °C. *Czechoslovak Journal of Physics*, **26**(3), 189–198., 1976
- Le May, I., & Furtado, H. C. Creep damage assessment and remaining life evaluation. *International Journal of Fracture*, **97**, 125–135., 1999
- Leckie, F. A., & Hayhurst, D. R. Constitutive equations for creep rupture. *Acta Metallurgica*, **25**(9), 1059–1070., 1977
- Liu, J., Hao, X. J., Zhou, L., Strangwood, M., Davis, C. L., & Peyton, a. J. Measurement of microstructure changes in 9Cr–1Mo and 2.25Cr–1Mo steels using an electromagnetic sensor. *Scripta Materialia*, **66**(6), 367–370., 2012
- Liu, J., Strangwood, M., Davis, C. L., & Peyton, A. J. Magnetic evaluation of microstructure changes in 9Cr-1Mo and 2.25Cr-1Mo steels using electromagnetic sensors. *Metallurgical and Materials Transactions A: Physical Metallurgy and Materials Science*, **44**(13), 5897–5909., 2013
- Liu, J., Wilson, J., Strangwood, M., Davis, C. L., Peyton, A. J., & Parker, J. D. Electromagnetic evaluation of the microstructure of Grade 91 tubes / pipes, **132**, 65–71., 2015
- Madhi, E. *In-Situ Creep Monitoring Using Directional Potential Drop Sensors*. University of Cincinnati., 2010
- Madhi, E., & Nagy, P. B. Material Gauge Factor of Directional Electric Potential Drop Sensors for Creep Monitoring, **1233**(2011), 1233–1240., 2011a
- Madhi, E., & Nagy, P. B. Sensitivity analysis of a directional potential drop sensor for creep monitoring. *NDT and E International*, **44**(8), 708–717., 2011b
- Maharaj, C., Dear, J. P., & Morris, a. A review of methods to estimate creep damage in low-alloy steel power station steam pipes. *Strain*, **45**, 316–331., 2009
- Masuyama, F. Creep degradation in welds of Mod.9Cr-1Mo steel. *International Journal of Pressure Vessels and Piping*, **83**, 819–825., 2006
- Matelect Ltd. AC or DC, A Primer for Decision Makers. Matelect Ltd., 2015
- Matlab. The Mathworks, Inc., 2014

-
- Mayer, K.-H., & Masuyama, F. The development of creep-resistant steels. In F. Abe, T. Kern, & R. Viswanathan (Eds.), *Creep-Resistant Steels* (p. 700). Elsevier., 2008
- McMaster, R. C. Electric current test principles. In *Nondestructive Testing Handbook* (1st ed., pp. 35.1–35.11). New York: Ronald Press., 1959
- McMaster, R. C., McIntire, P., & Mester, M. L. (Eds.). *Nondestructive Testing Handbook, Volume 4: Electromagnetic Testing* (2nd ed.). McGraw-Hill Education., 1986
- Mitra, a, Mohapatra, J. N., Swaminathan, J., Ghosh, M., Panda, a K., & Ghosh, R. N. Magnetic evaluation of creep in modified 9Cr – 1Mo steel, *57*, 813–816., 2007
- Monkman, F. C., & Grant, N. J. An Empirical Relationship Between Rupture Life and Minimum Creep Rate in Creep-Rupture Tests. In *ASTM Proceeding* (pp. 593–620)., 1956
- Morris, A. Personal Communication. EDF., 2015a
- Morris, A. Personal Communication., 2015b
- Morris, A., Dear, J., & Kourmpetis, M. High temperature steam pipelines - Development of the ARCMAC creep monitoring system. *Strain*, **42**, 181–185., 2006
- Morris, A., Kourmpetis, M., Dear, J., Puri, A., & Maharaj, C. Resolution of Creep Strain Measurements Using the ARCMAC Strain Monitoring System. In *ASME 2007 Pressure Vessels and Piping Conference* (pp. 25–33). American Society of Mechanical Engineers., 2007
- Nagy, P. B. Electromagnetic Nondestructive Evaluation. In T. Kundu (Ed.), *Ultrasonic and Electromagnetic NDE for Structure and Material Characterization: Engineering and Biomedical Applications* (p. 890). CRC Press., 2012
- Naumenko, K., & Altenbach, H. *Modeling of Creep for Structural Analysis*. Springer Berlin Heidelberg., 2007
- Neubauer, B., & Wedel, U. Restlife estimation of creeping components by means of replicas. *Advances in Life Prediction Methods*., 1983
- Noltingk, B. E. Measuring static strains at high temperatures. *Experimental Mechanics*, **14**(10), 420–423., 1974
- Oh, Y., Machmeier, P. M., Matuszewski, T., & Ayer, R. Evaluation of the nucleation and coarsening kinetic behavior of the secondary hardening carbide of Fe-HCo-10Ni-1Mo-0.16C steel at two chromium levels, using an analytical and modeling approach: Part II. *Journal of Materials Engineering and Performance*, **6**(3), 289–296., 1997
- Packard, K., & Morrett, B. The lowdown on low-alloy filler metals. *The Fabricator*., 2008
- Parker, J. D. Failures in Seam-welded Components. *Component Matters, EPRI*., 2014a
- Parker, J. D. Life Prediction of Cylindrical Components Operating Under High Temperature Creep Conditions. In B. Dooley & R. Vaswanathan (Eds.), *Life Extension and Assessment of Fossil Power Plants* (pp. 503–515). Washington D.C., 1986

-
- Parker, J. D. Review of the Application of Metallurgical Replicas to Detection of Component Damage. *Component Matters, EPRI.*, 2014b
- Parker, J. D., & Parsons, a W. J. High temperature deformation and fracture processes in 2 1/4Cr1/2Mo1/2Cr1/2Mo1/4V weldments, **161**(94), 45–54., 1995
- Pelloux, R. M., Peltier, J. M., & Zilberstein, V. a. Creep Testing of 2.25 Cr-1 Mo Welds by DC Potential Drop Technique. *Journal of Engineering Materials and Technology*, **111**(1), 19., 1989
- Penny, R. K. The use of damage concepts in component life assessment. *International Journal of Pressure Vessels and Piping*, **66**(1-3), 263–280., 1996
- Penny, R. K., & Marriott, D. L. *Design for Creep*. Springer Science & Business Media., 1995
- Pepperhoff, W., & Acet, M. *Constitution and Magnetism of Iron and its Alloys*. Springer Science & Business Media., 2001
- PerkinElmer, Inc. What is a Lock-in Amplifier?, Technical Note TN1000m, PerkinElmer., 2015
- Permasense Ltd. www.permasense.com., 2015
- Perrin, I. J., & Hayhurst, D. R. Continuum damage mechanics analyses of type IV creep failure in ferritic steel crossweld specimens. *International Journal of Pressure Vessels and Piping*, **76**(9), 599–617., 1999
- Perrin, I. J., & Hayhurst, D. R. Creep constitutive equations for a 0.5Cr–0.5Mo–0.25V ferritic steel in the temperature range 600–675°C. *The Journal of Strain Analysis for Engineering Design*, **31**(4), 299–314., 1996
- Pollock, D. D. *Physical Properties of Materials for Engineers*. CRC Press., 1993
- Prager, M. Development of the MPC Omega Method for Life Assessment in the Creep Range. *Journal of Pressure Vessel Technology*, **117**(May 1995), 95., 1995
- Prager, M. The Omega Method – An Engineering Approach to Life Assessment. *Journal of Pressure Vessel Technology*, **122**(3)., 2000
- Prajapati, S., Nagy, P. B., & Cawley, P. Potential drop detection of creep damage in the vicinity of welds. *AIP Conference Proceedings*, **1430**(31), 417–424., 2012
- Rabotnov, Y. N. *Creep problems in structural members*. North-Holland Pub. Co., 1969
- Raj, B., Moorthy, V., Jayakumar, T., & Rao, K. B. S. Assessment of microstructures and mechanical behaviour of metallic materials through non-destructive characterisation. *International Materials Reviews*, **48**(5), 273–325., 2003
- Robertson, D. G. *Traditional low alloy steels in power plant design. Coal Power Plant Materials and Life Assessment*. Woodhead Publishing Limited., 2014
- Rossiter, P. L. *The Electrical Resistivity of Metals and Alloys*. Cambridge University Press., 1991

-
- Schüller, H. J., Hagn, L., & Woitscheck, A. Risse im Schweißnahtbereich von Formstücken aus Heißdampfleitungen – Werkstoffuntersuchungen. *Werkstoffuntersuchungen*, **47**(1), 1974
- Seok, C.-S., Bae, B.-K., & Koo, J.-M. DC Potential Drop Method for Evaluating Material Degradation. *KSME International Journal*, **18**(8), 1368–1374., 2004
- Servi, I. S., & Turnbull, D. Thermodynamics and Kinetics of Precipitation in the Copper-Cobalt System. *Acta Metallurgica*, **14**, 161–169., 1966
- Shafiro, B., & Kachanov, M. L. Anisotropic effective conductivity of materials with nonrandomly oriented inclusions of diverse ellipsoidal shapes. *Journal of Applied Physics*, **87**(12), 8561–8569., 2000
- Shibli, I. A., & Coleman, K. *Failures of P91 Steel at the West Burton Plant in England Raise Concerns About the Long Term Behaviour of the Advanced Steel.*, 2006
- Singh Raman, R. K., & Al-Mazrouee, a. High-temperature oxidation of Cr-Mo steels and its relevance to accelerated rupture testing and life assessment of in-service components. *Metallurgical and Materials Transactions A: Physical Metallurgy and Materials Science*, **38**(8), 1750–1759., 2007
- SJB Engineering, High Temperature Strain Gauges, On-line monitoring. Retrieved May 15, 2015, from www.sjbengineering.com/hightemp_monitoring.html#creep, 2015
- Sposito, G. *Advances in Potential Drop Techniques*. Imperial College London., 2009
- Sposito, G., Cawley, P., & Nagy, P. B. Potential drop mapping for the monitoring of corrosion or erosion. *NDT and E International*, **43**(5), 394–402., 2010
- Sposito, G., Ward, C., Cawley, P., Nagy, P. B., & Scruby, C. A review of non-destructive techniques for the detection of creep damage in power plant steels. *NDT and E International*, **43**, 555–567., 2010
- Stanford Research Systems Inc. Model SR830 DSP Lock-In Amplifier User Manual., 2011
- Stanford Research Systems, Inc. About Lock-In Amplifiers, Application Note #3., 2015
- Sutton, M. A., Ortu, J. J., & Schreier, H. *Image Correlation for Shape, Motion and Deformation Measurements: Basic Concepts, Theory and Applications*. Springer Science & Business Media., 2009
- Tan, K. S., Hopkins, S. C., Astill, D., Majoros, M., Glowacki, B. A., Takeuchi, T., & Inoue, K. In-situ Resistometry for Heat Treatment Monitoring and Control. Retrieved August 26, 2015, from <http://www.msm.cam.ac.uk/ascg/processes/resistometry.php>, 2015
- Tanner, D. W. J., Sun, W., & Hyde, T. H. Cross-Weld Creep Comparison of Power Plant Steels CrMoV, P91 and P92. *Journal of Pressure Vessel Technology*, **135**(2), 021408., 2013
- Taplin, D. M. R. *Advances in Research on the Strength and Fracture of Materials*. Elsevier., 2013
- Tatarnikov, V. M. Use of probes for measuring the electrical conductance of anisotropic plates. *Measurement Techniques*, (6), 46–49., 1970

- Thomson, R. C. *Carbide Composition Changes in Power Plant Steels as a Method of Remanent Life Prediction*. University of Cambridge., 1992
- TWI Ltd. Safety and reliability concerns with P91 pressure vessels and piping. In *TWI Connect*, No. 156., 2008
- Van Wortel, H. Reliability and Limitations of the Non Destructive Replica Technique for the Assessment of Creep Damage in Welded Components. In *Volume 9: Eighth International Conference on Creep and Fatigue at Elevated Temperatures* (pp. 567–572). ASME., 2007
- Van Zyl, F. H., von dem Bongart, G., Bezuidenhout, M. E. J., Doubell, P., Havinga, F. C., Pegler, D. A. H., ... Smit, W. Life Assessment and Creep Damage Monitoring of High Temperature Pressure Components in South Africa's Power Plant. In *ECCC Creep Conference* (pp. 934–945)., 2005
- Vasatis, I. P. *The Creep Rupture of Notched Bars of IN-X750*. Massachusetts Institute of Technology., 1986
- Vasatis, I. P., & Pelloux, R. M. Application of the dc potential drop technique in investigating crack initiation and propagation under sustained load in notched rupture tests. *Metallurgical Transactions A*, **19**(4), 863–871., 1988
- Vasilescu, G. *Electronic Noise and Interfering Signals: Principles and Applications*. Springer Science & Business Media., 2006
- VGB-Kraftwerkstechnik GmbH. VGB-TW 507, Guideline for the Assessment of Microstructure and Damage Development of Creep Exposed Materials for Pipes and Boiler Components. Essen., 1992
- Vishay Precision Group, Inc. Special Use Strain Gages, Document Number 11530 (pp. 112–113)., 2010
- Viswanathan, R. *Damage Mechanisms and Life Assessment of High Temperature Components*. ASM International., 1989
- Viswanathan, R. Life Management of High-Temperature Piping and Tubing in Fossil Power Plants. *Journal of Pressure Vessel Technology*, **122**(3), 305., 2000
- Viswanathan, R., & Stringer, J. Failure Mechanisms of High Temperature Components in Power Plants. *Journal of Engineering Materials and Technology*, **122**(July), 246., 2000
- Voight, B. A relation to describe rate-dependent material failure. *Science (New York, N.Y.)*, **243**(1986), 200–203., 1989
- Voss, R. F. 1/f (Flicker) Noise: A Brief Review. In *33rd Annual Symposium on Frequency Control* (pp. 40–46). IEEE., 1979
- Wasmer, K. *Prediction of Creep Crack Growth in a Range of Steels*. Imperial College London., 2003
- Webster, G., & Ainsworth, R. A. *High Temperature Component Life Assessment*. Springer Science & Business Media., 1994
- Weiss, R. J., & Marotta, a. S. Spin-dependence of the resistivity of magnetic metals. *Journal of Physics and Chemistry of Solids*, **9**(3-4), 302–308., 1959

-
- Wert, C., & Zener, C. Interference of growing spherical precipitate particles. *Journal of Applied Physics*, **21**(1), 5–8., 1950
- Wheeler, A. J., & Ganji, A. R. *Introduction to Engineering Experimentation*. Prentice Hall., 2010
- Willems, H., & Dobmann, G. Early detection of creep damage by ultrasonic and electromagnetic techniques. *Nuclear Engineering and Design*, **128**(1), 139–149., 1991
- Wilshire, B., & Burt, H. Creep Strain Analysis for Steel. In F. Abe, T. Kern, & R. Viswanathan (Eds.), *Creep-Resistant Steels* (p. 700). Elsevier., 2008
- Wilshire, B., & Burt, H. Damage Evolution during Creep of Steels. In I. A. Shibli, S. R. Holdsworth, & G. Merckling (Eds.), *Creep and Fracture in High Temperature Components: Design and Life Assessment Issues* (p. 1115). DEStech Publications, Inc., 2005
- Wilson, J. W., Karimian, N., Liu, J., Yin, W., Davis, C. L., & Peyton, A. J. Measurement of the magnetic properties of P9 and T22 steel taken from service in power station. *Journal of Magnetism and Magnetic Materials*, **360**, 52–58., 2014
- Yaghi, A. H., Hyde, T. H., Becker, A. A., & Sun, W. Finite element simulation of welded P91 steel pipe undergoing post-weld heat treatment. *Science and Technology of Welding and Joining*, **16**(3), 232–238., 2011
- Yin, Y. F., & Faulkner, R. G. Creep damage and grain boundary precipitation in power plant metals. *Materials Science and Technology*, **21**(11), 1239–1246., 2005a
- Yin, Y. F., & Faulkner, R. G. Multi-scale Modelling of Creep in Power Plant Ferritic Steels. In I. A. Shibli, S. R. Holdsworth, & G. Merckling (Eds.), *ECCC Creep Conference* (pp. 478–487)., 2005b
- Yu, K. M., Nahm, S. H., & Kim, Y. I. Toughness degradation evaluation of 1Cr – 1Mo – 0.25V steel by electrical resistivity, **8**, 1175–1176., 1999